# Effects of Strong Electron Correlations in Three-Dimensional Topological Phases

博士論文

# Effects of Strong Electron Correlations in Three-Dimensional Topological Phases

（3次元トポロジカル相における強相関効果の理論）

関根 聡彦

平成 26 年

Thesis

# EFFECTS OF STRONG ELECTRON CORRELATIONS IN THREE-DIMENSIONAL TOPOLOGICAL PHASES

AKIHIKO SEKINE

*Department of Physics, Tohoku University*

January 2015

# Contents

# Chapter 1

# Introduction

Conventionally, metals and insulators had been distinguished by the existence of band gaps. About a decade ago, a novel phase which does not belong to either metals or insulators, called the topological insulator, was found. It is notable that time-reversal invariant topological insulators have bulk band gaps but also have gapless surface states. Further, topologically nontrivial phases and trivial phases cannot be connected smoothly to each other. Namely, bulk band-gap closings are required for the transitions between topologically nontrivial and trivial phases. Topologically nontrivial and trivial phases are distinguished by the "topological invariant". They are calculated from the wave functions of systems. In addition, before the establishment of the concept of topological phases, different phases had been distinguished by the order parameters which indicate spontaneous symmetry breaking. For example, magnetism can be understood as a consequence of spontaneous spin rotational symmetry breaking. However, topological phases cannot be distinguished by order parameters. From the viewpoint of symmetry analysis, time-reversal invariant band insulators and time-reversal invariant topological insulators cannot be distinguished. Topological invariants are not local quantities in contrast to conventional order parameters.

Recent extensive studies have revealed that spin-orbit coupling is essential to realize topologically nontrivial phases. On the other hand, it has been known that electron correlations play significant roles in condensed matter. Recent theoretical studies have shown that the interplay of spin-orbit coupling and electron correlation can lead to various exotic phases and phenomena. Especially, it is interesting that topological phases can emerge in strongly correlated systems. This suggests that electron correlations can also play an important role to realize topological phases. However, preceding studies have mainly focused on the effects of short-range interactions. What happens as a result of strong long-range interactions? The effects of long-range interactions in topological phases have not yet been revealed. In Dirac fermion systems, the effects of long-range interactions are expected to be important, since the screening effect is considered to be weak due to the vanishing density of states near the Fermi level.

Based on these facts, the purpose of this thesis can be divided into two parts:
(I) We study the effects of long-range interactions in three-dimensional topological phases, focusing on their stability against strong long-range interactions.
(II) We search for novel phases and phenomena which result from the interplay of spin-orbit coupling and electron correlation.

In this chapter, we review theoretical and experimental aspects of various topological phases. According to historical order, we start from quantum Hall insulators which are characterized by the Chern number. Then we review two-dimensional and three-dimensional topological insula-

tors which are characterized by the $Z_2$ invariants. We also review novel topological phases, Weyl semimetals and Dirac semimetals. Here we emphasize that strong spin-orbit coupling is essential to realize topologically nontrivial phases. Finally we review the interplay of spin-orbit coupling and electron correlation.

This chapter is organized as follows. In Sect. 1.1, we introduce the topological invariant for time-reversal invariant topological insulators. In Sect. 1.2, we introduce the experimental and theoretical properties and the effective model of three-dimensional topological insulators of $Bi_2Se_3$ family. In Sect. 1.3, we introduce the theoretical properties and theoretical models of Weyl semimetals. In Sect. 1.4, we introduce the experimental and theoretical properties of Dirac semimetals. In Sect. 1.5, we introduce novel phases and phenomena induced by the interplay of spin-orbit coupling and electron correlation. We also introduce theoretical studies on electron correlation effects in topological phases.

This thesis is organized as follows. In Chap. 2, we review an approach to interacting Dirac fermion systems, the lattice gauge theory. We review the formulations for the lattice regularization of Dirac fermions, and the lattice regularization of gauge fields. Then we review applications of the lattice gauge theory to graphene, an interacting two-dimensional (2D) Dirac fermion system. In Chap. 3, we study the effects of strong $1/r$ Coulomb interactions in a 3D topological insulator. Based on the U(1) lattice gauge theory, we analyze the system from the strong coupling limit. We propose a possible global phase diagram of the system. In Chap. 4, we study the effects of strong $1/r$ Coulomb interactions in a time-reversal symmetry broken Weyl semimetal with two nodes. Based on the U(1) lattice gauge theory, we analyze the system from the strong coupling limit. We propose a possible global phase diagram of the system. In Chap. 5, the effects of strong $1/r$ Coulomb interactions in Dirac semimetals with four and sixteen nodes. Based on the U(1) lattice gauge theory, we analyze the system from the strong coupling limit. We propose a possible global phase diagram of the system. In Chap. 6, we study the effects of short-range interactions in a 3D spin-orbit coupled system. We present the mean-field phase diagram of the system. Then we focus on the topological magnetoelectric response of the antiferromagnetic insulator phase. Finally in Chap. 7, we summarize this thesis.

# 1.1 Topological Invariants

In this section, we review an important concept, the topological invariant, which characterizes a phase. According to historical order, we start from the quantization of the Hall conductivity in quantum Hall insulators, and then move on to a recently discovered phase, quantum spin Hall (or two-dimensional topological) insulators. Finally we consider the $Z_2$ invariant which distinguishes topologically nontrivial phases from trivial phases in the presence of time-reversal symmetry.

## 1.1.1 Quantum Hall Insulators

The Quantum Hall insulator is a kind of topologically nontrivial phases, where its topological invariant is given by the Chern number. In the following, we derive an important expression for the Hall conductivity of a 2D system, known as the TKNN formula [1]. Let us start from the Kubo formula for conductivity given by [2]

$$\sigma_{\mu\nu}(\omega) = \frac{1}{L^2} \int_0^\infty dt e^{i(\omega+i\delta)t} \int_0^\beta d\lambda \left\langle J_\nu(-i\hbar\lambda)J_\mu(t) \right\rangle_{\text{eq.}}, \tag{1.1}$$

where $H$ is the unperturbed Hamiltonian of a system, $\beta = 1/T$, $J_\mu(t) = e^{iHt}J_\mu e^{-iHt}$, and $\langle \cdots \rangle_{\text{eq.}} = \text{Tr}[e^{-\beta H} \cdots]/Z$ with $Z = \text{Tr}[e^{-\beta H}]$. With the eigenvalues and eigenstates such that $H|n\rangle = E_n|n\rangle$, the above equation is rewritten as

$$\sigma_{\mu\nu}(\omega) = -\frac{i\hbar}{L^2} \sum_{m,n} \frac{f(E_n) - f(E_m)}{E_n - E_m} \frac{\langle n|J_\mu|m\rangle\langle m|J_\nu|n\rangle}{\omega + E_n - E_m + i\delta}, \quad (1.2)$$

where we have replaced $e^{-\beta E_n}/Z$ by the Fermi distribution function $f(E_n)$. In a system with translational symmetry ($\mathcal{H}(\boldsymbol{k}) = E_{n\boldsymbol{k}}|u_{n\boldsymbol{k}}\rangle$) and with an energy gap in the Brillouin zone ($E_{m\boldsymbol{k}} \neq E_{n\boldsymbol{k}}$), the static Hall conductivity $\sigma_{xy}$ is given by

$$\sigma_{xy} = -\frac{i\hbar e^2}{L^2} \sum_{m \neq n} \sum_{\boldsymbol{k}} f(E_{n\boldsymbol{k}}) \frac{\langle u_{n\boldsymbol{k}}|v_x|u_{m\boldsymbol{k}}\rangle\langle u_{m\boldsymbol{k}}|v_y|u_{n\boldsymbol{k}}\rangle - \langle u_{n\boldsymbol{k}}|v_y|u_{m\boldsymbol{k}}\rangle\langle u_{m\boldsymbol{k}}|v_x|u_{n\boldsymbol{k}}\rangle}{(E_{n\boldsymbol{k}} - E_{m\boldsymbol{k}})^2}, \quad (1.3)$$

where $\boldsymbol{k}$ is the crystal momentum, the subscript $n$ (and $m$) denotes the $n$-th band, and we have used $J_\mu = -ev_\mu$. Noting that the velocity operator is written as $v_\mu = \frac{\partial \mathcal{H}(\boldsymbol{k})}{\hbar \partial k_\mu}$, and the relation $0 = \frac{\partial}{\partial k_\mu}\langle u_{n\boldsymbol{k}}|u_{m\boldsymbol{k}}\rangle = \langle \frac{\partial}{\partial k_\mu}u_{n\boldsymbol{k}}|u_{m\boldsymbol{k}}\rangle + \langle u_{n\boldsymbol{k}}|\frac{\partial}{\partial k_\mu}u_{m\boldsymbol{k}}\rangle$, we obtain the quantized Hall conductivity

$$\sigma_{xy} = \frac{e^2}{h}\nu \quad (1.4)$$

with

$$\nu = \sum_n \int \frac{d^2k}{2\pi}\left(\frac{\partial \mathcal{A}_{n,y}}{\partial k_x} - \frac{\partial \mathcal{A}_{n,x}}{\partial k_y}\right) = \sum_n \int \frac{d^2k}{2\pi}(\boldsymbol{\nabla} \times \mathcal{A}_n) \cdot \boldsymbol{e}_z \in \mathbb{Z}, \quad (1.5)$$

where $\mathcal{A}_n = -i\langle u_{n\boldsymbol{k}}|\boldsymbol{\nabla}_{\boldsymbol{k}}|u_{n\boldsymbol{k}}\rangle$ and the summation with respect to $n$ is done over all occupied bands. The integer $\nu$ is called the (first) Chern number. The quantity $\sigma_{xy} = \frac{e^2}{h}\nu$ is identical to the Hall conductivity in the case where $\nu$ Landau levels are occupied and the rest are empty (i.e., there is an energy gap). The Hall conductivity is invariant as long as the number of occupied Landau levels $\nu$ is not changed. Namely, the Chern number can be said to be a topological invariant, since it does not change when the Hamiltonian changes smoothly with finite energy gap.

## 1.1.2 Quantum Spin Hall Insulators

Recently discovered topologically nontrivial phases have attracted many researchers and offered a new direction in modern physics [3–5]. The pioneering works appeared in 2005, where the realization of a topologically nontrivial phase termed the "quantum spin Hall insulator" due to intrinsic spin-orbit coupling was discussed in graphene [6, 7]. Note that quantum spin Hall insulators are also called two-dimensional topological insulators. In quantum spin Hall insulators, the spin Hall conductivity $\sigma_{xy}^s$ takes the quantized value [6–8]

$$\sigma_{xy}^s = 2\frac{e^2}{h} \times \frac{\hbar}{2e} = \frac{e}{2\pi}, \quad (1.6)$$

where $J_x^s = \sigma_{xy}^s E_y$ with $J_x^s(\equiv J_x^\uparrow - J_x^\downarrow)$ being a spin current and $E_y$ being an electric field. The factor $\frac{\hbar}{2e}$ represents the conversion from the charge conductance to the spin conductance. Quantum spin Hall insulators can be considered as the superposition of two quantum Hall insulators
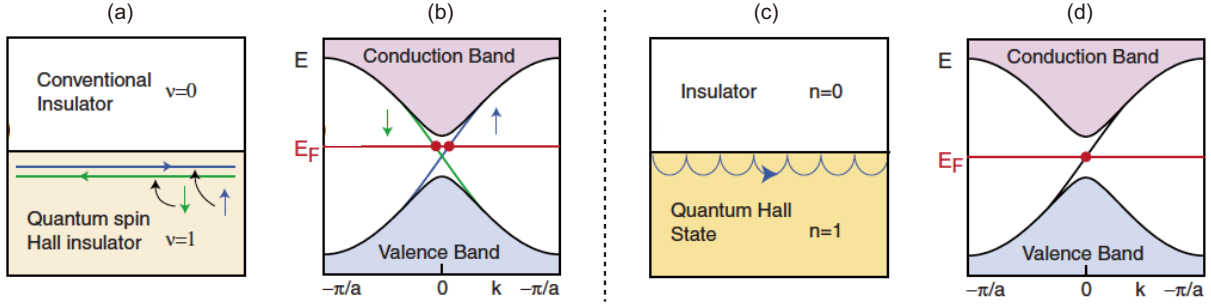
Figure 1.1: Schematic pictures of the (a) helical edge states and (b) energy spectrum in a quantum spin Hall insulator, and the (c) chiral edge states and (d) energy spectrum in a quantum Hall insulator [3].
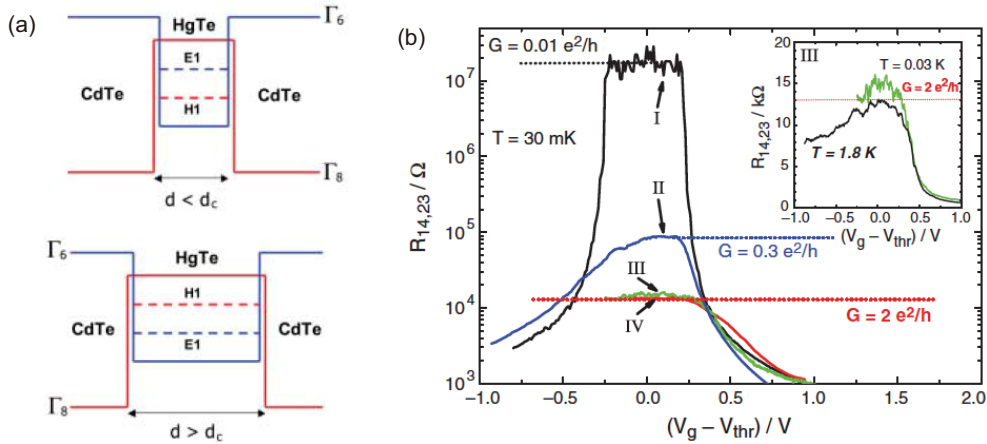


Figure 1.2: (a) Schematic diagram of energy bands near the Fermi level in HgTe/HgCdTe quantum well [9]. When the thickness of HgTe is larger than the critical value, the conduction and valence bands are inverted. In such a state, the quantum spin Hall effect emerges. (b) Experimentally observed longitudinal four-terminal resistance as a function of the gate voltage in HgTe/Hg$_{0.7}$Cd$_{0.3}$Te quantum well [10]. The Fermi level can be tuned by the gate voltage. The sample (I) [(II)-(IV)] is thinner (thicker) than the critical value. Although the samples (III) and (IV) are different in size, the resistivity is almost the same. This implies the direct evidence of the helical edge state.

with the chiral edge currents opposite to each other. Therefore, the Hall conductivity is zero, and time-reversal symmetry of the system is preserved. The most important feature of quantum spin Hall insulators is the existence of gapless helical edge states which are protected by time-reversal symmetry. Figures 1.1(a) and 1.1(b) show schematic pictures of the helical edge states and energy spectrum in a quantum spin Hall insulator, respectively. For comparison, those of the chiral edge states and energy spectrum in a quantum Hall insulator are shown in Figs. 1.1(c) and 1.1(d).

After the theoretical prediction in HgTe/CdTe quantum well [9], the first experimental observation of the quantum spin Hall effect in HgTe/Hg$_{0.7}$Cd$_{0.3}$Te quantum well was realized in 2007 [10]. Hg$_{1-x}$Cd$_x$Te is a semiconductor with strong spin-orbit coupling. As shown in Fig. 1.2(a), HgTe and CdTe have band structures opposite to each other near the Fermi level. In HgTe quantum well sandwiched by CdTe, the conduction and valence bands are inverted when the

thickness of HgTe is larger than the critical value. In such a state, the quantum spin Hall effect emerges. The mechanism of the emergence is the sign inversion of the mass of the Dirac fermions in the low-energy effective model [9], as in the case of three-dimensional topological insulators. Band inversion (or, equivalent, sign inversion of the mass of Dirac fermions) is essential to realize topologically nontrivial phases. In the experiment, the existence of the helical edge state was directly observed by measuring the longitudinal four-terminal resistance [see Fig. 1.2(b)]. Further, it was shown that in the presence of external magnetic fields, which break time-reversal symmetry of the system, the helical edge state is destroyed.

### 1.1.3 $Z_2$ Invariant

In the presence of time-reversal symmetry, topologically trivial and nontrivial phases can be distinguished by the "$Z_2$ invariant". Here let us define a time-reversal operator $\mathcal{T}$. When a system is time-reversal invariant, the single-particle Hamiltonian $\mathcal{H}(\boldsymbol{k})$ satisfies the relation $\mathcal{T}\mathcal{H}(\boldsymbol{k})\mathcal{T}^{-1} = \mathcal{H}(-\boldsymbol{k})$. Further let us define a unitary matrix $w_{ab}(\boldsymbol{k}) = \langle u_a(\boldsymbol{k})|\mathcal{T}|u_b(\boldsymbol{k})\rangle$ where $|u_b(\boldsymbol{k})\rangle$ is the Bloch functions of the occupied bands. Then we see that $w_{ba}(\boldsymbol{k}) = -w_{ab}(-\boldsymbol{k})$, due to the property $\mathcal{T}^2 = -1$. At the time-reversal invariant momenta in the Brillouin zone, namely at the momenta which satisfy $\boldsymbol{k} = -\boldsymbol{k}(\equiv \boldsymbol{\Lambda}_a)$, the matrix $w(\boldsymbol{\Lambda}_a)$ becomes antisymmetric. Recall that the determinant of a antisymmetric matrix is equal to the square of its Pfaffian, i.e., $\det[w(\boldsymbol{\Lambda}_a)] = \{\text{Pf}[w(\boldsymbol{\Lambda}_a)]\}^2$. This relation is equivalent to $\delta_a = \pm 1 = \text{Pf}[w(\boldsymbol{\Lambda}_a)]/\sqrt{\det[w(\boldsymbol{\Lambda}_a)]}$. The $Z_2$ invariant of the $d$-dimensional ($d$D) system is given by the product of all the $\delta_a$ in the Brillouin zone [7]:

$$(-1)^{\nu} = \prod_{a=1}^{2^d} \delta_a. \tag{1.7}$$

We see that $\nu$ can take two values, $\nu = 0, 1$. The $\nu = 1$ ($\nu = 0$) phases are called topologically nontrivial (trivial). This is a property of the bulk of a system. On the other hand, as mentioned above, topologically nontrivial phases (with $\nu = 1$) are characterized by the existence of gapless edge states (or surface states in three dimensions). This fact is referred to as the "bulk-boundary correspondence".

In the presence of spatial inversion (parity) symmetry, the $Z_2$ invariant has a simpler form given by [11, 12]

$$(-1)^{\nu} = \prod_{a=1}^{2^d} \prod_{m=1}^{N} \xi_{2m}(\boldsymbol{\Lambda}_a), \tag{1.8}$$

where $\xi_{2m}(\boldsymbol{\Lambda}_a)$ is the parity eigenvalue of the occupied $2m$-th band at the time-reversal invariant momenta $\boldsymbol{\Lambda}_a$, and $2N$ is the number of occupied bands. Note that the two Bloch states $|u_{2m-1}(\boldsymbol{k})\rangle$ and $|u_{2m}(\boldsymbol{k})\rangle$ has the same parity eigenvalue due to the Kramers degeneracy.

In three spatial dimensions, there exists the other three $Z_2$ invariants in addition to Eq. (1.7) [11–13]. The eight time-reversal invariant momenta $\boldsymbol{\Lambda}_i$ of a three-dimensional lattice system can be expressed as

$$\boldsymbol{\Lambda}_{a=(n_1 n_2 n_3)} = \frac{1}{2}(n_1 \boldsymbol{b}_1 + n_2 \boldsymbol{b}_2 + n_3 \boldsymbol{b}_3), \tag{1.9}$$

where $n_j = 0, 1$ ($j = 1, 2, 3$) and $\boldsymbol{b}_j$ are primitive reciprocal lattice vectors of the lattice. Then the three $Z_2$ invariant is given by [11, 12]

$$(-1)^{\nu_j} = \prod_{n_j=1;\; n_{i\neq j}=0,1} \delta_{a=(n_1 n_2 n_3)} \quad (j = 1, 2, 3). \tag{1.10}$$

The phases with $\nu = 0$ and at least one nonzero $\nu_j$ are referred to as "weak" topological insulators, while the phases with $\nu = 1$ are referred to as "strong" topological insulators. This is because weak topological insulators have even numbers of surface Dirac cones and the surface states are broken (i.e., becomes gapped) by disorder. On the other hand, strong topological insulators have odd numbers of surface Dirac cones and the surfaces states are robust against disorder. 3D topological insulators are usually labeled by the four $Z_2$ indices $(\nu; \nu_1 \nu_2 \nu_3)$.

In the following, we show that the calculation of the $Z_2$ invariant becomes much easier when the single-particle Hamiltonian of a system with time-reversal and inversion symmetries is represented in terms of matrices which satisfy the Clifford algebra. Let us define a single-particle Hamiltonian as $\mathcal{H}(\boldsymbol{k}) = \sum_{\mu=1}^{5} R(\boldsymbol{k}) \alpha_\mu$ with the $4 \times 4$ matrices $\alpha_\mu$ satisfying the Clifford algebra $\{\alpha_\mu, \alpha_\nu\} = 2\delta_{\mu\nu}\mathbf{1}$. Time-reversal $\mathcal{T}$ and spatial inversion (parity) $\mathcal{P}$ require the condition $\mathcal{T}\mathcal{H}(\boldsymbol{k})\mathcal{T}^{-1} = \mathcal{P}\mathcal{H}(\boldsymbol{k})\mathcal{P}^{-1} = \mathcal{H}(-\boldsymbol{k})$. To be concrete, we define the matrices $\alpha_\mu$ by the Dirac representation. Namely, we obtain

$$\alpha_j = \begin{bmatrix} 0 & \sigma_j \\ \sigma_j & 0 \end{bmatrix}, \quad \alpha_4 = \begin{bmatrix} 1 & 0 \\ 0 & -1 \end{bmatrix}, \quad \alpha_5 = \begin{bmatrix} 0 & -i \\ i & 0 \end{bmatrix}, \tag{1.11}$$

where $j = 1, 2, 3$ and $\sigma_j$ are the Pauli matrices. In this case, time-reversal and parity operators are written as $\mathcal{T} = \mathbf{1} \otimes (-i\sigma_2)\mathcal{K}$ ($\mathcal{K}$ is the complex conjugation operator) and $\mathcal{P} = \sigma_3 \otimes \mathbf{1}$. Then we see that

$$\begin{aligned} \mathcal{T}\alpha_\mu\mathcal{T}^{-1} &= \mathcal{P}\alpha_\mu\mathcal{P}^{-1} = -\alpha_\mu \quad (\mu \neq 4), \\ \mathcal{T}\alpha_4\mathcal{T}^{-1} &= \mathcal{P}\alpha_4\mathcal{P}^{-1} = \alpha_4. \end{aligned} \tag{1.12}$$

At the time-reversal invariant momenta $\boldsymbol{\Lambda}_a$, the Hamiltonian satisfies $\mathcal{T}\mathcal{H}(\boldsymbol{\Lambda}_a)\mathcal{T}^{-1} = \mathcal{P}\mathcal{H}(\boldsymbol{\Lambda}_a)\mathcal{P}^{-1} = \mathcal{H}(\boldsymbol{\Lambda}_a)$. Then it follows from Eq. (1.46) that $R_1(\boldsymbol{\Lambda}_a) = R_2(\boldsymbol{\Lambda}_a) = R_3(\boldsymbol{\Lambda}_a) = R_5(\boldsymbol{\Lambda}_a) = 0$. Here note that $\mathcal{P} = \alpha_4$. The energy eigenvalue at $\boldsymbol{\Lambda}_a$ is obtained as $E(\boldsymbol{\Lambda}_a) = \pm R_4(\boldsymbol{\Lambda}_a)$, where we have used the fact that the eigenvalues of $\mathcal{P}$ are $\pm 1$. When the system is half-filled and the energy gap exists throughout the Brillouin zone, we obtain an alternative expression for the $Z_2$ invatiant [11]:

$$(-1)^{\nu} = \prod_a \left\{ -\text{sgn}[R_4(\boldsymbol{\Lambda}_a)] \right\}, \tag{1.13}$$

where, in Eq. (1.8), we have used that $\xi_2(\boldsymbol{\Lambda}_a)$ is given by $\xi_2(\boldsymbol{\Lambda}_a) = -\text{sgn}[R_4(\boldsymbol{\Lambda}_a)]$.

# 1.2 Three-Dimensional Topological Insulators

In this section, first we review experimental facts of three-dimensional (3D) topological insulators, focusing on how they are realized and their peculiar surface properties. Then we introduce an low-energy effective Hamiltonian for 3D topological insulators, and an important bulk property, the topological magnetoelectric effect.
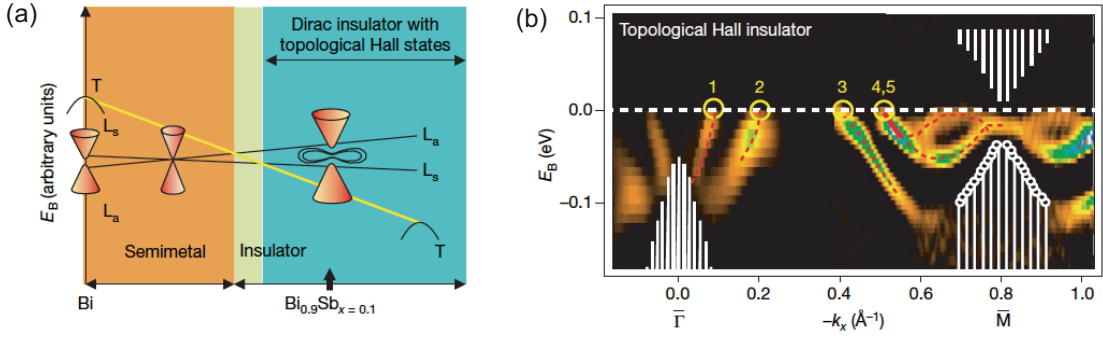
Figure 1.3: (a) Schematic diagram of the bulk band energies of $Bi_{1-x}Sb_x$ as a function of Sb substitution $x$ [14]. (b) Topological surface states on the (111) surface of $Bi_{0.9}Sb_{0.1}$ [14].

## 1.2.1 Basic Properties

Recently discovered topologically nontrivial phases have attracted many researchers and offered a new direction in modern physics [3–5]. After the theoretical predictions of three-dimensional (3D) topological insulators had been made in 2007 [11, 12], the first experimental observation was realized by an angle-resolved photoemission spectroscopy (ARPES) in the 3D topological insulator $Bi_{1-x}Sb_x$ in 2008 [14]. Pure bismuth is a semimetal with strong spin-orbit coupling. The 3D topological insulator phase is induced by substituting bismuth with antimony. Such a substitution in $Bi_{1-x}Sb_x$ causes the band inversion between the conduction and valence bands accompanied with the bulk energy gap opening, which results in the change of the $Z_2$ invariant (1.8). A schematic diagram of the bulk band energies of $Bi_{1-x}Sb_x$ as a function of Sb substitution $x$ is shown in Fig. 1.3(a). A direct experimental evidence for the (strong) topological insulator phase is the existence of the gapless surface states which cross the Fermi level odd (five in this case) times between two time-reversal invariant momenta $\bar{\Gamma}$ and $\bar{M}$ [see Fig 1.3(b)]. This is because, from the discussion on the $Z_2$ invariant, it can be shown that an odd number of crossings leads to topologically protected surface states [11, 12].

The discovery of $Bi_{1-x}Sb_x$ offered a possibility of experimental researches on 3D topological insulators. However, its bulk and surface band structure is rather complicated, since the band inversions occur at three equivalent $L$ points. In 2009, a new class of 3D topological insulators, $Bi_2Se_3$ family, was discovered by an ARPES experiment [15] and a first-principles calculation [16]. In these materials, the band inversion occurs only at single point (the $\Gamma$ point), resulting in a $(1; 000)$ topological insulator phase. Such a simple realization also leads to the existence of a single Dirac cone on the surface. A schematic diagram of the energy level evolution near the Fermi level in $Bi_2Se_3$ is shown in Fig.1.4(a). The three stages (I), (II), and (III) represent the effects of the chemical bonding, crystal field splitting, and spin-orbit coupling, respectively. We see that an energy level crossing occurs as the strength of atomic spin-orbit coupling becomes stronger. Figure 1.4(b) shows the energy levels of the $p$-orbitals $P1_z^+$ and $P2_z^-$ near the Fermi level as a function of a dimensionless parameter $x$ which represents the strength of atomic spin-orbit coupling as $\lambda^{Bi} = x\lambda_0^{Bi}$ and $\lambda^{Se} = x\lambda_0^{Se}$ ($x = 1$ represents the realistic value) [16]. These results indicate that *strong spin-orbit coupling is essential to realize topologically nontrivial phases.*

Surface band dispersion of $Bi_2Se_3$ near the $\Gamma$ point observed by an ARPES measurement and obtained by a first-principles calculation is shown in Fig. 1.5(a) and Fig. 1.5(b), respectively. From these figures, we see that the surface band is isotropic in momentum space and has a
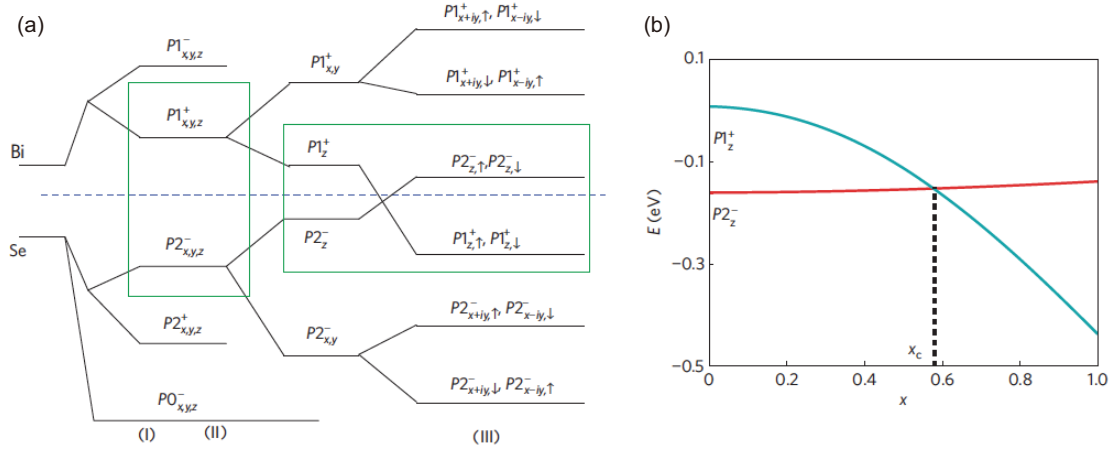
Figure 1.4: (a) Schematic diagram of the energy level evolution at the $\Gamma$ point in $Bi_2Se_3$. The three stages (I), (II), and (III) represent the effects of the chemical bonding, crystal field splitting, and spin-orbit coupling, respectively. The dashed line denotes the Fermi level [16]. (b) Energy levels of two $p$-orbitals $P1_z^+$ and $P2_z^-$ as a function of a dimensionless parameter $x$ which represents the strength of atomic spin-orbit coupling. $x = 1$ represents the realistic value [16].
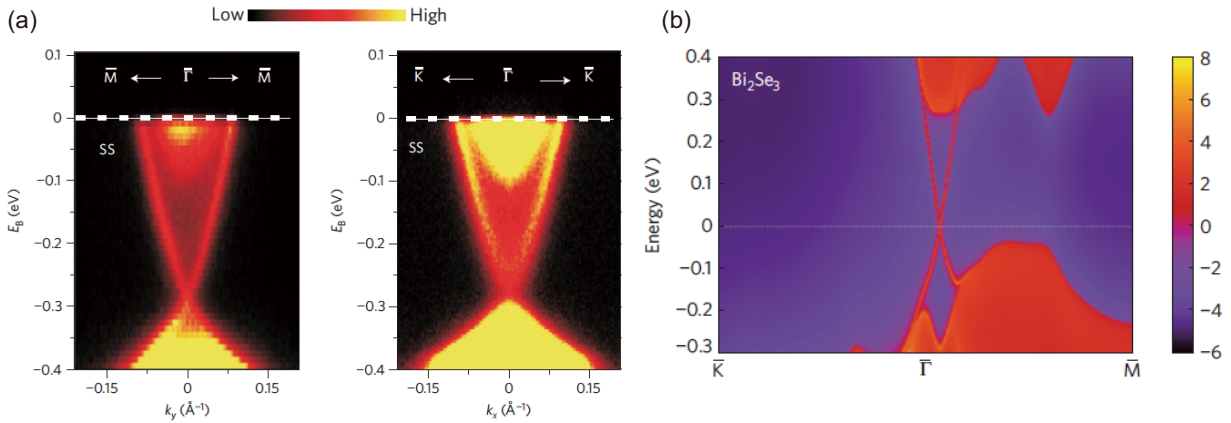


Figure 1.5: (a) Surface band dispersion of $Bi_2Se_3$ observed by an ARPES measurement for $k_x$ and $k_y$ directions [15]. (b) Surface and bulk band dispersion of $Bi_2Se_3$ obtained by a first-principles calculation [16].

linear dispersion near the band touching point. Namely, the topological surface state is described by 2D massless Dirac fermions. One of the most peculiar properties of surface states is the "spin-momentum locking" of surface electrons [18]. Such surface states are called to be helical. A spin-resolved ARPES data on the surface electronic structure of $Bi_{2-\delta}Ca_\delta Se_3$ is shown in Fig. 1.6. It can be seen that the directions of the spins of surface electrons are coupled to the electrons' momenta. This can be understood as a consequence of strong spin-orbit interactions and a requirement of time-reversal symmetry such that $E(k. \uparrow) = E(-k, \downarrow)$. However, in contrast to the bulk band structure, the spin-momentum locking requires non-degenerate band structure for the topological surface state. The resulting effective Hamiltonian for the surface state is
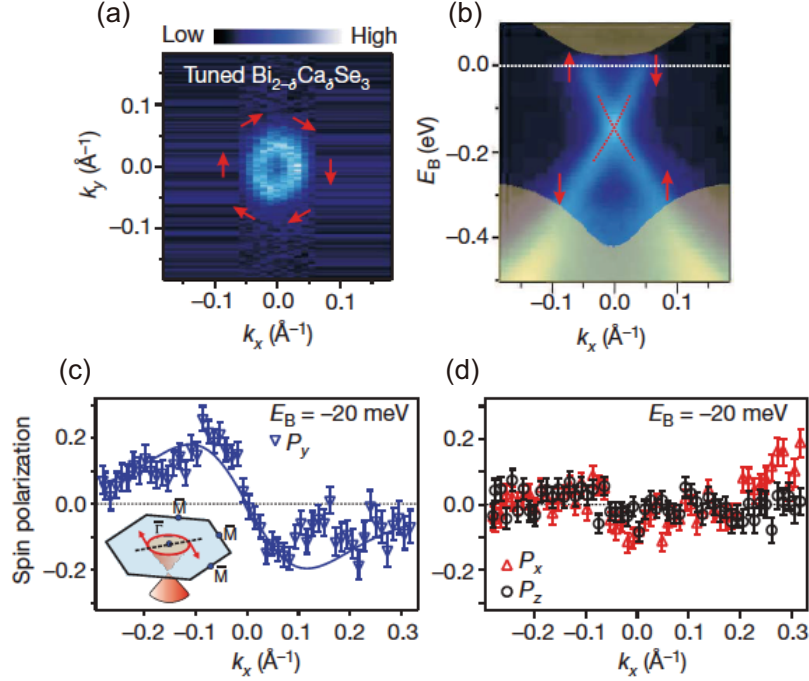
Figure 1.6: (a) Intensity plot of the surface state of $Bi_{2-\delta}Ca_\delta Se_3$ at the Fermi energy. Red arrows represent the directions of spins of electrons. (b) Surface band dispersion of $Bi_{2-\delta}Ca_\delta Se_3$ for the $k_x$ direction. (c) $y$ component of the spin polarization of surface electrons along the $\bar{\Gamma}$-$\bar{M}$ direction. (d) $x$ and $z$ components of the spin polarization of surface electrons along the $\bar{\Gamma}$-$\bar{M}$ direction. All figures are from Ref. 18.

described by two-component massless Dirac fermions:

$$\mathcal{H}_{\text{surface}}(\boldsymbol{k}) = v_{\text{F}}(k_y \sigma_x - k_x \sigma_y) = v_{\text{F}}(\boldsymbol{k} \times \boldsymbol{e}_z) \cdot \boldsymbol{\sigma}, \tag{1.14}$$

where $v_{\text{F}}$ is the Fermi velocity of the surface state (i.e., the slope of the Dirac cone), and $\sigma_x, \sigma_y$ are the Pauli matrices for the spin degree of freedom. The energy eigenvalues are readily obtained as $E_{\text{surface}}(\boldsymbol{k}) = \pm v_{\text{F}}\sqrt{k_x^2 + k_y^2}$. The value of the Fermi velocity of the surface states in $Bi_2Se_3$ is experimentally obtained as $v_{\text{F}} \approx 5 \times 10^5$ m/s [15], which is in agreement with a first-principles value $v_{\text{F}} \simeq 6.2 \times 10^5$ m/s [16].

So far we saw that the surface states of 3D topological insulators such as $Bi_2Se_3$ are described by 2D two-component massless Dirac fermions. Due to the spin-momentum locking, the surface states are robust against disorder, as long as time-reversal symmetry is preserved. Namely, the backscaterrings of surface electrons from $(\boldsymbol{k}, \uparrow)$ to $(-\boldsymbol{k}, \uparrow)$ are absent [19]. Theoretically, it have shown that 2D two-component massless Dirac fermions cannot be localized in the presence of nonmagnetic disorder [20, 21]. However, surface states are not robust against magnetic disorder which breaks time-reversal symmetry. This is because the surface Dirac fermions described by Eq. (1.14) can be massive by adding a term proportional to $\sigma_z$, i.e., $m\sigma_z$. More precisely, adding the exchange interaction such that $\mathcal{H}_{\text{exch.}}(\boldsymbol{k}) = J\boldsymbol{S}_{\text{imp}} \cdot \boldsymbol{\sigma}$ where $\boldsymbol{S}_{\text{imp}}$ is the spin of a magnetic impurity to the Hamiltonian (1.14) leads to a gapped spectrum

$$E_{\text{surface}}(\boldsymbol{k}) = \pm\sqrt{(v_{\text{F}}k_x + JS_{\text{imp}}^y)^2 + (v_{\text{F}}k_y - JS_{\text{imp}}^x)^2 + (JS_{\text{imp}}^z)^2}. \tag{1.15}$$
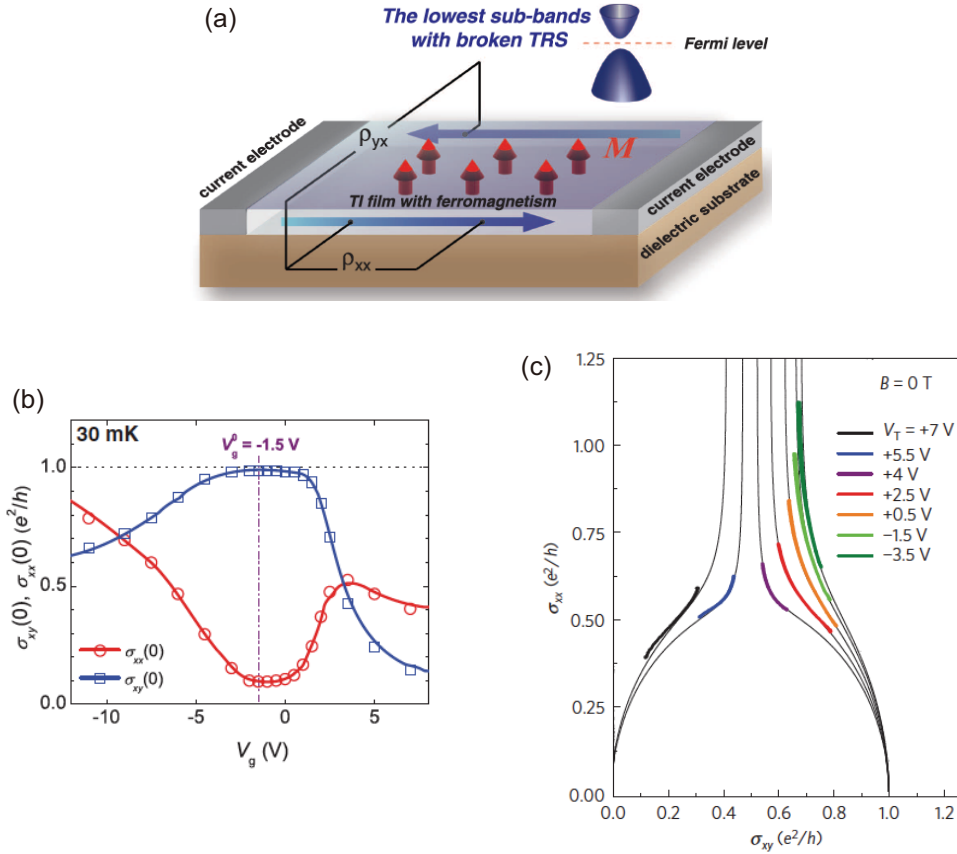
Figure 1.7: (a) Schematic picture of an experimental setup to detect the quantum anomalous Hall effect in a ferromagnetically ordered topological insulator thin film. The chemical potential of the film can be controlled by a gate-voltage applied on the back-side of the dielectric substrate [24]. (b) Gate-voltage $V_g$ dependence of the Hall conductivity $\sigma_{xy}$ and the longitudinal conductivity $\sigma_{xx}$ in $Cr_{0.15}(Bi_{0.1}Sb_{0.9})_{1.85}Te_3$ [24]. (c) Observed flow of the conductivity in the $(\sigma_{xy}, \sigma_{xx})$ plane in $Cr_{0.22}(Bi_{0.2}Sb_{0.8})_{1.78}Te_3$ thin film. With decreasing temperature, the system evolves toward two stable fixed points, $\sigma_{xy} = 0$ or $\sigma_{xy} = e^2/h$ [25].

Let us consider a general $2 \times 2$ Hamiltonian given by $\mathcal{H}(\boldsymbol{k}) = \boldsymbol{R}(\boldsymbol{k}) \cdot \boldsymbol{\sigma}$. In the case of massive Dirac fermions, $\boldsymbol{R}(\boldsymbol{k})$ is given by $\boldsymbol{R}(\boldsymbol{k}) = (k_x, k_y, m)$. The Hall conductivity of the system can be calculated by [1, 4]

$$\sigma_{xy} = \frac{e^2}{h}\frac{1}{4\pi}\int dk_x dk_y \hat{\boldsymbol{R}} \cdot \left(\frac{\partial \hat{\boldsymbol{R}}}{\partial k_x} \times \frac{\partial \hat{\boldsymbol{R}}}{\partial k_y}\right) = \text{sgn}(m)\frac{e^2}{2h}, \tag{1.16}$$

where $\hat{\boldsymbol{R}} = \boldsymbol{R}(\boldsymbol{k})/|\boldsymbol{R}(\boldsymbol{k})|$ is an unit vector. The integral is equivalent to the area where the unit vector $\hat{\boldsymbol{R}}$ moves on the unit sphere, which namely gives the winding number of $\hat{\boldsymbol{R}}$. At $\boldsymbol{k} = 0$, the unit vector $\hat{\boldsymbol{R}}$ points the north or south pole, that is, $\hat{\boldsymbol{R}} = (0, 0, \text{sgn}(m))$. At large $\boldsymbol{k}$ with $|\boldsymbol{k}| \gg |m|$, $\hat{\boldsymbol{R}}$ almost points the horizontal directions. Hence, varying $\boldsymbol{k}$, $\hat{\boldsymbol{R}}$ covers the half of the unit sphere, which gives $2\pi$.

Equation (1.16) indicates the (half-)quantum Hall effect occurs on the surfaces of 3D topological insulators, when magnetic impurities are doped or a magnetic film is put on the surface [22, 23]. The direction of the Hall current depends on the sign of $m$, i.e., the direction

10

of the magnetization of surface electrons. Actually, the surface quantum Hall effect has been observed experimentally [24, 25]. The observed surface quantum anomalous Hall effect in Cr-doped $Bi_y Sb_{1-y} Te_3$ thin film is shown in Fig. 1.7. Note that in those systems the magnetization directions of top and bottom surfaces are the same, and thus the observed Hall conductivity is $2 \times e^2/(2h) = e^2/h$. It can be seen from Fig. 1.7(b) that the Hall conductivity is quantized when the chemical potential lies in the surface band gap.

## 1.2.2 An Effective Lattice Model

In the following, we consider the low-energy effective Hamiltonian of 3D topological insulators such as $Bi_2 Se_3$. As mentioned above, the bulk electronic structure of $Bi_2 Se_3$ near the Fermi level is described by two $p$-orbitals $P1_z^+$ and $P2_z^-$ with $\pm$ denoting parity. Then defining the basis $[|P1_z^+, \uparrow\rangle, |P1_z^+, \downarrow\rangle, |P2_z^-, \uparrow\rangle, |P2_z^-, \uparrow\rangle]$ and retaining the wave vector $\boldsymbol{k}$ up to quadratic order, the low-energy effective Hamiltonian for the bulk around the $\Gamma$ point is given by [16, 17]

$$
\begin{aligned}
\mathcal{H}_{\text{eff}}(\boldsymbol{k}) &= \begin{bmatrix} \mathcal{M}(\boldsymbol{k}) & 0 & A_1 k_z & A_2 k_- \\ 0 & \mathcal{M}(\boldsymbol{k}) & A_2 k_+ & -A_1 k_z \\ A_1 k_z & A_2 k_- & -\mathcal{M}(\boldsymbol{k}) & 0 \\ A_2 k_+ & -A_1 k_z & 0 & -\mathcal{M}(\boldsymbol{k}) \end{bmatrix} \\
&= A_2 k_x \alpha_1 + A_2 k_y \alpha_2 + A_1 k_z \alpha_3 + \mathcal{M}(\boldsymbol{k}) \alpha_4,
\end{aligned} \tag{1.17}
$$

where $k_\pm = k_x \pm k_y$ and $\mathcal{M}(\boldsymbol{k}) = m_0 - B_1 k_z^2 - B_2 k_\perp^2$. The coefficients are fitted with a first-principles calculation for $Bi_2 Se_3$; $m_0 = 0.28$ [eV], $A_1 = 2.2$ [eV·Å], $A_2 = 4.1$ [eV·Å], $B_1 = 10$ [eV·Å$^2$], $B_2 = 56.6$ [eV·Å$^2$]. The $4 \times 4$ matrices $\alpha_\mu$ are given by

$$
\alpha_j = \begin{bmatrix} 0 & \sigma_j \\ \sigma_j & 0 \end{bmatrix}, \qquad \alpha_4 = \begin{bmatrix} 1 & 0 \\ 0 & -1 \end{bmatrix}, \tag{1.18}
$$

where the Clifford algebra $\{\alpha_\mu, \alpha_\nu\} = 2\delta_{\mu\nu} \mathbf{1}$ is satisfied. Namely, the above Hamiltonian is nothing but an anisotropic 3D Dirac Hamiltonian with a momentum-dependent mass.

In Subsect. 1.1.3, the $Z_2$ invariant, which identifies whether a phase is topologically nontrivial or not, was defined. Here note that the $Z_2$ invariant is calculated in lattice systems. Hence we cannot directly show that the phase which is described by the effective Hamiltonian (1.17) represents a 3D topological insulator. From this viewpoint, let us consider the effective Hamiltonian (1.17) on a cubic lattice. We replace $k_i$ and $k_i^2$ terms by $k_i \to \sin k_i$ and $k_i^2 \to 2(1 - \cos k_i)$. This replacement is valid when $k_i \ll 1$. Then we obtain the lattice version of the effective Hamiltonian as

$$
\begin{aligned}
\mathcal{H}_{\text{eff}}(\boldsymbol{k}) &= A_2 \alpha_1 \sin k_x + A_2 \alpha_2 \sin k_y + A_1 \alpha_3 \sin k_z \\
&\quad + \left[ m_0 - 2B_1(1 - \cos k_z) - 2B_2(1 - \cos k_x) - 2B_2(1 - \cos k_y) \right] \alpha_4 \\
&= v_{\text{F}}(\alpha_1 \sin k_x + \alpha_2 \sin k_y + \alpha_3 \sin k_z) + \left[ m_0 + r \sum_{i=x,y,z} (1 - \cos k_i) \right] \alpha_4,
\end{aligned} \tag{1.19}
$$

where, in the second line, we have simplified coefficients as $v_{\text{F}} = A_1 = A_2$ and $r = -2B_1 = -2B_2$. As will be mentioned later, this Hamiltonian is called the Wilson Hamiltonian, which was originally introduced in lattice quantum chromodynamics.

In cubic lattices, the 8 time-reversal invariant momenta $\Lambda_a$ are given by $(0, 0, 0)$, $(\pi/a, 0, 0)$, $(0, \pi/a, 0)$, $(0, 0, \pi/a)$, $(\pi/a, \pi/a, 0)$, $(\pi/a, 0, \pi/a)$, $(0, \pi/a, \pi/a)$, and $(\pi/a, \pi/a, \pi/a)$ where $a$ is
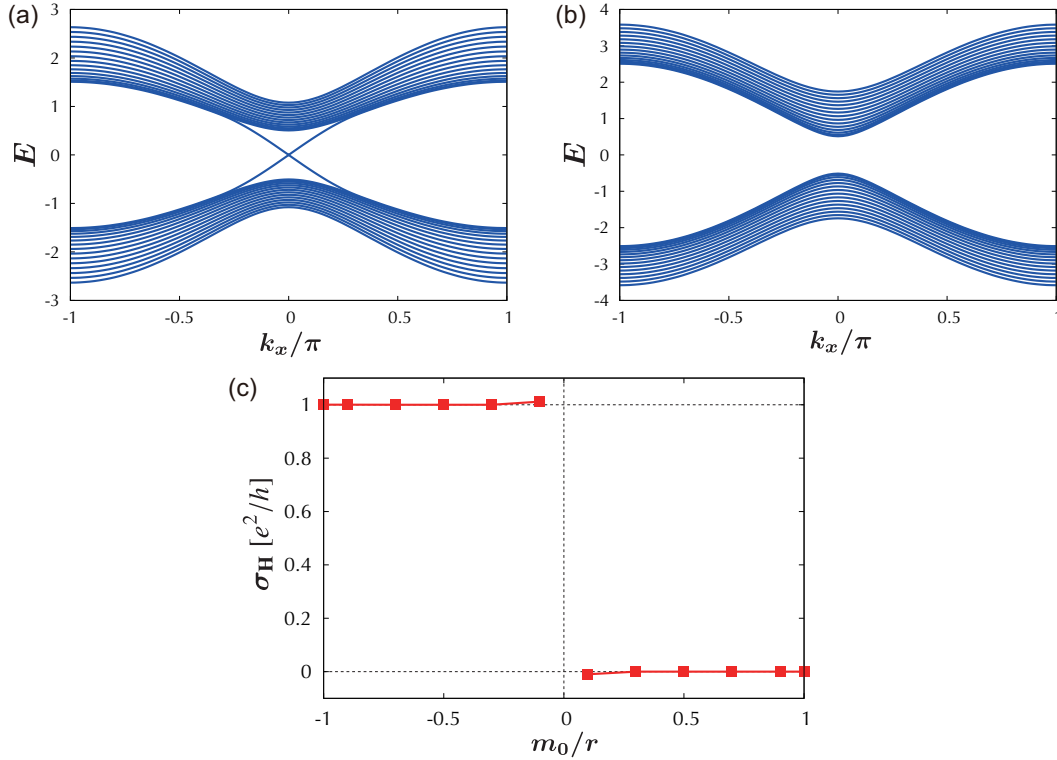
Figure 1.8: Energy spectrum of the effective model (1.19) in a slab geometry (i.e., finite layers in the $z$ direction) with (a) $m_0/r = -0.5$ and (b) $m_0/r = 0.5$. The surface state exists in the topologically nontrivial case ($0 > m_0/r > -2$). (c) $m_0$ dependence of the surface Hall conductivity $\sigma_H$ in the case where uniformly magnetized impurities are doped into the bulk and surface.

the lattice constant. With the use of the expression (1.13), we can calculate the $Z_2$ invariant of the system as

$$
\begin{aligned}
(-1)^\nu &= \prod_{a=1}^{8} \text{sgn} \left[ m_0 + r \sum_{i=x,y,z} (1 - \cos \Lambda_a^i) \right] \\
&= \begin{cases}
-1 & (0 > m_0/r > -2 \text{ or } -4 > m_0/r > -6) \\
+1 & (m_0/r > 0, \ -2 > m_0/r > -4 \text{ or } -6 > m_0/r).
\end{cases}
\end{aligned}
\tag{1.20}
$$

Indeed, the topological insulator phase with $0 > m_0/r > -2$ satisfies the above realistic value for Bi$_2$Se$_3$; $m_0/r \approx -0.28/(2 \times 10/3^2) = -0.13$ where we have assumed the value of the lattice constant as $a = 3$ [Å]. In this thesis, we adopt the lattice Hamiltonian (1.19) as a model Hamiltonian for 3D topological insulators.

Energy spectra of the effective model (1.19) in a slab geometry for the case of the topological insulator and for the normal insulator are shown in Fig. 1.8(a) and (b), respectively. Indeed, we can see the surface spectrum, the single Dirac cone around the $\Gamma$ point, in the topological insulator phase. Therefore, the effective model (1.19) can be regarded as an effective lattice model for 3D topological insulators such as Bi$_2$Se$_3$. Further, as shown in Eq. (1.16), the surface Hall current flows when the surface spectrum is gapped (i.e., for example, when magnetic impurities are doped to the surface). Figure 1.8(c) shows the surface Hall conductivity $\sigma_H$ as a function of $m_0$ in a slab geometry. In the topological insulator phase, we have $\sigma_H = e^2/h$. Here note that the

12
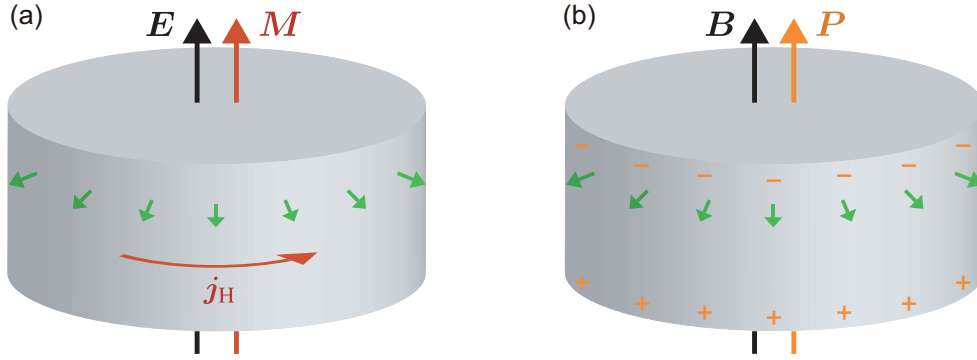
Figure 1.9: Schematic picture of the topological magnetoelectric effect in a 3D topological insulator with magnetic impurities doped to the surface (green arrows). (a) Magnetization $M$ induced by an external electric field $E$. (b) Electric polarization $P$ induced by an external magnetic field $B$.

obtained value of $\sigma_H$ is the sum of the contributions from the top and bottom surfaces, namely $\sigma_H = 2 \times \frac{e^2}{2h}$.

### 1.2.3 Topological Magnetoelectric Effect

Surface states of 3D topological insulators are robust against disorder by nonmagnetic impurities, as long as time-reversal symmetry is preserved. However, the surface states can be gapped (i.e., the surface Dirac fermions can be massive) by magnetic disorder which breaks time-reversal symmetry. This results in the surface quantum Hall effect. As a consequence, a novel phenomenon, the "topological magnetoelectric effect", emerges in 3D topological insulators [26]. Let us consider a case where the side surface of a cylindrical 3D topological insulator is ferromagnetically ordered, as shown in Fig. 1.9. When an external electric field $E$ is applied parallel to the cylinder, the surface Hall current $j_H$ is induced as

$$j_H = -\text{sgn}(m)\frac{e^2}{2h}\hat{n} \times E, \tag{1.21}$$

where $\hat{n}$ is an unit vector normal to the side surface. From the Ampère's law, the magnetization $M$ with $|M| = |j_H|/c$ ($c$ is the speed of light) is obtained as[see Fig. 1.9(a)]

$$M = \text{sgn}(m)\frac{e^2}{2hc}E. \tag{1.22}$$

Similarly, when an external magnetic field $B$ is applied parallel to the cylinder, the circulating electric field $E^{\text{ind}}$ normal to the magnetic field is induced as $\nabla \times E^{\text{ind}} = -\frac{\partial B}{\partial t}$. Then the induced electric field generates the surface Hall current parallel to the magnetic field as

$$j_H = \text{sgn}(m)\frac{e^2}{2h}\frac{\partial B}{\partial t}. \tag{1.23}$$

On the other hand, a polarization current is equivalent to the time derivative of the electric polarization. Finally the induced electric polarization $P$ is given by [see Fig. 1.9(b)]

$$P = \text{sgn}(m)\frac{e^2}{2hc}B. \tag{1.24}$$

Equations (1.22) and (1.24) clearly show the magnetoelectic effect. Here recall that the magnetization and polarization can be derived from the free energy as $\boldsymbol{M} = -\partial F/\partial \boldsymbol{B}$ and $\boldsymbol{P} = -\partial F/\partial \boldsymbol{E}$. To satisfy the relations (1.22) and (1.24), the free energy must have the following form:

$$F = -\int d^3x \frac{e^2}{2hc}\boldsymbol{E}\cdot\boldsymbol{B} = -\int d^3x \frac{\theta e^2}{4\pi^2\hbar c}\boldsymbol{E}\cdot\boldsymbol{B}, \tag{1.25}$$

where we have omitted sgn($m$) for simplicity, and $\theta = \pi$. The integrand can be regarded as the Hamiltonian density. The equivalent action is written as

$$S_\theta = \int d^4x \frac{\theta e^2}{4\pi^2\hbar c}\boldsymbol{E}\cdot\boldsymbol{B} = \int d^4x \frac{\theta e^2}{32\pi^2\hbar c}\epsilon^{\mu\nu\rho\lambda}F_{\mu\nu}F_{\rho\lambda}, \tag{1.26}$$

where $F_{\mu\nu} = \partial_\mu A_\nu - \partial_\nu A_\mu$ with $A_\mu$ being the electromagnetic four-potential, and $\epsilon^{\mu\nu\rho\lambda}$ is the Levi-Civita symbol. Note that $\frac{e^2}{\hbar c}$ ($\simeq 1/137$) is the fine-structure constant. This action is also called the theta term. In particle physics, the phenomenon described by the theta term is termed the axion electrodynamics, since $\theta$ is regarded as the field of an elementary particle, axion. Under time-reversal ($t \to -t$, $\boldsymbol{x} \to \boldsymbol{x}$), an electric field and magnetic field are transformed to be $\boldsymbol{E} \to \boldsymbol{E}$ and $\boldsymbol{B} \to -\boldsymbol{B}$, respectively. Hence the term $\boldsymbol{E}\cdot\boldsymbol{B}$ is odd under time-reversal. On the other hand, 3D topological insulators have time-reversal symmetry, which indicates that $S_\theta$ remains unchanged under time-reversal with $\theta \to -\theta$ satisfied. Namely, the value of $\theta$ has to be constant, i.e., $\theta = \pm\pi$. In normal (topologically trivial) insulators, $\theta = 0$. Unfortunately, regardless of intensive experimental searches, the topological magnetoelectric effect has not yet been observed.

So far we have derived the topological magnetoelectric effect from a surface property of 3D topological insulators. In the following, we briefly discuss the ways to derive of the theta term from the bulk. One way is the dimensional reduction from (4+1)-dimensions to (3+1)-dimensions [26]. Another way is to use the so-called Fujikawa's method [27, 28]. Here we show the derivation of the theta term based on the Fujikawa's method. Let us start from the low-energy continuum model for 3D topological insulators such as Bi$_2$Se$_3$. Namely, the Hamiltonian is given by setting $k_i \ll 1$ in Eq. (1.19) as

$$\mathcal{H}_{\text{TI}}(\boldsymbol{k}) = \boldsymbol{k}\cdot\boldsymbol{\alpha} + m_0\alpha_4, \tag{1.27}$$

where $m_0 < 0$. Except for the negative mass $m_0$, this Hamiltonian is the usual Dirac Hamiltonian. Then the action of the system in the presence of an external electromagnetic field is written as

$$S_{\text{TI}} = \int d^4x \bar{\psi}(x)[i\gamma^\mu(\partial_\mu + ieA_\mu) + m_0 e^{i\pi\gamma_5}]\psi(x), \tag{1.28}$$

where $\psi(x)$ is a four-component spinor, and we have used the fact that $m_0 = -m_0(\cos\pi + i\gamma_5\sin\pi) = -m_0 e^{i\pi\gamma_5}$. The gamma matrices $\gamma^\mu$ are given by the Dirac representation as

$$\gamma^0 = \begin{bmatrix} 1 & 0 \\ 0 & -1 \end{bmatrix}, \quad \gamma^j = \begin{bmatrix} 0 & \sigma_j \\ -\sigma_j & 0 \end{bmatrix}, \quad \gamma^5 = \begin{bmatrix} 0 & 1 \\ 1 & 0 \end{bmatrix}. \tag{1.29}$$

It is convenient to study the system in the imaginary time notation. Namely, we rewrite $t$, $A_0$ and $\gamma^j$ as $t \to -i\tau$, $A_0 \to iA_0$, and $\gamma^j \to i\gamma_j$. The Euclidean action of the system is written as

$$S_{\text{TI}} = \int d\tau d^3x \bar{\psi}(x)[\gamma_\mu(\partial_\mu + ieA_\mu) - m_0 e^{i\pi\gamma_5}]\psi(x). \tag{1.30}$$

First let us consider an infinitesimal chiral transformation defined by

$$\psi \to \psi' = e^{-i\pi d\phi\gamma_5/2}\psi, \qquad \bar{\psi} \to \bar{\psi}' = \bar{\psi}e^{-i\pi d\phi\gamma_5/2}, \tag{1.31}$$

where $\phi \in [0, 1]$. Then the partition function $Z$ is transformed as

$$Z = \int \mathcal{D}[\psi, \bar{\psi}]e^{-S_{\text{TI}}[\psi, \bar{\psi}]} \quad \to \quad Z' = \int \mathcal{D}[\psi', \bar{\psi}']e^{-S'_{\text{TI}}[\psi', \bar{\psi}']}. \tag{1.32}$$

The theta term comes from the Jacobian defined by $\mathcal{D}[\psi', \bar{\psi}'] = J\mathcal{D}[\psi, \bar{\psi}]$. The action (1.30) is transformed as

$$S'_{\text{TI}} = \int d\tau d^3x\bar{\psi}(x)[\gamma_\mu(\partial_\mu + ieA_\mu) - m_0 e^{i\pi(1-d\phi)\gamma_5}]\psi(x) + \frac{i}{2}\pi \int d\tau d^3x d\phi \partial_\mu(\bar{\psi}\gamma_\mu\gamma_5\psi). \tag{1.33}$$

The Jacobian is written as [27, 28]

$$J = \exp\left[-i \int d\tau d^3x d\phi \frac{\pi e^2}{32\pi^2\hbar c}\epsilon^{\mu\nu\rho\lambda}F_{\mu\nu}F_{\rho\lambda}\right]. \tag{1.34}$$

Here $F_{\mu\nu} = \partial_\mu A_\nu - \partial_\nu A_\mu$ and we have written $\hbar$ and $c$ explicitly. We repeat this procedure infinite times, i.e., integrate with respect to the variable $\phi$ from 0 to 1. Due to the invariance of the partition function, finally we arrive at the following expression of $S_{\text{TI}}$:

$$S_{\text{TI}} = \int d\tau d^3x\bar{\psi}(x)[\gamma_\mu(\partial_\mu + ieA_\mu) - m_0]\psi(x) + i \int d\tau d^3x \frac{\pi e^2}{32\pi^2\hbar c}\epsilon^{\mu\nu\rho\lambda}F_{\mu\nu}F_{\rho\lambda}, \tag{1.35}$$

where we have dropped the irrelevant surface term. The first term is the action of trivial Dirac fermions, since their mass $-m_0$ is positive. The second term is nothing but the theta term in imaginary time, and we obtain Eq. (1.26) by substituting $\tau = it$.

## 1.3 Weyl Semimetals

In this section, we review a novel three-dimensional topological phase, the Weyl semimetal. Weyl semimetals have not been experimentally observed so far. Thus we review the basic theoretical aspects, and introduce some theoretical models for Weyl semimetals. Finally we discuss the stability of Weyl semimetal phases against disorder or electron correlation.

### 1.3.1 Basic Properties

As a novel topological phase of matter, the Weyl semimetal has attracted much attention since a theoretical prediction in a realistic material was made [29]. Weyl semimetals have three-dimensional (3D) linear dispersions near the band touching points, the Weyl nodes, in the bulk band structure. The low-energy effective model near a band touching point $k_0$ is described by the Weyl fermions, namely by the $2 \times 2$ Hamiltonian such that $\mathcal{H}_{\text{Weyl}}(q) = \sum_{i=1}^3 v_i \cdot q\sigma_i$ where $q = k - k_0$ and $\sigma_i$ are the Pauli matrices. The energy dispersion of the Weyl fermion is obtained as $E_{\text{Weyl}}(q) = \pm\sqrt{\sum_{i=1}^3 (v_i \cdot q)^2}$. Each Weyl fermion possesses chirality defined by $c = \text{sgn}[v_1 \cdot (v_2 \times v_3)] = \pm 1$. In the simplest case, the Weyl Hamiltonian can be written as

$$\mathcal{H}_{\text{Weyl}}(q) = \pm v_{\text{F}}q \cdot \boldsymbol{\sigma}, \tag{1.36}$$
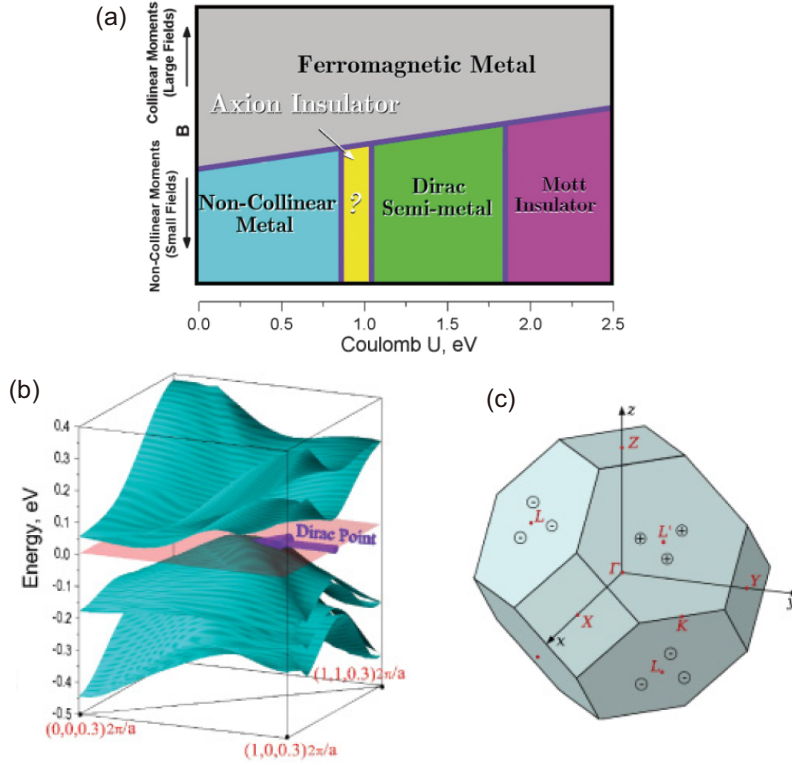
Figure 1.10: (a) Phase diagram obtained by a first-principles calculation for a class of pyrochlore iridates such as $Y_2Ir_2O_7$, as a function of the strengths of on-site interactions and an external magnetic field. The "Dirac Semi-metal" phase shown in the phase diagram corresponds to the Weyl semimetal phase [29]. (b) A band structure near a band touching point, a Weyl node, and (c) the locations of the 24 Weyl nodes, shown by circles with ± denoting the chirality, in the first Brillouin zone [29].

where $v_F$ is the Fermi velocity, i.e., the slope of the 3D cone, and ± denotes the chirality of the Weyl node. Here note that a single Weyl fermion cannot be massive by itself, since all the three Pauli matrices which anticommute with each other are used. Namely, the existence of a single Weyl node is robust against perturbations. An energy gap opens only if pairs of Weyl fermions with opposite chirality meet and annihilate each other. Therefore, it can be said that *the Weyl semimetal is a topological phase*. Breaking of at least time-reversal or inversion symmetry is required to realize the Weyl semimetal [30–36]. The Weyl nodes always appear in pairs, and thus the minimal number of the Weyl nodes in a Weyl semimetal is two.

One of the attractive aspects of Weyl semimetals is that the first theoretical prediction showed the emergence of a Weyl semimetal phase in a class of iridates $R_2Ir_2O_7$ (R is yttrium or a rare earth element), a strongly correlated $5d$ electron system with spin-orbit coupling on the pyrochlore lattice [29]. The predicted phase diagram as a function of the strengths of on-site interactions and an external magnetic field is shown in Fig. 1.10(a). Namely, Weyl semimetals can emerge as a consequence of the interplay of electron correlation and spin-orbit coupling. Remarkably, the predicted Weyl semimetal has 24 Weyl nodes in the Brillouin zone. See Fig. 1.10(b) for a energy band near a Weyl node, and see Fig. 1.10(c) for the locations of the 24 Weyl nodes. Other theoretical studies on $R_2Ir_2O_7$ have also suggested the existence of Weyl semimetal phases [37, 38].
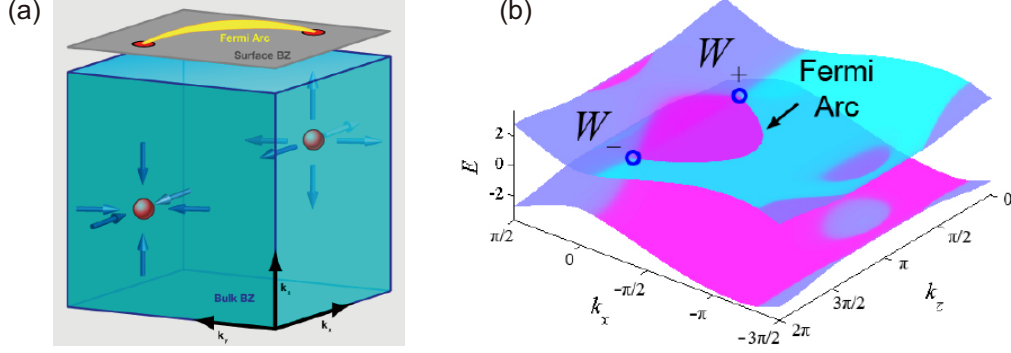
Figure 1.11: (a) Schematic picture of the Weyl nodes (red circles) and the surface Fermi arc (yellow line) in a Weyl semimetal in momentum space. Blue arrows indicate the directions of the Berry connection. [39]. (b) Surface bands of a Weyl semimetal with two nodes ($W_{\pm}$). The Fermi arc connecting two Weyl nodes appears in the projected surface Brillouin zone [40].

Topological nature of Weyl semimetals can be understood from the fact that each Weyl node can be regarded as a "monopole" with its charge given by the chirality [29], and from the resulting existence of surface Fermi arc [29, 33, 40]. Schematic pictures of a Weyl semimetal in momentum space and the surface Fermi arc are shown in Fig.1.11. To understand these natures, let us consider the anomalous Hall conductivity of a Weyl semimetal. In general, intrinsic anomalous Hall conductivity can be calculated by [41]

$$\sigma_{ab}^{\text{3D}} = \frac{e^2}{\hbar} \epsilon_{abc} \sum_n \int_{\text{BZ}} \frac{d^3k}{(2\pi)^3} f(E_{nk}) \mathcal{B}_{nk}^c, \tag{1.37}$$

where $\mathcal{A}_{nk}$ is the Berry connection given by $\mathcal{A}_{nk} = -i\langle u_{nk}|\nabla_k|u_{nk}\rangle$ with $|u_{nk}\rangle$ being the Bloch state at momentum $k$ in the $n$-th band, $\mathcal{B}_{nk}$ is the Berry curvature given by $\mathcal{B}_{nk} = \nabla_k \times \mathcal{A}_{nk}$, and $f(E_{nk})$ is the Fermi distribution function. The summation of $n$ is done over the occupied bands. The above equation can be rewritten as

$$\sigma_{xy}^{\text{3D}} = \int \frac{dk_z}{2\pi} \sigma_{xy}^{\text{2D}}(k_z). \tag{1.38}$$

Here $\sigma_{xy}^{\text{2D}}(k_z)$ is the Hall conductivity of a 2D system at a fixed $k_z$:

$$\sigma_{xy}^{\text{2D}}(k_z) = \frac{e^2}{\hbar} \sum_n \int_{\text{BZ}} \frac{d^2k_\perp}{(2\pi)^2} f(E_{nk_\perp}(k_z)) \mathcal{B}_{nk_\perp}^z(k_z), \tag{1.39}$$

where $k_\perp = (k_x, k_y)$. Except for the $k_z$ dependence, Eq. (1.39) is equivalent to the expression of TKNN formula [Eq. (1.5)]. In the following, we show that Weyl semimetals in momentum space can be regarded as the stacking of 2D quantum Hall layers.

To be specific, let us consider a minimal two-band model on a cubic lattice with broken time-reversal symmetry [42], whose Hamiltonian is given by

$$\mathcal{H}(k) = t \sin k_x \sigma_x + t \sin k_y \sigma_y + [t(\cos k_z - \cos Q) + r(2 - \cos k_x - \cos k_y)]\sigma_z$$
$$\equiv R(k) \cdot \sigma, \tag{1.40}$$

where $t > 0$, $r < -t(1-\cos Q)/2$ and $\sigma_i$ are the Pauli matrices for the spin degree of freedom. The two Weyl nodes appear at the points $W_\pm = (0, 0, \pm Q)$. Around the Weyl nodes, the Hamiltonian is expanded up to linear order in $q(= k - W_\pm)$ as

$$\mathcal{H}(q + W_\pm) = t q_x \sigma_x + t q_y \sigma_y \mp (t \sin Q) q_z \sigma_z. \tag{1.41}$$

This is nothing but the Weyl Hamiltonian. Recall that the TKNN formula is rewritten as Eq. (1.16), in the case where the Hamiltonian is given by the form $\mathcal{H}(k) = R(k) \cdot \sigma$. Namely, the Chern number $C$ is given by the Winding number:

$$C(k_z) = \frac{1}{4\pi} \int dk_x dk_y \, \hat{R} \cdot \left( \frac{\partial \hat{R}}{\partial k_x} \times \frac{\partial \hat{R}}{\partial k_y} \right). \tag{1.42}$$

The Hall conductivity is given by $\sigma_{xy}^{2D}(k_z) = \frac{e^2}{h} C(k_z)$. Consider a $k_x$-$k_y$ plane which lies between the Weyl nodes, i.e., the case of $-Q < k_z < Q$. Then the vector $R(k)$ points the north pole at $(k_x, k_y) = (0, 0)$, while it points the south pole at $(k_x, k_y) = (\pi, 0)$, $(0, \pi)$, $(\pi, \pi)$. This means that $C(k_z) = 1$. On the other hand, when $-\pi < k_z < -Q$ or $Q < k_z < \pi$, the vector $R(k)$ points the south pole at the above four points, which results in $C(k_z) = 0$. The above result such that the Chern number becomes unity can be also obtained by considering a torus enclosing a Weyl node. Therefore it can be said that a Weyl node is regarded as a monopole, since the Chern number is given by the integration of the Berry curvature. Further, recall that there exists a chiral edge state in a quantum Hall insulator. This means that the surface Fermi arc connecting two Weyl nodes is given by the intersection of such gapless chiral states and the Fermi level.

Finally, from the above discussion, we obtain an analytical expression for the anomalous Hall conductivity of Weyl semimetals with two Weyl nodes as

$$\sigma_{xy}^{3D} = \int_{-\pi}^{\pi} \frac{dk_z}{2\pi} \sigma_{xy}^{2D}(k_z) = \frac{e^2}{h} \frac{Q}{\pi}, \tag{1.43}$$

where $2Q$ is the distance between the two Weyl nodes in momentum space. When the two nodes meet and annihilate each other by the change of a parameter, the system becomes gapped, i.e becomes an anomalous Hall insulator, and the anomalous Hall conductivity reaches the quantized value $\sigma_{xy}^{3D} = e^2/(ha)$, where $a$ is the lattice constant.

## 1.3.2 Theoretical Models

As mentioned above, the realization of Weyl semimetals requires breaking of at least time-reversal or inversion symmetry [30–36]. To understand this nature, let us consider a simple model. We start from the 3D four-component Dirac fermions, which possess both time-reversal and inversion symmetries. The Hamiltonian is given by

$$\mathcal{H}_{\text{Dirac}}(k) = v_F k \cdot \alpha + m_0 \alpha_4, \tag{1.44}$$

where $v_F$ is the Fermi velocity, $m_0$ is the mass of Dirac fermions, and $\alpha_\mu$ are $4 \times 4$ matrices which satisfy the Clifford algebra $\{\alpha_\mu, \alpha_\nu\} = 2\delta_{\mu\nu} \mathbf{1}$. To be concrete, we adopt the Dirac representation for $\alpha_\mu$ as

$$\alpha_j = \begin{bmatrix} 0 & \sigma_j \\ \sigma_j & 0 \end{bmatrix}, \quad \alpha_4 = \begin{bmatrix} 1 & 0 \\ 0 & -1 \end{bmatrix}, \quad \alpha_5 = \begin{bmatrix} 0 & -i \\ i & 0 \end{bmatrix}. \tag{1.45}$$

Table 1.1: Transformation properties under time-reversal $\mathcal{T}$ and spatial inversion (parity) $\mathcal{P}$ of 16 independent matrices consisting of $\alpha_\mu$ with $\{\alpha_\mu, \alpha_\nu\} = 2\delta_{\mu\nu}\mathbf{1}$ ($\mu, \nu = 1, 2, 3, 4, 5$).

| Matrices | $\mathbf{1}$ | $\alpha_j$ | $\alpha_4$ | $\alpha_5$ | $\Sigma_j$ | $\Sigma'_j$ | $\Pi_j$ | $\Pi_0$ |
|---|---|---|---|---|---|---|---|---|
| Time-reversal $\mathcal{T}$ | + | − | + | − | − | − | + | + |
| Inversion $\mathcal{P}$ | + | − | + | − | + | + | − | − |

In this case, time-reversal and parity operators are written as $\mathcal{T} = \mathbf{1} \otimes (-i\sigma_2)\mathcal{K}$ ($\mathcal{K}$ is the complex conjugation operator) and $\mathcal{P} = \sigma_3 \otimes \mathbf{1}$. It is easy to show that the Hamiltonian (1.44) has time-reversal and inversion symmetries as $\mathcal{T}\mathcal{H}_{\text{Dirac}}(\boldsymbol{k})\mathcal{T}^{-1} = \mathcal{P}\mathcal{H}_{\text{Dirac}}(\boldsymbol{k})\mathcal{P}^{-1} = \mathcal{H}_{\text{Dirac}}(-\boldsymbol{k})$, which results from the fact that

$$\mathcal{T}\alpha_\mu\mathcal{T}^{-1} = \mathcal{P}\alpha_\mu\mathcal{P}^{-1} = -\alpha_\mu \ (\mu \neq 4),$$
$$\mathcal{T}\alpha_4\mathcal{T}^{-1} = \mathcal{P}\alpha_4\mathcal{P}^{-1} = \alpha_4. \tag{1.46}$$

Next we consider to add symmetry breaking perturbation terms to the Hamiltonian (1.44) [31,34]. It is known that there exist 16 independent matrices which consist of $\alpha_\mu$. The 16 matrices are given by $\mathbf{1}$ (the identity matrix), $\alpha_\mu$ ($\mu = 1, 2, 3, 4, 5$), and $\alpha_{\mu\nu} = -\frac{i}{2}[\alpha_\mu, \alpha_\nu]$ ($\mu < \nu$). The matrices $\mathbf{1}$ and $\alpha_\mu$ are trivial. Let us closely look at the 10 matrices $\alpha_{\mu\nu}$. In the Dirac representation, they are written explicitly as

$$\Sigma_j \equiv \alpha_{ik}\epsilon_{ikj} = \begin{bmatrix} \sigma_j & 0 \\ 0 & \sigma_j \end{bmatrix}, \quad \Sigma'_j \equiv \alpha_{j5} = \begin{bmatrix} \sigma_j & 0 \\ 0 & -\sigma_j \end{bmatrix},$$
$$\Pi_j \equiv \alpha_{j4} = \begin{bmatrix} 0 & -i\sigma_j \\ i\sigma_j & 0 \end{bmatrix}, \quad \Pi_0 \equiv \alpha_{45} = \begin{bmatrix} 0 & 1 \\ 1 & 0 \end{bmatrix}, \tag{1.47}$$

where $j = 1, 2, 3$. Note that these are Hermitian matrices. It is easily shown that $\Sigma_j$ and $\Sigma'_j$ are odd under time-reversal but even under parity:

$$\mathcal{T}\Sigma_j\mathcal{T}^{-1} = \mathcal{T}\Sigma'_j\mathcal{T}^{-1} = -1, \quad \mathcal{P}\Sigma_j\mathcal{P}^{-1} = \mathcal{P}\Sigma'_j\mathcal{P}^{-1} = +1. \tag{1.48}$$

On the other hand, $\Pi_\mu$ are even under time-reversal but odd under parity:

$$\mathcal{T}\Pi_\mu\mathcal{T}^{-1} = +1, \quad \mathcal{P}\Pi_\mu\mathcal{P}^{-1} = -1. \tag{1.49}$$

The properties of the 16 matrices are summarized in Table 1.1. With these matrices, the most general perturbation Hamiltonian can be expressed as

$$\mathcal{H}' = \Delta\alpha_5 + \boldsymbol{b} \cdot \boldsymbol{\Sigma} + \boldsymbol{b}' \cdot \boldsymbol{\Sigma}' + \rho_0\Pi_0 + \boldsymbol{\rho} \cdot \boldsymbol{\Pi}. \tag{1.50}$$

Let us consider the simplest realization of a Weyl semimetal with broken time-reversal symmetry and with two Weyl nodes in our setup. In this case, the Hamiltonian is given by

$$\mathcal{H}(\boldsymbol{k}) = k_j\alpha_j + m_0\alpha_4 + b\Sigma_3, \tag{1.51}$$

where we have set $\boldsymbol{b} = (0, 0, b)$ without loss of generality, and have set $v_{\text{F}} = 1$. Here note that repeated subscripts represent the summation over the subscript. The energy eigenvalues of this

Hamiltonian $E(\boldsymbol{k})$ are obtained easily by taking the square as follows:

$$
\begin{aligned}
\mathcal{H}^2 &= (k_j \alpha_j + m_0 \alpha_4 + b\Sigma_3) \cdot (k_l \alpha_l + m_0 \alpha_4 + b\Sigma_3) \\
&= k_j k_l \{\alpha_j, \alpha_l\}/2 + k_j m_0 \{\alpha_j, \alpha_4\} + m_0^2 + k_j b\{\alpha_j, \Sigma_3\} + m_0 b\{\alpha_4, \Sigma_3\} + b^2 \\
&= (k^2 + m_0^2 + b^2)\mathbf{1} + 2b \begin{bmatrix} m_0 \sigma_3 & k_3 \\ k_3 & -m_0 \sigma_3 \end{bmatrix}
\end{aligned}
\tag{1.52}
$$

with $k^2 = k_1^2 + k_2^2 + k_3^2$. The second term is diagonalized as

$$
\begin{bmatrix} m_0 \sigma_3 & k_3 \\ k_3 & -m_0 \sigma_3 \end{bmatrix}^2 = (k_3^2 + m_0^2)\mathbf{1},
\tag{1.53}
$$

which results in

$$
\mathcal{H}^2 = (k^2 + m_0^2 + b^2)\mathbf{1} + \pm 2b\sqrt{k_3^2 + m_0^2}\,\mathbf{1}.
\tag{1.54}
$$

Finally, we obtain the four eigenvalues

$$
E(\boldsymbol{k}) = \pm\sqrt{k_1^2 + k_2^2 + \left[\sqrt{k_3^2 + m_0^2} \pm b\right]^2},
\tag{1.55}
$$

and we see that the two Weyl nodes $W_\pm$ are given by $W_\pm = (0, 0, \pm\sqrt{b^2 - m_0^2})$ with $b > |m_0|$. Then the energy bands near the Weyl nodes are found to be $E(\boldsymbol{q}) = \pm\sqrt{q_1^2 + q_2^2 + (1 - m_0^2/b^2)q_3^2}$ where $\boldsymbol{q} = \boldsymbol{k} - W_\pm$. Note that these bands are not degenerate. Hence this is the dispersion of Weyl fermions, since $E(\boldsymbol{q})$ can be obtained by diagonalizing the Weyl Hamiltonian $\mathcal{H}_{\text{Weyl}}(\boldsymbol{q}) = \sum_{i=1}^{3} v_i q_i \sigma_i$ with $v_1 = v_2 = 1$ and $v_3 = \pm\sqrt{1 - m_0^2/b^2}$.

Similar discussions can be applied to the cases of $\Sigma'_j$, $\Pi_0$, or $\Pi_j$ [34]. For example, in the case where the Hamiltonian is given by $\mathcal{H}(\boldsymbol{k}) = k_j \alpha_j + m_0 \alpha_4 + b'\Sigma'_3$, there exists a line (circle) node when $b' > |m_0|$. In the case where the Hamiltonian is given by $\mathcal{H}(\boldsymbol{k}) = k_j \alpha_j + m_0 \alpha_4 + \rho_0 \Pi_0 + \rho_1 \Pi_1$, there exists a line (circle) node only when $m_0 = 0$.

### 1.3.3 Topological Magnetoelectric Effect

Another topological aspect of Weyl semimetals with broken time-reversal symmetry is the emergence of the topological magnetoelectric effect described by the theta term (1.26) [43–46]. Unlike 3D topological insulators, due to the breaking of time-reversal symmetry, the coefficient $\theta$ does not take the quantized value $\pi$. In the following, for simplicity and concreteness, we consider a simple model of a two-node Weyl semimetal with broken time-reversal symmetry described by Eq. (1.51). In this case, the value of $\theta$ reads

$$
\theta(\boldsymbol{x}) = 2\boldsymbol{b} \cdot \boldsymbol{x},
\tag{1.56}
$$

where $2\boldsymbol{b}$ is the vector connecting the two Weyl nodes in momentum space, and $\boldsymbol{x}$ is a real-space three-dimensional coordinate vector in the bulk.

Let us derive the above expression for $\theta$. To this end, we start from the Minkowski action of the system in the presence of an external electromagnetic field $A_\mu$:

$$S_{\text{WSM}} = \int d^4x \bar{\psi}(x)[i\gamma^\mu(\partial_\mu + ieA_\mu) - m_0 - b^j\gamma^j\gamma^5]\psi(x), \tag{1.57}$$

where $\psi(x)$ is a four-component spinor, and the gamma matrices $\gamma^\mu$ are given by the Dirac representation as

$$\gamma^0 = \begin{bmatrix} 1 & 0 \\ 0 & -1 \end{bmatrix}, \quad \gamma^j = \begin{bmatrix} 0 & \sigma_j \\ -\sigma_j & 0 \end{bmatrix}, \quad \gamma^5 = \begin{bmatrix} 0 & 1 \\ 1 & 0 \end{bmatrix}. \tag{1.58}$$

Noting that $\bar{\psi} = \psi^\dagger\gamma^0$, $\gamma^0 = \alpha_4$, and $\gamma^0\gamma^j = \alpha_j$, the noninteracting Hamiltonian of the system is given by

$$H = \int d^3x \psi^\dagger(x)[-i\alpha_j\partial_j + m_0\alpha_4 + \boldsymbol{b} \cdot \boldsymbol{\Sigma}]\psi(x), \tag{1.59}$$

which reproduce Eq. (1.51). For simplicity, we consider the case of $m_0 = 0$. Then the two Weyl nodes locate $\pm\boldsymbol{b}$. It is convenient to study the system in the imaginary time notation. Namely, we rewrite $t$, $A_0$ and $\gamma^j$ as $t \to -i\tau$, $A_0 \to iA_0$, and $\gamma^j \to i\gamma_j$. The Euclidean action of the system is written as

$$S_{\text{WSM}} = \int d\tau d^3x \bar{\psi}(x)[\gamma_0(\partial_0 + ieA_0) + \gamma_j(\partial_j + ieA_j + ib_j\gamma_5)]\psi(x). \tag{1.60}$$

From this action, we see that $b_j$, which generates the Weyl semimetal phase, can be regarded as a kind of gauge fields. To derive the theta term, we employ the so-called Fujikawa's method [27, 28]. The procedure is the same as in the case of 3D topological insulators [see Subsect. 1.2.3]. We write down again the procedure briefly in what follows. First let us consider an infinitesimal chiral transformation defined by

$$\psi \to \psi' = e^{-i\theta(\boldsymbol{x})d\phi\gamma_5/2}\psi, \qquad \bar{\psi} \to \bar{\psi}' = \bar{\psi}e^{-i\theta(\boldsymbol{x})d\phi\gamma_5/2}, \tag{1.61}$$

where $\phi \in [0, 1]$ and $\theta(\boldsymbol{x}) = 2b_jx_j = 2\boldsymbol{b} \cdot \boldsymbol{x}$. Then the partition function $Z$ is transformed as

$$Z = \int \mathcal{D}[\psi, \bar{\psi}]e^{-S_{\text{WSM}}[\psi, \bar{\psi}]} \quad \to \quad Z' = \int \mathcal{D}[\psi', \bar{\psi}']e^{-S'_{\text{WSM}}[\psi', \bar{\psi}']}. \tag{1.62}$$

The theta term comes from the Jacobian defined by $\mathcal{D}[\psi', \bar{\psi}'] = J\mathcal{D}[\psi, \bar{\psi}]$. The action (1.63) is transformed as

$$\begin{aligned} S'_{\text{WSM}} = &\int d\tau d^3x \bar{\psi}(x) \left\{\gamma_0(\partial_0 + ieA_0) + \gamma_j[\partial_j + ieA_j + ib_j(1 - d\phi)\gamma_5]\right\}\psi(x) \\ &+ \frac{i}{2}\int d\tau d^3x d\phi \partial_\mu[\theta(\boldsymbol{x})\bar{\psi}\gamma_\mu\gamma_5\psi]. \end{aligned} \tag{1.63}$$

The Jacobian is written as [27, 28]

$$J = \exp\left[-i\int d\tau d^3x d\phi \frac{\theta(\boldsymbol{x})e^2}{32\pi^2\hbar c}\epsilon^{\mu\nu\rho\lambda}F_{\mu\nu}F_{\rho\lambda}\right]. \tag{1.64}$$

Here $F_{\mu\nu} = \partial_\mu A_\nu - \partial_\nu A_\mu$ and we have written $\hbar$ and $c$ explicitly. We repeat this procedure infinite times, i.e., integrate with respect to the variable $\phi$ from 0 to 1. Due to the invariance of the partition function, finally we arrive at the following expression of $S_{\text{WSM}}$:

$$S_{\text{WSM}} = \int d\tau d^3x \bar{\psi}(x)\gamma_\mu(\partial_\mu + ieA_\mu)\psi(x) + i \int d\tau d^3x \frac{\theta(x)e^2}{32\pi^2\hbar c}\epsilon^{\mu\nu\rho\lambda}F_{\mu\nu}F_{\rho\lambda}, \qquad (1.65)$$

where we have dropped the irrelevant surface term. The first term is the usual action of the Dirac fermions with unbroken symmetries. The second term is nothing but the theta term in imaginary time.

Next let us consider the consequence of the existence of the theta term in Weyl semimetals. Notice that the theta term (in real time) can be rewritten as

$$S_\theta = \int d^4x \frac{\theta(x)e^2}{8\pi^2\hbar c}\epsilon^{\mu\nu\rho\lambda}\partial_\mu A_\nu \partial_\rho A_\lambda = -\int d^4x \frac{e^2}{8\pi^2\hbar c}\epsilon^{\mu\nu\rho\lambda}[\partial_\mu\theta(x)]A_\nu\partial_\rho A_\lambda, \qquad (1.66)$$

where in the second equality, we have dropped the surface term and used $\epsilon^{\mu\nu\rho\lambda}\partial_\mu\partial_\rho A_\lambda = 0$. The induced current $\boldsymbol{j}$ can be obtained from the variation of the above action with respect to the vector potential $A_n$:

$$j^n = -\frac{e^2}{2\pi^2\hbar c}b_m\epsilon^{mn\rho\lambda}\partial_\rho A_\lambda = \frac{e^2}{\pi hc}(\boldsymbol{b}\times\boldsymbol{E})_n, \qquad (1.67)$$

where $n = 1, 2, 3$. Apparently, this equation indicate the anomalous Hall current due to time-reversal symmetry breaking. For concreteness, let us set $\boldsymbol{b} = (0, 0, b)$. Then we get the Hall current $j_x = -\sigma_{xy}E_y$ with $\sigma_{xy} = \frac{e^2}{h}\frac{b}{\pi}$. This value of the Hall conducticity $\sigma_{xy}$ is exactly the same as Eq. (1.43). Similarly, we obtain the induced charge density $\rho$ as

$$\rho \equiv j^0 = -\frac{e^2}{2\pi^2\hbar c}b_m\epsilon^{m0\rho\lambda}\partial_\rho A_\lambda = -\frac{e^2}{\pi hc}\boldsymbol{b}\cdot\boldsymbol{B}. \qquad (1.68)$$

So far we have focused on a case where time-reversal symmetry is broken but inversion symmetry is not broken. What happens if we add an inversion symmetry breaking term $ib_0\gamma_0\gamma_5$ to the action (1.63)? The term $ib_0\gamma_0\gamma_5$ corresponds to $\Pi_0$ in the Hamiltonian formalism. In such a case, we can apply the same procedure as above to obtain the value of $\theta$. The result reads

$$\theta(\boldsymbol{x}, t) = 2(\boldsymbol{b}\cdot\boldsymbol{x} - b_0 t). \qquad (1.69)$$

The induced current is modified to

$$\boldsymbol{j} = \frac{e^2}{\pi hc}(\boldsymbol{b}\times\boldsymbol{E} - b_0\boldsymbol{B}), \qquad (1.70)$$

where the second term is referred to as the chiral magnetic effect [47]. The equation indicates that a dissipationless ground-state current proportional to an applied magnetic field is generated. If the chiral magnetic effect is present, it would lead to interesting applications. However, recent theoretical studies suggest that there does not exist the chiral magnetic effect in realistic (lattice) systems [45, 46].
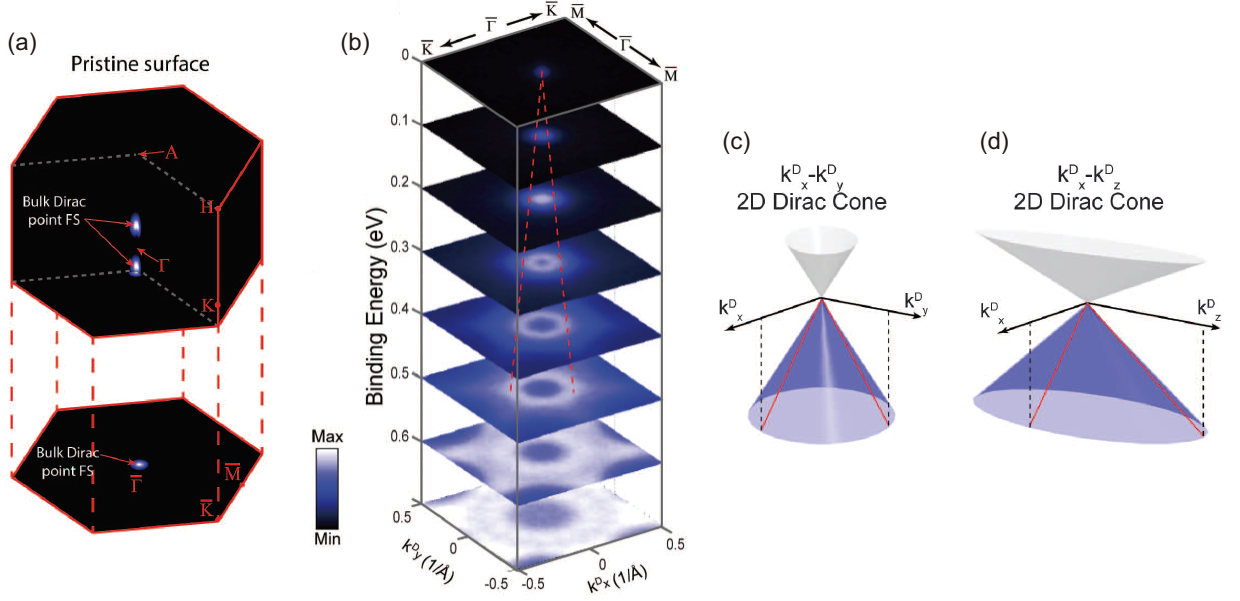
Figure 1.12: An ARPES data on the electronic structure of $Na_3Bi$ [51]. (a) Two Dirac nodes in the bulk and projected surface Brillouin zones. (b) Stacking plot of constant energy contours at different binding energies in the $k_x$-$k_y$ plane. (c) [(d)] Schematic picture of the Dirac cone in the $(k_x, k_y, E)$ [$(k_x, k_z, E)$] space.

## 1.4 Dirac Semimetals

Dirac semimetals in three spatial dimensions have gapless three-dimensional (3D) linear dispersions, i.e. 3D Dirac cones, in the bulk band structure. In contrast to Weyl semimetals, time-reversal and spatial inversion symmetries are not broken in Dirac semimetals. Hence they can be regarded as a 3D analog of graphene. After the theoretical predictions had been made [48–50], the Dirac semimetals such as $Na_3Bi$ and $Cd_3As_2$ were experimentally discovered recently [51–55]. The low-energy effective model near a band touching point (the Dirac node) $k_0$ is described by the Dirac fermions, namely by the $4 \times 4$ Hamiltonian such that

$$\mathcal{H}_{\text{Dirac}}(q) = \sum_{j=1}^{3} v_j q_j \alpha_j, \tag{1.71}$$

where $q = k - k_0$, $v_j$ is the Fermi velocity for the $k_j$-direction, and $\alpha_j$ are $4 \times 4$ matrices which satisfy the Clifford algebra $\{\alpha_\mu, \alpha_\nu\} = 2\delta_{\mu\nu}\mathbf{1}$. The doubly-degenerate energy eigenvalues are obtained as $E_{\text{Dirac}}(q) = \pm\sqrt{\sum_j (v_j q_j)^2}$. The observed Dirac semimetals $Na_3Bi$ and $Cd_3As_2$ possess two Dirac nodes which are protected by crystalline symmetry. The electronic structure of $Na_3Bi$ observed by an ARPES measurement is shown in Fig. 1.12. It can be seen that indeed, the Fermi surface consists of two points (Dirac nodes) and the dispersion is linear near the Dirac nodes. It should be noted that there exist large out-of-plane Fermi velocity anisotropy such that $v_{F\perp}/v_{F\parallel} \approx 0.25$ with $v_{F\parallel} = 3.74 \times 10^5$ [m/s] in $Na_3Bi$ [51] [see Fig. 1.12(c) and (d)], and $v_{F\perp}/v_{F\parallel} \sim 0.1$ with $v_{F\parallel} \simeq 1.5 \times 10^6$ [m/s] in $Cd_3As_2$ [52]. Here we have defined $v_F^z \equiv v_{F\perp}$ and $v_F^x \approx v_F^y \equiv v_{F\parallel}$. This contrasts to the case of graphene, where the Fermi velocity is isotropic ($v_F \simeq 1 \times 10^6$ [m/s]) [56].
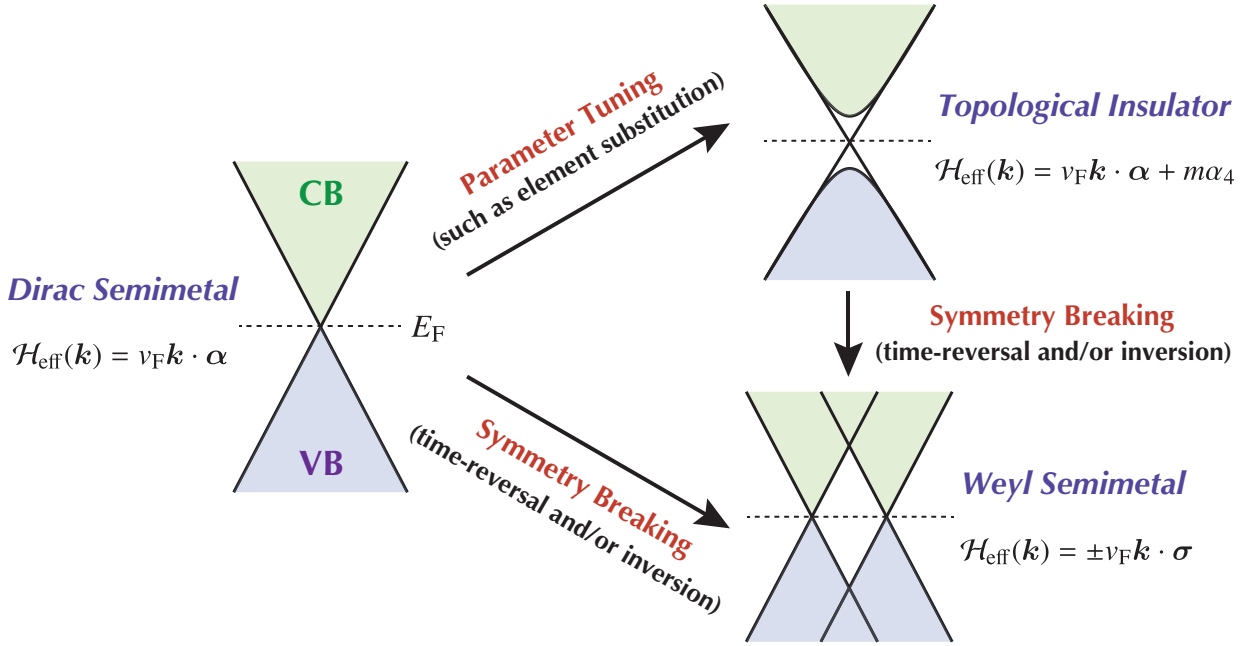
Figure 1.13: Schematic diagram of the relation of Dirac semimetals with Weyl semimetals and 3D topological insulators. $v_\text{F}$ is the Fermi velocity. "CB" and "VB" represent the conduction and valence bands, respectively. In 3D topological insulators such as $Bi_2Se_3$, the mass of Dirac fermions $m$ becomes negative. (Conversely, $m > 0$ in normal insulators.) The matrices $\alpha_j$ and $\sigma_j$ are $4 \times 4$ and $2 \times 2$ matrices, respectively, where $\{\alpha_i, \alpha_j\} = 2\delta_{ij}\mathbf{1}$ and $\{\sigma_i, \sigma_j\} = 2\delta_{ij}\mathbf{1}$.

One of the important meanings of the realization of Dirac semimetals is on the point that they can lead to various topological phases, since they lie next to various topological phases in the phase diagrams. In 3D topological insulators, the bulk energy gap closing is required to make the system turn into normal band insulators [11, 12, 16]. At these transition points, Dirac semimetals can be realized. Experimentally, such a continuous transition is observed in the solid-solution system $TlBi(S_{1-x}Se_x)_2$ [57]. Further, Weyl semimetals can be realized when time-reversal or inversion symmetry breaking occurs in Dirac semimetals [30–32, 34, 58]. Regardless of intensive searches, Weyl semimetal phases have not been experimentally observed so far. Hence, it is expected that recent experimental realization of the Dirac semimetals also gives rise to the realization of Weyl semimetal phases. A schematic diagram of the relation of Dirac semimetals with Weyl semimetals and 3D topological insulators is shown in Fig. 1.13. Here note that spin-orbit coupling is strong in experimentally observed Dirac semimetals $Na_3Bi$ and $Cd_3As_2$. As was shown in Sect. 1.1 and Sect. 1.2, strong spin-orbit coupling is essential to realize topologically nontrivial phases.

The low-energy effective model of Dirac semimetals and that of Weyl semimetals are resemble. To show this, let us consider a simplified low-energy effective model for a Weyl semimetal with $2N$ nodes. The Hamiltonian of such a system can be written as

$$
\begin{aligned}
H_{\text{Weyl}}^{\text{eff}} &= \sum_{\boldsymbol{k}} \sum_{f=1}^{N} v_{\text{F}\parallel} \left\{ \psi_{f+}^{\dagger}(\boldsymbol{k}) \left[ \xi_i k_i \sigma_i \right] \psi_{f+}(\boldsymbol{k}) + \psi_{f-}^{\dagger}(\boldsymbol{k}) \left[ -\xi_i k_i \sigma_i \right] \psi_{f-}(\boldsymbol{k}) \right\} \\
&= \sum_{\boldsymbol{k}} \sum_{f=1}^{N} \psi_{f}^{\dagger}(\boldsymbol{k}) v_{\text{F}\parallel} \begin{bmatrix} \xi_i k_i \sigma_i & 0 \\ 0 & -\xi_i k_i \sigma_i \end{bmatrix} \psi_f(\boldsymbol{k}),
\end{aligned}
\tag{1.72}
$$

where $\psi_f = [\psi_{f+}, \psi_{f-}]^T$ with $\psi_{f\pm}$ being a two-component spinor, the subscript $\pm$ denotes the chirality of each Weyl node, and we have introduced the Fermi velocity anisotropy $\xi_i$ defined by $\xi_1 = \xi_2 = 1$ and $\xi_3 = v_{\text{F}\perp}/v_{\text{F}\parallel}$. The second line of the Hamiltonian (1.72) represents a Dirac semimetal with $N$ nodes, since the $4 \times 4$ matrices $\tau_3 \otimes \sigma_i$ satisfy the Clifford algebra (usually this representation is called the Weyl or chiral representation). Namely, this indicates that in a rough approximation, the low-energy effective model of a $2N$-node Weyl semimetal is equivalent to that of a $N$-node Dirac semimetal. However, note that the mass term can be added (i.e., the spectrum can be gapped) in Dirac Hamiltonians, whereas it cannot be added in Weyl Hamiltonians. In this sense, it is expected as a bulk property that Weyl semimetals are more robust against perturbations than Dirac semimetals.

## 1.5 Spin-Orbit Coupling and Electron Correlation

So far we have reviewed "noninteracting" topologically nontrivial phases. We have seen the importance of spin-orbit coupling, namely, that strong spin-orbit coupling is essential to realize topologically nontrivial phases [3–5]. On the other hand, the importance of strong electron correlations has been acknowledged in the field of condensed matter physics [59–61]. For example, unconventional (and high temperature) superconductivity and colossal magnetoresistance can emerge as a consequence of strong electron correlations. Then it is a natural question that what happens when both spin-orbit coupling and electron correlation are present. In this section, we review phenomena and phases which emerge in the presence of both spin-orbit coupling and electron correlation.

### 1.5.1 Emergence of Novel Phases and Phenomena

One of the triggers to recent intensive studies on the interplay of spin-orbit coupling and electron correlation is due to the discovery of a novel Mott insulating state in $Sr_2IrO_4$, a correlated $5d$-electron system with spin-orbit coupling [62,63]. In the absence of spin-orbit coupling, electrons' spin $\boldsymbol{S}$ is a good quantum number. However, in the presence of spin-orbit coupling $\mathcal{H}_{\text{SO}} = \lambda \boldsymbol{L} \cdot \boldsymbol{S}$ where $\boldsymbol{L}$ is the orbital angular momentum of an electron, the total angular momentum $\boldsymbol{J} = \boldsymbol{L} + \boldsymbol{S}$ should be used instead of $\boldsymbol{S}$. In $Sr_2IrO_4$, the $5d$ orbitals are split into $e_g(x^2 - y^2, 3z^2 - r^2)$ and $t_{2g}(xy, yz, zx)$ orbitals by the crystal field with $O_h$ symmetry. Then the $5d$ electrons take $t_{2g}^5$ configuration due to the splitting of $10Dq$. Taking into account the spin-orbit coupling in the $t_{2g}$ orbitals results in the effective orbital angular momentum $L_{\text{eff}} = 1$. Then the $t_{2g}$ orbitals form effectively $J_{\text{eff}} = 1/2$ and $J_{\text{eff}} = 3/2$ bands where the $J_{\text{eff}} = 1/2$ band is half-filled. The wave
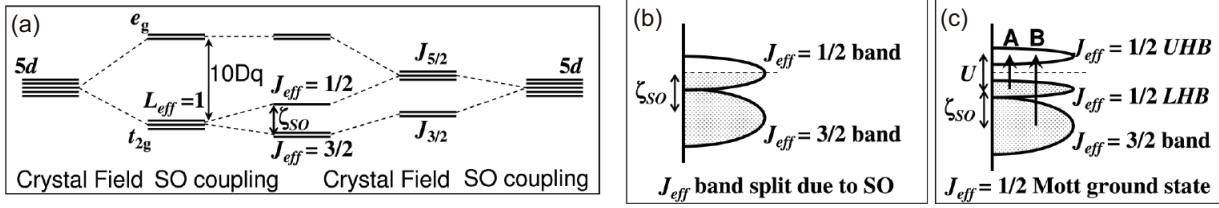
Figure 1.14: Schematic diagram for the realization of the $J_{\text{eff}} = 1/2$ Mott insulating state in $Sr_2IrO_4$ [62]. (a) $5d$ orbitals in the presence of crystal field and spin-orbit coupling. (b) Energy bands of $t_{2g}^5$ configuration with spin-orbit coupling and without electron correlation. (c) Those with spin-orbit coupling and electron correlation. $\zeta_{\text{SO}}$ and $U$ represent the strength of the spin-orbit coupling and on-site interaction, respectively.

functions of the $J_{\text{eff}} = 1/2$ state are given by [62, 63]

$$|J_{\text{eff}} = 1/2; m = \pm 1/2\rangle = \frac{1}{\sqrt{3}} \left[ |xy, \mp\sigma\rangle \mp |yz, \pm\sigma\rangle + i|zx, \pm\sigma\rangle \right], \qquad (1.73)$$

where $\sigma$ denotes the spin state. Finally the on-site electron-electron interactions open a gap in the $J_{\text{eff}} = 1/2$ band (i.e., the $J_{\text{eff}} = 1/2$ band is split into the upper and lower Hubbard bands). The realization of the $J_{\text{eff}} = 1/2$ Mott insulating state is schematically shown in Fig. 1.14. In similar $J_{\text{eff}} = 1/2$ Mott insulating systems, it has been shown that the quantum compass model can be derived [64] and the quantum spin Hall effect can emerge [65].

There are many theoretical studies which suggest that other phases and phenomena, especially topological phases, can emerge as a consequence of the interplay of spin-orbit coupling and electron correlation. The emergence of a quantum spin Hall insulator, which can exist without electron correlation as we saw in Subsect. 1.1.2, in a layered iridate (iridium oxide) is one of the examples [65]. In another iridate on the pyrochrore lattice, the topological Mott insulator (or fractionalized topological insulator) phase, where there is a bulk gap but the spinons have nontrivial topology, has been predicted [see Fig. 1.15(a)] [66]. In the antiferromagnetic insulator phase of correlated 3D topological insulators, the realization of the dynamical axion field by the spin-wave excitations has been predicted [67]. The resulting phenomenon, the axionic polariton, has a notable property such that the frequency for the total reflection of incident light can be tuned by external magnetic fields, compared to the phononic polariton where the frequency is determined by the materials parameter [see Fig. 1.15(b)]. The Weyl semimetal phase in pyrochlore iridates introduced in Subsect. 1.3.1 is also a topological phase [29]. It has also been reported that a topological order occurs in a 2D topological insulator [68] and a 3D topological insulator [69].

The possibility for the realization of topological insulator phases solely by electron correlations (i.e., without spin-orbit coupling) should be noted here. At the mean-field level, some studies have suggested the realization in two-dimensions [70] and three-dimensions [71,72]. The mechanism is that long-range (inter-site) interaction terms can result in the same form as spin-orbit interactions by the mean-field decoupling. However, recent studies beyond the mean-field approximation do not support the realization in at least two-dimensions [73, 74].
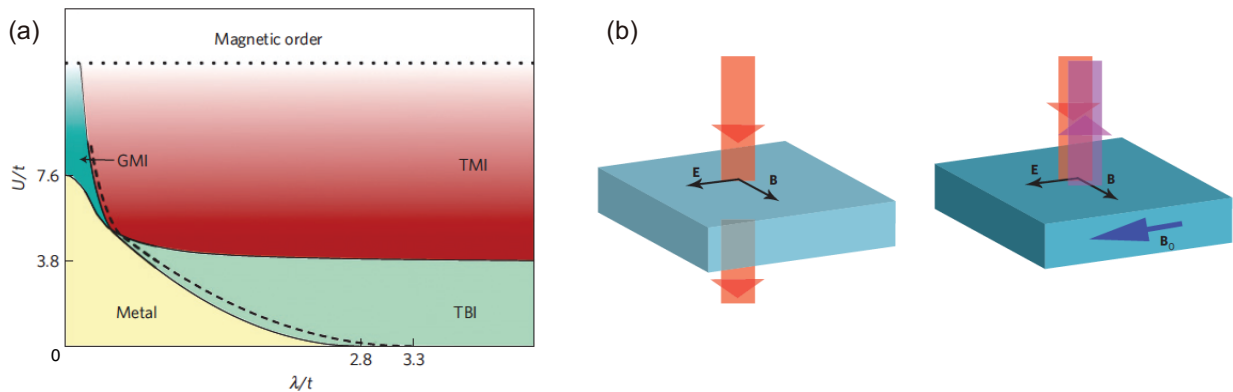
Figure 1.15: (a) Predicted phase diagram of a pyrochlore iridaite. $\lambda$ and $U$ represent the strength of the spin-orbit coupling and on-site interaction, respectively. TMI, TBI and GMI indicate the topological Mott insulator, topological band insulator, and gapless Mott insulator, respectively [66]. (b) (left) Without external magnetic fields, the incident light can transmit the material. (right) In the presence of external magnetic fields and when the dynamical axion field is realized, the incident light which frequency is within a range is totally reflected [67].

## 1.5.2 Stability of Topological Phases

Topological phases are stable against weak perturbations, since the topological invariants do not change when the Hamiltonians change smoothly, i.e., do not depend on the detail of band structures. Then what happens when strong perturbations are added to topological phases? Stability of topological phases against electron correlations is one of the attractive themes. Preceding studies have mainly focused on the effects of strong short-range interactions on the bulk of topological insulators. It has been shown that strong short-range interactions described by the Hubbard term break 2D topological insulator phases [75–88] and 3D topological insulator phases [66, 89]. The disappearance of these topological insulator phases is due to the development of time-reversal symmetry breaking orders, mainly antiferromagnetic phases, with increasing on-site interactions. Note that these topological insulators have half-filled bands. In the intermediate interaction-strength regions of topological insulators with short-range interactions, several interesting phases have been reported. For example, an antiferromagnetic topological insulator phase, where the antiferromagnetic order and nontrivial topology coexist, has been reported in two-dimensions [90], although the concept of antiferromagnetic topological insulators was originally proposed in a system without interactions [91]. Fractionalized topological insulator phases, where there is a bulk (charge) gap but the edge spinons are gapless, have also been reported in two-dimensions [75, 76] and three-dimensions [66].

Next we consider the stability of Weyl semimetals against electron correlations. As mentioned in Sect. 1.3, a single Weyl fermion cannot be massive by itself, since all the three Pauli matrices which anticommute with each other are used. Namely, the existence of a single Weyl node is robust against perturbations. An energy gap opens only if pairs of Weyl fermions with opposite chirality meet and annihilate each other. Recent theoretical studies have reported that strong short-range interactions open a gap, namely they break Weyl semimetal phases [89,92,93]. Another study has suggested that long-range interactions also break a Weyl semimetal phase [94].

# Chapter 2

# Lattice-Gauge-Theoretical Approach to Interacting Dirac Fermion Systems

In this chapter, we review the *lattice gauge theory*, an approach to interacting Dirac fermion systems. First we show how the quantum field theory is realized in interacting electron systems. Then we introduce the formulations for the lattice regularization of Dirac fermions, and the lattice regularization of gauge fields. Finally we introduce recent lattice-gauge-theoretical studies on graphene, a two-dimensional Dirac fermion system in condensed matter.

## 2.1 Introduction

The lattice gauge theory was first proposed in 1974 by K. G. Wilson to describe the confinement of quarks [95]. In quantum chromodynamics (QCD) which describes the strong interactions between quarks and gluons, it is difficult to perform perturbative calculations from weak coupling, compared to quantum electrodynamics (QED) where the interactions between electrons and photons are weak. One of the powerful methods which enable us to treat strong interactions properly is the lattice gauge theory. The lattice gauge theory defines Dirac fermions and gauge fields on lattices. Note that finite lattice spacing $a$ prevents physical quantities from diverging, since there exists momentum cutoff $\pi/a$. Another important point is that there is no need to do gauge fixings. Further, as we shall see later, the action of gauge fields have the coefficient $1/g^2$ with $g$ being the coupling strength between fermions and gauge fields. This enables us to perform perturbative calculations from the *strong coupling limit* $g \to \infty$. We will use such a calculation method, the strong coupling expansion of the lattice gauge theory.

In condensed matter physics, $1/r$ Coulomb interactions between electrons can be taken into account via the presence of U(1) gauge field (or scalar potential), as in the case of QED. Particularly, Dirac fermion systems with $1/r$ Coulomb interactions look very similar to QED, except for the small Fermi velocity compared to the speed of light and for the absence of spatial components of U(1) gauge field. Graphene is one of the most famous Dirac fermion systems in condensed matter [56], and the effects of long-range Coulomb interactions in graphene have been studied widely [96]. Monolayer graphene on a substrate with sufficiently small dielectric constant has been predicted theoretically to be insulating (i.e. Dirac fermions become massive) due to strong $1/r$ Coulomb interactions [97–106]. However, as the number of layers is increased, it has been found that the semimetal phase survives strong $1/r$ Coulomb interactions [97, 98, 100, 101, 113]. As a powerful method which enables us to treat strong $1/r$ Coulomb interactions properly,

the U(1) lattice gauge theory has been applied to discuss the semimetal-insulator transition in graphene [101–107]. In this theory, the value of the chiral condensate, which is the dynamically generated mass of Dirac fermions, is used as the order parameter for the transition. It should be noted that the value obtained in an analytical calculation, the strong coupling expansion of the lattice gauge theory [103], and the value obtained in a numerical calculation [101, 102] are in good agreement in the strong coupling region.

Here we mention an important point. In the lattice-gauge-theoretical description for electron systems with $1/r$ Coulomb interactions, the on-site interactions are *not* included. The reason is as follows. Introducing a finite lattice spacing $a$ is equivalent to introducing an ultraviolet momentum cutoff of $\pi/a$ in the continuum model. If on-site interactions in the $1/r$-type interaction are included, i.e., if $1/r$ with $r \to 0$, then the system diverges. This divergence corresponds to the ultraviolet divergence in the continuum model. Therefore, introducing a finite lattice spacing results in the absence of on-site interactions. Next we consider whether the system is well-defined on a lattice. As mentioned above, Dirac fermion systems with $1/r$ Coulomb interactions on a lattice are very similar to QED. In QED, up to all orders of perturbation theory, ultraviolet divergence can be eliminated [108]. Equivalently, QED is referred to as a *renormalizable* quantum field theory. Thanks to this nature, the lattice QED (QED on a lattice) is well-defined and has been studied so far [109–111]. Hence, it is expected that Dirac fermion systems with $1/r$ Coulomb interactions on a lattice are also well-defined. This suggests that unphysical states due to the absence of on-site interactions, such as phase separation, can be eliminated from consideration.

## 2.2 Quantum Field Theory in Condensed Matter

Let us consider the case of graphene as an introduction to interacting Dirac fermion systems in condensed matter. Graphene is a two-dimensional (2D) carbon material which forms a honeycomb lattice. The noninteracting Hamiltonian of graphene is well described by a tight-binding Hamiltonian on the honeycomb lattice, $H_0 = -t \sum_{\langle i,j \rangle} (b_{i\sigma}^\dagger a_{j\sigma} + \text{H.c.})$ where $a_{i\sigma}$ ($b_{i\sigma}$) is an electron annihilation operator at site $i$ on sublattice $A$ ($B$) with spin $\sigma$. Then the low-energy effective Hamiltonian near the Fermi level can be written as [112]

$$H_{\text{eff}} = v_{\text{F}} \sum_{\boldsymbol{k},\sigma} \psi_{\boldsymbol{k}\sigma}^\dagger (\boldsymbol{k} \cdot \boldsymbol{\alpha}) \psi_{\boldsymbol{k}\sigma}, \tag{2.1}$$

where $v_{\text{F}}(\simeq 1 \times 10^6 \, [\text{m/s}])$ is the Fermi velocity, $\psi_{\boldsymbol{k}\sigma} = [a_{K_+ + \boldsymbol{k},\sigma}, b_{K_+ + \boldsymbol{k},\sigma}, a_{K_- + \boldsymbol{k},\sigma}, b_{K_- + \boldsymbol{k},\sigma}]^T$ is a four-component spinor, and $\boldsymbol{K}_\pm$ are the two band-touching points. The matrices $\alpha_j$ are given by, for example, $\alpha_1 = 1 \otimes \sigma_1$ and $\alpha_2 = \tau_3 \otimes \sigma_2$, where the Clifford algebra $\{\alpha_i, \alpha_j\} = 2\delta_{ij}$ is satisfied. The doubly-degenerate energy eigenvalues are obtained as $E(\boldsymbol{k}) = \pm v_{\text{F}} |\boldsymbol{k}|$. The above Hamiltonian is nothing but the four-component massless Dirac Hamiltonian.

Let us recall that the density of states of massless Dirac fermion systems, where the dispersions are written as $E(\boldsymbol{k}) \propto \pm |\boldsymbol{k}|$, is given by $\rho(E) \propto |E|$ in two-dimensions and $\rho(E) \propto E^2$ in three-dimensions. Then the screened Coulomb interactions between electrons are written as

$$H_{\text{Coulomb}} = \frac{1}{2} \int d^3r \, d^3r' \, n(r) \left[ \frac{e^2}{4\pi\epsilon} \frac{e^{-k_0 R}}{R} \right] n(r'), \tag{2.2}$$

where $n(\boldsymbol{r}) = c_{\boldsymbol{r}}^\dagger c_{\boldsymbol{r}}$ is the electron density operator at $\boldsymbol{r}$, $\epsilon$ is the dielectric constant of the system, and $R = |\boldsymbol{r} - \boldsymbol{r}'|$ is the distance between two electrons at $\boldsymbol{r}$ and $\boldsymbol{r}'$. $k_0$ is the Thomas-Fermi

wavenumber given by $k_0 \propto \sqrt{\rho(E_F)}$ with $E_F$ being the Fermi energy. Note that when $E_F$ is located just at the Dirac node (Dirac point), i.e., when $E_F = 0$, the Coulomb interactions are not screened. This indicates that long-range interactions can be important in Dirac fermion systems.

Henceforth we consider the unscreened Coulomb interaction, namely we set $k_0 = 0$. In momentum space, Eq. (2.2) is written as

$$H_{\text{Coulomb}} = \frac{1}{2L^3} \sum_{q} \frac{4\pi e^2}{q^2} n_q n_{-q}, \tag{2.3}$$

where $L^3$ is the volume of the system and $n_q = \sum_k c_k^\dagger c_{k+q}$. Taking into account this Hamiltonian is equivalent to employing the (Euclidean) action of the form

$$\begin{aligned}
S_{\text{Coulomb}} &= \int d\tau d^3 x \, i e A_0(r) n(r) + \frac{1}{2} \int d\tau d^3 x \sum_j [\partial_j A_0(r)]^2 \\
&= \frac{T}{L^3} \sum_{q,\omega_n} i e A_{0,q} n_{-q} + \frac{1}{2} \frac{T}{L^3} \sum_{q,\omega_n} A_{0,q} q^2 A_{0,-q}
\end{aligned} \tag{2.4}$$

with $q = (\omega_n, q)$, $T$ being the temperature of the system, and $A_0$ being a scalar potential, since it follows from the Hubbard-Stratonovich transformation that

$$\exp\left[-\frac{1}{2}\frac{e^2}{q^2} n_q n_{-q}\right] = \int \mathcal{D}A_0 \exp\left[-\frac{1}{2} A_{0,q} q^2 A_{0,-q} - i e A_{0,q} n_{-q}\right]. \tag{2.5}$$

Combining Eq. (2.1) in real space and Eq. (2.4), we obtain the low-energy effective (Euclidean) action of graphene with $1/r$ Coulomb interactions given by [101, 113]

$$S_{\text{eff}} = \sum_{\sigma=\uparrow,\downarrow} \int d\tau d^2 x \, \bar{\psi}_\sigma(x) [\gamma_0(\partial_\tau + i e A_0) + v_F \gamma_j \partial_j] \psi_\sigma(x) + \frac{1}{2} \int d\tau d^3 x (\partial_j A_0)^2, \tag{2.6}$$

where we have used the fact that $\bar{\psi} = \psi^\dagger \gamma_0$ and $\alpha_j = \gamma_0 \gamma_j$ with $\{\gamma_\mu, \gamma_\nu\} = 2\delta_{\mu\nu}$. Repeated subscript represents the summation over the subscript. Note that the above action consists of (2+1)D Dirac fermions and the (3+1)D Coulomb potential. The kinetic term of the Coulomb potential can be rewritten as $(\partial_j A_0)^2 = \frac{1}{2} F_{\mu\nu} F_{\mu\nu}$, where $F_{\mu\nu} = \partial_\mu A_\nu - \partial_\nu A_\mu$ ($A_j = 0$). Namely, Eq. (2.6) can be regarded as a kind of (2+1)D QED where the electromagnetic four-potential $A_\mu$ is equivalent to the U(1) gauge field.

## 2.3 Lattice Gauge Theory

In this section, we show the formulation of gauge theories on a lattice. First we consider the naive discretization of Dirac fermions. However, this naive discretization suffers from the so-called fermion doubling problem. To solve this problem, we introduce two formulations, the Wilson fermions and the staggered fermions. Finally we consider the discretization of gauge fields.

### 2.3.1 Naive Discretization of Fermionic Action

In the following, we derive the action of noninteracting Dirac fermions regularized on a four-dimensional (4D) hypercubic lattice. To this end, let us start from continuum Dirac fermions,

whose Minkowski action is given by

$$S_F^{\text{M}} = \int d^4x \bar{\psi}(x)[i\gamma^\mu \partial_\mu - m]\psi(x), \tag{2.7}$$

where $\psi(x) = \psi^\dagger \gamma_0$ is a four-component spinor and $\gamma^\mu$ ($\mu = 0, 1, 2, 3$) are $4 \times 4$ matrices which satisfy $\{\gamma^\mu, \gamma^\nu\} = 2g^{\mu\nu}$. The metric is given by $g^{\mu\nu} = \text{diag}(1, -1, -1, -1)$. Let us move on to the Euclidean action, i.e., the imaginary time notation. We rewrite $t$ and $\gamma^\mu$ as $t \to -i\tau$, $\gamma^0 \to \gamma_0$, and $\gamma^j \to i\gamma_j$. The Euclidean action of the system is written as

$$S_F = -iS_F^{\text{M}} = \int d\tau d^3x \bar{\psi}(x)[\gamma_\mu \partial_\mu + m]\psi(x), \tag{2.8}$$

where $\gamma_\mu$ are Hermitian matrices with $\{\gamma_\mu, \gamma_\nu\} = 2\delta_{\mu\nu}$. Note that in the Euclidean spacetime, we do not distinguish between superscripts and subscripts. For example, the matrices $\gamma_\mu$ are given by the Dirac representation as

$$\gamma_0 = \begin{bmatrix} 1 & 0 \\ 0 & -1 \end{bmatrix}, \quad \gamma_j = \begin{bmatrix} 0 & -i\sigma_j \\ i\sigma_j & 0 \end{bmatrix}, \quad \gamma_5 = \begin{bmatrix} 0 & 1 \\ 1 & 0 \end{bmatrix}, \tag{2.9}$$

where $j = 1, 2, 3$ and $\sigma_j$ are the Pauli matrices.

Next let us consider to discretize the action (2.8) on a 4D hypercubic lattice with lattice constant $a$. Up to linear order in $a$, we can readily show that

$$\frac{\psi_{n+\hat{\mu}} - \psi_{n-\hat{\mu}}}{2a} \approx \frac{(\psi_n + a\partial_\mu \psi_n) - (\psi_n - a\partial_\mu \psi_n)}{2a} = \partial_\mu \psi_n, \tag{2.10}$$

where $n = (n_0, n_1, n_2, n_3)$ is a site on the hypercubic lattice, and $\hat{\mu}$ denotes the unit vector along the $\mu$ direction. Then redefining variables to make them dimensionless as $a^{3/2}\psi \to \psi$ and $ma \to m$, we obtain the fermionic action on a lattice:

$$S_F = \frac{1}{2} \sum_{n,\mu} \left[ \bar{\psi}_n \gamma_\mu \psi_{n+\hat{\mu}} - \bar{\psi}_{n+\hat{\mu}} \gamma_\mu \psi_n \right] + m \sum_n \bar{\psi}_n \psi_n. \tag{2.11}$$

At first sight, it seems that we have succeeded in discretizing the action of Dirac fermions. However, it is well known that the action (2.11) suffers from the so-called "fermion doubling problem". To understand this problem, let us consider the Green's function of the system. Applying the Fourier transform $\psi_n = \frac{1}{\sqrt{V}} \sum_k e^{ik \cdot r_n} \psi_k$ with $V$ being the 4D volume of the system, we obtain $S_F = \sum_k \bar{\psi}_k \left[ i\gamma_\mu \sin k_\mu + m \right] \psi_k$. The Green's function is readily obtained as

$$G_F(k) = \frac{1}{i\gamma_\mu \sin k_\mu + m}. \tag{2.12}$$

In the low-energy limit, i.e., in the continuum limit, $k_\mu$ satisfies the condition $\sin k_\mu \ll 1$. There are 16 solutions such that $k = (q_1, q_2, q_3, q_4)$, $k = (\pi + q_1, q_2, q_3, q_4)$, $k = (q_1, \pi + q_2, q_3, q_4)$, $\cdots$, and $k = (\pi + q_1, \pi + q_2, \pi + q_3, \pi + q_4)$ ($q_\mu \ll 1$). Then, for example, the above Green's functions with $k = q$ and $k = \pi + q$ become

$$G_F(q) = \frac{1}{i\gamma_\mu q_\mu + m}, \qquad G_F(\pi + q) = \frac{1}{-i\gamma_\mu q_\mu + m}. \tag{2.13}$$

These two describe apparently the same physics. This means that equivalent $16(= 2^4)$ Dirac fermions appear due to the discretization of the original action (2.8). This problem is referred to as the fermion doubling problem. The famous Nielsen-Ninomiya theorem has proved that lattice fermions with chiral symmetry can have fermion doublers [114]. Although there exist several ways to remove fermion doublers, we show two basic ways in the following subsections.

## 2.3.2 Wilson Fermions

One of the basic lattice formulations without fermion doublers is called the Wilson fermions. Let us consider to add an $O(a)$ term, the "Wilson term", which vanish in the continuum limit $(a \to 0)$:

$$-\frac{ar}{2} \int d^4 x \bar{\psi}_n \partial_\mu^2 \psi_n \approx -\frac{r}{2} \sum_{n,\mu} \bar{\psi}_n \left[ \psi_{n+\hat{\mu}} + \psi_{n-\hat{\mu}} - 2\psi_n \right], \qquad (2.14)$$

where $r > 0$. Then the total lattice action of the system is given by

$$S_F^{\text{Wilson}} = -\frac{1}{2} \sum_{n,\mu} \left[ \bar{\psi}_n P_\mu^- \psi_{n+\hat{\mu}} + \bar{\psi}_{n+\hat{\mu}} P_\mu^+ \psi_n \right] + (m + 4r) \sum_n \bar{\psi}_n \psi_n$$

$$= \sum_k \bar{\psi}_k \left[ i\gamma_\mu \sin k_\mu + m + r \sum_\mu (1 - \cos k_\mu) \right] \psi_k \qquad (2.15)$$

where $P_\mu^\pm = (r \pm \gamma_\mu)/2$. The momentum-dependent mass $M(k) \equiv m + r \sum_\mu (1 - \cos k_\mu)$ at the momenta around which the doublers appeared in the naively discretized action (2.11) is written as

$$M(k) = \begin{cases} m & \text{at } k = 0, \\ m + 2rN & \text{at } k = (\pi, 0, 0, 0), \cdots, \end{cases} \qquad (2.16)$$

where $N = 1, 2, 3, 4$. Note that $m$ is written as $ma$, when the dimension of mass is recovered. Then the masses of fermion doublers become $M(k) = m + 2rN/a \to \infty$ in the continuum limit $(a \to 0)$. Therefore, the Wilson fermion describes single-flavor Dirac fermion with the mass $m$ in the continuum limit. This is because the Wilson fermions break chiral symmetry, i.e., the action (2.15) are not invariant under the chiral transformation $\psi_n \to e^{i\alpha\gamma_5}\psi_n$, $\bar{\psi}_n \to \bar{\psi}_n e^{i\alpha\gamma_5}$ in the limit $m = 0$ (chiral limit).

It must be noted that the Wilson fermion with negative mass ($m < 0$) is equivalent to the effective lattice model for 3D topological insulators such as $Bi_2Se_3$ [see Eq.(1.19)]. The Wilson term (the term proportional to $r$) arises as a result of strong spin-orbit coupling. We adopt the Wilson fermions with scalar potential as the model for a 3D topological insulator with $1/r$ Coulomb interactions.

## 2.3.3 Staggered Fermions

Another formulation without fermion doublers is called the staggered fermions [115, 116]. As mentioned above, in four-dimension, $2^4 = 16$ doublers appear due to discretization. The staggered fermion (Kogut-Susskind fermion) formalism takes advantage of the fermion doubling problem. Namely, the staggered fermion formalism interprets this doubling problem such that there exist four-component Dirac fermions of four flavors. First let us consider the following transformation called the spin diagonalization (or the Kawamoto-Smit transformation) [121]:

$$\psi_n = (\gamma_0)^{n_0} (\gamma_1)^{n_1} (\gamma_2)^{n_2} (\gamma_3)^{n_3} \xi_n, \qquad (2.17)$$

where $n = (n_0, n_1, n_2, n_3)$ and $\xi_n$ is a four-component spinor given by $\xi_n \equiv [\chi_n^1, \chi_n^2, \chi_n^3, \chi_n^4]^T$. For example, the term $\bar{\psi}_n \gamma_2 \psi_{n+\hat{2}}$ becomes

$$\bar{\psi}_n \gamma_2 \psi_{n+\hat{2}} = \left[ \bar{\xi}_n (\gamma_3)^{n_3} (\gamma_2)^{n_2} (\gamma_1)^{n_1} (\gamma_0)^{n_0} \right] \gamma_2 \left[ (\gamma_0)^{n_0} (\gamma_1)^{n_1} (\gamma_2)^{n_2+1} (\gamma_3)^{n_3} \xi_{n+\hat{2}} \right]$$

$$= (-1)^{n_0+n_1} \bar{\xi}_n \xi_{n+\hat{2}}. \qquad (2.18)$$

Then we can rewrite the naively discretized action (2.11) as

$$S_F = \frac{1}{2} \sum_{\alpha=1}^{4} \sum_{n,\mu} \eta_{n,\mu} \left[ \bar{\chi}_n^{\alpha} \chi_{n+\hat{\mu}}^{\alpha} - \bar{\chi}_{n+\hat{\mu}}^{\alpha} \chi_n^{\alpha} \right] + m \sum_{\alpha=1}^{4} \sum_n \bar{\chi}_n^{\alpha} \chi_n^{\alpha}, \tag{2.19}$$

where $\eta_{n,\mu} = (-1)^{n_0 + \cdots + n_{\mu-1}}$. The staggered fermion is obtained by retaining one of the four components in $\chi_\alpha$:

$$S_F^{\text{staggered}} = \frac{1}{2} \sum_{n,\mu} \eta_{n,\mu} \left[ \bar{\chi}_n \chi_{n+\hat{\mu}} - \bar{\chi}_{n+\hat{\mu}} \chi_n \right] + m \sum_n \bar{\chi}_n \chi_n, \tag{2.20}$$

Note that 16 four-component fermion doublers appear in the continuum limit of the action (2.19). Then, 4 four-component fermion doublers appear in the continuum limit of the staggered fermion formalism. Since $\chi_n$ is a single-component operator, there is no spinor structure in the staggered fermions. The absence of spinor structures makes practical calculations much easier. The existence of fermion doublers results in the possession of chiral symmetry in the chiral limit ($m \to 0$). Namely, the action of staggered fermions is invariant under the chiral transformation defined by $\chi_n \to e^{i\alpha\epsilon(n)}\chi_n$, $\bar{\chi}_n \to e^{i\alpha\epsilon(n)}\bar{\chi}_n$ with $\epsilon(n) = (-1)^{n_0+n_1+n_2+n_3}$, when $m = 0$.

### 2.3.4 Discretization of Gauge Action

Let us consider the discretization of the action of gauge fields. Here we follow the discussions in Ref. 118. First let us derive the Euclidean gauge action. In the Minkowski spacetime, the continuum SU($N_G$) gauge action is given by

$$S_G^{\text{M}} = -\frac{1}{2}\text{tr} \int d^4x (F_{\mu\nu})^2 = -\frac{1}{4} \int d^4x (F_{\mu\nu}^i)^2, \tag{2.21}$$

where $F_{\mu\nu} = \frac{1}{ig}[D_\mu, D_\nu] = \partial_\mu A_\nu - \partial_\nu A_\mu + ig[A_\mu, A_\nu]$ with the covariant detivative $D_\mu = \partial_\mu + igA_\mu$. Here $A_\mu = A_\mu^a T^a$ is an SU($N_G$) gauge field with $N_G \times N_G$ matrices $T^a$ satisfying $(T^a)^\dagger = T^a$, $\text{tr}T^a = 0$, $\text{tr}(T^a T^b) = \delta_{ab}/2$, and $[T^a, T^b] = if^{abc}T^c$. The Euclidean spacetime (i.e., imaginary time) is obtained by rewriting $t$ and $A_0$ as $t \to -i\tau$ and $A_0 \to iA_0$. Then the Euclidean action is given by

$$S_G = -iS_G^{\text{M}} = \frac{1}{2}\text{tr} \int d\tau d^3x (F_{\mu\nu})^2 = \frac{1}{4} \int d\tau d^3x (F_{\mu\nu}^i)^2. \tag{2.22}$$

Next we consider the fermionic action with an SU($N_G$) gauge field $A_\mu$:

$$S_F = \int d^4x \bar{\psi}(x)(\gamma_\mu D_\mu + m)\psi(x). \tag{2.23}$$

As in the noninteracting case, up to linear order in $a$ (the lattice constant), we can readily show that

$$\frac{U_{n,\mu}\psi_{n+\hat{\mu}} - U_{n,\mu}^\dagger \psi_{n-\hat{\mu}}}{2a} = \frac{[1 + iagA_\mu(n)][\psi_n + a\partial_\mu\psi_n] - [1 - iagA_\mu(n)][\psi_n - a\partial_\mu\psi_n]}{2a}$$
$$= \partial_\mu\psi_n + igA_\mu(n)\psi_n = D_\mu\psi_n, \tag{2.24}$$

where $U_{n,\mu} = e^{iagA_\mu(n+\hat{\mu}/2)} \in$ SU($N_G$) is the "link variable". More precisely, $U_{n,\mu}$ is given by

$$U_{n,\mu} \equiv P \exp\left[ig \int_n^{n+\hat{\mu}} A_\mu(X)dX^\mu\right] = \lim_{N\to\infty} \prod_{m=0}^{N-1} \left[1 + igA_\mu(n + m\Delta)\Delta^\mu\right] \tag{2.25}$$
$$\simeq e^{iagA_\mu(n+\hat{\mu}/2)},$$

where $\Delta = |n + \hat{\mu} - n|/N = a/N$. We obtain the naively discretized fermionic action with an SU($N_G$) gauge field on a 4D hypercubic lattice given by

$$S_F = \frac{1}{2} \sum_{n,\mu} \left[\bar{\psi}_n U_{n,\mu} \gamma_\mu \psi_{n+\hat{\mu}} - \bar{\psi}_{n+\hat{\mu}} U_{n,\mu}^\dagger \gamma_\mu \psi_n\right] + m \sum_n \bar{\psi}_n \psi_n. \tag{2.26}$$

Finally we consider the discretization of pure SU($N_G$) gauge action. The actions (2.22) and (2.23) are invariant under the gauge transformation such that

$$\psi'(x) = \Omega(x)\psi(x), \quad \bar{\psi}'(x) = \bar{\psi}(x)\Omega^\dagger(x), \quad A'_\mu(x) = \Omega(x)A_\mu(x)\Omega^\dagger(x) + \frac{1}{ig}\Omega(x)\partial_\mu\Omega^\dagger(x), \tag{2.27}$$

where $\Omega(x)$ with $\Omega^\dagger(x)\Omega(x) = 1$ is a local gauge transformation matrix. Then the lattice gauge action must also be invariant under the above transformation. We can show that $U'_{n,\mu} = \Omega_n U_{n,\mu} \Omega^\dagger_{n+\hat{\mu}} + O(a^2)$. This indicates that on a closed path $C_n$, the trace of the product of link variables is gauge-invariant:

$$\text{tr} \prod_{C_n} U_{n,\mu_1} U_{n+\hat{\mu}_1,\mu_2} \cdots U_{n+\hat{\mu}_k,\mu_k} \to \text{tr} \prod_{C_n} \Omega_n U_{n,\mu_1} U_{n+\hat{\mu}_1,\mu_2} \cdots U_{n+\hat{\mu}_k,\mu_k} \Omega^\dagger_n \tag{2.28}$$
$$= \text{tr} \prod_{C_n} U_{n,\mu_1} U_{n+\hat{\mu}_1,\mu_2} \cdots U_{n+\hat{\mu}_k,\mu_k}.$$

Therefore, we need to find a closed path which reproduce the continuum action (2.22) in the limit $a \to 0$. The simplest path is a square lattice of of size $a^2$, which results in the product of four link variables. Such an action is called the plaquette action (see Fig. 2.1), and can be written as $\sum_{n,\mu\neq\nu} \text{tr} \, U_{\mu\nu,n}$ with

$$U_{\mu\nu,n} = U_{n,\mu} U_{n+\hat{\mu},\nu} U^\dagger_{n+\hat{\nu},\mu} U^\dagger_{n,\nu}. \tag{2.29}$$

Then it can be shown that

$$\begin{aligned}
\text{tr} \, U_{\mu\nu,n} &= \text{tr} \left(\exp\left\{iag\left[A_\mu(n + \hat{\mu}/2) + A_\nu(n + \hat{\mu} + \hat{\nu}/2) + \frac{iag}{2}[A_\mu, A_\nu] + \cdots\right]\right\}\right. \\
&\quad \left. \times \exp\left\{-iag\left[A_\mu(n + \hat{\nu} + \hat{\mu}/2) + A_\nu(n + \hat{\nu}/2) - \frac{iag}{2}[A_\mu, A_\nu] + \cdots\right]\right\}\right) \\
&= \text{tr} \left(\exp\left\{iag[A_\nu(n + \hat{\mu}/2) - A_\nu(n - \hat{\mu}/2)] - iag[A_\mu(n + \hat{\nu}/2) - A_\mu(n - \hat{\nu}/2)]\right.\right. \\
&\quad \left.\left. + (iag)^2[A_\mu, A_\nu] + \cdots\right\}\right) \\
&= \text{tr} \left\{\exp\left[ia^2gF_{\mu\nu}(n_c) + a^3X_3 + a^4X_4 + O(a^5)\right]\right\} \\
&= \text{tr} \left[1 + ia^2gF_{\mu\nu}(n_c) + a^3X_3 + a^4X_4 - \frac{a^4g^2}{2}F^2_{\mu\nu}(n_c) + O(a^6)\right],
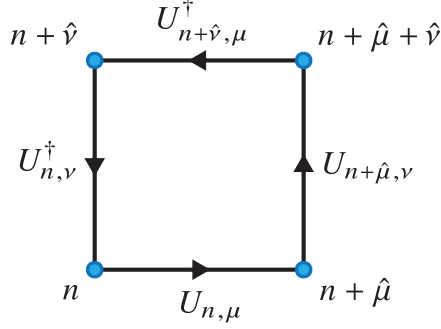\end{aligned} \tag{2.30}$$

Figure 2.1: The plaquette action for a gauge filed. Blue circles represent lattice sites on a 4D hypercubic lattice. It can be seen that the link variable is regarded as a quantity which have a "direction". $\hat{\mu}$ denotes the unit vector along the $\mu$ direction.

where we have used the formula $e^A e^B = e^{A+B+\frac{1}{2}[A,B]+\cdots}$, and $n_c$ is the center of the plaquette given by $n_c = n + \hat{\mu}/2 + \hat{v}/2$. From the identity $\text{tr} T^a = 0$, we see that $\text{tr} F_{\mu v} = \text{tr} X_3 = \text{tr} X_4 = 0$. Finally in the limit $a \to 0$, we obtain

$$\sum_{n,\mu\neq v} \text{tr}\, U_{\mu v,n} \to \sum_{n,\mu\neq v} \text{tr}\left[1 - \frac{a^4 g^2}{2} F_{\mu v}^2(n_c) + O(a^6)\right]. \tag{2.31}$$

This indicates that the gauge action on a lattice can be written as

$$S_G = \frac{2N_G}{g^2} \sum_n \sum_{\mu<v} \left[1 - \frac{1}{2N_G}(\text{tr}\, U_{\mu v,n} + \text{tr}\, U_{\mu v,n}^\dagger)\right], \tag{2.32}$$

where we have used the fact that $\text{tr} 1 = N_G$ ($N_G \geq 2$). In the case of $N_G = 1$, we have

$$S_G = \frac{1}{g^2} \sum_n \sum_{\mu<v} \left[1 - \frac{1}{2}(U_{\mu v,n} + U_{\mu v,n}^\dagger)\right]. \tag{2.33}$$

## 2.4 Lattice-Gauge-Theoretical Analysis of Graphene

We have seen that the low-energy effective model for graphene is described by (2+1)D four-component Dirac fermions of two flavors (i.e., spin degree of freedom). Such a system on a lattice can be described by the (2+1)D staggered fermions, since they reproduce four-component Dirac fermions of two flavors in the continuum limit [119]. Then the lattice version of the action (2.6) with a scalar potential resulting in the $1/r$ Coulomb interactions reads [101–107]

$$\begin{aligned}
S = &\frac{1}{2} \sum_n \left[\bar{\chi}_n U_{n,0} \chi_{n+\hat{0}} - \bar{\chi}_{n+\hat{0}} U_{n,0}^\dagger \chi_n\right] + \frac{1}{2} \sum_n \sum_{j=1,2} \eta_{n,j} \left[\bar{\chi}_n \chi_{n+\hat{j}} - \bar{\chi}_{n+\hat{j}} \chi_n\right] \\
&+ m_0 \sum_n \bar{\chi}_n \chi_n + \beta \sum_n \sum_{j=1,2,3} \left[1 - \text{Re}\left(U_{n,0} U_{n+j,0}^\dagger\right)\right],
\end{aligned} \tag{2.34}$$

where $\eta_{n,1} = (-1)^{n_0}$, $\eta_{n,2} = (-1)^{n_0+n_1}$, and $U_{n,0} = e^{i\theta_n}$ ($-\pi \leq \theta_n \leq \pi$). The parameter $\beta$, which represents the strength of $1/r$ Coulomb interactions, is given by $\beta = v_F \epsilon / e^2$ with $\epsilon$ and $e$ being
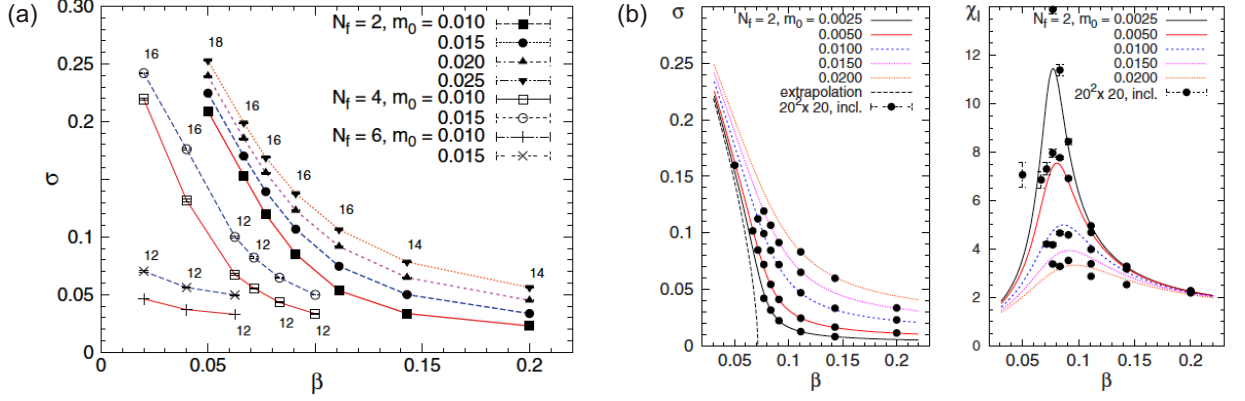
Figure 2.2: (a) $\beta$ dependence of the chiral condensate $\sigma$ in the model (2.34) obtained by a Monte Carlo simulation [101]. (b) $\beta$ dependences of the chiral condensate $\sigma$ (left panel) and the chiral susceptibility $\chi_{\text{chiral}} = \partial\sigma/\partial m_0$ (right panel) in the model (2.34) obtained by a Monte Carlo simulation [102].

the dielectric constant of substrate and the electric charge, respectively. This expression of $\beta$ means that small Fermi velocity and small dielectric constant makes the Coulomb interactions effectively stronger. In graphene suspended in vacuum with $v_F/c \simeq 1/300$ ($c$ is the speed of light in vacuum), the value of $\beta$ is approximated to be 0.036. Namely, we can perform perturbative calculations from the strong coupling limit $\beta = 0$.

The physical quantity which should be calculated in the model (2.34) is the chiral condensate $\sigma$ defined by

$$\sigma = |\langle \bar{\chi}_n \chi_n \rangle| = \frac{1}{V} \int \mathcal{D}[\chi, \bar{\chi}, U_0] \sum_n \bar{\chi}_n \chi_n \frac{e^{-S}}{Z} = \frac{1}{V} \frac{\partial \ln Z}{\partial m_0} \bigg|_{m_0 \to 0}. \tag{2.35}$$

The value of $\sigma$ in the limit $m_0 \to 0$ is regarded as the order parameter for the semimetal-insulator transition in graphene, since $\sigma$ is the dynamically generated mass (gap). The value of $\sigma$ as a function of $\beta$ obtained by a Monte Carlo simulation is shown in Fig. 2.2(a). "$N_f$" in the figure represents the number of flavors of four-component Dirac fermions, where $N_f = 2N_{\text{staggered}}$ with $N_{\text{staggered}}$ being the number of flavors of staggered fermions. In monolayer graphene ($N_f = 2$), the system becomes insulating (i.e., becomes gapped) as the $1/r$ Coulomb interactions becomes stronger. However, it should be mentioned that there exists the critical number $N_f^c$ ($4 < N_f^c < 6$) above which the semimetal phase survives in the strong coupling limit. The critical strength of the Coulomb interactions $\beta_c$, below which the system becomes insulating, can be obtained by examining the chiral susceptibility defined by $\chi_{\text{chiral}} = \partial\sigma/\partial m_0$ [see the right panel of Fig. 2.2(b)]. $\beta_c$ in monolayer graphene is estimated as $\beta_c \approx 0.072$. Finally we note that the value of $\sigma$ obtained in an analytical calculation, the strong coupling expansion of the lattice gauge theory [103], and the value obtained in a numerical calculation [101, 102] are in good agreement in the strong coupling region.

# Chapter 3

# 3D Topological Insulator with Strong Long-Range Correlations

In this chapter, we study the effects of strong $1/r$ long-range Coulomb interactions in a three-dimensional (3D) topological insulator, where the effective Hamiltonian is described by the Wilson fermions. We take into account $1/r$ Coulomb interactions between the bulk electrons. Based on the U(1) lattice gauge theory, we analyze the system from the strong coupling limit. It is shown that the effect of Coulomb interactions is equivalent to the renormalization of the bare mass of the Wilson fermions, and that as a result, the topological insulator phase survives in the strong coupling limit. A possible global phase diagram of a correlated 3D topological insulator is presented. The contents in this chapter have been published in:
A. Sekine, T. Z. Nakano, Y. Araki, and K. Nomura, Phys. Rev. B **87**, 165142-1-9 (2013),
A. Sekine, T. Z. Nakano, Y. Araki, and K. Nomura, JPS Conf. Proc. **3**, 016008-1-5 (2014).

## 3.1 Theoretical Model

In this section, we introduce a lattice model for a 3D topological insulator with $1/r$ Coulomb interactions. The noninteracting model we adopt is the Wilson fermions, the effective lattice model for 3D topological insulators such as $Bi_2Se_3$. The motivations for considering the effects of $1/r$ Coulomb interactions are as follows. The first is that the effects of long-range interactions have not yet been revealed. We have studied the effects of short-range interactions in the Wilson fermions [89], and found that the topological insulator phase is broken in the region where the interactions are strong. The second is that $Bi_2Se_3$ is a $p$-electron system. This suggests that the on-site interactions are not strong. On the other hand, in Dirac fermion systems, the effects of long-range interactions are expected to be important, since the screening effect is considered to be weak due to the vanishing density of states near the Fermi level.

### 3.1.1 Isotropic Case

As we saw in Subsect. 1.2.2, the low-energy effective model of three-dimensional (3D) topological insulators such as $Bi_2Se_3$ is described by the Wilson fermions [16, 17], whose Hamiltonian
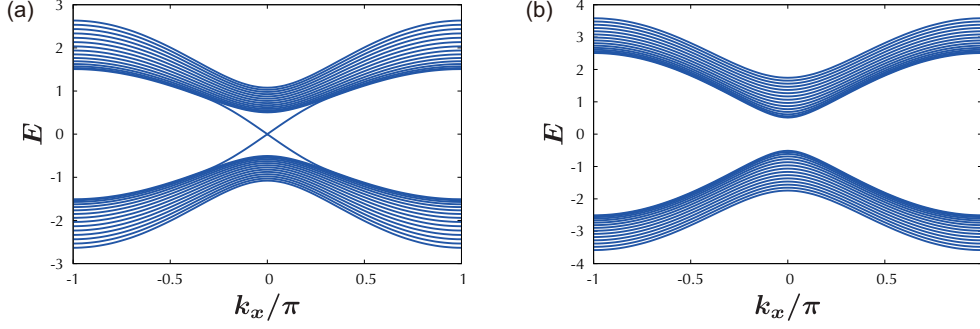
Figure 3.1: Energy spectrum of the effective model (3.1) in a slab geometry (i.e., finite layers in the $z$ direction) with (a) $m_0/r = -0.5$ and (b) $m_0/r = 0.5$. The surface state exists in the topologically nontrivial case ($0 > m_0/r > -2$). However, note that in this chapter we do *not* study the model in a slab geometry. We study the model in a periodic boundary condition for all the four (spatial and timelike) directions.

is given by

$$\mathcal{H}_0(\boldsymbol{k}) = v_{\mathrm{F}} \sum_{j=1}^{3} \alpha_j \sin k_j + m(\boldsymbol{k}) \alpha_4, \tag{3.1}$$

where $\boldsymbol{k}$ is the momentum, $v_{\mathrm{F}}$ is the Fermi velocity, $m(\boldsymbol{k}) = m_0 + r \sum_j (1 - \cos k_j)$, $r > 0$, $j(= 1, 2, 3)$ denotes spacial axis. When $r = 0$, the Hamiltonian is a naively discretized Dirac Hamiltonian. The Wilson term (the term proportional to $r$) arises as a result of strong spin-orbit coupling. The above Hamiltonian is described on a cubic lattice with the lattice constant $a$. In the following, we set $a = 1$. $\alpha_\mu$ are $4 \times 4$ matrices which satisfy the Clifford algebra $\{\alpha_\mu, \alpha_\nu\} = 2\delta_{\mu\nu}$ given by the Dirac representation:

$$\alpha_j = \begin{bmatrix} 0 & \sigma_j \\ \sigma_j & 0 \end{bmatrix}, \qquad \alpha_4 = \begin{bmatrix} 1 & 0 \\ 0 & -1 \end{bmatrix} \tag{3.2}$$

with $\sigma_j$ being the Pauli matrices. The energy of this system is measured in units of $v_{\mathrm{F}}/a$. The Hamiltonian (3.1) has time-reversal ($\mathcal{T}$) symmetry and spatial inversion ($\mathcal{P}$) symmetry, i.e., $\mathcal{T}\mathcal{H}_0(\boldsymbol{k})\mathcal{T}^{-1} = \mathcal{H}_0(-\boldsymbol{k})$ and $\mathcal{P}\mathcal{H}_0(\boldsymbol{k})\mathcal{P}^{-1} = \mathcal{H}_0(-\boldsymbol{k})$ are satisfied, where $\mathcal{T} = 1 \otimes (-i\sigma_2)\mathcal{K}$ ($\mathcal{K}$ is the complex conjugation operator) and $\mathcal{P} = \sigma_3 \otimes 1$. In the Hamiltonian (3.1), the spinor is written in the basis of $\psi_{\boldsymbol{k}} = [c_{\boldsymbol{k}+\uparrow}, c_{\boldsymbol{k}+\downarrow}, c_{\boldsymbol{k}-\uparrow}, c_{\boldsymbol{k}-\downarrow}]^T$, where $c$ is the annihilation operator of an electron, $+, -$ denote two orbitals, and $\uparrow (\downarrow)$ denotes up-(down-)spin [16, 17].

In the presence of time-reversal symmetry and inversion symmetry, the $Z_2$ invariant of the system is given by [11, 12]

$$(-1)^\nu = \prod_{i=1}^{8} \left\{ -\mathrm{sgn}\left[ m(\boldsymbol{\Lambda}_i) \right] \right\}, \tag{3.3}$$

where $\boldsymbol{\Lambda}_i$ are the eight time-reversal invariant momenta; $(0, 0, 0)$, $(\pi, 0, 0)$, $(0, \pi, 0)$, $(0, 0, \pi)$, $(\pi, \pi, 0)$, $(\pi, 0, \pi)$, $(0, \pi, \pi)$, and $(\pi, \pi, \pi)$. It is easily shown that if $0 > m_0 > -2r$ or $-4r > m_0 > -6r$ ($m_0 > 0$, $-2r > m_0 > -4r$, or $-6r > m_0$), then the system is topologically nontrivial (trivial).

40

Next let us consider a strongly correlated topological insulator in the Euclidean spacetime, which is described by the Wilson fermions with $1/r$ Coulomb interactions between the bulk electrons. We start from the Euclidean action of (3+1)D Wilson fermions interacting with an electromagnetic field on a 4D hypercubic lattice, which is given by

$$S_F = - \sum_{n,\mu} \left[ \bar{\psi}_n P_\mu^- U_{n,\mu} \psi_{n+\hat{\mu}} + \bar{\psi}_{n+\hat{\mu}} P_\mu^+ U_{n,\mu}^\dagger \psi_n \right] + (m_0 + 4r) \sum_n \bar{\psi}_n \psi_n, \tag{3.4}$$

where $\bar{\psi} = \psi^\dagger \gamma_0$, $P_\mu^\pm = (r_\mu \pm \gamma_\mu)/2$. Here $n = (n_0, n_1, n_2, n_3)$ denotes a site on the 4D lattice and $\hat{\mu}$ ($\mu = 0, 1, 2, 3$) denotes the unit vector along the $\mu$ direction. In this isotropic model, we set $r_0 = r_1 = r_2 = r_3 \equiv r$. $U_{n,\mu}$ is the link variable defined by $U_{n,\mu} = e^{igA_\mu(n+\hat{\mu}/2)}$, where $A_\mu = (A_0, \boldsymbol{A})$ is the electromagnetic four-potential, and $g^2 = e^2/\epsilon$ with $e$ and $\epsilon$ being electric charge and the dielectric constant of the system, respectively. Although the timelike Wilson term (the term proportional to $r_0$) is introduced artificially to eliminate fermion doublers, the spatial Wilson terms have a physical meaning (they arise due to strong spin-orbit coupling). In this paper, according to the noninteracting Hamiltonian (3.1), we adopt the Dirac representation in the Euclidean spacetime ($\{\gamma_\mu, \gamma_\nu\} = 2\delta_{\mu\nu}$):

$$\gamma_0 = \begin{bmatrix} 1 & 0 \\ 0 & -1 \end{bmatrix}, \quad \gamma_j = \begin{bmatrix} 0 & -i\sigma_j \\ i\sigma_j & 0 \end{bmatrix}, \quad \gamma_5 = \begin{bmatrix} 0 & 1 \\ 1 & 0 \end{bmatrix}, \tag{3.5}$$

where $j = 1, 2, 3$ and $\sigma_j$ are the Pauli matrices.

In the case of 3D topological insulators, the Fermi velocity $v_F$ is about $3 \times 10^{-3} c$ where $c$ is the speed of light in vacuum. Here recall that the interactions with spatial components of electromagnetic fields have the coefficient $v_F/c$. Then the interactions between the bulk electrons can be regarded as only the instantaneous Coulomb interaction ($A_j = 0$) like in the case of graphene [101–107], so the action (3.4) is rewritten as

$$S_F = S_F^{(\tau)} + S_F^{(s)} + (m_0 + 4r) \sum_n \bar{\psi}_n \psi_n, \tag{3.6}$$

where

$$S_F^{(\tau)} = - \sum_n \left[ \bar{\psi}_n P_0^- U_{n,0} \psi_{n+\hat{0}} + \bar{\psi}_{n+\hat{0}} P_0^+ U_{n,0}^\dagger \psi_n \right], \tag{3.7}$$

$$S_F^{(s)} = - \sum_{n,j} \left[ \bar{\psi}_n P_j^- \psi_{n+\hat{j}} + \bar{\psi}_{n+\hat{j}} P_j^+ \psi_n \right], \tag{3.8}$$

and $U_{n,0} = e^{i\theta_n}$ ($-\pi \leq \theta_n \leq \pi$). The Wilson fermions breaks chiral symmetry by itself (the terms proportional to $r$ and $m_0$), i.e., the action (3.6) is not invariant under the chiral transformation $\psi_n \to e^{i\theta\gamma_5} \psi_n$, $\bar{\psi}_n \to \bar{\psi}_n e^{i\theta\gamma_5}$. In our model, chiral symmetry is equivalent to the symmetry of the pseudospin for two $p$-orbitals $+$ and $-$. The pure U(1) gauge action on a lattice is given by

$$S_G = \beta \sum_n \sum_{\mu > \nu} \left[ 1 - \frac{1}{2} \left( U_{n,\mu\nu} + U_{n,\mu\nu}^\dagger \right) \right], \tag{3.9}$$

where $\beta = v_F/g^2$. The plaquette contribution $U_{n,\mu\nu}$ is defined by

$$U_{n,\mu\nu} = U_{n,\mu} U_{n+\hat{\mu},\nu} U_{n+\hat{\nu},\mu}^\dagger U_{n,\nu}^\dagger, \tag{3.10}$$

where $U_{n,j} = 1$ ($j = 1, 2, 3$) in our case. The total action of the system on a lattice is written as

$$S = S_F + S_G. \tag{3.11}$$

The dielectric constant $\epsilon_r$ of $Bi_2Se_3$ is rather large [120] ($\epsilon_r = \epsilon/\epsilon_0 \approx 100$). This means that the Coulomb interaction between the bulk electrons in $Bi_2Se_3$ is considered to be weak. In fact, the value of $\beta$ is approximated as

$$\beta = \frac{v_F \epsilon_r}{4\pi c} \times \frac{4\pi \epsilon_0 \hbar c}{e^2} \approx 3, \tag{3.12}$$

and we cannot perform the strong coupling expansion in $Bi_2Se_3$. Note that $\frac{e^2}{4\pi\epsilon_0\hbar} \simeq 1/137$ is the fine-structure constant. However, we think it would be important from a theorerical viewpoint to examine the strong electron correlation effect in Dirac fermion systems which describe topologically nontrivial states.

### 3.1.2 Anisotropic Case

So far we have introduced the isotropic Wilson fermions as a lattice model for 3D topological insulators such as $Bi_2Se_3$. However, in real materials, there exist anisotropies in the momentum-dependent mass (the Wilson term) and in the Fermi velocity [16, 17]. We take into account the former anisotropy but neglect the latter, since the former is much larger than the latter. Then the Hamiltonian of the anisotropic Wilson fermions as a model for 3D topological insulators is written as

$$\mathcal{H}_0(\boldsymbol{k}) = v_F \sum_{j=1}^{3} \alpha_j \sin k_j + \left[ m_0 + r_\perp \sum_{j=1}^{2} (1 - \cos k_j) + r_3 (1 - \cos k_3) \right] \alpha_4, \tag{3.13}$$

where the $4 \times 4$ matrices $\alpha_\mu$ are the same as Eq. (3.2). The topological insulator phase and the normal insulator phase are distinguished by the $Z_2$ invariant. It is found that when $-2r_3 < m_0 < 0$ or $-4r_\perp - 2r_3 < m_0 < -4r_\perp$ ($0 < m_0$, $-4r_\perp < m_0 < -2r_3$ or $m_0 < -4r_\perp - 2r_3$) with $r_3 < 2r_\perp$, the system is topologically nontrivial (trivial).

Next we consider the $1/r$ Coulomb interactions between the bulk electrons. This enables us to describe the system by the U(1) lattice gauge theory (lattice quantum electrodynamics). Due to the smallness of the Fermi velocity compared to the speed of light, the interactions between the electrons and the spatial components of the electromagnetic field can be neglected. Then the Euclidean action of the system is given by

$$S = S_F^{(\tau+s)} + (m_0 + r_\tau + 2r_\perp + r_3) \sum_n \bar{\psi}_n \psi_n + S_G, \tag{3.14}$$

where $S_F^{(\tau+s)}$ is the fermionic action without the mass term

$$S_F^{(\tau+s)} = - \sum_n \left[ \bar{\psi}_n P_0^- U_{n,0} \psi_{n+\hat{0}} + \bar{\psi}_{n+\hat{0}} P_0^+ U_{n,0}^\dagger \psi_n \right] - \sum_{n,j} \left[ \bar{\psi}_n P_j^- \psi_{n+\hat{j}} + \bar{\psi}_{n+\hat{j}} P_j^+ \psi_n \right], \tag{3.15}$$

and $S_G$ is the action of the U(1) gauge field

$$S_G = \beta \sum_n \sum_{\mu>\nu} \left[ 1 - \frac{1}{2} \left( U_{n,\mu} U_{n+\hat{\mu},\nu} U_{n+\hat{\nu},\mu}^\dagger U_{n,\nu}^\dagger + \text{H.c.} \right) \right]. \tag{3.16}$$

Here $P_\mu^\pm = (r_\mu \pm \gamma_\mu)/2$ with $r_0 = r_\tau$ and $r_1 = r_2 = r_\perp$, $U_{n,j} = 1$ ($j = 1, 2, 3$), and $U_{n,0} = e^{i\theta_n}$ ($-\pi \le \theta_n \le \pi$). $\beta = v_F \epsilon/e^2$, with $\epsilon$ being the dielectric constant of the system and $e$ being the electric charge, is a parameter which represents the strength of the $1/r$ Coulomb interaction. According to the noninteracting Hamiltonian (3.13), the gamma matrices $\gamma_\mu$ are given by the Dirac representation.

In what follows, we concentrate on the isotropic case. However, the calculation for the anisotropic case is exactly the same as the isotropic case.

## 3.2 Effective Action

Let us perform the strong coupling expansion from the strong coupling limit (SCL) $\beta = 0$. The strong coupling expansion has been often used in lattice quantum chromodynamics (QCD) [121–125] where the coupling between fermions (quarks) and gauge fields (gluons) are strong. We can carry out the $U_0$ integral by using the SU($N_G$) group integral formulas:

$$\int dU 1 = 1, \qquad \int dU U_{ab} = 0, \qquad \int dU U_{ab} U_{cd}^\dagger = \frac{1}{N_G} \delta_{ad} \delta_{bc}. \qquad (3.17)$$

Our case corresponds to the case of $N_G = 1$. We can derive the effective action $S_{\text{eff}}[\psi, \bar\psi]$ by integrating out the U(1) gauge link variable $U_{0,n}$ in the partition function $Z$ up to the arbitrary order in $\beta$ as follows:

$$Z = \int \mathcal{D}[\psi, \bar\psi, U_0] e^{-S_F - S_G} = \int \mathcal{D}[\psi, \bar\psi] e^{-S_{\text{eff}}}. \qquad (3.18)$$

First we consider the strong coupling limit ($\beta = 0$). In this case, the timelike partition function is given by

$$Z_{\text{SCL}}^{(\tau)}[\psi, \bar\psi] = \int \mathcal{D}U_0 e^{-S_F^{(\tau)}}. \qquad (3.19)$$

The integration with respect to $U_0$ is evaluated as

$$\begin{aligned}
\int \mathcal{D}U_0 e^{-S_F^{(\tau)}} &= \prod_n \int_{-\pi}^{\pi} \frac{d\theta_n}{2\pi} \exp\left[ \bar\psi_n P_0^- U_{n,0} \psi_{n+\hat{0}} + \bar\psi_{n+\hat{0}} P_0^+ U_{n,0}^\dagger \psi_n \right] \\
&= \prod_n \left[ 1 + \bar\psi_n P_0^- \psi_{n+\hat{0}} \bar\psi_{n+\hat{0}} P_0^+ \psi_n + \cdots \right] \\
&\approx e^{\sum_n \bar\psi_n P_0^- \psi_{n+\hat{0}} \bar\psi_{n+\hat{0}} P_0^+ \psi_n},
\end{aligned} \qquad (3.20)$$

where we have used the property of the Grassmann variables $\psi_\alpha$ and $\bar\psi_\alpha$, $\psi_\alpha^2 = \bar\psi_\alpha^2 = 0$ with $\alpha$ denoting the component of the spinors. In the second line, we have neglected the terms which consist of 8, 12, and 16 different Grassmann variables. The contributions of those terms appear in higher orders of the order parameters, and thus the results will not be changed qualitatively even if those terms are taken into account. We can rewrite the exponent as

$$\bar\psi_{n,\alpha} (P_0^-)_{\alpha\beta} \psi_{n+\hat{0},\beta} \bar\psi_{n+\hat{0},\gamma} (P_0^+)_{\gamma\delta} \psi_{n,\delta} = -\text{tr}\left[ M_n P_0^+ M_{n+\hat{0}} P_0^- \right], \qquad (3.21)$$

where we have defined $(M_n)_{\alpha\beta} = \bar\psi_{n,\alpha} \psi_{n,\beta}$ and used $(P_0^\pm)_{\alpha\beta} = (P_0^\pm)_{\beta\alpha}$. The subscripts $\alpha$ and $\beta$ denote the component of the spinors.

Next we evaluate the term of the order of $\beta$. In order to evaluate the plaquette contributions from $S_G$, we use the cumulant expansion [125, 126]. Let us define an expectation value

$$\langle A \rangle \equiv \frac{1}{Z_{\text{SCL}}^{(\tau)}} \int \mathcal{D}U_0 A[U_0] e^{-S_F^{(\tau)}}. \tag{3.22}$$

Then using this definition, the full timelike partition function can be expressed as

$$Z^{(\tau)} = \int \mathcal{D}U_0 e^{-S_F^{(\tau)}-S_G} = Z_{\text{SCL}}^{(\tau)} \langle e^{-S_G} \rangle. \tag{3.23}$$

The contribution from $S_G$ is given by

$$\Delta S \equiv -\ln\langle e^{-S_G} \rangle = -\sum_{n=1}^{\infty} \frac{(-1)^n}{n!} \left\langle S_G^n \right\rangle_c, \tag{3.24}$$

where $\langle \cdots \rangle_c$ is a cumulant. The correction to the action up to $O(\beta)$ is given by

$$\Delta S = \langle S_G \rangle_c = \langle S_G \rangle = -\frac{\beta}{2} \sum_n \sum_{\mu>\nu} \langle U_{n,\mu\nu} + U_{n,\mu\nu}^{\dagger} \rangle. \tag{3.25}$$

The expectation value of $U_{n,\mu\nu}$ is evaluated as follows [125]:

$$\langle U_{n,\mu\nu} \rangle \simeq \int dU_{n,0} U_{n,\mu\nu} e^{-s_P^{(\tau)}}, \tag{3.26}$$

where $s_P^{(\tau)}$ is the plaquette-related part of $S_F^{(\tau)}$. We see that the terms with $(\mu, \nu) = (i, j)$ become constant and find only $(\mu, \nu) = (j, 0)$ terms to survive:

$$\begin{aligned}
\langle U_{n,j0} \rangle &= -\text{tr} \left[ V_{n,j}^+ P_0^+ V_{n+\hat{0},j}^- P_0^- \right], \\
\langle U_{n,j0}^{\dagger} \rangle &= -\text{tr} \left[ V_{n,j}^- P_0^+ V_{n+\hat{0},j}^+ P_0^- \right],
\end{aligned} \tag{3.27}$$

where we have defined $(V_{n,j}^+)_{\alpha\beta} = \bar{\psi}_{n,\alpha} \psi_{n+\hat{j},\beta}$ and $(V_{n,j}^-)_{\alpha\beta} = \bar{\psi}_{n+\hat{j},\alpha} \psi_{n,\beta}$. The procedure of the strong coupling expansion up to $O(\beta)$ in our model is illustrated in Fig. 3.2.

Finally, substituting Eqs. (3.20) and (3.25) into Eq. (3.23), we obtain the effective action up to $O(\beta)$:

$$\begin{aligned}
S_{\text{eff}} = {}& (m_0 + 4r) \sum_n \bar{\psi}_n \psi_n - \sum_{n,j} \left[ \bar{\psi}_n P_j^- \psi_{n+\hat{j}} + \bar{\psi}_{n+\hat{j}} P_j^+ \psi_n \right] + \sum_n \text{tr} \left[ M_n P_0^+ M_{n+\hat{0}} P_0^- \right] \\
&+ \frac{\beta}{2} \sum_{n,j} \left\{ \text{tr} \left[ V_{n,j}^+ P_0^+ V_{n+\hat{0},j}^- P_0^- \right] + \text{tr} \left[ V_{n,j}^- P_0^+ V_{n+\hat{0},j}^+ P_0^- \right] \right\} + O(\beta^2).
\end{aligned} \tag{3.28}$$

## 3.3 Free Energy and Order Parameters

As mentioned in Chap. 2, the lattice-gauge-theoretical description of $1/r$ Coulomb interactions does not contain the on-site interactions. Unphysical states due to the absence of on-site interactions, such as phase separation, are eliminated by assuming uniform mean-field ground states. This assumption is also supported by the fact that lattice quantum electrodynamics (QED) is a well-defined (renormalizable) theory.
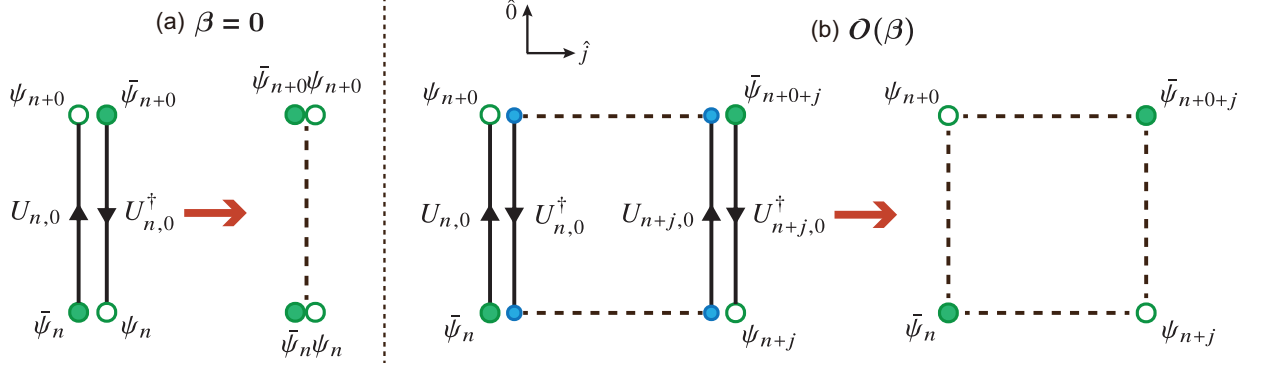
Figure 3.2: Illustration of the strong coupling expansion (a) in the strong coupling limit $\beta = 0$, and (b) in the order of $\beta$. Black arrowed lines represent the link variables $U_0$. Filled (open) Green circles represent $\bar{\psi}$ ($\psi$).

### 3.3.1 Extended Hubbard-Stratonovich Transformation

In this section, we derive the free energy at zero temperature with the use of the extended Hubbard-Stratonovich transformation (EHS) [103, 107, 125], and then we obtain the ground state as the stationary point of the free energy. To this end, let us apply the EHS transformation to the trace of two arbitrary matrices. Introducing two auxiliary fields $R$ and $R'$, we obtain

$$e^{\kappa \mathrm{tr} AB} \propto \int \mathcal{D}[R, R'] \exp\left\{-\kappa \sum_{\alpha\beta} \left[ (R_{\alpha\beta})^2 + (R'_{\alpha\beta})^2 - (A_{\alpha\beta} + B^T_{\alpha\beta})R_{\beta\alpha} - i(A_{\alpha\beta} - B^T_{\alpha\beta})R'_{\beta\alpha} \right] \right\},$$

(3.29)

where $\kappa$ is a positive constant and the superscript $T$ denotes the transpose of a matrix. The integrand has the saddle point values $R_{\alpha\beta} = \langle A + B^T \rangle_{\beta\alpha}/2$ and $R'_{\alpha\beta} = i\langle A - B^T \rangle_{\beta\alpha}/2$. Defining $Q = R + iR'$ and $Q' = R - iR'$, Eq. (3.29) is rewritten as

$$e^{\kappa \mathrm{tr} AB} \propto \int \mathcal{D}[Q, Q'] \exp\left\{-\kappa \left[ Q_{\alpha\beta}Q'_{\alpha\beta} - A_{\alpha\beta}Q_{\beta\alpha} - B^T_{\alpha\beta}Q'_{\beta\alpha} \right] \right\}$$

(3.30)

with the saddle point values $Q_{\alpha\beta} = \langle B^T \rangle_{\beta\alpha}$ and $Q'_{\alpha\beta} = \langle A \rangle_{\beta\alpha}$.

### 3.3.2 Free Energy in the Strong Coupling Limit

Let us consider decoupling the third term in the effective action (3.28) to fermion bilinear form. To do this, we set $(\kappa, A, B) = (1, M_n P_0^+, -M_{n+\hat{0}} P_0^-)$ with $(M_n)_{\alpha\beta} = \bar{\psi}_{n,\alpha}\psi_{n,\beta}$ in Eq. (3.30). In this case, the saddle point values are given by $Q_{\alpha\beta} = -\langle M_{n+\hat{0}} P_0^- \rangle_{\alpha\beta}$ and $Q'_{\alpha\beta} = \langle M_n P_0^+ \rangle_{\beta\alpha}$. We apply the mean-field approximation to the form of $\langle M_n \rangle$.

Here recall that the purpose of this study is to discuss the stability of the topological insulator phase. From the expression for the $Z_2$ invariant [Eq. (3.3)], we see that the mass term [the term proportional to $\alpha_4$ (or the identity matrix)] is important when determining whether the the phase is topologically trivial or nontrivial. Further, time-reversal symmetry breaking orders break the topological insulator phase. In our model where the Hamiltonian is described in terms of $\alpha_\mu$ which satisfy the Clifford algebra, only the $\alpha_5 = -i\gamma_0\gamma_5$ order can break time-reversal symmetry

and lower the energy of the system. Note that the other three matrices $\alpha_j$ merely shift the location of the Dirac cone. Therefore it is natural at the mean-field level to assume that

$$\langle M_n \rangle = \sigma e^{i\theta\gamma_5} = \sigma(\cos\theta + i\gamma_5 \sin\theta) \equiv \phi_\sigma + \phi_\pi i\gamma_5, \tag{3.31}$$

where $\phi_\sigma$ and $\phi_\pi$ are called the chiral condensate and the pion condensate, respectively. The Wilson fermions break chiral symmetry by themselves (the terms proportional to $r$ and $m_0$). Hence we cannot use the value of $\phi_\sigma$ as an order parameter, unlike in the case of graphene where chiral symmetry is not broken in the noninteracting limit and hence the value of $\phi_\sigma$ can be used as the order parameter for the semimetal-insulator transition.

In this study we regard $\phi_\sigma$ as a correction to the bare mass $m_0$. On the other hand, the value of $\phi_\pi$ can be used as an order parameter for the time-reversal symmetry breaking. To understand this, let us consider the mean-field Hamiltonian given by

$$\mathcal{H}_{\mathrm{MF}}(k) = \mathcal{H}_0(k) + \gamma_0 \langle M_n \rangle = \mathcal{H}_0(k) + \phi_\sigma \alpha_4 + \phi_\pi \alpha_5, \tag{3.32}$$

where $\alpha_4 = \sigma_3 \otimes 1$ and $\alpha_5 = i\gamma_0\gamma_5 = \sigma_2 \otimes 1$. Then it can be seen that $\phi_\sigma$ gives a correction to the bare mass $m_0$. The matrix $\alpha_5$ represents a kind of "orbital order", since the spinor is written in the basis of $\psi_k = [c_{k+\uparrow}, c_{k+\downarrow}, c_{k-\uparrow}, c_{k-\downarrow}]^T$, where $c$ is the annihilation operator of an electron, $+, -$ denote two orbitals, and $\uparrow$ ($\downarrow$) denotes up-(down-)spin [16, 17].

Setting $(\kappa, A, B) = (1, M_n P_0^+, -M_{n+\hat{0}} P_0^-)$, we obtain

$$
\begin{aligned}
Q_{\alpha\beta} Q'_{\alpha\beta} &= \mathrm{tr}[\langle A \rangle \langle B \rangle] = -\sigma^2 \mathrm{tr}\left[e^{i\theta\gamma_5} P_0^+ e^{i\theta\gamma_5} P_0^-\right] \\
&= -\frac{\sigma^2}{4} \mathrm{tr}\left[e^{i\theta\gamma_5}(r + \gamma_0) e^{i\theta\gamma_5}(r - \gamma_0)\right] \\
&= -\frac{\sigma^2}{4} \mathrm{tr}\left[(r^2 - 1)\cos^2\theta + 2i\gamma_5 r^2 \sin\theta\cos\theta - (1 + r^2)\sin^2\theta\right] \\
&= \sigma^2[(1 - r^2)\cos^2\theta + (1 + r^2)\sin^2\theta],
\end{aligned}
\tag{3.33}
$$

$$
\begin{aligned}
A_{\alpha\beta} Q_{\beta\alpha} &= \mathrm{tr}[A \langle B \rangle] = -\sigma \mathrm{tr}\left[M_n P_0^+ e^{i\theta\gamma_5} P_0^-\right] \\
&= -\frac{\sigma}{4} \mathrm{tr}\left[M_n(r + \gamma_0) e^{i\theta\gamma_5}(r - \gamma_0)\right] \\
&= -\frac{\sigma}{4} \mathrm{tr}\left\{M_n[(r^2 - 1)\cos\theta + (r^2 + 1)\sin\theta i\gamma_5 + 2r i\gamma_0\gamma_5 \sin\theta]\right\} \\
&= \frac{\sigma}{4}\sigma^2\left[(1 - r^2)\cos\theta \bar{\psi}_n \psi_n - (1 + r^2)\sin\theta \bar{\psi}_n i\gamma_5^T \psi_n - 2r\sin\theta \bar{\psi}_n i(\gamma_0\gamma_5)^T \psi_n\right],
\end{aligned}
\tag{3.34}
$$

$$
\begin{aligned}
B_{\alpha\beta}^T Q'_{\beta\alpha} &= \mathrm{tr}[B \langle A \rangle] = -\sigma \mathrm{tr}\left[M_{n+0} P_0^- e^{i\theta\gamma_5} P_0^+\right] \\
&= -\frac{\sigma}{4} \mathrm{tr}\left[M_n(r - \gamma_0) e^{i\theta\gamma_5}(r + \gamma_0)\right] \\
&= -\frac{\sigma}{4} \mathrm{tr}\left\{M_n[(r^2 - 1)\cos\theta + (r^2 + 1)\sin\theta i\gamma_5 - 2r i\gamma_0\gamma_5 \sin\theta]\right\} \\
&= \frac{\sigma}{4}\sigma^2\left[(1 - r^2)\cos\theta \bar{\psi}_n \psi_n - (1 + r^2)\sin\theta \bar{\psi}_n i\gamma_5^T \psi_n + 2r\sin\theta \bar{\psi}_n i(\gamma_0\gamma_5)^T \psi_n\right],
\end{aligned}
\tag{3.35}
$$

where we have used $\gamma_0^2 = 1$ and $\text{tr}\gamma_5 = 0$. Substituting Eqs. (3.33), (3.34) and (3.35) into Eq. (3.30), we obtain

$$
\begin{aligned}
&\exp\left\{ -\sum_n \text{tr}\left[ M_n P_0^+ M_{n+\hat{0}} P_0^- \right] \right\} \\
&\sim \exp\left\{ -\sum_n \left[ (1-r^2)\phi_\sigma^2 + (1+r^2)\phi_\pi^2 + \frac{1}{2}\bar{\psi}_n \left[ -(1-r^2)\phi_\sigma + i\gamma_5^T(1+r^2)\phi_\pi \right] \psi_n \right] \right\},
\end{aligned}
\tag{3.36}
$$

where we have applied the mean-field approximation to $\langle M_n \rangle$ and $\langle M_{n+0} \rangle$. Then the effective action in the strong coupling limit expressed by the two auxiliary fields $\phi_\sigma$ and $\phi_\pi$ is given by

$$
S_{\text{eff}}(\phi_\sigma, \phi_\pi) = N_s N_\tau \left[ (1-r^2)\phi_\sigma^2 + (1+r^2)\phi_\pi^2 \right] + \sum_k \bar{\psi}_k \mathcal{M}(k; \phi_\sigma, \phi_\pi)\psi_k,
\tag{3.37}
$$

with

$$
\mathcal{M} = \sum_j i\gamma_j \sin k_j + m_0 + r\left( 4 - \sum_j \cos k_j \right) - \frac{1}{2}(1-r^2)\phi_\sigma + i\gamma_5^T \frac{1}{2}(1+r^2)\phi_\pi.
\tag{3.38}
$$

Here $N_s = V$ and $N_\tau = 1/T$ with $V$ and $T$ being the volume and the temperature of the system, respectively and we have done the Fourier transform from $n = (n_0, \boldsymbol{n})$ to $k = (k_0, \boldsymbol{k})$.

The free energy at zero temperature per unit spacetime volume is given by

$$
\mathcal{F}(\phi_\sigma, \phi_\pi) = -\frac{1}{N_s N_\tau} \ln Z(\phi_\sigma, \phi_\pi).
\tag{3.39}
$$

Integration with respect to $\psi$ and $\bar{\psi}$ is carried out by the formula $\int D[\psi, \bar{\psi}]e^{-\bar{\psi}\mathcal{M}\psi} = \det\mathcal{M}$. Therefore we need to calculate the determinant of $\mathcal{M}$. From Eq. (3.38), the matrix $\mathcal{M}$ is written explicitly as

$$
\mathcal{M} = \begin{bmatrix} \tilde{m}(\boldsymbol{k}) + r & \sigma_j \sin k_j + i\frac{1+r^2}{2}\phi_\pi \\ -\sigma_j \sin k_j + i\frac{1+r^2}{2}\phi_\pi & \tilde{m}(\boldsymbol{k}) + r \end{bmatrix} \equiv \begin{bmatrix} A & B \\ C & D \end{bmatrix},
\tag{3.40}
$$

where

$$
\tilde{m}(\boldsymbol{k}) = m_0 - \frac{1-r^2}{2}\phi_\sigma + r\sum_j \left( 1 - \cos k_j \right).
\tag{3.41}
$$

As we see from Eq. (3.41), the chiral condensate $\phi_\sigma$ corresponds to a correction to the bare mass $m_0$ in the original Hamiltonian (3.1). That is, $m(\boldsymbol{k})$ in the noninteracting Hamiltonian (3.1) changes to $\tilde{m}(\boldsymbol{k})$ in the strong coupling limit. The term "$r$" of $\tilde{m}(\boldsymbol{k}) + r$ in Eq. (3.40) originates in the timelike components of the action. After a straightforward calculation, we have

$$
\det\mathcal{M} = \det A \cdot \det\left( D - CA^{-1}B \right) = \left\{ \sum_j \sin^2 k_j + [\tilde{m}(\boldsymbol{k}) + r]^2 + \frac{(1+r^2)^2}{4}\phi_\pi^2 \right\}^2.
\tag{3.42}
$$

47

The same result can be derived by the formula $\det \mathcal{M} = \sqrt{\det(\mathcal{M}\mathcal{M}^\dagger)}$. Finally we arrive at the free energy at zero temperature in the strong coupling limit:

$$
\begin{aligned}
\mathcal{F}(\phi_\sigma, \phi_\pi) = {}& (1 - r^2)\phi_\sigma^2 + (1 + r^2)\phi_\pi^2 \\
& - 2 \int_{-\pi}^{\pi} \frac{d^3k}{(2\pi)^3} \ln \left\{ \sum_j \sin^2 k_j + [\tilde{m}(\mathbf{k}) + r]^2 + \frac{(1 + r^2)^2}{4}\phi_\pi^2 \right\}.
\end{aligned}
\tag{3.43}
$$

The values of $\phi_\sigma$ and $\phi_\pi$ are obtained by the stationary conditions $\partial \mathcal{F}(\phi_\sigma, \phi_\pi)/\partial \phi_\sigma = \partial \mathcal{F}(\phi_\sigma, \phi_\pi)/\partial \phi_\pi = 0$. When $r = 1$, Eq. (3.43) does not depend on $\phi_\sigma$. In this case, the stationary point is obtained by the following equation:

$$
\phi_\sigma = \frac{1}{4N_s N_\tau} \frac{\int \mathcal{D}[\psi, \bar{\psi}] \sum_n \bar{\psi}_n \psi_n e^{-S_{\text{eff}}}}{\int \mathcal{D}[\psi, \bar{\psi}] e^{-S_{\text{eff}}}} = -\frac{1}{4N_s N_\tau} \frac{1}{Z} \frac{dZ}{dm_0} = \frac{1}{4} \frac{d\mathcal{F}}{dm_0}.
\tag{3.44}
$$

When $r > 1$, the coefficient of the first term in Eq. (3.43), $1 - r^2$, becomes negative and thus Eq. (3.43) does not have the stationary point. This is because the logarithmic term is doninant when $\phi_\sigma$ is small and then $\phi_\sigma^2$ term becomes dominant as $\phi_\sigma$ gets larger. Therefore the condition that the coefficient of $\phi_\sigma^2$ must be positive is needed for Eq. (3.43) to have the stationary point. This fact is consistent with the requirement of the reflection positivity of lattice gauge theories with Wilson fermions [127].

In the chiral limit ($r = m_0 = 0$), the free energy is a function of only $\sigma$, reflecting the chiral symmetry of the action. This is understood as follows: in the chiral limit, the action is invariant under the chiral transformation $\psi_n \to e^{i\theta\gamma_5}\psi_n$. This transformation does not depend on the value of $\theta$, and thus the free energy also does not depend on it.

The free energy in the anisotropic case described by the action (3.14) can be obtained in the same way as above. After a straightforward calculation, we arrive at the free energy at zero temperature given by

$$
\begin{aligned}
\mathcal{F}_{\text{aniso}}(\phi_\sigma, \phi_\pi) = {}& (1 - r_\tau^2)\phi_\sigma^2 + (1 + r_\tau^2)\phi_\pi^2 \\
& - 2 \int_{-\pi}^{\pi} \frac{d^3k}{(2\pi)^3} \ln \left\{ \sum_j \sin^2 k_j + [\tilde{m}(\mathbf{k}) + r_\tau]^2 + \frac{(1 + r_\tau^2)^2}{4}\phi_\pi^2 \right\},
\end{aligned}
\tag{3.45}
$$

where $\tilde{m}(\mathbf{k}) = m_0 - (1 - r_\tau^2)\phi_\sigma/2 + r_\perp[\sum_{j=1}^{2}(1 - \cos k_j) + \eta(1 - \cos k_3)]$ with the anisotropy $\eta = r_3/r_\perp$. The ground state is obtained by the stationary condition $\partial \mathcal{F}_{\text{aniso}}(\phi_\sigma, \phi_\pi)/\partial \phi_\sigma = \partial \mathcal{F}_{\text{aniso}}(\phi_\sigma, \phi_\pi)/\partial \phi_\pi = 0$. Note that the free energy does not have the stationary point when $r_\tau > 1$. This is due to the reflection positivity of the lattice gauge theories with Wilson fermions [127].

### 3.3.3 Free Energy up to the Order of $\beta$

Let us evaluate the $O(\beta)$ contribution to the free energy for the isotropic case. We write the fourth term in the effective action (3.28) as $\Delta S_1 + \Delta S_2(\equiv \Delta S)$. Then we should choose such that $(\kappa, A, B) = (\beta/2, V_{n,j}^+ P_0^+, -V_{n+0,j}^- P_0^-)$ in Eq. (3.30) for $\Delta S_1$:

$$
e^{-\Delta S_1} \propto \exp \left\{ -\frac{\beta}{2} \sum_{n,j} \left[ S_{\alpha\beta} S'_{\alpha\beta} - A_{\alpha\beta} S_{\beta\alpha} - B_{\alpha\beta}^T S'_{\beta\alpha} \right] \right\},
\tag{3.46}
$$

with the saddle point values $S_{\alpha\beta} = \langle B^T \rangle_{\beta\alpha} = -\langle V^-_{n+0,j} P^-_0 \rangle_{\alpha\beta}$ and $S'_{\alpha\beta} = \langle A \rangle_{\beta\alpha} = \langle V^+_{n,j} P^+_0 \rangle_{\beta\alpha}$.
Similarly, setting $(\kappa, A, B) = (\beta/2, V^-_{n,j} P^+_0, -V^+_{n+0,j} P^-_0)$ in Eq. (3.30) for $\Delta S_2$, we obtain

$$e^{-\Delta S_2} \propto \exp\left\{ -\frac{\beta}{2} \sum_{n,j} \left[ T_{\alpha\beta} T'_{\alpha\beta} - A_{\alpha\beta} T_{\beta\alpha} - B^T_{\alpha\beta} T'_{\beta\alpha} \right] \right\}, \tag{3.47}$$

with the saddle point values $T_{\alpha\beta} = \langle B^T \rangle_{\beta\alpha} = -\langle V^+_{n+0,j} P^-_0 \rangle_{\alpha\beta}$ and $T'_{\alpha\beta} = \langle A \rangle_{\beta\alpha} = \langle V^-_{n,j} P^+_0 \rangle_{\beta\alpha}$.

Next we decompose $\langle V^+_{n,j} \rangle$ and $\langle V^-_{n,j} \rangle$ into spinor components as follows:

$$\langle V^+_{n,j} \rangle \equiv v^+_s + i\gamma_5 v^+_p + \sum_\mu \gamma_\mu v^+_{v\mu} + \sum_\mu i\gamma_5\gamma_\mu v^+_{a\mu},$$

$$\langle V^-_{n,j} \rangle \equiv v^-_s + i\gamma_5 v^-_p + \sum_\mu \gamma_\mu v^-_{v\mu} + \sum_\mu i\gamma_5\gamma_\mu v^-_{a\mu}, \tag{3.48}$$

where the first through fourth terms are the components of the scalar, pseudoscalar, vector and pseudovector (axial vector) mode, respectively. The terms $\langle V^+_{n,j} \rangle$ and $\langle V^-_{n,j} \rangle$ are equivalent to the propagator from a point to another point. Only the scalar and vector modes appear when parity is not broken, and the pseudoscalar and pseudovector modes may also appear when parity is broken. Therefore these four modes should be considered in Eq. (3.48).

The exponent in Eq. (3.46) is computed as in the case of the strong coupling limit. After a calculation, we obtain

$$S_{\alpha\beta} S'_{\alpha\beta} = \text{tr}[\langle B \rangle \langle A \rangle] = -\text{tr}\left[ \langle V^-_{n,j} \rangle P^-_0 \langle V^+_{n,j} \rangle P^+_0 \right]$$

$$= (1 - r^2)v^-_s v^+_s + (1 + r^2)v^-_p v^+_p + (1 - r^2)v^-_{v0}v^+_{v0} - (1 + r^2)\sum_l v^-_{vl}v^+_{vl}$$

$$- (1 + r^2)v^-_{a0}v^+_{a0} + (1 - r^2)\sum_l v^-_{al}v^+_{al} \tag{3.49}$$

for the constant part, and

$$-A_{\alpha\beta} S_{\beta\alpha} = \text{tr}\left[ V^+_{n,j} P^+_0 \langle V^-_{n+\hat{0},j} P^-_0 \rangle \right] = \bar{\psi}_n \left( P^+_0 \langle V^-_{n,j} \rangle P^-_0 \right)^T \psi_{n+\hat{j}} \tag{3.50}$$

with

$$P^+_0 \langle V^-_{n,j} \rangle P^-_0 = \frac{1}{4}\left[ (r^2 - 1)v^-_s + i\gamma_5 \left\{ (r^2 + 1)v^-_p - 2rv^-_{a0} \right\} + \gamma_0(r^2 - 1)v^-_{v0} \right.$$

$$\left. + \sum_k \gamma_k(r^2 + 1)v^-_{vk} + i\gamma_5\gamma_0 \left\{ -2rv^-_p + (r^2 + 1)v^-_{a0} \right\} + \sum_k i\gamma_5\gamma_k(r^2 - 1)v^-_{ak} \right], \tag{3.51}$$

and

$$-B^T_{\alpha\beta} S'_{\beta\alpha} = \text{tr}\left[ V^-_{n+\hat{0},j} P^-_0 \langle V^+_{n,j} P^+_0 \rangle \right] = \bar{\psi}_{n+\hat{j}} \left( P^-_0 \langle V^+_{n,j} \rangle P^+_0 \right)^T \psi_n \tag{3.52}$$

with

$$P^-_0 \langle V^+_{n,j} \rangle P^+_0 = \frac{1}{4}\left[ (r^2 - 1)v^+_s + i\gamma_5 \left\{ (r^2 + 1)v^+_p + 2rv^+_{a0} \right\} + \gamma_0(r^2 - 1)v^+_{v0} \right.$$

$$\left. + \sum_k \gamma_k(r^2 + 1)v^+_{vk} + i\gamma_5\gamma_0 \left\{ 2rv^+_p + (r^2 + 1)v^+_{a0} \right\} + \sum_k i\gamma_5\gamma_k(r^2 - 1)v^+_{ak} \right] \tag{3.53}$$

for the fermionic part.

Similarly, the exponent in Eq. (3.47) can be computed as

$$
\begin{aligned}
T_{\alpha\beta}T'_{\alpha\beta} &= \mathrm{tr}[\langle B\rangle\langle A\rangle] = -\mathrm{tr}\left[\langle V^+_{n,j}\rangle P^-_0 \langle V^-_{n,j}\rangle P^+_0\right] \\
&= (1-r^2)v^-_s v^+_s + (1+r^2)v^-_p v^+_p + (1-r^2)v^-_{v0}v^+_{v0} - (1+r^2)\sum_l v^-_{vl}v^+_{vl} \\
&\quad - (1+r^2)v^-_{a0}v^+_{a0} + (1-r^2)\sum_l v^-_{al}v^+_{al}
\end{aligned}
\tag{3.54}
$$

for the constant part, and

$$
-A_{\alpha\beta}T_{\beta\alpha} = \mathrm{tr}\left[V^-_{n,j}P^+_0 \langle V^+_{n+\hat{0},j}P^-_0\rangle\right] = \bar{\psi}_{n+\hat{j}}\left(P^+_0\langle V^+_{n,j}\rangle P^-_0\right)^T \psi_n
\tag{3.55}
$$

with

$$
\begin{aligned}
P^+_0\langle V^+_{n,j}\rangle P^-_0 = \frac{1}{4}\Big[& (r^2-1)v^+_s + i\gamma_5\left\{(r^2+1)v^+_p - 2rv^+_{a0}\right\} + \gamma_0(r^2-1)v^+_{v0} \\
&+ \sum_k \gamma_k(r^2+1)v^+_{vk} + i\gamma_5\gamma_0\left\{-2rv^+_p + (r^2+1)v^+_{a0}\right\} + \sum_k i\gamma_5\gamma_k(r^2-1)v^+_{ak}\Big],
\end{aligned}
\tag{3.56}
$$

and

$$
-B^T_{\alpha\beta}T'_{\beta\alpha} = \mathrm{tr}\left[V^+_{n+\hat{0},j}P^-_0 \langle V^-_{n,j}P^+_0\rangle\right] = \bar{\psi}_n\left(P^-_0\langle V^-_{n,j}\rangle P^+_0\right)^T \psi_{n+\hat{j}}
\tag{3.57}
$$

with

$$
\begin{aligned}
P^-_0\langle V^-_{n,j}\rangle P^+_0 = \frac{1}{4}\Big[& (r^2-1)v^-_s + i\gamma_5\left\{(r^2+1)v^-_p + 2rv^-_{a0}\right\} + \gamma_0(r^2-1)v^-_{v0} \\
&+ \sum_k \gamma_k(r^2+1)v^-_{vk} + i\gamma_5\gamma_0\left\{2rv^-_p + (r^2+1)v^-_{a0}\right\} + \sum_k i\gamma_5\gamma_k(r^2-1)v^-_{ak}\Big]
\end{aligned}
\tag{3.58}
$$

for the fermionic part.

Combining $e^{-\Delta S_1}$ and $e^{-\Delta S_2}$, we obtain the $O(\beta)$ contribution to the action as

$$
\begin{aligned}
\Delta S = \beta \sum_{n,j}\Big[& (1-r^2)v^-_s v^+_s + (1+r^2)v^-_p v^+_p + (1-r^2)v^-_{v0}v^+_{v0} - (1+r^2)\sum_l v^-_{vl}v^+_{vl} \\
&- (1+r^2)v^-_{a0}v^+_{a0} + (1-r^2)\sum_l v^-_{al}v^+_{al}\Big] + \sum_{n,j}\left[\bar{\psi}_n\mathcal{A}_-\psi_{n+\hat{j}} + \bar{\psi}_{n+\hat{j}}\mathcal{A}_+\psi_n\right],
\end{aligned}
\tag{3.59}
$$

where

$$
\begin{aligned}
\langle\mathcal{A}_-\rangle = \frac{\beta}{4}\Big[& -(1-r^2)v^-_s + (1+r^2)i\gamma_5 v^-_p - (1-r^2)\gamma_0 v^-_{v0} + (1+r^2)\sum_l \gamma_l v^-_{vl} \\
&+ (1+r^2)i\gamma_5\gamma_0 v^-_{a0} - (1-r^2)\sum_l i\gamma_5\gamma_l v^-_{al}\Big]^T,
\end{aligned}
\tag{3.60}
$$

$$\langle \mathcal{A}_+ \rangle = \frac{\beta}{4} \left[ -(1-r^2)v_s^+ + (1+r^2)i\gamma_5 v_p^+ - (1-r^2)\gamma_0 v_{v0}^+ + (1+r^2)\sum_l \gamma_l v_{vl}^+ \right.$$
$$\left. +(1+r^2)i\gamma_5\gamma_0 v_{a0}^+ - (1-r^2)\sum_l i\gamma_5\gamma_l v_{al}^+ \right]^T . \tag{3.61}$$

Then doing the Fourier transform and combining Eqs. (3.37) and (3.59), we get the effective action up to $O(\beta)$ with auxiliary fields:

$$S_{\text{eff}} = S_{\text{eff}}^{\text{aux}}(\phi_\sigma, \phi_\pi, v_s^\pm, v_p^\pm, v_{v\mu}^\pm, v_{a\mu}^\pm) + \sum_k \bar\psi_k \mathcal{M}(\boldsymbol{k}; \phi_\sigma, \phi_\pi, v_s^\pm, v_p^\pm, v_{v\mu}^\pm, v_{a\mu}^\pm)\psi_k, \tag{3.62}$$

where

$$S_{\text{eff}}^{\text{aux}} = N_s N_\tau \left\{ (1-r^2)\phi_\sigma^2 + (1+r^2)\phi_\pi^2 + \beta \sum_j \left[ (1-r^2)v_s^- v_s^+ + (1+r^2)v_p^- v_p^+ + (1-r^2)v_{v0}^- v_{v0}^+ \right. \right.$$
$$\left. \left. -(1+r^2)\sum_l v_{vl}^- v_{vl}^+ - (1+r^2)v_{a0}^- v_{a0}^+ + (1-r^2)\sum_l v_{al}^- v_{al}^+ \right] \right\}, \tag{3.63}$$

and

$$\mathcal{M} = m_0 + r\left(4 - \sum_j \cos k_j\right) + \frac{\sigma}{2}(r^2-1)\cos\theta + \sum_j \frac{\beta}{4}(r^2-1)\left[v_s^- e^{ik_j} + v_s^+ e^{-ik_j}\right]$$
$$+ i\gamma_5^T \left\{\frac{\sigma}{2}(r^2+1)\sin\theta + \sum_j \frac{\beta}{4}(r^2+1)\left[v_p^- e^{ik_j} + v_p^+ e^{-ik_j}\right]\right\}$$
$$+ \gamma_0^T \sum_j \frac{\beta}{4}(r^2-1)\left[v_{v0}^- e^{ik_j} + v_{v0}^+ e^{-ik_j}\right] + \sum_j i\gamma_j \sin k_j + \sum_{j,l} \gamma_k^T \frac{\beta}{4}(r^2+1)\left[v_{vl}^- e^{ik_j} + v_{vl}^+ e^{-ik_j}\right]$$
$$+ i(\gamma_5\gamma_0)^T \sum_j \frac{\beta}{4}(r^2+1)\left[v_{a0}^- e^{ik_j} + v_{a0}^+ e^{-ik_j}\right] + \sum_{j,l} i(\gamma_5\gamma_l)^T \frac{\beta}{4}(r^2-1)\left[v_{al}^- e^{ik_j} + v_{al}^+ e^{-ik_j}\right]. \tag{3.64}$$

Next we replace the auxiliary fields to make the calculation easier as follows:

$$v_s^\mp = S_1 \mp iS_2, \quad v_p^\mp = \mp iP_1 + P_2, \quad v_{v0}^\mp = iV_{0,1} \pm V_{0,2},$$
$$v_{vk}^\mp = \mp V_{k,1} - iV_{k,2}, \quad v_{a0}^\mp = \mp A_{0,1} - iA_{0,2}, \quad v_{ak}^\mp = -iA_{k,1} \mp A_{k,2}. \tag{3.65}$$

Using the formula $\det\mathcal{M} = \sqrt{\det(\mathcal{M}\mathcal{M}^\dagger)}$, we obtain

$$\det\mathcal{M} = \left[\mathcal{M}_s^2 + \mathcal{M}_p^2 + \mathcal{M}_{v0}^2 + \sum_j \mathcal{M}_{vj}^2 + \mathcal{M}_{a0}^2 + \sum_j \mathcal{M}_{aj}^2\right]^2, \tag{3.66}$$

where we have defined $\mathcal{M}$ as

$$\mathcal{M} = \mathcal{M}_s + i\gamma_5^T \mathcal{M}_p + i\gamma_0^T \mathcal{M}_{v0} + \sum_j i\gamma_j \mathcal{M}_{vj} + (\gamma_5\gamma_0)^T \mathcal{M}_{a0} + \sum_j \left(\gamma_5\gamma_j\right)^T \mathcal{M}_{aj}. \tag{3.67}$$

The free energy at zero temperature per unit spacetime volume is given by

$$\mathcal{F}(\phi_\sigma, \phi_\pi, S_a, P_a, V_\mu, A_\mu) = -\frac{1}{N_s N_\tau} \ln Z(\phi_\sigma, \phi_\pi, S_a, P_a, V_\mu, A_\mu), \tag{3.68}$$

where $a = 1, 2$ and $\mu = 0, 1, 2, 3$. Here $N_s = V$ and $N_\tau = 1/T$ with $V$ and $T$ being the volume and the temperature of the system, respectively. Further we eliminate the auxiliary fields $S_a$, $P_a$, $V_\mu$ and $A_\mu$ by the stationary condition such that

$$\frac{\partial \mathcal{F}}{\partial S_a} = \frac{\partial \mathcal{F}}{\partial P_a} = \frac{\partial \mathcal{F}}{\partial V_\mu} = \frac{\partial \mathcal{F}}{\partial A_\mu} = 0. \tag{3.69}$$

The final form of the free energy for the isotropic case at zero temperature up to $O(\beta)$ is given by

$$\mathcal{F}(\phi_\sigma, \phi_\pi)$$

$$= (1 - r^2)\phi_\sigma^2 + (1 + r^2)\phi_\pi^2 - 2\int_{-\pi}^{\pi} \frac{d^3k}{(2\pi)^3} \log X_0 - \frac{\beta}{3}(1 + r^2) \sum_j \left[ \int_{-\pi}^{\pi} \frac{d^3k}{(2\pi)^3} \frac{\sin^2 k_j}{X_0} \right]^2$$

$$- \frac{\beta}{3}(1 + r^2) \left[ \frac{1 + r^2}{2} \phi_\pi \int_{-\pi}^{\pi} \frac{d^3k}{(2\pi)^3} \frac{\sum_j \cos k_j}{X_0} \right]^2 - \frac{\beta}{3}(1 - r^2) \left[ \int_{-\pi}^{\pi} \frac{d^3k}{(2\pi)^3} \frac{\tilde{m}(\boldsymbol{k}) + r}{X_0} \sum_j \cos k_j \right]^2, \tag{3.70}$$

where we have defined $X_0 = \sum_j \sin^2 k_j + [\tilde{m}(\boldsymbol{k}) + r]^2 + \frac{(1+r^2)^2}{4}\phi_\pi^2$.

## 3.4 Numerical Results

### 3.4.1 Isotropic Case

At first, up to $O(\beta)$, we found that the value of $\phi_\pi$ is zero at the stationary point for any set of $(r, m_0)$. Hence in the following, we set $\phi_\sigma = -\sigma$ and $\phi_\pi = 0$ in Eq. (3.70) to calculate the value of the chiral condensate $\sigma$. Let us consider the meaning of $\phi_\pi = 0$. From Eq. (3.38), we see that nonzero $\phi_\pi$ generates the term $i\bar{\psi}\gamma_5\psi$. The term $i\bar{\psi}\gamma_5\psi$ is odd under both time-reversal and inversion. Therefore, this indicates that the phase with spontaneously broken time-reversal and parity (spatial inversion) symmetries does not arise in the strong coupling region of our model. Such a phase, i.e., the "Aoki phase" (where parity and flavor symmetry are spontaneously broken) was originally proposed in the lattice QCD with Wilson fermions [128–130]. A mean-field study of Wilson fermions with short-range Coulomb interactions from weak coupling [89] and a lattice strong coupling expansion study of the Kane-Mele model with $1/r$ Coulomb interactions on a honeycomb lattice [131] suggest the existence of this phase. Here we mention the main difference between our model and lattice QCD except for the gauge group. Our model has only temporal (timelike) link variables, in contrast to lattice QCD. Spatial link variables are absent, like in the case of free fermions. It is obvious that parity symmetry is not spontaneously broken in free fermions. This will be one of the reasons why the parity broken phase does not appear in our model.

The $m_0$ dependence of the chiral condensate $\sigma$ for some values of $r$ in the strong coupling limit is shown in Fig. 3.3(a). The value of $\sigma$ is expected to be quantitatively correct, based on the fact that the result of a strong coupling expansion study in graphene [103] is in good
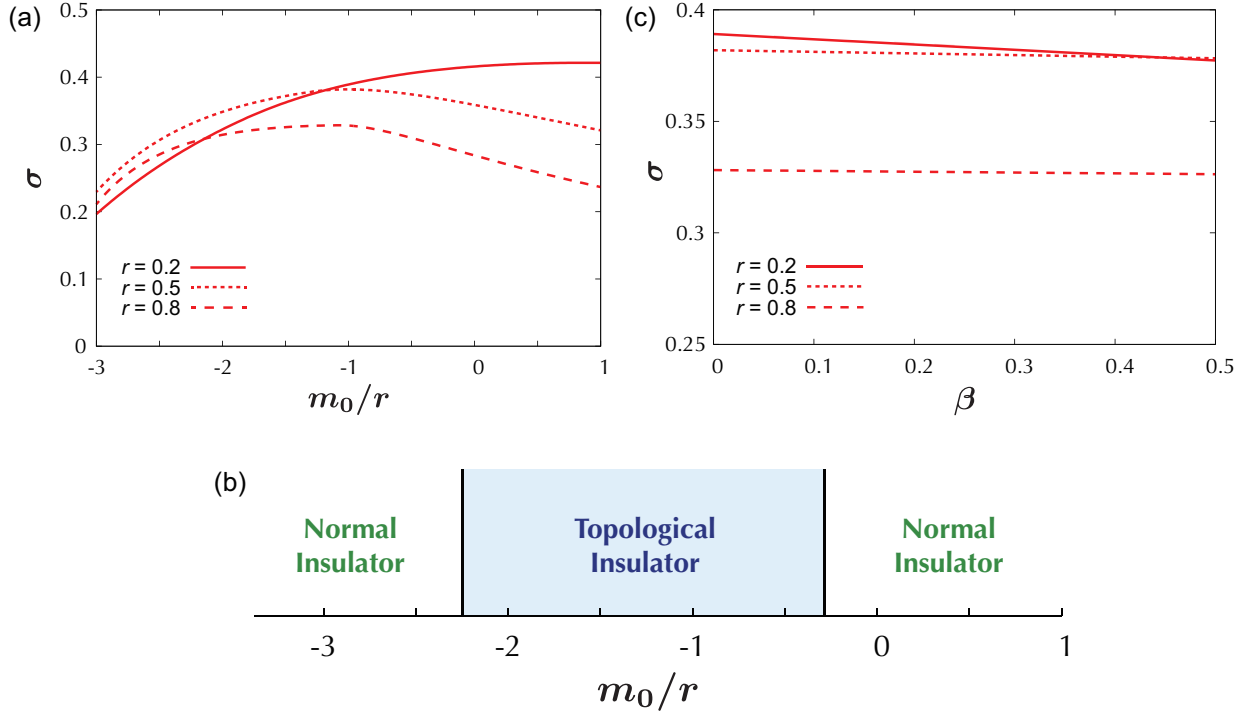
Figure 3.3: (a) $m_0$ dependence of the chiral condensate $\sigma$ in the strong coupling limit ($\beta = 0$). (b) Phase diagram with $r = 0.5$ in the strong coupling limit. The phase boundaries are determined by the condition $m_{\text{eff}} = 0$ or $m_{\text{eff}} = -2r$. (c) $\beta$ dependence of the chiral condensate $\sigma$ at $m_0 = -r$.

agreement with that of lattice Monte Carlo studies [100–102, 104]. As mentioned in Sect. 3.1, in the noninteracting limit (i.e., at $\beta = \infty$), the system with $0 > m_0 > -2r$ ($m_0 > 0$) is identified as a topological (normal) insulator. In this study, the chiral condensate is equivalent to a correction to the bare mass. Hence it is natural to define the effective mass in Eq. (3.41) as

$$m_{\text{eff}} = m_0 + (1 - r^2)\sigma/2. \tag{3.71}$$

Note that time-reversal symmetry is not broken in the strong coupling limit. This means that we can compute the $Z_2$ invariant [Eq. (3.3)]. In the strong coupling region, the system with $0 > m_{\text{eff}} > -2r$ ($m_{\text{eff}} > 0$) is identified as a topological (normal) insulator. The phase diagram with $r = 0.5$ in the strong coupling limit calculated by the $Z_2$ invariant is shown in Fig. 3.3(b). The width $2r$ of the topological insulator phase in the noninteracting limit seems nearly unchanged in the strong coupling limit. From this phase diagram, we see that the effect of $1/r$ Coulomb interactions is to shift the region of the topological insulator phase.

From Fig. 3.3(c), it is concluded that the gapped phases (normal and topological insulator). The $\beta$ dependence of the chiral condensate $\sigma$ for some values of $r$ is shown in Fig. 3.3(c). We see that $\sigma$ is a monotonically decreasing function of the coupling strength $\beta$. Our result shows that the mass gap remains finite even in the strong coupling limit, in contrast to a mean-field analysis of Wilson fermions with short-range Coulomb interactions [89] in which the mass gap becomes infinity in the strong coupling limit. This is because the effects of strong $1/r$ Coulomb interactions are renormalized properly in our analysis. We see also that as $r$ becomes smaller, the rate of decrease of $\sigma$ becomes notable. That is, as the original masses of fermion doublers become smaller, the energy gap of the system becomes smaller, as is understood intuitively.

From Fig. 3.3(c), it is concluded that the gapped phases (normal and topological insulator
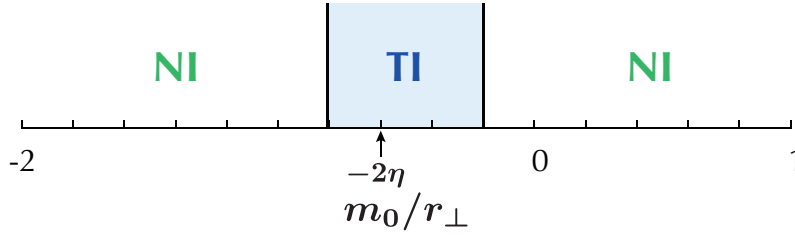
Figure 3.4: Phase diagram in the strong coupling limit with $r_\tau = r_\perp = 0.6$ and $\eta = 0.3$. The phase boundaries between the topological insulator (TI) phase and the normal insulator (NI) phase are determined by the condition $m_{\mathrm{eff}}/r_\perp = 0$ or $m_{\mathrm{eff}}/r_\perp = -2\eta$.
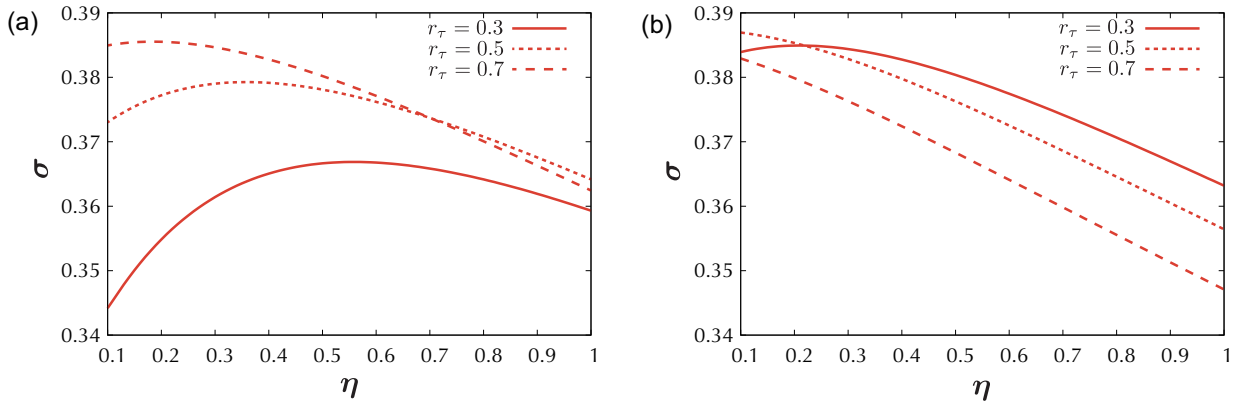


Figure 3.5: $\eta$ dependence of $\sigma$ in the strong coupling limit with $r_\perp = 0.6$, in the case of (a) $m_0/r_\perp = -1.0$ and (b) $m_0/r_\perp = -0.5$.

phases) are stable in the strong coupling region. This contrasts with the result of the strong coupling expansion in graphene [103]. In graphene, the rate of decrease of $\sigma$ from $\beta = 0$ to $\beta = 0.5$ is about 60% [103], whereas that of our model is about 3% at $r = 0.2$. This suggests that the topological insulator phase in our model survives in the strong coupling limit, although graphene undergoes the phase transition (semimetal-insulator transition) in the strong coupling region.

## 3.4.2 Anisotropic Case

As in the isotropic case, with any set of $(m_0, r_\tau, r_\perp, \eta)$, it was found that the value of $\phi_\pi$ is zero in the strong coupling limit. This means that the phase in which time-reversal and inversion symmetries are spontaneously broken does not arise in the strong coupling limit, and that the effect of $1/r$ Coulomb interactions in this system is the renormalization of the bare mass of Wilson fermions. Thus in the following, we set $\phi_\sigma = -\sigma$ in Eq. (3.45) and define the effective mass modified by the chiral condensate $\sigma$:

$$m_{\mathrm{eff}} = m_0 + (1 - r_\tau^2)\sigma/2. \tag{3.72}$$

The phase boundary in the strong coupling limit is determined by the $Z_2$ invariant. Namely, if $0 > m_{\mathrm{eff}}/r_\perp > -2\eta$, then the system is identified as a topological insulator. The phase diagram with $r_\tau = r_\perp = 0.6$ and $\eta = 0.3$ are shown in Fig. 3.4. We see that the topological insulator
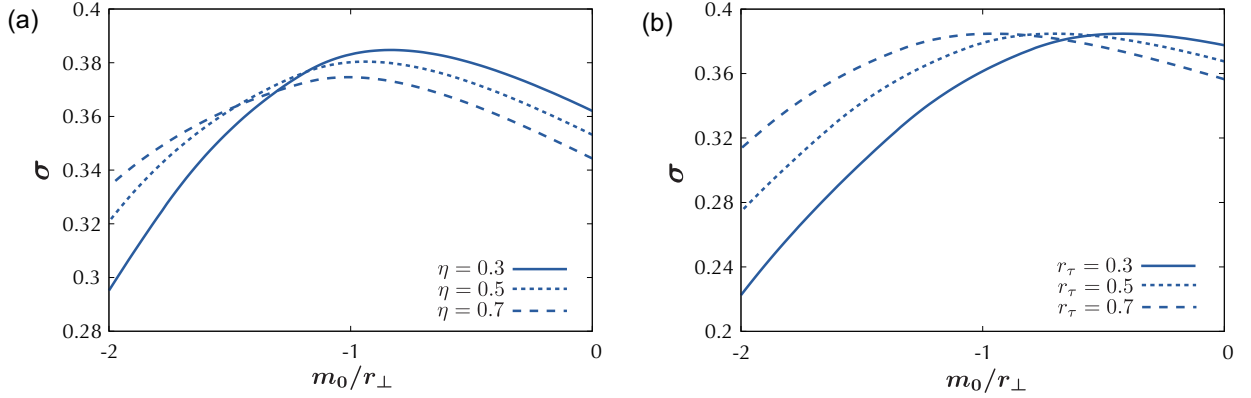
54

Figure 3.6: $m_0$ dependence of $\sigma$ in the strong coupling limit with $r_\perp = 0.6$, in the case of (a) $r_\tau = 0.6$ and (b) $\eta = 0.3$.

phase survives in the strong coupling limit. The width $2\eta$ of the topological insulator phase in the noninteracting limit seems nearly unchanged in the strong coupling limit. Namely, the effect of $1/r$ Coulomb interactions is to shift the region of the topological insulator phase.

Figure 3.5 shows the anisotropy $\eta$ dependence of $\sigma$ for some values of $r_\tau$. In both cases of $m_0/r_\perp = -1.0$ [Fig. 3.5(a)] and $m_0/r_\perp = -0.5$ [Fig. 3.5(b)], $\sigma$ approaches a monotonically decreasing function of $\eta$ with larger $r_\tau$. Although the $\eta$ dependence of $\sigma$ changes with $r_\tau$, there is a tendency that the mass renormalization due to the Coulomb interactions becomes stronger as the anisotropy becomes larger. This could result from the fact that quantum effects become pronounced in lower dimensions in general. Finally we show the $m_0$ dependence of $\sigma$ for some values of $\eta$ and $r_\tau$. From Fig. 3.6(a) where $r_\tau$ is fixed to 0.6 [Fig. 3.6(b) where $\eta$ is fixed to 0.3], we see that the value of the bare mass $m_0$ which has the strongest renormalization effect in the strong coupling limit moves to left as $\eta$ ($r_\tau$) becomes larger.

## 3.5 Discussions

So far we have found that there is no spontaneous symmetry breaking (signaled by the $\bar{\psi} i \gamma_5 \psi$ term) in the strong coupling region. This implies that the topological insulator phase is stable in the strong coupling region. We have also obtained the value of the effective mass up to of the order of the coupling strength $\beta$. Then we can connect the phase boundary obtained from the $Z_2$ invariant [Eq. (3.3)] in the noninteracting limit and that in the strong coupling region. A possible global phase diagram of a correlated 3D topological insulator described by the (isotropic) Wilson fermions with $1/r$ Coulomb interactions is shown in Fig. 3.7. Here let us recall that the value of $|m_0|$ can be regarded as the strength of spin-orbit coupling [16], since the negative $m_0$ is obtained as a result of the band inversion due to strong spin-orbit coupling. Hence it can be seen from the predicted phase diagram that when spin-orbit coupling is not strong (i.e., $m_0/r > -0.25$), the topological insulator phase changes to a normal insulator phase in the strong coupling limit. On the other hand, when spin-orbit coupling is sufficiently strong (i.e., $m_0/r < -0.25$), the topological insulator phase survives in the strong coupling limit. We think these results are not so surprising. Note that a lattice strong coupling expansion study of the Kane-Mele model on a honeycomb lattice [131] also shows that when spin-orbit coupling is sufficiently strong, the topological insulator phase survives in the strong coupling limit.
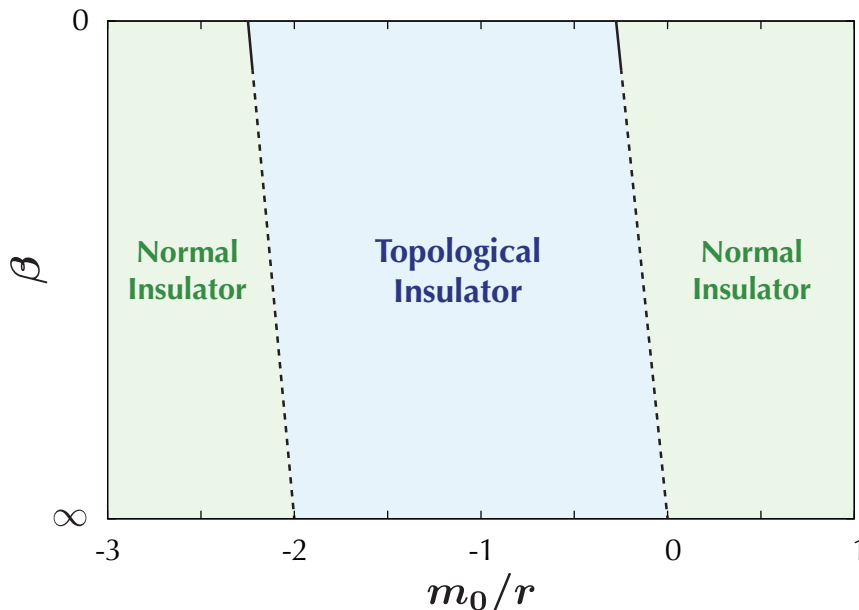
Figure 3.7: A possible global phase diagram of a correlated 3D topological insulator described by the (isotropic) Wilson fermions with $1/r$ Coulomb interactions. The $\beta = 0$ ($\beta = \infty$) line represents the strong coupling (noninteracting) limit.

Let us compare the result in present study with the result in the case of short-range interactions. We have studied the effects of short-range interactions in the Wilson fermions [89]. The phase diagram of the Wilson fermions with short-range interactions is shown in Fig. 3.8. We can see that the behaviors of the phase boundary between the topological insulator phase and the normal insulator phase are similar in both short-range and long-range cases. However, in the case of short-range interactions, the value of $\phi_\pi$ becomes nonzero when the interactions are strong. Namely the topological insulator phase is broken due to the presence of $\bar{\psi} i \gamma_5 \psi$ term which breaks time-reversal symmetry. Therefore the difference between short-range and long-range interactions can result in the presence or absence of the symmetry broken phase ("Aoki phase"). This could be understood intuitively as follows. If the interactions are short-range, then the antiferromagnetic order, which breaks time-reversal symmetry, is considered to develop as the interactions become strong. However, in the present case, the interactions are the unscreened $1/r$ long-range Coulomb interactions. It is not obvious that time-reversal symmetry breaking occurs in the case of long-range interactions.

Finally we would like to mention the possibility of the Mott transition in our model. The important point is that on-site interactions are not included in this model. If the Mott transition occurs, the phase with nonzero $\phi_\pi$, where both time-reversal and inversion symmetries are broken, could be regarded as the Mott insulator phase. However, it was found that $\phi_\pi$ is always zero in the strong coupling region. From these viewpoints, we believe that the Mott transition does not occur. The absence of on-site interactions in our model will be justified by that on-site interactions are considered to be weak in 3D topological insulators such as $Bi_2Se_3$, i.e., in $p$-electron systems.

56
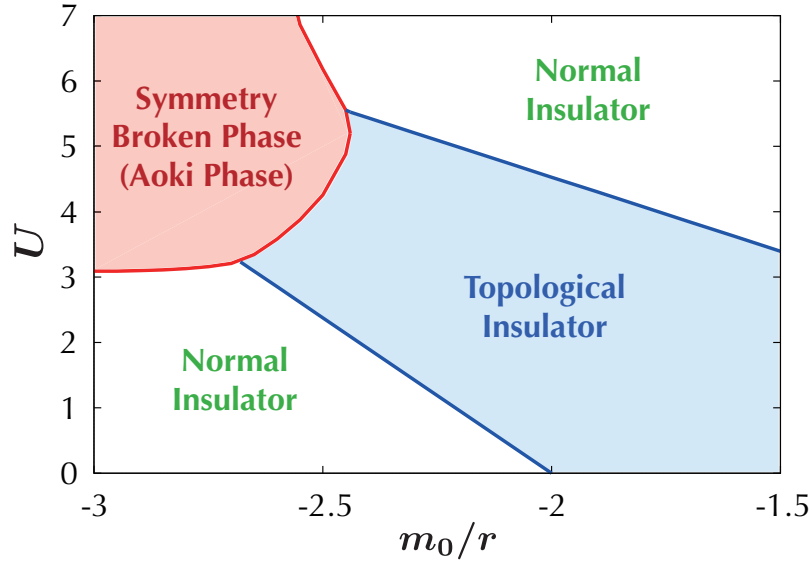
Figure 3.8: Mean-field phase diagram of the Wilson fermions with short-range interactions. $U$ is the strength of the short-range interaction.

## 3.6 Summary

To summarize, we have studied the effects of strong $1/r$ long-range Coulomb interactions in a 3D topological insulator where the effective Hamiltonian can be described by the Wilson fermions. Based on the U(1) lattice gauge theory, we have performed the strong coupling expansion accompanied with the mean-field approximation. It was found that the effect of $1/r$ Coulomb interactions in our model corresponds to the renormalization of the bare mass of Wilson fermions. The value of the chiral condensate, which is regarded as a correction to the bare mass in the strong coupling region, is expected to be correct quantitatively. The phase where time-reversal and inversion symmetries are spontaneously broken (Aoki phase) was not found in the strong coupling region, in contrast to the case of lattice QCD with Wilson fermions. It was found that the gapped phases are stable in the strong coupling region. This suggests that the topological insulator phase survives in the strong coupling limit. In this study, the bulk property of a 3D topological insulator was examined. It will be interesting to examine the strong correlation effect in the surface Dirac fermions.

# Chapter 4

# Weyl Semimetal with Strong Long-Range Correlations

In this chapter, we study the effects of strong $1/r$ long-range Coulomb interactions in a Weyl semimetal. We consider a three-dimensional (3D) Dirac fermion system on a lattice with a time-reversal symmetry breaking term, and take into account $1/r$ long-range Coulomb interactions between the bulk electrons. This model is regarded as the case where magnetic impurities are doped into the bulk of a 3D topological insulator. With the use of the strong coupling expansion of the lattice gauge theory and the mean-field approximation, we analyze the system from the strong coupling limit. It is shown that parity symmetry of the system is spontaneously broken in the strong coupling limit, and a different type of the Weyl semimetal, in which time-reversal and parity symmetries are broken, appears in the strong coupling limit. A possible global phase diagram of a correlated Weyl semimetal is presented. The contents in this chapter have been published in:

A. Sekine and K. Nomura, J. Phys. Soc. Jpn. **83**, 094710-1-8 (2014).

## 4.1 Theoretical Model

In this section, we introduce a lattice model for a Weyl semimetal with $1/r$ Coulomb interactions. The motivations for considering the effects of $1/r$ Coulomb interactions are as follows. The first is that the effects of long-range interactions in Weyl semimetals have not yet been revealed. We have studied the effects of short-range interactions in a Weyl semimetal [89], and found that the Weyl semimetal phase is broken in the region where the interactions are strong. The second is that the effects of long-range interactions are expected to be important in Dirac fermion systems, since the screening effect is considered to be weak due to the vanishing density of states near the Fermi level.

### 4.1.1 Noninteracting Model

Let us start from a continuum model for a noninteracting Weyl semimetal. We consider a Weyl semimetal which consists of two Weyl nodes separated in momentum space introduced in Subsect. 1.3.2. In this case, the general Hamiltonian is written by the three-dimensional (3D) Dirac Hamiltonian with a time-reversal symmetry breaking term as

$$\mathcal{H}_0(\boldsymbol{k}) = v_\mathrm{F}\boldsymbol{k}\cdot\boldsymbol{\alpha} + m_0\alpha_4 + \boldsymbol{b}\cdot\boldsymbol{\Sigma}, \tag{4.1}$$
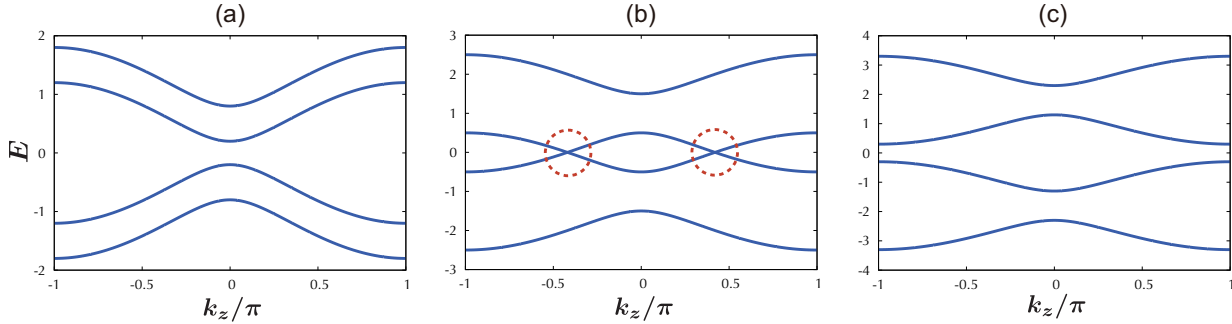
Figure 4.1: $k_z$ dependence of the energy spectrum of the lattice model (4.4) with $k_x = k_y = 0$, $m_0 = -0.5$ and $r = 1$ in the case of (a) $b = 0.3$, (b) $b = 1.0$, and (c) $b = 1.8$. When the strength of $b$ is intermediate, the two bands near the Fermi level $E_F = 0$ touch at two points (Weyl nodes).

where $v_F$ is the Fermi velocity, $m_0$ is the mass of the Dirac fermion, and $\alpha_j$ ($j = 1, 2, 3, 4$) are the $4 \times 4$ alpha matrices. The term $\boldsymbol{b} \cdot \boldsymbol{\Sigma}$, with $\boldsymbol{\Sigma} = -i/2([\alpha_2, \alpha_3], [\alpha_3, \alpha_1], [\alpha_1, \alpha_2])$, is a time-reversal symmetry breaking perturbation. Without loss of generality, we can set $\boldsymbol{b} = (0, 0, b)$. The eigenvalues of this Hamiltonian are obtained analytically as

$$E(\boldsymbol{k}) = \pm\sqrt{v_F^2(k_1^2 + k_2^2) + \left[\sqrt{v_F^2 k_3^2 + m_0^2} \pm b\right]^2}, \tag{4.2}$$

and we see that the band touching points (the Weyl nodes) $W_\pm$ are given by $W_\pm = (0, 0, \pm\sqrt{b^2 - m_0^2})$ with $b > |m_0|$. Then the energy bands near the Weyl nodes are found to be

$$E(\boldsymbol{q}) = \pm v_F \sqrt{q_1^2 + q_2^2 + (1 - m_0^2/b^2)q_3^2}, \tag{4.3}$$

where $\boldsymbol{q} = \boldsymbol{k} - W_\pm$. This is just the dispersion of the Weyl fermions, since this can be obtained by diagonalizing the Weyl Hamiltonian $\mathcal{H}(\boldsymbol{q}) = \sum_{i=1}^{3} v_i \cdot \boldsymbol{q}\sigma_i$.

Next let us consider the Hamiltonian (4.1) on a cubic lattice. In the following, as the unperturbed part, we adopt the Wilson fermion which is known as a lattice model without fermion doublers. The Wilson fermion can also be regarded as the effective lattice model for 3D topological insulators such as $Bi_2Se_3$ [16, 17]. Hence, our model is regarded as the case where magnetic impurities are doped into the bulk of a 3D topological insulator, because the term $b\Sigma_3$ can be considered as the exchange (ferromagnetic) coupling between the bulk electrons and magnetic impurities. The non-interacting Hamiltonian we consider is given by

$$\mathcal{H}_0(\boldsymbol{k}) = v_F \sum_{j=1}^{3} \alpha_j \sin k_j + m(\boldsymbol{k})\alpha_4 + b\Sigma_3, \tag{4.4}$$

where $m(\boldsymbol{k}) = m_0 + r\sum_{j=1}^{3}(1 - \cos k_j)$. The alpha matrices are given by the Dirac representation, $\alpha_j = \tau_1 \otimes \sigma_j$ and $\alpha_4 = \tau_3 \otimes \mathbf{1}$ where the Pauli matrices $\tau_j$ and $\sigma_j$ denote the orbital and spin degree of freedom, respectively. Namely, the spinor in the Hamiltonian (4.4) is written in the basis of $\psi_{\boldsymbol{k}}^\dagger = [c_{k+\uparrow}^\dagger, c_{k+\downarrow}^\dagger, c_{k-\uparrow}^\dagger, c_{k-\downarrow}^\dagger]$, where $c^\dagger$ is the creation operator of an electron, $+, -$ denote two orbitals, and $\uparrow$ ($\downarrow$) denotes up-(down-)spin. The matrix $\Sigma_3$ is given explicitly as $\Sigma_3 = \mathbf{1} \otimes \sigma_3$. The Weyl nodes appear where the wave vector $\boldsymbol{k}$ satisfies the condition $b^2 =$

$[m_0 + r\sum_j(1 - \cos k_j)]^2 + \sin^2 k_3$ and $\sin k_1 = \sin k_2 = 0$. $k_1$ and $k_2$ can take the value 0 or $\pi$. In this study, we set $|m_0|$ small to restrict the existence of the Weyl nodes on the $(k_1, k_2) = (0, 0)$ line. The $k_z$ dependence of the energy spectrum of the lattice model (4.4) for some values of $b$ is shown in Fig. 4.1.

## 4.1.2 Interacting Model

We introduce $1/r$ Coulomb interactions between the bulk electrons according to the U(1) lattice gauge theory (lattice quantum electrodynamics). In condensed matter, the Fermi velocity is rather small compared to the speed of light $c$, i.e., $v_F/c \sim 10^{-3}$. In this case, the interactions with the spatial components of the four-vector potential are suppressed by the factor $v_F/c$, and thus we can regard that the Dirac fermions interact only via the electric field i.e. $1/r$ Coulomb interactions. Then the Euclidean action of the system is given by

$$S = S_F^{(\tau)} + S_F^{(s)} + (m_0 + 3r + r_\tau) \sum_n \bar{\psi}_n \psi_n + b \sum_n \bar{\psi}_n \gamma_0 \Sigma_3 \psi_n + S_G, \qquad (4.5)$$

where $S_F^{(\tau)} + S_F^{(s)}$ is the fermionic part without the mass term

$$\begin{aligned}
S_F^{(\tau)} &= -\sum_n \left[ \bar{\psi}_n P_0^- U_{n,0} \psi_{n+\hat{0}} + \bar{\psi}_{n+\hat{0}} P_0^+ U_{n,0}^\dagger \psi_n \right], \\
S_F^{(s)} &= -\sum_{n,j} \left[ \bar{\psi}_n P_j^- \psi_{n+\hat{j}} + \bar{\psi}_{n+\hat{j}} P_j^+ \psi_n \right],
\end{aligned} \qquad (4.6)$$

and $S_G$ is the pure U(1) gauge part

$$S_G = \beta \sum_n \sum_{\mu > \nu} \left[ 1 - \frac{1}{2} \left( U_{n,\mu} U_{n+\hat{\mu},\nu} U_{n+\hat{\nu},\mu}^\dagger U_{n,\nu}^\dagger + \text{H.c.} \right) \right]. \qquad (4.7)$$

Here $\bar{\psi} = \psi^\dagger \gamma_0$, $n = (n_0, n_1, n_2, n_3)$ denotes a spacetime lattice site on a 4D hypercubic lattice, $\hat{\mu}$ denotes the unit vector along the $\mu$ direction, and $P_\mu^\pm = (r_\mu \pm \gamma_\mu)/2$ with $r_0 = r_\tau$ and $r_1 = r_2 = r_3 = r$. $U_{n,\mu}$ are the U(1) link variables with $U_{n,j} = 1$ and $U_{n,0} = e^{i\theta_n}$ ($-\pi \le \theta_n \le \pi$). The timelike Wilson term (the term proportional to $r_\tau$) is introduced to the unperturbed part (the $b = 0$ part) to eliminate the fermion doublers. This is because when $b = 0$, the system should possess a single Dirac cone around the $\Gamma$ point. According to the non-interacting Hamiltonian of 3D topological insulators such as $Bi_2Se_3$, the gamma matrices $\gamma_\mu$ are given by the Dirac representation in the Euclidean spacetime ($\{\gamma_\mu, \gamma_\nu\} = 2\delta_{\mu\nu}$):

$$\gamma_0 = \begin{bmatrix} 1 & 0 \\ 0 & -1 \end{bmatrix}, \quad \gamma_j = \begin{bmatrix} 0 & -i\sigma_j \\ i\sigma_j & 0 \end{bmatrix}, \quad \gamma_5 = \begin{bmatrix} 0 & 1 \\ 1 & 0 \end{bmatrix}, \qquad (4.8)$$

where $j = 1, 2, 3$ and $\sigma_j$ are the Pauli matrices.

A parameter $\beta$ which represents the strength of $1/r$ Coulomb interactions is given by

$$\beta = \frac{v_F \epsilon}{e^2} = \frac{v_F \epsilon}{4\pi c \alpha}, \qquad (4.9)$$

where $\epsilon$ is the dielectric constant of the system, $e$ is the electric charge, and $\alpha (\simeq 1/137)$ is the fine-structure constant. The smallness of the Fermi velocity makes the Coulomb interactions effectively strong. In the following, we consider the case with $\beta \ll 1$ i.e., the case with small dielectric constant.

## 4.2 Strong Coupling Expansion

Let us analyze the system from the strong coupling limit ($\beta = 0$). We derive the effective action which is defined by carrying out the integration with respect to the gauge field variables $U_{n,0}$:

$$Z = \int \mathcal{D}[\psi, \bar{\psi}, U_0] e^{-S} = \int \mathcal{D}[\psi, \bar{\psi}] e^{-S_{\text{eff}}}. \tag{4.10}$$

In the strong coupling limit, $U_{n,0}$ is contained only in $S_F^{(\tau)}$. Then the integral $\int \mathcal{D}U_0 e^{-S_F^{(\tau)}}$ is evaluated as

$$
\begin{aligned}
\int \mathcal{D}U_0 e^{-S_F^{(\tau)}} &= \prod_n \int_{-\pi}^{\pi} \frac{d\theta_n}{2\pi} \exp\left[ \bar{\psi}_n P_0^- U_{n,0} \psi_{n+\hat{0}} + \bar{\psi}_{n+\hat{0}} P_0^+ U_{n,0}^\dagger \psi_n \right] \\
&= \prod_n \left[ 1 + \bar{\psi}_n P_0^- \psi_{n+\hat{0}} \bar{\psi}_{n+\hat{0}} P_0^+ \psi_n + \cdots \right] \\
&\approx e^{\sum_n \bar{\psi}_n P_0^- \psi_{n+\hat{0}} \bar{\psi}_{n+\hat{0}} P_0^+ \psi_n},
\end{aligned}
\tag{4.11}
$$

where we have used the property of the Grassmann variables $\psi_\alpha$ and $\bar{\psi}_\alpha$, $\psi_\alpha^2 = \bar{\psi}_\alpha^2 = 0$ with $\alpha$ denoting the component of the spinors. In the second line, we have neglected the terms which consist of 8, 12, and 16 different Grassmann variables. The contributions of those terms appear in higher orders of the order parameters, and thus the results will not be changed qualitatively even if those terms are taken into account. We can rewrite the exponent as

$$\bar{\psi}_{n,\alpha} (P_0^-)_{\alpha\beta} \psi_{n+\hat{0},\beta} \bar{\psi}_{n+\hat{0},\gamma} (P_0^+)_{\gamma\delta} \psi_{n,\delta} = -\text{tr}\left[ N_n P_0^+ N_{n+\hat{0}} P_0^- \right], \tag{4.12}$$

where we have defined $(N_n)_{\alpha\beta} = \bar{\psi}_{n,\alpha} \psi_{n,\beta}$ and used $(P_0^\pm)_{\alpha\beta} = (P_0^\pm)_{\beta\alpha}$. The subscripts $\alpha$ and $\beta$ denote the component of the spinors. In general, we can perform the integration with respect to the SU($N$) gauge field variables $U$ in Eq. (4.10) by using the SU($N$) group integral formulas: $\int dU 1 = 1$, $\int dU U_{ab} = 0$, $\int dU U_{ab} U_{cd}^\dagger = \delta_{ad}\delta_{bc}/N$, and so on. We obtain the effective action in the strong coupling limit given by

$$
\begin{aligned}
S_{\text{eff}} = &- \sum_{n,j} \left[ \bar{\psi}_n P_j^- \psi_{n+\hat{j}} + \bar{\psi}_{n+\hat{j}} P_j^+ \psi_n \right] + (m_0 + 3r + r_\tau) \sum_n \bar{\psi}_n \psi_n + b \sum_n \bar{\psi}_n \gamma_0 \Sigma_3 \psi_n \\
&+ \sum_n \text{tr}\left[ N_n P_0^+ N_{n+\hat{0}} P_0^- \right].
\end{aligned}
\tag{4.13}
$$

From this equation, we see that the electron-electron interactions in the strong coupling limit are spatially on-site interactions but not in (imaginary) time. As we shall see below, the competition between this effective on-site interactions and the exchange interactions occurs.

## 4.3 Possible Instabilities and the Free Energies in the Strong Coupling Limit

As mentioned in Chap. 2, the lattice-gauge-theoretical description of $1/r$ Coulomb interactions does not contain the on-site interactions. Unphysical states due to the absence of on-site interactions, such as phase separation, are eliminated by assuming uniform mean-field ground states. This assumption is also supported by the fact that lattice quantum electrodynamics (QED) is a well-defined (renormalizable) theory.

We apply the extended Hubbard-Stratonovich transformation to derive the free energy. Introducing the two complex auxiliary fields $Q$ and $Q'$ (these are matrices), $e^{\kappa \text{tr} AB}$ with $\kappa > 0$ and $A$, $B$ being matrices is deformed as follows (see Subsect. 3.3.1):

$$e^{\kappa \text{tr} AB} = (\text{const.}) \times \int \mathcal{D}[Q, Q'] \exp\left\{-\kappa \left[Q_{\alpha\beta} Q'_{\alpha\beta} - A_{\alpha\beta} Q_{\beta\alpha} - B^T_{\alpha\beta} Q'_{\beta\alpha}\right]\right\}, \qquad (4.14)$$

where the superscript $T$ denotes the transpose of a matrix. This integral is approximated by the saddle point values $Q_{\alpha\beta} = \langle B^T \rangle_{\beta\alpha}$ and $Q'_{\alpha\beta} = \langle A \rangle_{\beta\alpha}$.

We set $(\kappa, A, B) = (1, N_n P_0^+, -N_{n+\hat{0}} P_0^-)$ to decouple the interaction term (the second term) in Eq. (4.13) to fermion bilinear form. In this process, we assume the matrix form of $\langle N_n \rangle$ with the mean-field approximation. Let us recall that, in the formalism of the quantum electrodynamics, the form is restricted to the sum of independent 16 matrices which are consist of the $4 \times 4$ gamma matrices. The 16 matrices are given as follows: (i) scalar $\mathbf{1}$, (ii) vector $\gamma_\mu$ ($\mu = 0, 1, 2, 3$), (iii) tensor $\sigma_{\mu\nu} = \frac{i}{2}[\gamma_\mu, \gamma_\nu]$, (iv) pseudovector $\gamma_\mu \gamma_5$, (v) pseudoscalar $\gamma_5$, where these terminology comes from how the terms are transformed under the Lorentz transformation.

### 4.3.1 Fermion Bilinears and Instabilities

Here we give the explicit expression of the possible instabilities. As shown later, the interaction term in the effective action (4.13) is written like $\bar{\psi}_n \langle N_n \rangle \psi_n$ after the Hubbard-Stratonovich transformation. Then, to be specific and for simplicity, let us consider the Hamiltonian of a continuum model

$$\mathcal{H}(\mathbf{k}) = \mathcal{H}_0(\mathbf{k}) + \gamma_0 \langle N_n \rangle \qquad (4.15)$$

with $\mathcal{H}_0(\mathbf{k}) = k_j \alpha_j + m_0 \alpha_4 + b \Sigma_3$ [Eq. (4.1)]. Note that the following terminology of the instabilities is not for $\gamma_0 \langle N_n \rangle$, but for $\langle N_n \rangle$.

• *Scalar component:* $\gamma_0 \langle N_n \rangle = \sigma \alpha_4$. Here we have used the fact that $\gamma_0 = \alpha_4$. In this case, it is found that the bare mass $m_0$ is renormalized to be $m_0 + \sigma$.

• *Vector component:* $\gamma_0 \langle N_n \rangle = p_\mu \alpha_\mu$ ($\alpha_0 \equiv \mathbf{1}$). Here we have used the fact that $\gamma_0 \gamma_j = \alpha_j$ and $\gamma_0^2 = \mathbf{1}$. In this case, it is found that the wave vectors $k_j$ are shifted to be $k_j + p_j$, and that the energy level is shifted by $p_0$.

• *Tensor component:* $\gamma_0 \langle N_n \rangle = \frac{i}{2} c_{\mu\nu} \gamma_0 [\gamma_\mu, \gamma_\nu]$. The six matrices $\gamma_0 \langle N_n \rangle$ are given explicitly by the Dirac representation as

$$\Sigma'_j \equiv \begin{bmatrix} \sigma_j & 0 \\ 0 & -\sigma_j \end{bmatrix}, \qquad \Pi_j \equiv i \begin{bmatrix} 0 & \sigma_j \\ -\sigma_j & 0 \end{bmatrix}. \qquad (4.16)$$

• *Pseudovector component:* $\gamma_0 \langle N_n \rangle = d_\mu \gamma_0 \gamma_\mu \gamma_5$. The four matrices $\gamma_0 \langle N_n \rangle$ are given explicitly by the Dirac representation as

$$\Sigma_j \equiv \begin{bmatrix} \sigma_j & 0 \\ 0 & \sigma_j \end{bmatrix}, \qquad \Pi_0 \equiv \begin{bmatrix} 0 & 1 \\ 1 & 0 \end{bmatrix}. \qquad (4.17)$$

• *Pseudoscalar component:* $\gamma_0 \langle N_n \rangle = \Delta \alpha_5$. The matrix $\alpha_5 (\equiv -i\gamma_0 \gamma_5)$ is given explicitly by the Dirac representation as $\alpha_5 = \tau_2 \otimes \mathbf{1}$, and this anticommutes with the other four alpha matrices, i.e. the Clifford algebra $\{\alpha_\mu, \alpha_\nu\} = 2\delta_{\mu\nu}$ is satisfied.

Table 4.1: Transformation properties under time-reversal $\mathcal{T}$ and spatial inversion (parity) $\mathcal{P}$ of 16 independent matrices consisting of $\alpha_\mu$ with $\{\alpha_\mu, \alpha_\nu\} = 2\delta_{\mu\nu}\mathbf{1}$ ($\mu, \nu = 1, 2, 3, 4, 5$).

| Matrices | $\mathbf{1}$ | $\alpha_j$ | $\alpha_4$ | $\alpha_5$ | $\Sigma_j$ | $\Sigma'_j$ | $\Pi_j$ | $\Pi_0$ |
|---|---|---|---|---|---|---|---|---|
| Time-reversal $\mathcal{T}$ | $+$ | $-$ | $+$ | $-$ | $-$ | $-$ | $+$ | $+$ |
| Inversion $\mathcal{P}$ | $+$ | $-$ | $+$ | $-$ | $+$ | $+$ | $-$ | $-$ |

Let us look at the properties of the matrices $\Sigma_j$, $\Sigma'_j$, $\Pi_\mu$, and $\alpha_5$. In the Dirac representation, the time-reversal operator $\mathcal{T}$ and the parity (spatial inversion) operator $\mathcal{P}$ are given by $\mathcal{T} = \mathbf{1} \otimes (-i\sigma_2)\mathcal{K}$ and $\mathcal{P} = \sigma_3 \otimes \mathbf{1}$, where $\mathcal{K}$ is the complex conjugation operator. It is easily shown that $\Sigma_j$ and $\Sigma'_j$ are odd under time-reversal but even under parity:

$$\mathcal{T}\Sigma_j\mathcal{T}^{-1} = \mathcal{T}\Sigma'_j\mathcal{T}^{-1} = -1, \qquad \mathcal{P}\Sigma_j\mathcal{P}^{-1} = \mathcal{P}\Sigma'_j\mathcal{P}^{-1} = +1. \tag{4.18}$$

On the other hand, $\Pi_\mu$ are even under time-reversal but odd under parity:

$$\mathcal{T}\Pi_\mu\mathcal{T}^{-1} = +1, \qquad \mathcal{P}\Pi_\mu\mathcal{P}^{-1} = -1. \tag{4.19}$$

$\alpha_5$ is odd under both time-reversal and parity:

$$\mathcal{T}\alpha_5\mathcal{T}^{-1} = -1, \qquad \mathcal{P}\alpha_5\mathcal{P}^{-1} = -1. \tag{4.20}$$

The properties of the 16 matrices are summarized in Table 4.1. In our model, the spinor is written in the basis of $\psi_{\boldsymbol{k}}^\dagger = [c_{\boldsymbol{k}+\uparrow}^\dagger, c_{\boldsymbol{k}+\downarrow}^\dagger, c_{\boldsymbol{k}-\uparrow}^\dagger, c_{\boldsymbol{k}-\downarrow}^\dagger]$ where $+, -$ denote the two orbitals and $\uparrow$ ($\downarrow$) denotes up(down)-spin. Then we see that $\Sigma_j$ represents the ferromagnetism, and that $\Sigma'_j$ represents a kind of the "antiferromagnetism". As for $\Pi_\mu$ and $\alpha_5$, the physical interpretation is somewhat difficult. We see that $\Pi_0$ and $\alpha_5$ represent spin-independent orbital-ordered states, and $\Pi_j$ represents a spin-dependent orbital-ordered state.

To study the stability of the Weyl semimetals, let us consider which matrices we should take into account among these 16 matrices as a mean-field ansatz for $\langle N_n \rangle$. First of all, the mass renormalization, i.e. the identity matrix $\mathbf{1}$ term must be considered. The $\gamma_\mu$ terms, which result in the momentum and energy level shifts, could be dropped. In addition, note that the non-interacting Hamiltonian (4.4) contains the $\Sigma_3$ term. This indicates that the $\gamma_0\Sigma_j$ and $\gamma_0\Sigma'_j$ terms can also be dropped. Furthermore, it is known that these terms can generate other Weyl semimetal phases rather than open band gaps [34]. On the other hand, the $\gamma_0\Pi_\mu$ and $i\gamma_5$ terms can break the Weyl semimetal phase and open band gaps. In the following, we take into account the $\mathbf{1}$, $\gamma_0\Pi_\mu$, and $i\gamma_5$ terms as the matrix form of $\langle N_n \rangle$.

## 4.3.2 The $\alpha_5$ Instability

In this case, we assume that $\langle N_n \rangle = -\sigma\mathbf{1} + \Delta i\gamma_5$. The interaction term is decoupled according to Eq. (4.14). Setting $(\kappa, A, B) = (1, N_n P_0^+, -N_{n+\hat{0}}P_0^-)$, we obtain

$$\begin{aligned}
Q_{\alpha\beta}Q'_{\alpha\beta} = \mathrm{tr}[\langle A \rangle \langle B \rangle] &= -\mathrm{tr}\left[\langle N_n \rangle P_0^+ \langle N_{n+\hat{0}} \rangle P_0^-\right] \\
&= -\frac{1}{4}\mathrm{tr}\left[(\sigma - i\Delta\gamma_5)(r_\tau + \gamma_0)(\sigma - i\Delta\gamma_5)(r_\tau - \gamma_0)\right] \\
&= -\frac{1}{4}\mathrm{tr}\left[(r_\tau^2 - 1)\sigma^2 + 2i\gamma_5 r_\tau^2 \sigma\Delta - (1 + r_\tau^2)\Delta^2\right] \\
&= (1 - r_\tau^2)\sigma^2 + (1 + r_\tau^2)\Delta^2,
\end{aligned} \tag{4.21}$$

64

$$\begin{aligned}
A_{\alpha\beta}Q_{\beta\alpha} &= \text{tr}[A\langle B\rangle] = -\text{tr}\left[N_n P_0^+ \langle N_{n+\hat{0}}\rangle P_0^-\right] \\
&= \frac{1}{4}\text{tr}\left[N_n(r_\tau + \gamma_0)(\sigma - i\Delta\gamma_5)(r_\tau - \gamma_0)\right] \\
&= \frac{1}{4}\text{tr}\left\{N_n[(r_\tau^2 - 1)\sigma - (r_\tau^2 + 1)i\gamma_5\Delta - 2i\gamma_0\gamma_5 r_\tau\Delta]\right\} \\
&= \frac{1}{4}\left[(r_\tau^2 - 1)\sigma\bar{\psi}_n\psi_n - (r_\tau^2 + 1)\Delta\bar{\psi}_n i\gamma_5^T\psi_n - 2r_\tau\Delta\bar{\psi}_n i(\gamma_0\gamma_5)^T\psi_n\right],
\end{aligned}$$
(4.22)

$$\begin{aligned}
B_{\alpha\beta}^T Q'_{\beta\alpha} &= \text{tr}[B\langle A\rangle] = -\sigma\text{tr}\left[N_{n+0}P_0^-(\sigma - i\Delta\gamma_5)P_0^+\right] \\
&= \frac{1}{4}\text{tr}\left[N_n(r_\tau - \gamma_0)(\sigma - i\Delta\gamma_5)(r_\tau + \gamma_0)\right] \\
&= \frac{1}{4}\text{tr}\left\{N_n[(r_\tau^2 - 1)\sigma - (r_\tau^2 + 1)i\gamma_5\Delta + 2i\gamma_0\gamma_5 r_\tau\Delta]\right\} \\
&= \frac{1}{4}\left[(r_\tau^2 - 1)\sigma\bar{\psi}_n\psi_n - (r_\tau^2 + 1)\Delta\bar{\psi}_n i\gamma_5^T\psi_n + 2r_\tau\Delta\bar{\psi}_n i(\gamma_0\gamma_5)^T\psi_n\right],
\end{aligned}$$
(4.23)

where we have used $\gamma_0^2 = 1$ and $\text{tr}\gamma_5 = 0$. Substituting Eqs. (4.21), (4.22) and (4.23) into Eq. (4.14), we obtain

$$e^{-\sum_n \text{tr}\left[N_n P_0^+ N_{n+\hat{0}} P_0^-\right]} \sim \exp\left\{-\sum_n\left[(1 - r_\tau^2)\sigma^2 + (1 + r_\tau^2)\Delta^2 + \bar{\psi}_n\Gamma\psi_n\right]\right\},$$
(4.24)

where $\Gamma = \frac{1}{2}\left[(1 - r_\tau^2)\sigma + i\gamma_5^T(1 + r_\tau^2)\Delta\right]$. We are now in a position to derive the free energy at zero temperature in the strong coupling limit. Combining Eqs. (4.13) and (4.24), the effective action expressed by the auxiliary fields $\sigma$ and $\Delta$ is given by

$$S_{\text{eff}}(\sigma, \Delta) = \frac{V}{T}\left[(1 - r_\tau^2)\sigma^2 + (1 + r_\tau^2)\Delta^2\right] + \sum_k \bar{\psi}_k \mathcal{M}(k; \sigma, \Delta)\psi_k,$$
(4.25)

where the matrix $\mathcal{M}$ is given explicitly as

$$\mathcal{M} = \begin{bmatrix} \tilde{m}(k) + r_\tau + b\sigma_3 & \sigma_j \sin k_j + i\tilde{\Delta} \\ -\sigma_j \sin k_j + i\tilde{\Delta} & \tilde{m}(k) + r_\tau - b\sigma_3 \end{bmatrix} \equiv \begin{bmatrix} A & B \\ C & D \end{bmatrix}.$$
(4.26)

Here $\tilde{\Delta} = \frac{1}{2}(1 + r_\tau^2)\Delta$, $V$ and $T$ are the volume and temperature of the system, respectively, and we have done the Fourier transform from $n = (n_0, \boldsymbol{n})$ to $k = (k_0, \boldsymbol{k})$. The term $\tilde{m}(\boldsymbol{k})$ is given by

$$\tilde{m}(\boldsymbol{k}) = m_0 + \frac{1}{2}(1 - r_\tau^2)\sigma + r\sum_j(1 - \cos k_j).$$
(4.27)

This term is understood as a term to which $m(\boldsymbol{k})$ in the non-interacting Hamiltonian (4.4) changes in the strong coupling limit. $r_\tau$ in $A$ and $D$ of Eq. (4.26) comes from the timelike Wilson term of the original action. From the effective action, we derive the free energy at zero temperature per unit of spacetime volume, according to the usual formula $\mathcal{F} = -\frac{T}{V}\ln Z$. The partition function $Z$ is calculated by the Grassmann integral formula $Z = \int D[\psi, \bar{\psi}]e^{-\bar{\psi}\mathcal{M}\psi} = \det\mathcal{M}$ and the determinant of $\mathcal{M}$ is calculated by the formula $\det\mathcal{M} = \det A \cdot \det\left(D - CA^{-1}B\right)$. After a straightforward calculation, finally we arrive at the free energy in the strong coupling limit:

$$\begin{aligned}
\mathcal{F}(\sigma, \Delta) = &(1 - r_\tau^2)\sigma^2 + (1 + r_\tau^2)\Delta^2 \\
&- \int_{-\pi}^{\pi}\frac{d^3k}{(2\pi)^3}\ln\left\{\left[s^2(\boldsymbol{k}) + [\tilde{m}(\boldsymbol{k}) + r_\tau]^2 + \tilde{\Delta}^2 - b^2\right]^2 + 4b^2 s_\perp^2(\boldsymbol{k})\right\},
\end{aligned}$$
(4.28)

where $s^2(\boldsymbol{k}) = \sum_{j=1}^{3} \sin^2 k_j$, and $s_\perp^2(\boldsymbol{k}) = \sum_{l=1}^{2} \sin^2 k_l$. The ground state is determined by the stationary condition $\partial \mathcal{F}(\sigma, \Delta)/\partial \sigma = \partial \mathcal{F}(\sigma, \Delta)/\partial \Delta = 0$.

Note that the free energy at $b = 0$ corresponds to that of the Wilson fermions with $1/r$ Coulomb interactions in the strong coupling limit [Eq. (3.43)]. When $r_\tau > 1$, the free energy doesn't have the stationary point, because both the first and third term decrease the value of $\mathcal{F}(\sigma, \Delta)$ with increasing $\sigma$. This phenomenon is known as the reflection positivity of the lattice gauge theories with Wilson fermions [127]. Although the timelike Wilson term (the term proportional to $r_\tau$) is artificial in the physics of a Weyl semimetal presented here, we cannot avoid this problem as far as we use the Wilson fermion formalism.

### 4.3.3 The $\Pi_0$ Instability

In this case, we assume that $\langle N_n \rangle = -\sigma \mathbf{1} + \rho_0 \gamma_0 \Pi_0$. The procedure for the derivation of the free energy is the same as the case of $i\gamma_5$. The mean-field decoupling of the interaction term is done to be

$$e^{-\sum_n \mathrm{tr}\left[N_n P_0^+ N_{n+\hat{0}} P_0^-\right]} \sim \exp\left\{-\sum_n \left[(1 - r_\tau^2)\sigma^2 + (1 + r_\tau^2)\rho_0^2 + \bar{\psi}_n \Gamma \psi_n\right]\right\}, \qquad (4.29)$$

where $\Gamma = \frac{1}{2}\left[(1 - r_\tau^2)\sigma + (\gamma_0 \Pi_0)^T (1 + r_\tau^2)\rho_0\right]$. Combining Eqs. (4.13) and (4.29), the effective action expressed by the auxiliary fields $\sigma$ and $\rho_0$ is given by

$$S_{\mathrm{eff}}(\sigma, \rho_0) = \frac{V}{T}\left[(1 - r_\tau^2)\sigma^2 + (1 + r_\tau^2)\rho_0^2\right] + \sum_k \bar{\psi}_k \mathcal{M}(\boldsymbol{k}; \sigma, \rho_0)\psi_k, \qquad (4.30)$$

where the matrix $\mathcal{M}$ is given explicitly as

$$\mathcal{M} = \begin{bmatrix} \tilde{m}(\boldsymbol{k}) + r_\tau + b\sigma_3 & \sigma_j \sin k_j - \tilde{\rho}_0 \\ -\sigma_j \sin k_j + \tilde{\rho}_0 & \tilde{m}(\boldsymbol{k}) + r_\tau - b\sigma_3 \end{bmatrix} \qquad (4.31)$$

with $\tilde{\rho}_0 = \frac{1}{2}(1 + r_\tau^2)\rho_0$. By calculating the determinant of $\mathcal{M}$, the free energy is obtained as

$$\mathcal{F}(\sigma, \rho_0) = (1 - r_\tau^2)\sigma^2 + (1 + r_\tau^2)\rho_0^2 - \int_{-\pi}^{\pi} \frac{d^3 k}{(2\pi)^3} \ln\left\{\frac{G(\boldsymbol{k}, b, \tilde{\rho}_0)G(\boldsymbol{k}, -b, -\tilde{\rho}_0) - H(\boldsymbol{k}, b, \tilde{\rho}_0)}{[\tilde{m}(\boldsymbol{k}) + r_\tau]^2 - b^2}\right\}, \qquad (4.32)$$

where

$$G(\boldsymbol{k}, b, \tilde{\rho}_0) = [\tilde{m}(\boldsymbol{k}) + r_\tau - b]\left\{[\tilde{m}(\boldsymbol{k}) + r_\tau]^2 - b^2 + (\sin k_3 - \tilde{\rho}_0)^2\right\} + s_\perp^2(\boldsymbol{k})[\tilde{m}(\boldsymbol{k}) + r_\tau + b],$$

$$H(\boldsymbol{k}, b, \tilde{\rho}_0) = 4s_\perp^2(\boldsymbol{k})\{\tilde{\rho}_0[\tilde{m}(\boldsymbol{k}) + r_\tau] + b\sin k_3\}^2. \qquad (4.33)$$

The ground state is determined by the stationary condition $\partial \mathcal{F}(\sigma, \rho_0)/\partial \sigma = \partial \mathcal{F}(\sigma, \rho_0)/\partial \rho_0 = 0$.

### 4.3.4 The $\Pi_3$ Instability

In this case, we assume that $\langle N_n \rangle = -\sigma \mathbf{1} + \rho_3 \gamma_0 \Pi_3$. The procedure for the derivation of the free energy is the same as the case of $i\gamma_5$. The mean-field decoupling of the interaction term is done

to be

$$e^{-\sum_n \text{tr}\left[N_n P_0^+ N_{n+\hat{0}} P_0^-\right]} \sim \exp\left\{-\sum_n \left[(1-r_\tau^2)\sigma^2 + (1+r_\tau^2)\rho_3^2 + \bar{\psi}_n \Gamma \psi_n\right]\right\}, \qquad (4.34)$$

where $\Gamma = \frac{1}{2}\left[(1-r_\tau^2)\sigma + (\gamma_0 \Pi_3)^T (1+r_\tau^2)\rho_3\right]$. Combining Eqs. (4.13) and (4.34), the effective action expressed by the auxiliary fields $\sigma$ and $\rho_3$ is given by

$$S_{\text{eff}}(\sigma, \rho_3) = \frac{V}{T}\left[(1-r_\tau^2)\sigma^2 + (1+r_\tau^2)\rho_3^2\right] + \sum_k \bar{\psi}_k \mathcal{M}(k; \sigma, \rho_3)\psi_k, \qquad (4.35)$$

where the matrix $\mathcal{M}$ is given explicitly as

$$\mathcal{M} = \begin{bmatrix} \tilde{m}(k) + r_\tau + b\sigma_3 & \sigma_j \sin k_j + i\tilde{\rho}_3 \sigma_3 \\ -\sigma_j \sin k_j + i\tilde{\rho}_3 \sigma_3 & \tilde{m}(k) + r_\tau - b\sigma_3 \end{bmatrix} \qquad (4.36)$$

with $\tilde{\rho}_3 = \frac{1}{2}(1+r_\tau^2)\rho_3$. By calculating the determinant of $\mathcal{M}$, the free energy is obtained as

$$\mathcal{F}(\sigma, \rho_3) = (1-r_\tau^2)\sigma^2 + (1+r_\tau^2)\rho_3^2 - \int_{-\pi}^{\pi} \frac{d^3 k}{(2\pi)^3} \ln\left\{\left[s^2(k) + [\tilde{m}(k) + r_\tau]^2 - \mu\right]^2 + 4\mu s_\perp^2(k)\right\}, \qquad (4.37)$$

where $\mu = b^2 - \tilde{\rho}_3^2$. The ground state is determined by the stationary condition $\partial \mathcal{F}(\sigma, \rho_3)/\partial\sigma = \partial \mathcal{F}(\sigma, \rho_3)/\partial\rho_3 = 0$.

## 4.3.5 The $\Pi_{1,2}$ Instability

In this case, we assume that $\langle N_n \rangle = -\sigma \mathbb{1} + \rho_1 \gamma_0 \Pi_1$ or $\langle N_n \rangle = -\sigma \mathbb{1} + \rho_2 \gamma_0 \Pi_2$. Since there exists a spin degree of freedom in the $xy$-plane, we show the calculation for $\Pi_1$. The procedure for the derivation of the free energy is the same as the case of $i\gamma_5$. The mean-field decoupling of the interaction term is done to be

$$e^{-\sum_n \text{tr}\left[N_n P_0^+ N_{n+\hat{0}} P_0^-\right]} \sim \exp\left\{-\sum_n \left[(1-r_\tau^2)\sigma^2 + (1+r_\tau^2)\rho_1^2 + \bar{\psi}_n \Gamma \psi_n\right]\right\}, \qquad (4.38)$$

where $\Gamma = \frac{1}{2}\left[(1-r_\tau^2)\sigma + (\gamma_0 \Pi_1)^T (1+r_\tau^2)\rho_1\right]$. Combining Eqs. (4.13) and (4.38), the effective action expressed by the auxiliary fields $\sigma$ and $\rho_0$ is given by

$$S_{\text{eff}}(\sigma, \rho_1) = \frac{V}{T}\left[(1-r_\tau^2)\sigma^2 + (1+r_\tau^2)\rho_1^2\right] + \sum_k \bar{\psi}_k \mathcal{M}(k; \sigma, \rho_1)\psi_k, \qquad (4.39)$$

where the matrix $\mathcal{M}$ is given explicitly as

$$\mathcal{M} = \begin{bmatrix} \tilde{m}(k) + r_\tau + b\sigma_3 & \sigma_j \sin k_j + i\tilde{\rho}_1 \sigma_1 \\ -\sigma_j \sin k_j + i\tilde{\rho}_1 \sigma_1 & \tilde{m}(k) + r_\tau - b\sigma_3 \end{bmatrix} \qquad (4.40)$$

with $\tilde{\rho}_1 = \frac{1}{2}(1+r_\tau^2)\rho_1$. By calculating the determinant of $\mathcal{M}$, the free energy is obtained as

$$\mathcal{F}(\sigma, \rho_1) = (1-r_\tau^2)\sigma^2 + (1+r_\tau^2)\rho_1^2 - \int_{-\pi}^{\pi} \frac{d^3 k}{(2\pi)^3} \ln\left\{\frac{I(k, b, \tilde{\rho}_1)I(k, -b, -\tilde{\rho}_1) - J(k, b, \tilde{\rho}_1)}{[\tilde{m}(k) + r_\tau]^2 - b^2}\right\}, \qquad (4.41)$$
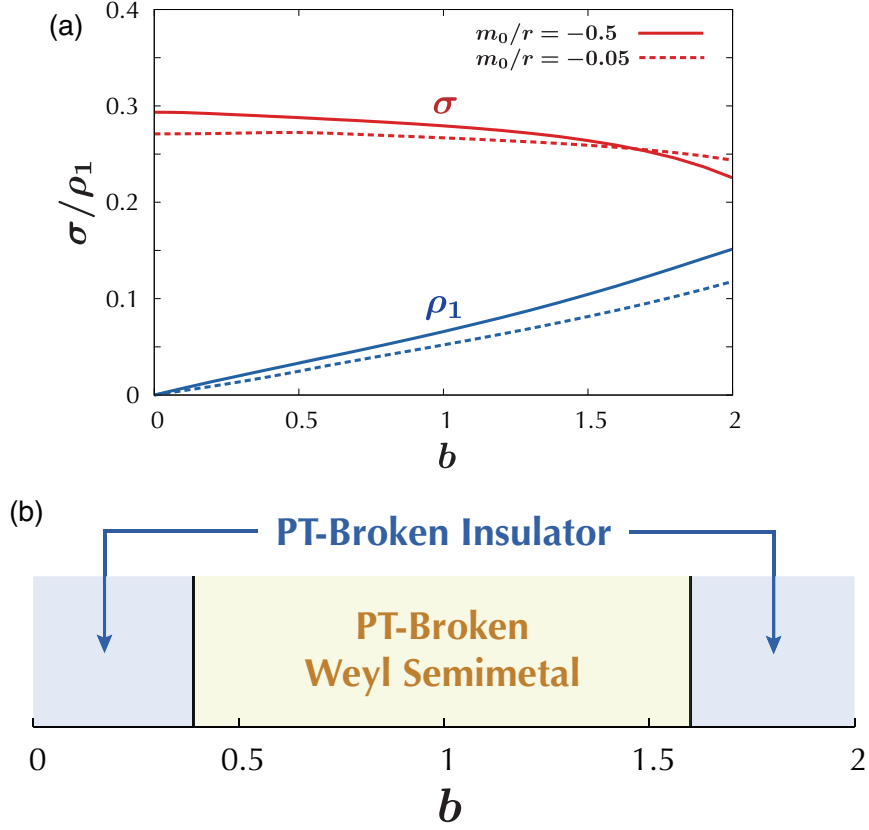
Figure 4.2: (a) $b$ dependences of $\sigma$ and $\rho_1$ with $r_\tau = 0.5$ and $r = 1$. (b) Phase diagram in the strong coupling limit ($\beta = 0$) with $m_0/r = -0.5$, $r_\tau = 0.5$ and $r = 1$. The PT-broken Weyl semimetal represents a Weyl semimetal with broken time-reversal and parity symmetries.

where

$$
\begin{aligned}
I(\boldsymbol{k}, b, \tilde{\rho}_1) &= [\tilde{m}(\boldsymbol{k}) + r_\tau - b] \left\{ [\tilde{m}(\boldsymbol{k}) + r_\tau]^2 + \sin^2 k_3 - b^2 \right\} \\
&\quad + [\tilde{m}(\boldsymbol{k}) + r_\tau + b] \left[ \sin^2 k_1 + (\sin k_2 + \tilde{\rho}_1)^2 \right], \\
J(\boldsymbol{k}, b, \tilde{\rho}_1) &= 4 \sin^2 k_3 \left( \{ \tilde{\rho}_1 [\tilde{m}(\boldsymbol{k}) + r_\tau] + b \sin k_2 \}^2 + b^2 \sin^2 k_1 \right).
\end{aligned}
\tag{4.42}
$$

The ground state is determined by the stationary condition $\partial \mathcal{F}(\sigma, \rho_1)/\partial \sigma = \partial \mathcal{F}(\sigma, \rho_1)/\partial \rho_1 = 0$.

## 4.4 Numerical Results

For any set of $(m_0, b, r, r_\tau)$, it was found that the values of $\Delta$, $\rho_0$ and $\rho_3$ are always zero. It was also found that the values of $\sigma$ and $\rho_1$ (or $\rho_2$) are nonzero. This means that the ground state of the system in the strong coupling limit is the parity and time-reversal symmetries (PT) broken phase signaled by nonzero $\rho_1$, and that the symmetry-broken phases signaled by nonzero $\Delta$, $\rho_0$ or $\rho_3$ do not arise. Note that time-reversal symmetry of the system is originally broken in the non-interacting Weyl semimetal phase.

Throughout this paper, we set $r_\tau = 0.5$ and $r = 1$. The $b$ dependence of $\sigma$ is shown in Fig. 4.2(a). $\sigma$ is a decreasing function of $b$. The term proportional to $\sigma$ gives a correction to the bare

mass $m_0$, i.e., is regarded as a mass renormalization induced by $1/r$ Coulomb interactions, as is seen from Eq. (4.27). Hence we should define the effective mass in the strong coupling limit as $m_{\text{eff}} = m_0 + \frac{1}{2}(1 - r_\tau^2)\sigma$. The renormalization becomes weaker as the time-reversal symmetry breaking perturbation $b$ becomes larger. This is understood as follows: When the exchange coupling between the magnetic impurities and bulk electrons is strong, the bulk electrons prefer the ferromagnetic configuration. Then the effective on-site interactions [the second term in Eq. (4.13)] become weaker and as a result, the renormalization effect becomes weaker.

The $b$ dependence of $\rho_1$ is also shown in Fig. 4.2(a). $\rho_1$ is an increasing function of $b$. It is worthy to note that $\rho_1 = 0$ when $b = 0$. This means that time-reversal and parity symmetries of the system is preserved even in the strong coupling limit. When $b = 0$, we can distinguish by the $Z_2$ invariant whether the system is topologically nontrivial or trivial. Namely, if $0 > m_{\text{eff}}/r > -2$ ($m_{\text{eff}}/r > 0$), then the system is topologically nontrivial (trivial). In the case of $m_0/r = -0.5$, the effective mass is obtained as $m_{\text{eff}}/r \simeq -0.39$. This indicates that the topological insulator phase survives in the strong coupling limit. On the other hand, in the case of $m_0/r = -0.05$, i.e. in the case of small $|m_0|$, the effective mass is obtained as $m_{\text{eff}}/r \simeq 0.05$ and we see that the topological insulator phase changes to the normal insulator phase.

Let us look at the energy spectrum in the presence of the $\rho_1 \Pi_1$ term, when $m_0/r = -0.5$. In this case, the mean-field single-particle Hamiltonian is written as

$$\mathcal{H}(\boldsymbol{k}) = \alpha_j \sin k_j + \tilde{m}(\boldsymbol{k})\alpha_4 + b\Sigma_3 + \rho_1 \Pi_1. \tag{4.43}$$

We can obtain the energy spectrum analytically as

$$E(\boldsymbol{k}) = \pm\sqrt{s^2(\boldsymbol{k}) + [\tilde{m}(\boldsymbol{k})]^2 + b^2 + \rho_1^2 \pm 2\sqrt{[\tilde{m}(\boldsymbol{k})b - \rho_1 \sin k_2]^2 + (b^2 + \rho_1^2)\sin^2 k_3}}, \tag{4.44}$$

where $s^2(\boldsymbol{k}) = \sum_{i=1}^{3} \sin^2 k_i$. By plotting this equation numerically, we find that there exists the region where the spectrum is gapless even when $\rho_1 \neq 0$. In the small $b$ region, there is a finite gap in the spectrum. At $b \simeq 0.39$, the two bands of Eq. (4.44) start to touch at the momentum point $(k_1, k_2, k_3) \simeq (0, 0.005\pi, 0)$. As $b$ is increased, the two Weyl nodes move from the $k_3 = 0$ point toward the $k_3 = \pm\pi$ directions, crossing the $k_3$-axis. The important point is that the two Weyl nodes do not exist at $k_2 = 0$ due to nonzero $\rho_1$. Then at $b \simeq 1.60$, the two Weyl nodes meet at the point $(k_1, k_2, k_3) \simeq (0, -0.022\pi, \pi)$ and the band gap opens. The phase diagram in the strong coupling limit is shown in Fig. 4.2(b). We call the gapped phases the parity and time-reversal symmetries (PT) broken insulator, and call the gapless phase the PT-broken Weyl semimetal. In the PT-broken Weyl semimetal phase, we have confirmed that the $k_2$ dependence of the energy dispersions (4.44) near the band touching points is linear.

## 4.5  Possible Global Phase Diagram

Let us discuss a global phase diagram of a correlated Weyl semimetal. First, we consider the phase diagram in the non-interacting limit ($\beta = \infty$) where the Hamiltonian is given by Eq. (4.4) (see also Fig. 4.1). When $b \neq 0$, time-reversal symmetry is broken and we cannot define the $Z_2$ invariant. In this paper we call the phase with $0 > m_0/r > -2$ the magnetic topological insulator. This is because the phase transition from a topological insulator phase to another phase generally requires the gap closing. Further, 3D topological insulator phases are characterized by the theta term with $\theta = \pi$. A recent study shows that the value of $\theta$ remains $\pi$ even in the presence of the
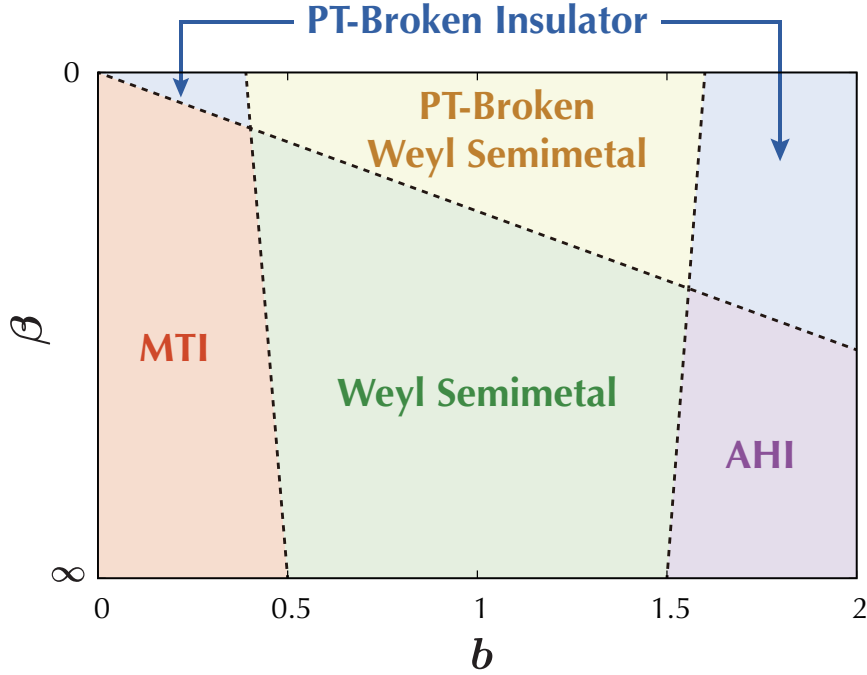
Figure 4.3: A possible global phase diagram of a correlated Weyl semimetal with $m_0/r = -0.5$, $r_\tau = 0.5$ and $r = 1$. The phase boundary between the magnetic topological insulator (MTI) phase and the Weyl semimetal phase is determined by the condition $b = |m_{\text{eff}}|$. The phase boundary between the Weyl semimetal phase and the anomalous Hall insulator (AHI) phase is determined by the condition $b = 2r + m_{\text{eff}}$. The parity and time-reversal symmetries (PT) broken Weyl semimetal phase and the PT-broken insulator phase are signaled by nonzero $\rho_1$( or $\rho_2$). The phase boundaries between these two phases are determined (numerically) by the appearance or disappearance of the Weyl nodes. The $\beta = 0$ ($\beta = \infty$) line represents the strong coupling (non-interacting) limit.

time-reversal symmetry breaking term $b\Sigma_3$ with not large $b$ [132]. Thus as far as the band gap opens, we call this phase the magnetic topological insulator.

As $b$ is increased, the energy bands touch and the two Weyl nodes start to split from the point $k_3 = 0$ toward $k_3 = \pm\pi$ at $b = |m_0|$. Then the Weyl nodes reach $k_3 = \pm\pi$ to annihilate each other and the energy gap opens at $b = 2r + m_0$. These results are obtained from the equation for the appearance of the Weyl semimetal phase, $b^2 = [m_0 + r(1 - \cos k_3)]^2 + \sin^2 k_3$. It is known that the Weyl semimetals have a nonzero Hall conductivity. In the present case where the two Weyl nodes exist, as discussed in Ref. 33 and in Subsect. 1.3.1, the Hall conductivity of the system $\sigma_{xy}^{\text{3D}}$ is proportional to the distance of the two Weyl nodes in the momentum space $\Delta_{\text{W}}$: $\sigma_{xy}^{\text{3D}} = e^2 \Delta_{\text{W}}/(2\pi h)$. Thus in the gapped phase realized with $b > 2r + m_0$, the Hall conductivity reaches $e^2/(ha)$ where $a$ is the lattice constant. We call this phase the anomalous Hall insulator.

In the presence of $1/r$ Coulomb interactions, the mass $m_0$ is renormalized to be $m_{\text{eff}}$. This renormalization effect stabilizes the Weyl semimetal phase, i.e. makes the region of the Weyl semimetal phase larger. When the interactions are strong enough, the order parameter $\rho_1$ (or $\rho_2$) for the PT-broken phase becomes nonzero and, as a result, the Weyl semimetal phase changes to another Weyl semimetal phase with broken parity and time-reversal symmetries. From the numerical values in the strong coupling limit (see the previous section), the phase boundaries

between the PT-broken Weyl semimetal and the PT-broken insulator phases seem to be approximated by $b \simeq |m_{\text{eff}}|$ and $b \simeq 2r + m_{\text{eff}}$. In Chap. 3, it has been shown that the gapped phases (topological and normal insulators) with $b = 0$ are stable in the strong coupling region. Thus in the case of not small $|m_0|$ ($m_0 < 0$), the topological insulator phase would be continuous from the non-interacting limit to the strong coupling limit. On the other hand, in the case of small $|m_0|$, the phase in the strong coupling limit is the normal insulator, although the phase in the non-interacting limit is the topological insulator. In such a case, there would exist the coupling strength at which $m_{\text{eff}}$ becomes zero. By connecting the phase boundaries between the strong coupling region and the weak coupling region, we propose a possible global phase diagram of a correlated Weyl semimetal shown in Fig. 4.3.

Here we would like to mention the relation between the proposed phase diagram and real materials. As possible host materials, 3D topological insulators of $Bi_2Se_3$ family have large dielectric constant ($\epsilon \approx 100$) [120]. From this value, we estimate the strength of $1/r$ Coulomb interactions in $Bi_2Se_3$ family as $\beta \approx 3$. This suggests that the Coulomb interactions in $Bi_2Se_3$-family-based Weyl semimetals are not strong. Therefore it is difficult to predict the behavior of real materials from the present study. However, the following could be mentioned. When the value of $b$ is small, i.e. the exchange interactions with magnetic impurities are weak, parity symmetry of the system will not be broken. On the other hand, when the value of $b$ is large, the PT-broken Weyl semimetal or the PT-broken insulator might be observed. The energy spectra of $Bi_2Se_3$ family have been experimentally observed by angle-resolved photoemission spectroscopy (ARPES). Thus those of $Bi_2Se_3$-family-based Weyl semimetals will be also observed when they are experimentally realized. Theoretically, a Weyl semimetal phase in $Bi_2(Se_xTe_{1-x})_3$ doped with magnetic impurities has been predicted [58]. As mentioned in the previous section, the PT-broken Weyl semimetal phase is characterized by the Weyl nodes located in the points which are deviated from the original location. It is expected that such a locational deviation of Weyl nodes can be observed by ARPES.

## 4.6 Discussions

Let us consider the possible gapped phases in our model. From our numerical results and the discussion in Ref. 34, we see that only the $\alpha_5$ instability can lead to a gapped phase among the five instabilities $\alpha_5$ and $\Pi_\mu$. In the presence of the $\alpha_5$ term, the mean-field Hamiltonian is written as

$$\mathcal{H}(\boldsymbol{k}) = \alpha_j \sin k_j + \tilde{m}(\boldsymbol{k})\alpha_4 + b\Sigma_3 + \Delta\alpha_5, \qquad (4.45)$$

and we can obtain the energy spectrum analytically as

$$E(\boldsymbol{k}) = \pm\sqrt{s_\perp^2(\boldsymbol{k}) + \left[\sqrt{[\tilde{m}(\boldsymbol{k})]^2 + \Delta^2 + \sin^2 k_3} \pm b\right]^2}, \qquad (4.46)$$

where $s_\perp^2(\boldsymbol{k}) = \sum_{i=1}^2 \sin^2 k_i$. In this case, the two Weyl nodes arise on the $k_3$ axis when the conditions $k_1 = k_2 = 0$ and $b^2 > [\tilde{m}(0,0,k_3)]^2 + \Delta^2$ are satisfied. Conversely, the energy gap opens when $\Delta^2 > b^2 - [\tilde{m}(0,0,k_3)]^2$ is satisfied. Actually, such a gapped phase has been obtained in a Weyl semimetal with short-range interactions [89].

Further, we note that the inter-nodal scattering, which can lead to gap openings [42, 92], is contained in the low-energy limit of our model. In the following, we briefly discuss this process

in our model. We express $\psi_k$ in terms of the annihilation operator in the $\lambda$-th band $a_{k\lambda}$ and the eigenfunction of the $\lambda$-th band $|u_{k\lambda}\rangle$ as $\psi_k = \sum_{\lambda=1}^{4} a_{k\lambda}|u_{k\lambda}\rangle$. Here we label the two bands near the Fermi level as $\lambda = 2, 3$. Then we can approximate $\psi_n$ in the low-energy limit as

$$\psi_n \simeq \left( \int_{|\boldsymbol{k}-W_+|<\Lambda} \frac{d^3k}{(2\pi)^3} + \int_{|\boldsymbol{k}-W_-|<\Lambda} \frac{d^3k}{(2\pi)^3} \right) e^{i\boldsymbol{k}\cdot\boldsymbol{r}_n} \sum_{\lambda=2,3} a_{k\lambda}|u_{k\lambda}\rangle$$

$$\equiv e^{iQz}\psi_{R,n} + e^{-iQz}\psi_{L,n}, \tag{4.47}$$

where $\Lambda$ is a momentum cutoff, $W_\pm = (0, 0, \pm Q)$ with $Q = \sqrt{b^2 - [\tilde{m}(0,0,k_3)]^2}$, and $\psi_{R(L),n}$ is the annihilation operator around the Weyl node $W_{+(-)}$. With the use of this expression, the mean-field decoupled interaction term $\bar{\psi}_n\langle N_n\rangle\psi_n$ is written as

$$\begin{aligned}
\bar{\psi}_n\langle N_n\rangle\psi_n \simeq\ &\bar{\psi}_{R,n}\langle\bar{\psi}_{R,n}\psi_{R,n}\rangle\psi_{R,n} + \bar{\psi}_{R,n}\langle\bar{\psi}_{L,n}\psi_{R,n}\rangle\psi_{L,n} \\
&+ \bar{\psi}_{R,n}\langle\bar{\psi}_{L,n}\psi_{L,n}\rangle\psi_{R,n} + \bar{\psi}_{L,n}\langle\bar{\psi}_{R,n}\psi_{R,n}\rangle\psi_{L,n} \\
&+ \bar{\psi}_{L,n}\langle\bar{\psi}_{R,n}\psi_{L,n}\rangle\psi_{R,n} + \bar{\psi}_{L,n}\langle\bar{\psi}_{L,n}\psi_{L,n}\rangle\psi_{L,n},
\end{aligned} \tag{4.48}$$

where we have omitted the oscillating terms. The terms $\bar{\psi}_R\langle\bar{\psi}_L\psi_R\rangle\psi_L$ and $\bar{\psi}_L\langle\bar{\psi}_R\psi_L\rangle\psi_R$ can be a mass term in the low-energy effective model. This can be understood easily by defining $\Psi^\dagger M\Psi \equiv \bar{\psi}_R\langle\bar{\psi}_L\psi_R\rangle\psi_L + \bar{\psi}_L\langle\bar{\psi}_R\psi_L\rangle\psi_R$, where $\Psi \equiv [\psi_R, \psi_L]^T$ is a four-component spinor and $M = \delta\sigma_x$ with $\delta = \langle\bar{\psi}_L\psi_R\rangle = \langle\bar{\psi}_R\psi_L\rangle$. If the mass term is induced by interactions in the low-energy effective model, then the energy gap opens and the Weyl semimetal phase is broken. Therefore, note that the effects which can lead to the gapped phase are taken into account in our calculation of a bulk model for a correlated Weyl semimetal. However, our result suggests the existence of the gapless phase, the PT-broken Weyl semimetal phase in the strong coupling limit.

Finally, we mention the difference between the Weyl semimetal and the graphene. In graphene, there are also gapless linear dispersions which can be described by the Weyl Hamiltonian around two inequivalent momentum points. It is known that parity symmetry breaking in graphene leads to a gap opening [112, 133, 134]. However, in the case of the Weyl semimetal, the system can remain gapless even when parity symmetry is (spontaneously) broken. This results from the topological nature of the Weyl semimetal, namely that a gap opens only when the Weyl nodes with opposite chirality meet and annihilate each other.

## 4.7 Summary

To summarize, based on the U(1) lattice gauge theory, we have studied the effects of strong $1/r$ long-range Coulomb interactions in a Weyl semimetal with broken time-reversal symmetry. We have considered all the possible 16 instabilities within the mean-field approximation. It was shown that parity symmetry of the system is spontaneously broken but the Weyl semimetal phase, which is different from the non-interacting phase, survives in the strong coupling limit. We have presented a possible global phase diagram of a correlated Weyl semimetal. From the proposed global phase diagram, it is expected that the Weyl semimetal phase is stabilized by $1/r$ long-range Coulomb interactions. In this study, the number of the Weyl nodes is two. It would be interesting to study the correlation effects in Weyl semimetals with more than two nodes.

# Chapter 5

# Dirac Semimetals with Strong Long-Range Correlations

In this chapter, we study the stability of Dirac semimetals with $N$ nodes in three spatial dimensions against strong $1/r$ long-range Coulomb interactions. We particularly study the cases of $N = 4$ and $N = 16$, where the $N = 4$ Dirac semimetal is described by the staggered fermions and the $N = 16$ Dirac semimetal is described by the doubled lattice fermions. We take into account the $1/r$ long-range Coulomb interactions between the bulk electrons. Based on the U(1) lattice gauge theory, we analyze the system from the strong coupling limit. It is shown that the Dirac semimetals survive in the strong coupling limit when the out-of-plane Fermi velocity anisotropy of the Dirac cones is weak, whereas they change to insulators when the anisotropy is strong. A Possible global phase diagram of correlated multinode Dirac semimetals is presented. Implications of our result to the stability of Weyl semimetals and three-dimensional topological insulators are discussed. The contents in this chapter have been published in:
A. Sekine and K. Nomura, Phys. Rev. B **90**, 075137-1-7 (2014).

## 5.1  Theoretical Models

In this section, we introduce two lattice models for Dirac semimetals with $1/r$ Coulomb interactions. The motivations for considering the effects of $1/r$ Coulomb interactions are as follows. The first is that Dirac semimetals can lead to various topologica phases such as topological insulators and Weyl semimetals, as shown in Sect. 1.4. Therefore, to study the effects of long-range interactions in Dirac semimetals will supplement the results in Chap. 3 and Chap. 4. The second is that the effects of long-range interactions are expected to be important in Dirac fermion systems, since the screening effect is considered to be weak due to the vanishing density of states near the Fermi level.

### 5.1.1  Effective Continuum Model

Let us start from the effective continuum model for correlated $N$-node Dirac semimetals. Experimentally observed Dirac semimetals such as $Na_3Bi$ and $Cd_3As_2$ have two Dirac nodes [51–55]. The model we consider is the (3+1)D four-component massless Dirac fermions of $N$ flavors interacting with the electromagnetic [U(1) gauge] field. Compared to the usual quantum electrodynamics, our model is characterized by the Fermi velocity of Dirac fermions $v_F$ which is much

smaller than the speed of light $c$. Due to this nature, the interactions via the vector potential (spatial components of the electromagnetic field) is suppressed by the factor $v_F/c \sim 10^{-3}$. Then the Euclidean action of the system can be written as

$$S = \int d^4x \sum_{f=1}^{N} \bar{\psi}_f(x) \left[ \gamma_0(\partial_0 + iA_0) + \xi_j \gamma_j \partial_j \right] \psi_f(x) + \frac{\beta}{2} \int d^4x (\partial_i A_0)^2, \tag{5.1}$$

where $\psi_f(x)$ is a four-component spinor with $f$ denoting the flavor of Dirac fermions, $\gamma_\mu$ ($\mu = 0, 1, 2, 3$) are the $4 \times 4$ gamma matrices which satisfy the Clifford algebra $\{\gamma_\mu, \gamma_\nu\} = 2\delta_{\mu\nu}$, and $A_0$ is the scalar potential. Here we have introduced parameters for the Fermi velocity anisotropy $\xi_j$ with $\xi_1 = \xi_2 = 1$ and $\xi_3 = v_{F\perp}/v_{F\parallel}$. This is because there exist large out-of-plane Fermi velocity anisotropy in experimentally observed Dirac semimetals such that $v_{F\perp}/v_{F\parallel} \approx 0.25$ in Na$_3$Bi [51] and $v_{F\perp}/v_{F\parallel} \sim 0.1$ in Cd$_3$As$_2$ [52]. Note that we have rescaled variables as $v_{F\parallel}x_0 \to x_0$, $A_0/v_{F\parallel} \to A_0$ in Eq. (5.1). A parameter $\beta$, which represents the effective strength of the $1/r$ Coulomb interactions, is given by

$$\beta = \frac{v_{F\parallel}\epsilon}{e^2} = \frac{v_{F\parallel}\epsilon}{4\pi c\alpha}, \tag{5.2}$$

where $e$ is the electric charge, $\epsilon$ is the dielectric constant of the system, and $\alpha (\simeq 1/137)$ is the fine-structure constant. The smallness of the Fermi velocity makes the Coulomb interactions effectively strong. $\beta = 0$ corresponds to the strong coupling limit. In this study we consider the case of $\beta \ll 1$, i.e. the case of small dielectric constant.

In the following, we introduce two specific effective lattice models for $N$-node Dirac semimetals with $N = 4$ and $N = 16$. We take advantage of the so-called "fermion doubling problem" which occurs when considering Dirac fermions on lattices. It is known that the fermion doublers can emerge in the cases where lattice fermions possess chiral symmetry, which has been proved by the Nielsen-Ninomiya theorem [114].

## 5.1.2 The $N = 16$ Dirac Semimetal

First we consider a (3+1)D $N = 16$ Dirac semimetal interacting via $1/r$ Coulomb interactions on a lattice. As the noninteracting action, we adopt the doubled lattice fermions (in the chiral limit) which reproduce the four-component massless Dirac fermions of 16 flavors in the continuum limit [95] (see Subsect. 2.3.1). The Euclidean action of the system is given by $S^{(N=16)} = S_F^{(N=16)} + S_G$. The fermionic part $S_F^{(N=16)}$ is written as

$$S_F^{(N=16)} = \frac{1}{2} \sum_n \left[ \bar{\psi}_n \gamma_0 U_{n,0} \psi_{n+\hat{0}} - \bar{\psi}_{n+\hat{0}} \gamma_0 U_{n,0}^\dagger \psi_n \right] + \frac{1}{2} \sum_{n,j} \xi_j \left[ \bar{\psi}_n \gamma_j \psi_{n+\hat{j}} - \bar{\psi}_{n+\hat{j}} \gamma_j \psi_n \right], \tag{5.3}$$

where $\psi_n$ is a four-component spinor. This action is understood as the naively discretized action of the four-component Dirac fermions of single flavor. The U(1) gauge part $S_G$ is written as

$$S_G = \beta \sum_n \sum_{\mu > \nu} \left[ 1 - \frac{1}{2} \left( U_{n,\mu} U_{n+\hat{\mu},\nu} U_{n+\hat{\nu},\mu}^\dagger U_{n,\nu}^\dagger + \text{H.c.} \right) \right]. \tag{5.4}$$

Here $\hat{\mu}$ ($\mu = 0, 1, 2, 3$) denotes the unit vector along the $\mu$ direction, and $n = (n_0, n_1, n_2, n_3)$ is a lattice site on a four-dimensional isotropic lattice. The U(1) gauge link variables $U_{n,\mu}$ are given by $U_{n,0} = e^{iA_0(n)} \equiv e^{i\theta_n}$ ($-\pi \le \theta_n \le \pi$) and $U_{n,j} = 1$.

### 5.1.3 The $N = 4$ Dirac Semimetal

Next we consider a (3+1)D $N = 4$ Dirac semimetal interacting via $1/r$ Coulomb interactions on a lattice. As the noninteracting action, we adopt the staggered fermions (in the chiral limit) which reproduce the four-component massless Dirac fermions of 4 flavors in the continuum limit [115, 116] (see Subsect. 2.3.3). The Euclidean action of the system is given by $S^{(N=4)} = S_F^{(N=4)} + S_G$. The fermionic part $S_F^{(N=4)}$ is written as

$$S_F^{(N=4)} = \frac{1}{2} \sum_n \eta_{n,0} \left[ \bar{\chi}_n U_{n,0} \chi_{n+\hat{0}} - \bar{\chi}_{n+\hat{0}} U_{n,0}^\dagger \chi_n \right] + \frac{1}{2} \sum_{n,j} \xi_j \eta_{n,j} \left[ \bar{\chi}_n \chi_{n+\hat{j}} - \bar{\chi}_{n+\hat{j}} \chi_n \right], \quad (5.5)$$

where $\chi_n$ is a single-component spinor, $\eta_{n,0} = 1$, $\eta_{n,1} = (-1)^{n_0}$, $\eta_{n,2} = (-1)^{n_0+n_1}$, and $\eta_{n,3} = (-1)^{n_0+n_1+n_2}$. The gauge part $S_G$ is the same as Eq. (5.4). The action (5.5) can be understood as an action obtained by doing the spin diagonalization (the Kawamoto-Smit transformation) [121] to $\psi_n$ in the action (5.3) as

$$\psi_n = T_n \xi_n, \qquad \bar{\psi}_n = \bar{\xi}_n T_n^\dagger \qquad (5.6)$$

with $T_n = (\gamma_0)^{n_0}(\gamma_1)^{n_1}(\gamma_2)^{n_2}(\gamma_3)^{n_3}$ and $\xi_n \equiv [\chi_n^1, \chi_n^2, \chi_n^3, \chi_n^4]^T$, and then by retaining one of the four components in $\xi_n$. However, to be precise, the action of staggered fermions after recovering the spinor structure does not coincide with that of Wilson fermions. This is known as the taste breaking of staggered fermions. The (2+1)D staggered fermions have been used as an effective lattice model for graphene [101–106], since they reproduce the four-component massless Dirac fermions of 2 flavors in the continuum limit [119].

## 5.2  Strong Coupling Expansion

Let us derive the effective actions in the strong coupling limit ($\beta = 0$). We can derive the effective action $S_{\text{eff}}$ by integrating out the U(1) gauge link variable $U_{0,n}$ in the partition function $Z$ up to the arbitrary order in $\beta$ as follows:

$$Z^{(N=16)} = \int \mathcal{D}[\psi, \bar{\psi}, U_0] e^{-S^{(N=16)}} = \int \mathcal{D}[\psi, \bar{\psi}] e^{-S_{\text{eff}}^{(N=16)}}. \quad (5.7)$$

Here we have written down the case of the $N = 16$ Dirac semimetal explicitly. The same method can be applied to the case of $N = 4$ by replacing $\psi$ to $\chi$. In the strong coupling limit, $S_G$ vanishes and thus $U_{n,0}$ is contained only in $S_F^{(N=16)}$ and $S_F^{(N=4)}$. Then the integral $\int \mathcal{D}U_0 e^{-S_F^{(N=16)}}$ is performed as

$$\int \mathcal{D}U_0 e^{-S_F^{(N=16)}} = \prod_n \int_{-\pi}^{\pi} \frac{d\theta_n}{2\pi} \exp\left\{ \frac{1}{2} \left[ \bar{\psi}_n \gamma_0 U_{n,0} \psi_{n+\hat{0}} - \bar{\psi}_{n+\hat{0}} \gamma_0 U_{n,0}^\dagger \psi_n \right] \right\}$$

$$= \prod_n \left[ 1 - \frac{1}{4} \bar{\psi}_n \gamma_0 \psi_{n+\hat{0}} \bar{\psi}_{n+\hat{0}} \gamma_0 \psi_n + \cdots \right] \qquad (5.8)$$

$$\approx e^{\frac{1}{4} \sum_n \text{tr}\left[ \gamma_0^T \bar{\psi}_n \psi_n \gamma_0^T \bar{\psi}_{n+\hat{0}} \psi_{n+\hat{0}} \right]},$$

where we have used the fact that the Grassmann variables $\psi_\alpha$ and $\bar{\psi}_\alpha$ satisfy $\psi_\alpha^2 = \bar{\psi}_\alpha^2 = 0$ with $\alpha$ denoting the component of the spinors. In the second line, we have neglected the terms

which consist of 8, 12 and 16 different Grassmann variables. As is mentioned in Sec. 5.4, their contributions appear in higher orders of the order parameter, and do not affect the discussion on the semimetal-insulator transition in this model. Further in the last line, we have rewritten the exponent as

$$\bar{\psi}_{n,\alpha}(\gamma_0)_{\alpha\beta}\psi_{n+\hat{0},\beta}\bar{\psi}_{n+\hat{0},\gamma}(\gamma_0)_{\gamma\delta}\psi_{n,\delta} = -\mathrm{tr}\left[\gamma_0^T\bar{\psi}_n\psi_n\gamma_0^T\bar{\psi}_{n+\hat{0}}\psi_{n+\hat{0}}\right]. \tag{5.9}$$

The subscripts $\alpha$ and $\beta$ denote the component of the spinors, and the superscript $T$ denotes the transpose of a matrix. In the general cases of SU($N_c$) gauge field ($N_c \geq 1$), we can perform the integration with respect to the gauge link variables $U$ in Eq. (5.7) by using the SU($N_c$) group integral formulas: $\int dU 1 = 1$, $\int dU U_{ab} = 0$, $\int dU U_{ab}U_{cd}^\dagger = \delta_{ad}\delta_{bc}/N_c$, and so on. Finally we obtain the effective action of the $N = 16$ Dirac semimetal in the strong coupling limit given by

$$S_{\mathrm{eff}}^{(N=16)} = \frac{1}{2}\sum_{n,j}\xi_j\left[\bar{\psi}_n\gamma_j\psi_{n+\hat{j}} - \bar{\psi}_{n+\hat{j}}\gamma_j\psi_n\right] - \frac{1}{4}\sum_n\mathrm{tr}\left[\gamma_0^T\bar{\psi}_n\psi_n\gamma_0^T\bar{\psi}_{n+\hat{0}}\psi_{n+\hat{0}}\right]. \tag{5.10}$$

From this equation, we see that the electron-electron interactions in the strong coupling limit is spatially on-site interaction but not in the (imaginary) time.

In the $N = 4$ case, $\chi$ is a single-component Grassmann variable. Therefore, due to the nature of Grassmann variables $\chi^2 = \bar{\chi}^2 = 0$, the approximation done in the second line of Eq. (5.8) is not needed. Finally we obtain the effective action of the $N = 4$ Dirac semimetal in the strong coupling limit as

$$S_{\mathrm{eff}}^{(N=4)} = \frac{1}{2}\sum_{n,j}\xi_j\eta_{n,j}\left[\bar{\chi}_n\chi_{n+\hat{j}} - \bar{\chi}_{n+\hat{j}}\chi_n\right] - \frac{1}{4}\sum_n\bar{\chi}_n\chi_n\bar{\chi}_{n+\hat{0}}\chi_{n+\hat{0}}. \tag{5.11}$$

Note that this action is exact in the strong coupling limit, although we call it "effective action".

## 5.3 Free Energies in the Strong Coupling Limit

As mentioned in Chap. 2, the lattice-gauge-theoretical description of $1/r$ Coulomb interactions does not contain the on-site interactions. Unphysical states due to the absence of on-site interactions, such as phase separation, are eliminated by assuming uniform mean-field ground states. This assumption is also supported by the fact that lattice quantum electrodynamics (QED) is a well-defined (renormalizable) theory.

Let us derive the free energies in the strong coupling limit at zero temperature. To this end, we apply the extended Hubbard-Stratonovich transformation to the interaction terms. First let us consider the case of the $N = 16$ Dirac semimetal. In this case, introducing the two complex matrix auxiliary fields $Q$ and $Q'$, $e^{\kappa\mathrm{tr}AB}$ with $\kappa > 0$ and $A$, $B$ being matrices is deformed as follows (see Subsect. 3.3.1):

$$e^{\kappa\mathrm{tr}AB} = (\mathrm{const.}) \times \int \mathcal{D}[Q, Q']\exp\left\{-\kappa\left[Q_{\alpha\beta}Q'_{\alpha\beta} - A_{\alpha\beta}Q_{\beta\alpha} - B_{\alpha\beta}^T Q'_{\beta\alpha}\right]\right\}, \tag{5.12}$$

This integral is approximated by the saddle point values $Q_{\alpha\beta} = \langle B^T\rangle_{\beta\alpha}$ and $Q'_{\alpha\beta} = \langle A\rangle_{\beta\alpha}$. In the case of the $N = 4$ Dirac semimetal, we can apply Eq. (5.12) with the subscripts removed, since there is no spinor structure in the action.

## 5.3.1 Free Energy of the $N = 16$ Dirac Semimetal

We set $(\kappa, A, B) = (1/4, \gamma_0^T \bar{\psi}_n \psi_n, \gamma_0^T \bar{\psi}_{n+\hat{0}} \psi_{n+\hat{0}})$ to decouple the interaction term (the second term) of Eq. (5.10) to fermion bilinear form. In this process, we need to assume the form of the $4 \times 4$ matrix $\langle \bar{\psi}_n \psi_n \rangle$ by the mean-field approximation. Recall that the purpose of this study is to discuss the semimetal-insulator transition induced by strong long-range Coulomb interactions. Here let us consider the possible gapped phases in our model. In the action (5.3) with $U_{n,0} = 1$, only the identity matrix $\mathbf{1}$ and the matrix $\gamma_5$ can open energy gaps. This is because, in the presence of these matrices, the single-particle Hamiltonian of the system is given by

$$\mathcal{H}(\mathbf{k}) = \xi_j \alpha_j \sin k_j + m_4 \alpha_4 + m_5 \alpha_5 \tag{5.13}$$

with $\alpha_j = \gamma_0 \gamma_j$, $\alpha_4 = \gamma_0$ and $\alpha_5 = i\gamma_0 \gamma_5$, which leads to the gapped energy spectrum $E(\mathbf{k}) = \pm\sqrt{\sum_j (\xi_j \sin k_j)^2 + m_4^2 + m_5^2}$. Note that the action (5.3) possesses chiral symmetry, namely, the action is invariant under the chiral transformation $\psi_n \to e^{i\alpha\gamma_5}\psi_n$. In such cases, as in the case of graphene [100–106], the identity matrix (i.e. the mass term) serves as the order parameter for the semimetal-insulator transition. Therefore we can set $\langle \bar{\psi}_n \psi_n \rangle = -\sigma \mathbf{1}$. If the value of $\sigma$ is nonzero in the strong coupling limit, then the value of $\sigma$ corresponds to $\sigma = \sqrt{m_4^2 + m_5^2}$ in the energy spectrum $E(\mathbf{k})$. Namely, we obtain the gapped spectrum. We can regard the value of $\sigma$ as the dynamically generated mass of Dirac fermions. In the lattice QCD, $\sigma$ is known as the "chiral condensate".

Then the terms $Q_{\alpha\beta} Q'_{\alpha\beta}$, $A_{\alpha\beta} Q_{\beta\alpha}$ and $B^T_{\alpha\beta} Q'_{\beta\alpha}$ in the integrand of Eq. (5.12) are calculated explicitly as

$$Q_{\alpha\beta} Q'_{\alpha\beta} = \langle B^T \rangle_{\beta\alpha} \langle A \rangle_{\beta\alpha} = \text{tr}\left[\langle B \rangle \langle A \rangle\right] = \sigma^2 \text{tr}\left[(\gamma_0^T)^2\right] = 4\sigma^2, \tag{5.14}$$

$$A_{\alpha\beta} Q_{\beta\alpha} = A_{\alpha\beta} \langle B^T \rangle_{\alpha\beta} = \text{tr}\left[A\langle B \rangle\right] = -\sigma \text{tr}\left[\gamma_0^T \bar{\psi}_n \psi_n \gamma_0^T\right] = -\sigma \bar{\psi}_n \psi_n, \tag{5.15}$$

$$B^T_{\alpha\beta} Q'_{\beta\alpha} = B^T_{\alpha\beta} \langle A \rangle_{\alpha\beta} = \text{tr}\left[B\langle A \rangle\right] = -\sigma \text{tr}\left[\gamma_0^T \bar{\psi}_n \psi_n \gamma_0^T\right] = -\sigma \bar{\psi}_n \psi_n, \tag{5.16}$$

where we have used $\langle \bar{\psi}_{n+\hat{0}} \psi_{n+\hat{0}} \rangle = \langle \bar{\psi}_{n-\hat{0}} \psi_{n-\hat{0}} \rangle = \langle \bar{\psi}_n \psi_n \rangle = -\sigma \mathbf{1}$ and $(\gamma_0^T)^2 = (\gamma_0^2)^T = \mathbf{1}$. Combining these three equations, we obtain the interaction term decoupled to fermion bilinear:

$$\frac{1}{4} \sum_n \text{tr}\left[\gamma_0^T \bar{\psi}_n \psi_n \gamma_0^T \bar{\psi}_{n+\hat{0}} \psi_{n+\hat{0}}\right] \sim -\frac{1}{4} \sum_n \left[4\sigma^2 + 2\sigma \bar{\psi}_n \psi_n\right]. \tag{5.17}$$

We are now in a position to derive the free energy at zero temperature in the strong coupling limit. Combining Eqs. (5.10) and (5.17), the effective action expressed by the auxiliary field $\sigma$ is given by

$$S_{\text{eff}}^{(N=16)}(\sigma) = \frac{V}{T}\sigma^2 + \sum_{k=-\pi}^{\pi} \bar{\psi}_k \mathcal{M}(\mathbf{k}; \sigma)\psi_k \tag{5.18}$$

with $\mathcal{M}(\mathbf{k}; \sigma) = \sum_j \xi_j i\gamma_j \sin k_j + \sigma/2$. As mentioned above, the value $\sigma/2$ can be regarded as the dynamically generated mass. Here $V$ and $T$ are the volume and temperature of the system, respectively, and we have done the Fourier transform from $n = (n_0, \mathbf{n})$ to $k = (k_0, \mathbf{k})$. From this action,

we derive the free energy at zero temperature per unit spacetime volume $\mathcal{F}^{(N=16)}(\sigma)$, according to the usual formula $\mathcal{F}^{(N=16)} = -\frac{T}{V} \ln Z^{(N=16)}$. The partition function $Z^{(N=16)}$ is calculated by the Grassmann integral formula $Z^{(N=16)} = \int D[\psi, \bar{\psi}] e^{-\bar{\psi} \mathcal{M} \psi} = \det \mathcal{M}$. The determinant of $\mathcal{M}$ is calculated by the formula $\det \mathcal{M} = \sqrt{\det(\mathcal{M}\mathcal{M}^\dagger)}$. Finally, after a straightforward calculation, we arrive at the free energy in the strong coupling limit:

$$\mathcal{F}^{(N=16)}(\sigma) = \sigma^2 - 2 \int_{-\pi}^{\pi} \frac{d^3 k}{(2\pi)^3} \ln \left[ \sum_j \xi_j^2 \sin^2 k_j + \frac{1}{4}\sigma^2 \right]. \tag{5.19}$$

The ground state is determined by the stationary condition $d\mathcal{F}^{(N=16)}(\sigma)/d\sigma = 0$.

## 5.3.2 Free Energy of the $N = 4$ Dirac Semimetal

We set $(\kappa, A, B) = (1/4, \bar{\chi}_n \chi_n, \bar{\chi}_{n+\hat{0}} \chi_{n+\hat{0}})$ to decouple the interaction term (the second term) of Eq. (5.11) to fermion bilinear form. Like in the $N = 16$ case above, we need to assume the value of $\langle \bar{\chi}_n \chi_n \rangle$ by the mean-field approximation. Note that the lattice action (5.5) also possesses chiral symmetry, namely, the action is invariant under the chiral transformation defined by $\chi_n \to e^{i\alpha\epsilon(n)} \chi_n$, $\bar{\chi}_n \to e^{i\alpha\epsilon(n)} \bar{\chi}_n$ with $\epsilon(n) = (-1)^{n_0 + n_1 + n_2 + n_3}$. Hence we can set $\langle \bar{\chi}_n \chi_n \rangle = -\sigma$. Then with this approximation, the interaction term is decoupled to fermion bilinear as

$$\frac{1}{4} \sum_n \bar{\chi}_n \chi_n \bar{\chi}_{n+\hat{0}} \chi_{n+\hat{0}} \sim -\frac{1}{4} \sum_n \left[ \sigma^2 + 2\sigma \bar{\chi}_n \chi_n \right]. \tag{5.20}$$

It is convenient to perform the Fourier transform only to the spatial directions, due to the factor $\eta_{n,j}$ in the noninteracting part of the effective action (5.11). By introducing the eight-component spinor $\Psi_{n_0, \boldsymbol{k}}$ as

$$\Psi_{n_0, \boldsymbol{k}} = \begin{bmatrix} \chi_{n_0}(k_1, k_2, k_3) \\ \chi_{n_0}(k_1 - \pi, k_2, k_3) \\ \chi_{n_0}(k_1, k_2 - \pi, k_3) \\ \chi_{n_0}(k_1, k_2, k_3 - \pi) \\ \chi_{n_0}(k_1, k_2 - \pi, k_3 - \pi) \\ \chi_{n_0}(k_1 - \pi, k_2, k_3 - \pi) \\ \chi_{n_0}(k_1 - \pi, k_2 - \pi, k_3) \\ \chi_{n_0}(k_1 - \pi, k_2 - \pi, k_3 - \pi) \end{bmatrix}, \tag{5.21}$$

and substituting Eq. (5.20) into Eq. (5.11), the effective action is rewritten as

$$S_{\text{eff}}^{(N=4)}(\sigma) = \frac{1}{4} \frac{V}{T} \sigma^2 + \sum_{n_0} \sum_{\boldsymbol{k}=0}^{\pi} \bar{\Psi}_{n_0, \boldsymbol{k}}^T \mathcal{V}(n_0, \boldsymbol{k}; \sigma) \Psi_{n_0, \boldsymbol{k}}, \tag{5.22}$$

where the $8 \times 8$ symmetric matrix $\mathcal{V}(n_0, \boldsymbol{k}; \sigma)$ is given by

$$\begin{bmatrix} \frac{1}{2}\sigma + s_1 & s_2 & 0 & 0 & 0 & 0 & s_3 & 0 \\ s_2 & \frac{1}{2}\sigma - s_1 & s_3 & 0 & 0 & 0 & 0 & 0 \\ 0 & s_3 & \frac{1}{2}\sigma + s_1 & 0 & 0 & 0 & -s_2 & 0 \\ 0 & 0 & 0 & \frac{1}{2}\sigma + s_1 & 0 & s_2 & 0 & -s_3 \\ 0 & 0 & 0 & 0 & \frac{1}{2}\sigma + s_1 & -s_3 & 0 & -s_2 \\ 0 & 0 & 0 & s_2 & -s_3 & \frac{1}{2}\sigma - s_1 & 0 & 0 \\ s_3 & 0 & -s_2 & 0 & 0 & 0 & \frac{1}{2}\sigma - s_1 & 0 \\ 0 & 0 & 0 & -s_3 & -s_2 & 0 & 0 & \frac{1}{2}\sigma - s_1 \end{bmatrix}. \tag{5.23}$$

Here $s_1 = i(-1)^{n_0}\xi_1 \sin k_1$, $s_2 = i(-1)^{n_0}\xi_2 \sin k_2$, and $s_3 = i(-1)^{n_0}\xi_3 \sin k_3$. Note that the sum over the wave vector $k_j$ is from 0 to $\pi$. The procedure to derive the free energy at zero temperature per unit spacetime volume $\mathcal{F}^{(N=4)}(\sigma)$ is the same as the case of $N = 16$. The calculation of $\det\mathcal{V}$ is a little complicated but can be done analytically to be $\det\mathcal{V} = [\sum_j \xi_j^2 \sin^2 k_j + \frac{1}{4}\sigma^2]^4$. Finally we arrive at the free energy in the strong coupling limit:

$$\mathcal{F}^{(N=4)}(\sigma) = \frac{1}{4}\sigma^2 - \frac{1}{2}\int_{-\pi}^{\pi}\frac{d^3k}{(2\pi)^3}\ln\left[\sum_j \xi_j^2 \sin^2 k_j + \frac{1}{4}\sigma^2\right], \tag{5.24}$$

where we have used the fact that the integrand is an even function. The ground state is determined by the stationary condition $d\mathcal{F}^{(N=4)}(\sigma)/d\sigma = 0$.

## 5.4 Numerical Results

First we consider the result for the $N = 4$ case. The Fermi velocity anisotropy $v_{F\perp}/v_{F\parallel}(= \xi_3)$ dependence of the chiral condensate $\sigma$ in the strong coupling limit is shown in Fig. 5.1. It was found that the the value of $\sigma$ becomes zero when the ratio $v_{F\perp}/v_{F\parallel}$ is larger than about 0.24, whereas the value of $\sigma$ is nonzero when $v_{F\perp}/v_{F\parallel}$ is smaller than about 0.24. As mentioned in Sec. 5.3, the value of $\sigma$, the chiral condensate, is regarded as the dynamically generated mass of Dirac fermions, and can be used as the order parameter for the semimetal-insulator transition. Hence the result indicates that whether the system is insulating or semimetallic (i.e. gapped or gapless) in the strong coupling limit depends on the value of the Fermi velocity anisotropy. Namely, the $N = 4$ Dirac semimetals survive in the strong coupling limit when the anisotropy is weak, whereas they change to insulators when the anisotropy is strong. We see from Fig. 5.1 that the transition is of the second order.

The result, that the system becomes gapped in the strong coupling limit when the Fermi velocity anisotropy is strong (i.e. the ratio $v_{F\perp}/v_{F\parallel}$ is small), could be understood by the fact that in general quantum effects become stronger in lower dimensions. In the case of monolayer graphene, theoretical studies have shown that the graphene suspended in vacuum (or the graphene on a substrate with sufficiently small dielectric constant) becomes gapped due to strong $1/r$ Coulomb interactions [97–106]. In the the $N = 4$ case, the interaction term in the effective action [Eq. (5.11)] describes spatially on-site interactions. This means that our model with $v_{F\perp} = 0$ in the strong coupling limit is equivalent to a model for a stacked 2D system. To be more precise, our model with $v_{F\perp} = 0$ in the strong coupling limit corresponds to an effective lattice model for monolayer graphene in the strong coupling limit, since the (2+1)D staggered fermions reproduce the four-component Dirac fermions of 2 flavors in the continuum limit [119]. Actually, the value of $\sigma$ when $v_{F\perp} = 0$ in our model, $\sigma \simeq 0.24$, is equal to the value obtained by a lattice strong coupling expansion study of monolayer graphene [103].

Here we would like to mention the correctness of our value of $\sigma$ in the strong coupling limit. As for monolayer graphene which is described by (2+1)D staggered fermions, the value of $\sigma$ obtained in a lattice strong coupling expansion study with the mean-field approximation [103] is in qualitative agreement (within about 10% of difference) with the values obtained in Monte Carlo studies [101, 102]. Hence it is expected that our value of $\sigma$ for the $N = 4$ case is quantitatively correct, because the mean-field approximation gives more proper results in higher dimensions in general.

Finally we consider the result for the $N = 16$ case. We see easily that $\mathcal{F}^{(N=16)}(\sigma) = 4\mathcal{F}^{(N=4)}(\sigma)$. Namely, within our calculation the values of $\sigma$ for both the $N = 4$ and the $N = 16$
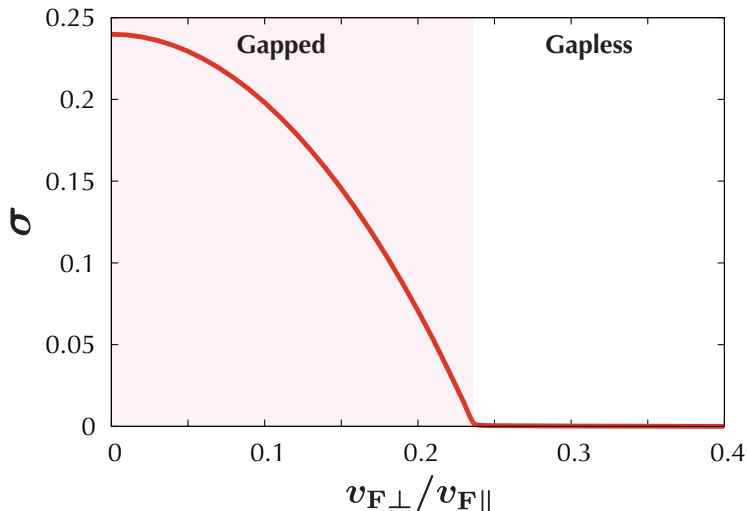
Figure 5.1: Fermi velocity anisotropy $v_{F\perp}/v_{F\parallel}$ dependence of the chiral condensate $\sigma$ for the $N = 4$ case in the strong coupling limit ($\beta = 0$). When $v_{F\perp}/v_{F\parallel} = 0$, the system corresponds to monolayer graphene in the strong coupling limit.

cases, which serve as the order parameter for the semimetal-insulator transition, are equivalent in the strong coupling limit. Here note that we have neglected the interaction terms which consist of 8, 12 and 16 fermion fields when deriving the effective action of the $N = 16$ Dirac semimetal [Eq. (5.10)]. If the 8 fermion field term, $S_8 \sim \bar{\psi}\psi\bar{\psi}\psi\bar{\psi}\psi\bar{\psi}\psi$, is taken into account, then we obtain $S_8 \sim \sigma^4 + \sigma^3\bar{\psi}\psi$ by a rough mean-field approximation. The 12 and 16 fermion field terms can be approximated in the same way. When $\sigma = 0$ at the stationary point of the free energy $\mathcal{F}^{(N=16)}(\sigma)$, i.e. when the Fermi velocity anisotropy is weak, the effects of these higher order terms in the free energy can be neglected near $\sigma = 0$. In other words, the result that the $N = 16$ Dirac semimetal survives in the strong coupling limit will not be changed even though such terms are taken into account.

However, when $\sigma \neq 0$ at the stationary point of $\mathcal{F}^{(N=16)}(\sigma)$, i.e. when the anisotropy is strong, such terms will modify the value of $\sigma$ at the stationary point. Here note that the interaction term in the effective action [Eq. (5.10)] describes spatially on-site interactions. Namely, our model with $v_{F\perp} = 0$ in the strong coupling limit corresponds to a model of stacked (2+1)D four-component Dirac fermions of 8 flavors in the strong coupling limit. It has been reported in the (2+1)D cases that the value of $\sigma$ becomes smaller as the number of Dirac fermion flavor $N^{2D}$ becomes larger and the semimetal phase with large $N^{2D}$ survives in the strong coupling limit [100, 101, 113]. Therefore, when we take into account those higher order terms in the free energy, it is expected that the value of $\sigma$ is suppressed in the case of small $v_{F\perp}/v_{F\parallel}$. To verify this prediction, further study is needed.

## 5.5 Discussions

Firstly, we note the relations between our models and the experimentally observed Dirac semimetals. In the observed Dirac semimetals, there exist large out-of-plane Fermi velocity anisotropy such that $v_{F\perp}/v_{F\parallel} \approx 0.25$ in $Na_3Bi$ [51] and $v_{F\perp}/v_{F\parallel} \sim 0.1$ in $Cd_3As_2$ [52]. Therefore we expect that our result gives some perception to realistic materials. On the other hand, as for the number
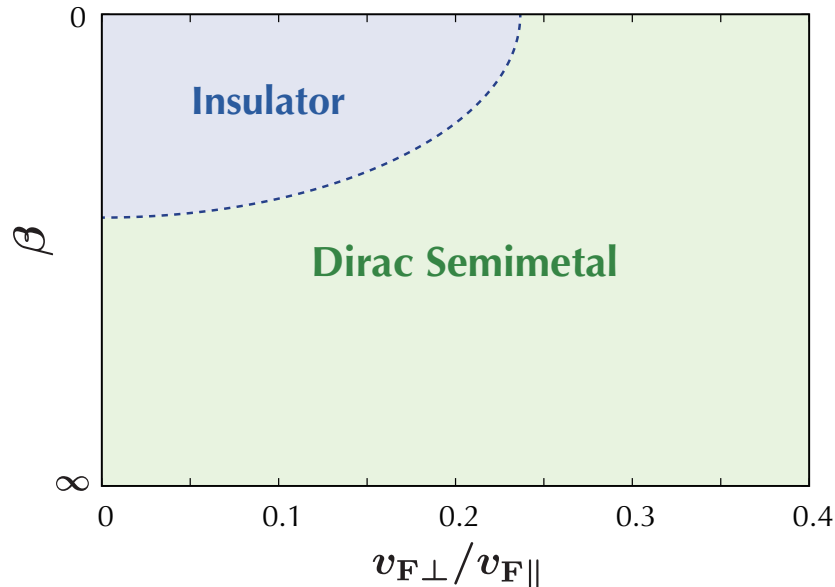
Figure 5.2: A possible global phase diagram of a correlated $N$-node Dirac semimetal with $N = 4$. The $\beta = 0$ ($\beta = \infty$) line represents the strong coupling limit (noninteracting limit). The insulator phase is defined as the phase with nonzero value of $\sigma$.

of the Dirac nodes $N$, $N$ is two in both $Na_3Bi$ and $Cd_3As_2$. From the results in the (2+1)D case, i.e. multilayer graphene [101], it is expected that the dynamically generated mass gap $\sigma$ in the strong coupling limit becomes larger with decreasing $N$. However, it is difficult to show such a behavior explicitly in our study. Hence the stability of the $N = 2$ case is a remaining problem.

Secondly, let us discuss a possible global phase diagram of correlated $N$-node Dirac semimetals with $N = 4$ and $N = 16$. We see from Fig. 5.1 that as the ratio $v_{F\perp}/v_{F\parallel}$ is increased from zero, the value of $\sigma$ becomes smaller and eventually reaches zero. The chiral condensate $\sigma$ can be used as the order parameter for the semimetal-insulator transition. Namely, the system is gapless in the strong coupling limit ($\beta = 0$) when the ratio $v_{F\perp}/v_{F\parallel}$ is large, whereas the system is gapped when the ratio $v_{F\perp}/v_{F\parallel}$ is small. We call the gapped phase with nonzero $\sigma$ the insulator. On the other hand, the system is obviously a Dirac semimetal in the noninteracting limit ($\beta = \infty$). Therefore, there must exist the critical strength of the $1/r$ Coulomb interactions $\beta_c$, below which the system becomes semimetallic, i.e. the value of $\sigma$ becomes zero. This critical value $\beta_c$ will become smaller as the value of $\sigma$ in the strong coupling limit becomes smaller. A schematic global phase diagram for the $N = 4$ case based on this analysis is shown in Fig. 5.2. In the case of $N = 16$, as mentioned in the previous section, it is expected that the value of $\sigma$ in the strong coupling limit is suppressed when the ratio $v_{F\perp}/v_{F\parallel}$ is small. Namely, it is expected that the region of the insulator phase shrinks in the global phase diagram.

In this study, we have focused only on the energy gap generation by strong $1/r$ Coulomb interactions, and thus the detailed information of the spinors in the low-energy effective model [Eq. (5.1)] is not required. However, if we construct a low-energy effective model of some realistic material, then the spinors should be associated with the lattice structure and the spins of electrons, as in the case of graphene. Hence it is expected that some order such as a magnetic or charge order is realized in the insulator phase in Fig. 5.2, although it is difficult in this study to identify what the order is. This can be understood from the fact that the two possible orders in

the Hamiltonian (5.13), the $\alpha_4$ order where no symmetry is broken and the $\alpha_5$ order where both time-reversal and inversion symmetries are broken, are energetically degenerate. The result of this paper is not changed even though the $\alpha_5$ order is considered as the gapped order instead of the $\alpha_4$ order.

Thirdly, let us discuss the implications of our results to the stability of Weyl semimetals. Weyl semimetals have gapless 3D linear dispersions in the bulk, and the effective Hamiltonians around the Weyl nodes are described by not the Dirac Hamiltonian but the Weyl Hamiltonian $\mathcal{H}_{\text{Weyl}}(\boldsymbol{k}) = \sum_{i=1}^{3} \boldsymbol{v}_i \cdot \boldsymbol{k}\sigma_i$ where $\sigma_i$ are the Pauli matrices. At least either time-reversal or inversion symmetry breaking is required to realize a Weyl semimetal phase [29–36, 58]. Each Weyl node possesses chirality defined by $c = \text{sgn}[\boldsymbol{v}_1 \cdot (\boldsymbol{v}_2 \times \boldsymbol{v}_3)] = \pm 1$. The number of the Weyl nodes with chirality $+1$ and that of chirality $-1$ must be equal in time-reversal symmetry broken Weyl semimetals. For example, the Weyl semimetal phase predicted by a first-principles calculation in pyrochlore iridates possesses 24 Weyl nodes [29]. Here let us consider a simplified low-energy effective model for a Weyl semimetal with $2N$ nodes. The Hamiltonian of such a system can be written as

$$
\begin{aligned}
H_{\text{Weyl}}^{\text{eff}} &= \sum_{\boldsymbol{k}} \sum_{f=1}^{N} v_{\text{F}\|} \left\{ \psi_{f+}^{\dagger}(\boldsymbol{k}) \left[ \xi_i k_i \sigma_i \right] \psi_{f+}(\boldsymbol{k}) + \psi_{f-}^{\dagger}(\boldsymbol{k}) \left[ -\xi_i k_i \sigma_i \right] \psi_{f-}(\boldsymbol{k}) \right\} \\
&= \sum_{\boldsymbol{k}} \sum_{f=1}^{N} \psi_f^{\dagger}(\boldsymbol{k}) v_{\text{F}\|} \begin{bmatrix} \xi_i k_i \sigma_i & 0 \\ 0 & -\xi_i k_i \sigma_i \end{bmatrix} \psi_f(\boldsymbol{k}),
\end{aligned}
\tag{5.25}
$$

where $\psi_f = [\psi_{f+}, \psi_{f-}]^T$ with $\psi_{f\pm}$ being a two-component spinor, the subscript $\pm$ denotes the chirality of each Weyl node, and we have introduced the Fermi velocity anisotropy $\xi_i$. By introducing the $4 \times 4$ gamma matrices $\gamma_\mu$ in the chiral representation, we obtain the low-energy effective action (5.1). Namely, this indicates that in a rough approximation, the low-energy effective model of a $2N$-node Weyl semimetal is equivalent to that of a $N$-node Dirac semimetal. Weyl semimetals have a topological property such that the energy gap opens only if the Weyl nodes with opposite chirality meet each other, since a single Weyl fermion cannot be massive by itself. Due to this property, Weyl semimetals are expected to be more stable against strong $1/r$ Coulomb interactions than Dirac semimetals. However, it is not easy to treat strong $1/r$ Coulomb interactions properly in multinode Weyl semimetals. In this study, it was found that the $N$-node Dirac semimetals with $N = 4$ and $N = 16$ survive in the strong coupling limit. Hence, it could be said that the $N_{\text{W}}$-node Weyl semimetals with $N_{\text{W}} = 8$ and $N_{\text{W}} = 32$ also survive in the strong coupling limit when the Fermi velocity anisotropy is weak. As for the cases of $N_{\text{W}} < 8$, we have shown that a Weyl semimetal with $N_{\text{W}} = 2$ survives in this limit (see Chap. 4).

Finally, let us discuss the implications of our results to the stability of 3D topological insulators. It is known that 3D topological insulators can be regarded as 3D Dirac fermion systems. In the noninteracting cases, the bulk energy gap closes when the phase transition from the topological insulator phase to the normal band insulator phase occurs. In other words, there exist Dirac point(s) in the bulk when the system is on the phase boundary between the topological insulator phase and the normal band insulator phase. For example, the Fu-Kane-Mele model has three Dirac points [11, 12], and the effective model for $Bi_2Se_3$ has one Dirac point [16] on their phase boundaries. What about in the interacting cases? The phase transitions from the topological insulator phase to the other phases can occur without the gap closing, when accompanying the breaking of symmetry of the system such as time-reversal symmetry or inversion symmetry. However, the gap closing is required when no symmetry is broken, as in the noninteracting cases.

From this viewpoint, our result, that the Dirac semimetals survives in the strong coupling limit, suggests that 3D topological insulator phases can be stable against strong $1/r$ Coulomb interactions. Actually, we have shown that a 3D topological insulator phase of $Bi_2Se_3$-type survives in the strong coupling limit when the spin-orbit interaction of the system is strong (see Chap. 3).

## 5.6   Summary

In summary, based on the U(1) lattice gauge theory, we have studied the stability of $N$-node Dirac semimetals in three spatial dimensions with $N = 4$ and $N = 16$ against strong $1/r$ long-range Coulomb interactions. It was shown that the Dirac semimetals survive in the strong coupling limit when the Fermi velocity anisotropy is weak, whereas they change to insulators when the anisotropy is strong. This means that the three-dimensionality of the Dirac cones plays an important role in the stability. The value of the dynamically generated mass gap at least for the $N = 4$ case is expected to be quantitatively correct. A possible global phase diagram of correlated Dirac semimetals was presented. Dirac semimetals can lead to various topological phases by the change of parameters or symmetry breakings. Our result, that Dirac semimetals are stable against strong $1/r$ long-range Coulomb interactions, implies the stability of other topological phases. Namely, it is suggested that Weyl semimetals, which correspond to Dirac semimetals in a rough approximation, can survive in the strong coupling limit. The existence of 3D topological insulator phases in the strong coupling limit is also suggested.

# Chapter 6

# Axionic Antiferromagnetic Insulator

In this chapter, we study theoretically a three-dimensional correlated and spin-orbit coupled system, the half-filled extended Fu-Kane-Mele-Hubbard model on a diamond lattice, focusing on the topological magnetoelectric response of the antiferromagnetic insulator phase. In the antiferromagnetic insulator phase, the Dirac-like low-energy effective Hamiltonian is obtained. Then the theta term, which results in the magnetoelectric response, is derived as a consequence of the chiral anomaly. The realization of the dynamical axion field in our model is discussed. The relation with a symmetry broken phase induced by interactions in lattice quantum chromodynamics is also discussed. The contents in this chapter have been partly published in:
A. Sekine and K. Nomura, J. Phys. Soc. Jpn. **83**, 104709-1-7 (2014).

## 6.1  Axion Electrodynamics

A great number of studies on topological insulators have been done since the pioneering works [7] appeared, in the search for novel phenomena due to the topological properties of the system. The most prominent feature common to two-dimensional (2D) and 3D topological insulators is the existence of the edge (surface) states which are protected by time-reversal symmetry. These edge or surface states are known to be robust against perturbations. On the one hand, as introduced in Sect. 1.2, one of the noteworthy characters peculiar to 3D topological insulators is the topological magnetoelectric effect which is described by the theta term [26]. The theta term is written as

$$S_\theta = \int dt d^3 x \frac{\theta e^2}{4\pi^2 \hbar c} \boldsymbol{E} \cdot \boldsymbol{B}, \qquad (6.1)$$

where $\boldsymbol{E}$ and $\boldsymbol{B}$ are an electric field and magnetic field, respectively. From this action, we obtain the cross-correlated responses expressed by $\boldsymbol{P} = \theta e^2/(4\pi^2 \hbar c)\boldsymbol{B}$ and $\boldsymbol{M} = \theta e^2/(4\pi^2 \hbar c)\boldsymbol{E}$, with $\boldsymbol{P}$ the electric polarization and $\boldsymbol{M}$ the magnetization. A schematic picture of the topological magnetoelectric effect is shown in Fig. 6.1.

In the field theory literature, the action (6.1) is termed the axion electrodynamics [135]. The axion is an elementary particle proposed about forty years ago to solve the so-called strong CP problem in quantum chromodynamics (QCD) [136–138]. By subsequent studies, the axion is now considered to be essential to explain experimental results in particle physics and astrophysics [139]. The axion is also considered as a candidate for dark matter [139]. However, regardless of intensive experimental searches, the axion has not yet been found. The axions interact with photons, and the axion-photon coupling is described by Eq. (6.1) with $\theta$ being the axion field.
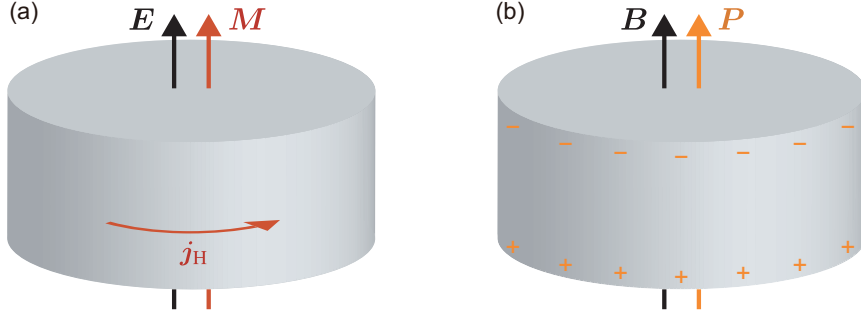
Figure 6.1: Schematic picture of the topological magnetoelectric effect in a 3D system. (a) Magnetization $M = \theta e^2/(4\pi^2\hbar c)E$ is induced by an external electric field $E$. $j_H$ is the Hall current induced by $E$. (b) Electric polarization $P = \theta e^2/(4\pi^2\hbar c)B$ is induced by an external magnetic field $B$. $+(-)$ denotes the positive (negative) charge induced by $B$.

Therefore, observing the magnetoelectric responses originating from Eq. (6.1) in condensed matter is equivalent to realizing the (dynamical) axion field. There have been some theoretical studies which propose ways to observe experimentally the dynamical axion field in condensed matter [67, 140].

When the system is time-reversal invariant, the condition that $\theta = \pi$ (mod $2\pi$) is imposed for 3D topological insulators, and $\theta = 0$ for normal insulators. On the other hand, when time-reversal symmetry of the system is broken, the value of $\theta$ can be arbitrary. In general, the value of $\theta$ can be calculated according to the formula [26]

$$\theta = \frac{1}{4\pi} \int_{BZ} d^3 k \epsilon^{ijk} \text{Tr} \left[ \mathcal{A}_i \partial_j \mathcal{A}_k - i\frac{2}{3} \mathcal{A}_i \mathcal{A}_j \mathcal{A}_k \right], \tag{6.2}$$

where $\mathcal{A}_j^{\mu\nu} = i\langle u_\mu | \partial/\partial k_j | u_\nu \rangle$, and $|u_\nu\rangle$ is the periodic Bloch function with $\nu$ the occupied bands. We can calculate $\theta$ from other equivalent expressions [141–143]. However, some techniques (such as choosing a gauge for $\mathcal{A}$) are required to calculate numerically. In systems where the single-particle Hamiltonian can be described as $\mathcal{H}(k) = \sum_{\mu=1}^5 R_\mu(k)\alpha_\mu$ with matrices $\alpha_\mu$ satisfying the Clifford algebra $\{\alpha_\mu, \alpha_\nu\} = 2\delta_{\mu\nu}$, there exists an explicit expression for $\theta$ [67, 144]:

$$\theta = \frac{1}{4\pi} \int_{BZ} d^3 k \frac{2|R| + R_4}{(|R| + R_4)^2 |R|^3} \epsilon^{ijkl} R_i \frac{\partial R_j}{\partial k_x} \frac{\partial R_k}{\partial k_y} \frac{\partial R_l}{\partial k_z}, \tag{6.3}$$

where $i, j, k, l = 1, 2, 3, 5$ and $|R| = \sqrt{\sum_{\mu=1}^5 R_\mu^2}$. Here note that only the matrix $\alpha_4$ is even under time-reversal. In this work, we derive an analytical expression for $\theta$ in a time-reversal symmetry broken phase with the use of a field-theoretical method.

## 6.2 Theoretical Model

Let us consider a 3D lattice model with electron correlation and spin-orbit coupling. The model we adopt is the extended Fu-Kane-Mele-Hubbard model on a diamond lattice at half-filling, in which the Hamiltonian is given by $H = H_0 + H_{\text{int}}$ with the non-interacting part

$$H_0 = \sum_{\langle i,j \rangle, \sigma} t_{ij} c_{i\sigma}^\dagger c_{j\sigma} + i\frac{4\lambda}{a^2} \sum_{\langle\langle i,j \rangle\rangle} c_i^\dagger \boldsymbol{\sigma} \cdot (d_{ij}^1 \times d_{ij}^2) c_j, \tag{6.4}$$
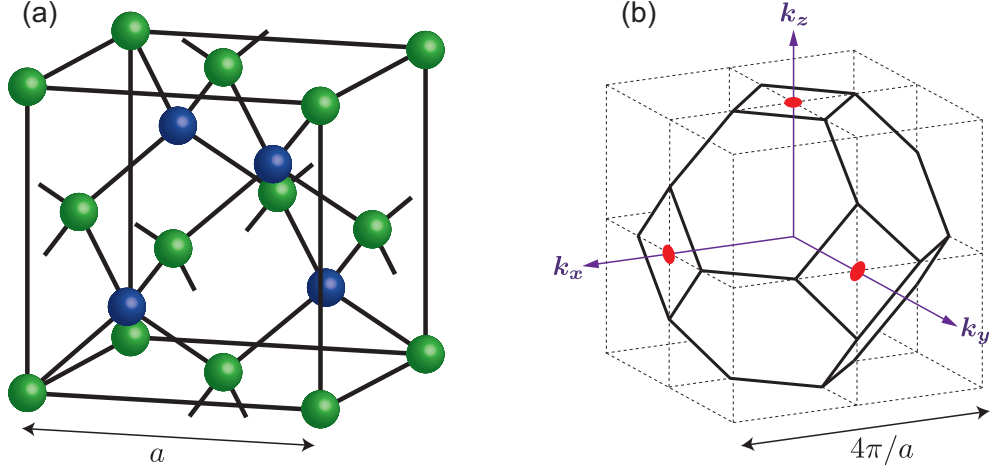
Figure 6.2: (a) A diamond lattice, which consists of two sublattices (green and blue), and each sublattice forms a fcc lattice. (b) The first Brillouin zone of a fcc lattice. Red circles represent the $X$ points.

and the interaction part

$$H_{\text{int}} = U \sum_i n_{i\uparrow} n_{i\downarrow} + \sum_{\langle i,j \rangle} V_{ij} n_i n_j, \tag{6.5}$$

where $c_{i\sigma}^\dagger$ is an electron creation operator at a site $i$ with spin $\sigma (=\uparrow, \downarrow)$, $n_{i\sigma} = c_{i\sigma}^\dagger c_{i\sigma}$, $n_i = n_{i\uparrow} + n_{i\downarrow}$, and $a$ is the lattice constant of the fcc lattice. The first and second terms of $H_0$ represent the nearest-neighbor hopping and the next-nearest-neighbor spin-orbit coupling, respectively. $d_{ij}^1$ and $d_{ij}^2$ are the two vectors which connect two sites $i$ and $j$ of the same sublattice. They are given by two of the four nearest-neighbor vectors, $\frac{a}{4}(1,1,1)$, $\frac{a}{4}(-1,-1,1)$, $\frac{a}{4}(1,-1,-1)$, and $\frac{a}{4}(-1,1,-1)$, with proper signs (directions of the vectors). $\boldsymbol{\sigma} = (\sigma_1, \sigma_2, \sigma_3)$ are the Pauli matrices for the spin degree of freedom. The first and second terms of $H_{\text{int}}$ describe the on-site and nearest-neighbor repulsive electron-electron interactions, respectively. The lattice structure of a diamond lattice is shown in Fig. 6.2(a).

It is convenient to express the non-interacting part $H_0$ of the Hamiltonian in terms of the $4 \times 4$ alpha (gamma) matrices. The diamond lattice consists of two sublattices ($A$ and $B$), with each sublattice forming a fcc lattice. In such a case, we can define the basis $c_{\boldsymbol{k}} \equiv [c_{\boldsymbol{k}A\uparrow}, c_{\boldsymbol{k}A\downarrow}, c_{\boldsymbol{k}B\uparrow}, c_{\boldsymbol{k}B\downarrow}]^T$ where the wave vector $\boldsymbol{k}$ is given by the points in the first Brillouin zone of the fcc lattice [see Fig. 6.2(b)]. Then the single-particle Hamiltonian $\mathcal{H}_0(\boldsymbol{k})$ [$H_0 \equiv \sum_{\boldsymbol{k}} c_{\boldsymbol{k}}^\dagger \mathcal{H}_0(\boldsymbol{k}) c_{\boldsymbol{k}}$] is written as [11, 12]

$$\mathcal{H}_0(\boldsymbol{k}) = \sum_{\mu=1}^{5} R_\mu(\boldsymbol{k}) \alpha_\mu, \tag{6.6}$$

where the coefficients $R_\mu(\boldsymbol{k})$ are given by

$$\begin{aligned}
R_1(\boldsymbol{k}) &= \lambda[\sin u_2 - \sin u_3 - \sin(u_2 - u_1) + \sin(u_3 - u_1)], \\
R_2(\boldsymbol{k}) &= \lambda[\sin u_3 - \sin u_1 - \sin(u_3 - u_2) + \sin(u_1 - u_2)], \\
R_3(\boldsymbol{k}) &= \lambda[\sin u_1 - \sin u_2 - \sin(u_1 - u_3) + \sin(u_2 - u_3)], \\
R_4(\boldsymbol{k}) &= t + \delta t_1 + t(\cos u_1 + \cos u_2 + \cos u_3), \\
R_5(\boldsymbol{k}) &= t(\sin u_1 + \sin u_2 + \sin u_3).
\end{aligned} \tag{6.7}$$

Here $u_1 = \mathbf{k} \cdot \mathbf{a}_1$, $u_2 = \mathbf{k} \cdot \mathbf{a}_2$, and $u_3 = \mathbf{k} \cdot \mathbf{a}_3$ with $\mathbf{a}_1 = \frac{a}{2}(0, 1, 1)$, $\mathbf{a}_2 = \frac{a}{2}(1, 0, 1)$ and $\mathbf{a}_3 = \frac{a}{2}(1, 1, 0)$ being the primitive translation vectors. In the following, we set $a = 1$. The $4 \times 4$ alpha matrices $\alpha_\mu$ are given by the chiral representation:

$$\alpha_j = \begin{bmatrix} \sigma_j & 0 \\ 0 & -\sigma_j \end{bmatrix}, \qquad \alpha_4 = \begin{bmatrix} 0 & 1 \\ 1 & 0 \end{bmatrix}, \qquad \alpha_5 = \begin{bmatrix} 0 & -i \\ i & 0 \end{bmatrix}, \tag{6.8}$$

where $j = 1, 2, 3$. In the present basis, the time-reversal operator and spatial inversion (parity) operator are given by $\mathcal{T} = \mathbf{1} \otimes (-i\sigma_2)\mathcal{K}$ ($\mathcal{K}$ is the complex conjugation operator) and $\mathcal{P} = \tau_1 \otimes \mathbf{1}$, respectively. We have introduced the hopping strength anisotropy $\delta t_1$ due to the lattice distortion along the [111] direction. Namely, we have set such that $t_{ij} = t + \delta t_1$ for the [111] direction, and $t_{ij} = t$ for the other three directions. When $\delta t_1 = 0$, the system is a semimetal, i.e., the energy bands touch at the three points $X^r = 2\pi(\delta_{rx}, \delta_{ry}, \delta_{rz})$ ($r = x, y, z$). Finite $\delta t_1$ opens a gap of $2|\delta t_1|$ at the $X^r$ points.

The $Z_2$ invariant of the system is given by

$$(-1)^{\gamma_0} = \prod_{i=1}^{8} \mathrm{sgn} \left[ t + \delta t_1 + t \sum_{p=1}^{3} \cos \left( \mathbf{\Gamma}_i \cdot \mathbf{a}_p \right) \right] = \begin{cases} -1 & (0 < \delta t_1 < 2t) \\ +1 & (\delta t_1 < 0 \text{ or } \delta t_1 > 2t). \end{cases} \tag{6.9}$$

where $\mathbf{\Gamma}_i$ are the eight time-reversal invariant momenta: $(0, 0, 0)$, $(2\pi, 0, 0)$, $(0, 2\pi, 0)$, $(0, 0, 2\pi)$, $(\pi, \pi, \pi)$, $(\pi, \pi, -\pi)$, $(\pi, -\pi, \pi)$, and $(-\pi, \pi, \pi)$. We see that the system is a topological insulator (normal insulator) when $0 < \delta t_1 < 2t$ ($\delta t_1 < 0$ or $\delta t_1 > 2t$). Note that in this paper we do not distinguish a weak topological insulator from a normal insulator.

Let us look at closely $\mathcal{H}_0(\mathbf{k})$ around the $X^r$ points. ,We obtain the low-energy effective Hamiltonian near the Fermi level around each $X$ point by setting $\mathbf{k} = X^r + \mathbf{q}$ and retaining the terms up to the order of $q$ [11, 12]. Around the $X^x$ point, we have $\mathbf{k} \cdot \mathbf{a}_1 = (q_y + q_z)/2$, $\mathbf{k} \cdot \mathbf{a}_2 = (2\pi + q_x + q_z)/2$, and $\mathbf{k} \cdot \mathbf{a}_3 = (2\pi + q_x + q_y)/2$ with $\mathbf{k} = X^x + \mathbf{q} = (2\pi + q_x, q_y, q_z)$. Then the coefficients $R_\mu(\mathbf{k})$ are approximated as

$$\begin{aligned} R_1(\mathbf{k}) &= \lambda \left[ \sin \left( \pi + \frac{q_x + q_z}{2} \right) - \sin \left( \pi + \frac{q_x + q_y}{2} \right) - \sin \left( \pi + \frac{q_x - q_y}{2} \right) + \sin \left( \pi + \frac{q_x - q_z}{2} \right) \right] \\ &\simeq \lambda \left( -\frac{q_x + q_z}{2} + \frac{q_x + q_y}{2} + \frac{q_x - q_y}{2} - \frac{q_x - q_z}{2} \right) = 0, \end{aligned}$$
$$\tag{6.10}$$

$$R_2(\mathbf{k}) \simeq \lambda \left( -\frac{q_x + q_y}{2} - \frac{q_y + q_z}{2} - \frac{q_y - q_z}{2} - \frac{q_y - q_x}{2} \right) = -2\lambda q_y, \tag{6.11}$$

$$R_3(\mathbf{k}) \simeq \lambda \left( \frac{q_y + q_z}{2} + \frac{q_x + q_z}{2} + \frac{q_z - q_x}{2} + \frac{q_z - q_y}{2} \right) = 2\lambda q_z, \tag{6.12}$$

$$R_4(\mathbf{k}) \simeq t + \delta t_1 + t(1 - 1 - 1) = \delta t_1, \tag{6.13}$$

$$R_5(\mathbf{k}) \simeq t \left( \frac{q_y + q_z}{2} - \frac{q_x + q_z}{2} - \frac{q_x + q_y}{2} \right) = -t q_x. \tag{6.14}$$

Finally the effective Hamiltonians around the $X^x$ point is given by

$$\mathcal{H}_0(X^x + \boldsymbol{q}) = tq_x\alpha_5 + 2\lambda q_y\alpha_2 - 2\lambda q_z\alpha_3 + \delta t_1\alpha_4. \tag{6.15}$$

Similarly, we obtain the effective Hamiltonians around the $X^y$ and $X^z$ points as

$$\begin{aligned}
\mathcal{H}_0(X^y + \boldsymbol{q}) &= tq_y\alpha_5 + 2\lambda q_z\alpha_3 - 2\lambda q_x\alpha_1 + \delta t_1\alpha_4, \\
\mathcal{H}_0(X^z + \boldsymbol{q}) &= tq_z\alpha_5 + 2\lambda q_x\alpha_1 - 2\lambda q_y\alpha_2 + \delta t_1\alpha_4.
\end{aligned} \tag{6.16}$$

Note that we have redefined $\boldsymbol{q}$ as $\boldsymbol{q} \to -\boldsymbol{q}$. These are so-called the Dirac Hamiltonian. For example, the energy spectrum around the $X^x$ point is readily obtained as

$$E(X^x + \boldsymbol{q}) = \pm\sqrt{(tq_x)^2 + (2\lambda q_y)^2 + (2\lambda q_z)^2 + (\delta t_1)^2}. \tag{6.17}$$

As mentioned above, we see that the system is gapless when $\delta t_1 = 0$ and nonzero $\delta t_1$ is regarded as the mass of the Dirac quasiparticles. At each $X^r$ point, one of the three components which originate from spin-orbit coupling $R_r(\boldsymbol{k})$ disappears and instead $R_5(\boldsymbol{k})$ compensates for the $q_r$-dependence of the effective Hamiltonian.

# 6.3 Mean-Field Phase Diagram

## 6.3.1 Spin-Density Wave Instability

Let us perform the mean-field approximation to the interaction term and derive the mean-field Hamiltonian of the system. First we consider the spin-density wave (SDW) instability. To do this, we firstly approximate the on-site interaction $H_U = U\sum_i n_{i\uparrow}n_{i\downarrow}$ as

$$H_U \approx U\sum_i \left[ \langle n_{i\downarrow}\rangle n_{i\uparrow} + \langle n_{i\uparrow}\rangle n_{i\downarrow} - \langle n_{i\uparrow}\rangle\langle n_{i\downarrow}\rangle - \langle c_{i\uparrow}^\dagger c_{i\downarrow}\rangle c_{i\downarrow}^\dagger c_{i\uparrow} - \langle c_{i\downarrow}^\dagger c_{i\uparrow}\rangle c_{i\uparrow}^\dagger c_{i\downarrow} + \langle c_{i\uparrow}^\dagger c_{i\downarrow}\rangle\langle c_{i\downarrow}^\dagger c_{i\uparrow}\rangle \right]. \tag{6.18}$$

Due to the spin-orbit coupling, the spin SU(2) symmetry is broken and the orientations of the spins are coupled to the lattice structure. We assume the antiferromagnetic ordering between the two sublattices in terms of the spherical coordinate $(m, \theta, \varphi)$:

$$\begin{aligned}
\langle \boldsymbol{S}_{i'A}\rangle = -\langle \boldsymbol{S}_{i'B}\rangle &= (m\sin\theta\cos\varphi, m\sin\theta\sin\varphi, m\cos\theta) \\
&\equiv m_1\boldsymbol{e}_x + m_2\boldsymbol{e}_y + m_3\boldsymbol{e}_z,
\end{aligned} \tag{6.19}$$

where $\langle \boldsymbol{S}_{i'\mu}\rangle = \frac{1}{2}\langle c_{i'\mu\alpha}^\dagger \boldsymbol{\sigma}_{\alpha\beta} c_{i'\mu\beta}\rangle$ ($\mu = A, B$) with $i'$ denoting the $i'$-th unit cell. It follows that

$$\langle n_{iA\uparrow}\rangle = \frac{2m_z + n_A}{2}, \quad \langle n_{iA\downarrow}\rangle = \frac{-2m_z + n_A}{2}, \quad \langle c_{iA\uparrow}^\dagger c_{iA\downarrow}\rangle = m_x + im_y, \quad \langle c_{iA\downarrow}^\dagger c_{iA\uparrow}\rangle = m_x - im_y$$

$$\langle n_{iB\uparrow}\rangle = \frac{-2m_z + n_B}{2}, \quad \langle n_{iB\downarrow}\rangle = \frac{2m_z + n_B}{2}, \quad \langle c_{iB\uparrow}^\dagger c_{iB\downarrow}\rangle = -m_x - im_y, \quad \langle c_{iB\downarrow}^\dagger c_{iB\uparrow}\rangle = -m_x + im_y. \tag{6.20}$$

Then after a calculation, the Hartree term is given by

$$U\sum_i \left[ -\langle n_{i\uparrow}\rangle\langle n_{i\downarrow}\rangle + \langle c_{i\uparrow}^\dagger c_{i\downarrow}\rangle\langle c_{i\downarrow}^\dagger c_{i\uparrow}\rangle \right] = 2NU\sum_f m_f^2, \tag{6.21}$$

and the Fock term is given by

$$U \sum_i \left[ \langle n_{i\downarrow} \rangle n_{i\uparrow} + \langle n_{i\uparrow} \rangle n_{i\downarrow} - \langle c_{i\uparrow}^\dagger c_{i\downarrow} \rangle c_{i\downarrow}^\dagger c_{i\uparrow} - \langle c_{i\downarrow}^\dagger c_{i\uparrow} \rangle c_{i\uparrow}^\dagger c_{i\downarrow} \right]$$

$$= -U \sum_{i'} \sum_{f=1,2,3} c_{i'A}^\dagger [m_f \sigma_f] c_{i'A} + U \sum_{i'} \sum_{f=1,2,3} c_{i'B}^\dagger [m_f \sigma_f] c_{i'B} \qquad (6.22)$$

$$= -U \sum_{\boldsymbol{k}} c_{\boldsymbol{k}}^\dagger [m_1 \alpha_1 + m_2 \alpha_2 + m_3 \alpha_3] c_{\boldsymbol{k}},$$

where $N$ is the number of the unit cells and the wave vectors $\boldsymbol{k}$ take $N$ points in the first Brillouin zone of the fcc lattice. This equation means that the on-site interaction term has the same matrix form as the spin-orbit interaction term in the mean-field level. A similar result has been obtained in the Kane-Mele-Hubbard model on a honeycomb lattice [76]. Here we have omitted irrelevant constant terms in Eqs. (6.21) and (6.22).

Secondly, we approximate the nearest-neighbor interaction $H_V = \sum_{\langle i,j \rangle} V_{ij} n_i n_j$ as

$$H_V \approx - \sum_{\langle i,j \rangle} \sum_{\sigma,\sigma'} V_{ij} \left[ \langle c_{i\sigma}^\dagger c_{j\sigma'} \rangle c_{j\sigma'}^\dagger c_{i\sigma} + \langle c_{j\sigma'}^\dagger c_{i\sigma} \rangle c_{i\sigma}^\dagger c_{j\sigma'} - \langle c_{i\sigma}^\dagger c_{j\sigma'} \rangle \langle c_{j\sigma'}^\dagger c_{i\sigma} \rangle \right]. \qquad (6.23)$$

We assume that the values of $\langle c_{i\sigma}^\dagger c_{j\sigma'} \rangle$ depend on the hopping strength, namely we set $\langle c_{i\sigma}^\dagger c_{j\sigma'} \rangle = -\Delta \delta_{\sigma\sigma'} t_{ij}/t$. On the other hand, we neglect the interaction strength anisotropy due to the lattice distortion for simplicity, i.e., we set $V_{ij} = V$. This does not change the resulting phase diagram qualitatively. After a calculation, we obtain

$$H_V^{\mathrm{MF}} = 2NV \left[ 3 + (1 + \delta t_1/t)^2 \right] \Delta^2 + V\Delta/t \sum_{\langle i,j \rangle, \sigma} t_{ij} c_{i\sigma}^\dagger c_{j\sigma}. \qquad (6.24)$$

Finally combining Eqs. (6.6), (6.21), (6.22), and (6.24), the mean-field Hamiltonian of the system is given by

$$H_{\mathrm{SDW}}^{\mathrm{MF}} = 2NUm^2 + 2NV \left[ 3 + (1 + \delta t_1/t)^2 \right] \Delta^2 + \sum_{\boldsymbol{k}} c_{\boldsymbol{k}}^\dagger \left[ \sum_{\mu=1}^5 \tilde{R}_\mu(\boldsymbol{k}) \alpha_\mu \right] c_{\boldsymbol{k}}, \qquad (6.25)$$

where $\tilde{R}_1(\boldsymbol{k}) = R_1(\boldsymbol{k}) - Um_1$, $\tilde{R}_2(\boldsymbol{k}) = R_2(\boldsymbol{k}) - Um_2$, $\tilde{R}_3(\boldsymbol{k}) = R_3(\boldsymbol{k}) - Um_3$, $\tilde{R}_4(\boldsymbol{k}) = (1 + V\Delta/t)R_4(\boldsymbol{k})$, and $\tilde{R}_5(\boldsymbol{k}) = (1 + V\Delta/t)R_5(\boldsymbol{k})$. Note that $m_1^2 + m_2^2 + m_3^2 = m^2$. The free energy at zero temperature for the SDW instability is readily obtained as

$$F_{\mathrm{SDW}}(m, \theta, \varphi, \Delta) = 2NUm^2 + 2NV \left[ 3 + (1 + \delta t_1/t)^2 \right] \Delta^2 - 2 \sum_{\boldsymbol{k}} \sqrt{\sum_{\mu=1}^5 \left[ \tilde{R}_\mu(\boldsymbol{k}) \right]^2}. \qquad (6.26)$$

## 6.3.2 Charge-Density Wave Instability

Next we consider the charge-density wave (CDW) instability. To do this, we approximate the interaction terms $H_U$ and $H_V$ as

$$H_U \approx U \sum_i \left[ \langle n_{i\downarrow} \rangle n_{i\uparrow} + \langle n_{i\uparrow} \rangle n_{i\downarrow} - \langle n_{i\uparrow} \rangle \langle n_{i\downarrow} \rangle \right], \qquad (6.27)$$

$$H_V \approx \sum_{\langle i,j \rangle} V_{ij} \Big\{ \langle n_i \rangle n_j + \langle n_j \rangle n_i - \langle n_i \rangle \langle n_j \rangle - \sum_{\sigma,\sigma'} \Big[ \langle c^\dagger_{i\sigma} c_{j\sigma'} \rangle c^\dagger_{j\sigma'} c_{i\sigma} \\ + \langle c^\dagger_{j\sigma'} c_{i\sigma} \rangle c^\dagger_{i\sigma} c_{j\sigma'} - \langle c^\dagger_{i\sigma} c_{j\sigma'} \rangle \langle c^\dagger_{j\sigma'} c_{i\sigma} \rangle \Big] \Big\}. \tag{6.28}$$

We assume a charge imbalance between the two sublattices such that $\langle n_{i'A\sigma} \rangle = (1 + \rho)/2$ and $\langle n_{i'B\sigma} \rangle = (1 - \rho)/2$. As for $H_V$, we assume $\langle c^\dagger_{i\sigma} c_{j\sigma'} \rangle = -\Delta \delta_{\sigma\sigma'} t_{ij}/t$ and $V_{ij} = V$ as in the case of SDW instability. Then the mean-field Hamiltonian of the interaction term is obtained as

$$H^{\mathrm{MF}}_{\mathrm{int}} = NC\rho^2 + 2NV \Big[ 3 + (1 + \delta t_1/t)^2 \Big] \Delta^2 - C\rho \sum_{\boldsymbol{k}} c^\dagger_{\boldsymbol{k}} (\tau_3 \otimes 1) c_{\boldsymbol{k}} + V\Delta/t \sum_{\langle i,j \rangle,\sigma} t_{ij} c^\dagger_{i\sigma} c_{j\sigma}, \tag{6.29}$$

where $C = 4V - U/2$, $N$ is the number of the unit cells, and the wave vectors $\boldsymbol{k}$ take $N$ points in the first Brillouin zone of the fcc lattice. Combining Eqs. (6.6) and (6.29), we obtain the mean-field Hamiltonian of the system. The matrix $\tau_3 \otimes 1$ is different from the alpha matrices $\alpha_\mu$, and thus the free energy for the CDW instability is a little complicated but can be obtained analytically as

$$F_{\mathrm{CDW}}(\rho, \Delta) = NC\rho^2 + 2NV \Big[ 3 + (1 + \delta t_1/t)^2 \Big] \Delta^2 - \sum_{\boldsymbol{k}} \sum_{\epsilon = \pm 1} \sqrt{\tilde{R}^2 + C^2\rho^2 + 2C\rho\epsilon\sqrt{\gamma^2}}, \tag{6.30}$$

where $\tilde{R}^2 = \sum_{\mu=1}^5 [\tilde{R}_\mu(\boldsymbol{k})]^2$ and $\gamma^2 = \sum_{j=1}^3 [\tilde{R}_j(\boldsymbol{k})]^2$ with $\tilde{R}_1(\boldsymbol{k}) = R_1(\boldsymbol{k})$, $\tilde{R}_2(\boldsymbol{k}) = R_2(\boldsymbol{k})$, $\tilde{R}_3(\boldsymbol{k}) = R_3(\boldsymbol{k})$, $\tilde{R}_4(\boldsymbol{k}) = (1 + V\Delta/t)R_4(\boldsymbol{k})$, and $\tilde{R}_5(\boldsymbol{k}) = (1 + V\Delta/t)R_5(\boldsymbol{k})$.

### 6.3.3 Mean-Field Phase Diagram

First we consider the case of $V = 0$. In this case, there will not occur the CDW instability. To obtain the mean-field ground-state phase diagram, we have to minimize the free energy (6.26)
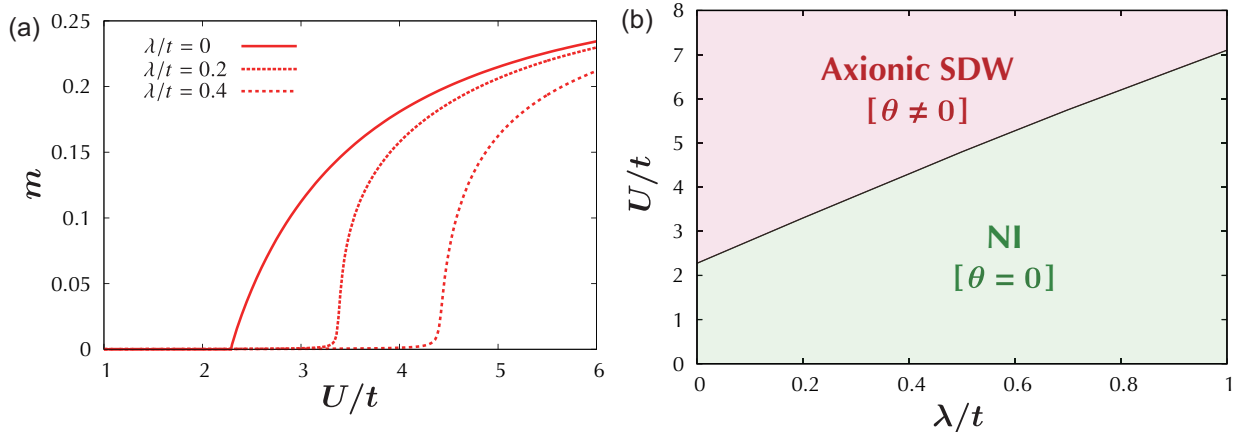


Figure 6.3: (a) $U$ dependence of the SDW order parameter $m$ with the antiferromagnetic ordering set to the [111] direction, i.e., with $\langle \boldsymbol{S}_{i'A} \rangle = -\langle \boldsymbol{S}_{i'B} \rangle = m\boldsymbol{e}_x + m\boldsymbol{e}_y + m\boldsymbol{e}_z$, when $V = 0$ and $\delta t_1/t = -0.4$. (b) Phase diagram with the antiferromagnetic ordering set to the [111] direction when $V = 0$ and $\delta t_1/t = -0.4$.
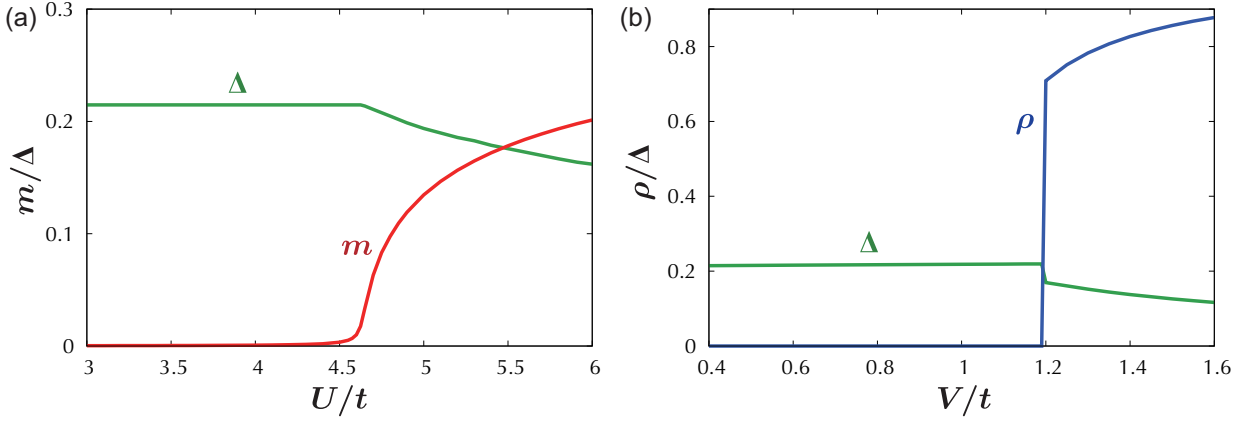
Figure 6.4: (a) $U$ dependences of the SDW order parameter $m$ and the hopping strength modification $\Delta$ with $V/t = 0.4$ and $\delta t_1/t = -0.4$. The antiferromagnetic ordering is set to the [111] direction. (b) $V$ dependences of the CDW order parameter $\rho$ and the hopping strength moidification $\Delta$ with $U/t = 3$ and $\delta t_1/t = -0.4$.

by the conditions $\partial F_{\mathrm{SDW}}/\partial m = \partial F_{\mathrm{SDW}}/\partial \theta = \partial F_{\mathrm{SDW}}/\partial \varphi = \partial F_{\mathrm{SDW}}/\partial \Delta = 0$. The spin SU(2) symmetry breaking due to the presence of spin-orbit coupling makes the procedure to obtain the true ground state complicated. Therefore we set the antiferromagnetic ordering to the [111] direction, i.e., we set $\langle \boldsymbol{S}_{i'A} \rangle = -\langle \boldsymbol{S}_{i'B} \rangle = m\boldsymbol{e}_x + m\boldsymbol{e}_y + m\boldsymbol{e}_z$ as an example. We have checked that the results for other directions are qualitatively the same as the [111] direction. Figure 6.3(a) shows the $U$ dependence of the SDW order parameter $m$. The transition from the normal insulator (or topological insulator) phase to the SDW phase is of the second order. We see from the phase diagram [Fig. 6.3(b)] that the critical strength of the on-site interaction $U_c$ becomes larger as the strength of the spin-orbit interaction $\lambda$ becomes larger. Such a behavior can be understood from that the free energy (6.26) is characterized by the factor $U/\lambda$ in $\tilde{R}_j(\boldsymbol{k})$ ($j = 1, 2, 3$). Namely, the strong spin-orbit interaction effectively makes the on-site interaction weaker. Similar results have been obtained in the Kane-Mele-Hubbard model, a 2D analog of our model [76, 78]. However, as is shown later, what is peculiar to the SDW phase in the 3D Fu-Kane-Mele-Hubbard model is the emergence of the topological magnetoelectric response described by the theta term [Eq. (6.1)].

Next we consider the case of $V \neq 0$. To obtain the mean-field ground-state phase diagram, we have to minimize the free energies (6.26) and (6.30) by the conditions $\partial F_{\mathrm{SDW}}/\partial m = \partial F_{\mathrm{SDW}}/\partial \theta = \partial F_{\mathrm{SDW}}/\partial \varphi = \partial F_{\mathrm{SDW}}/\partial \Delta = 0$ and $\partial F_{\mathrm{CDW}}/\partial \rho = \partial F_{\mathrm{CDW}}/\partial \Delta = 0$, and then we have to compare them. We set the antiferromagnetic ordering to the [111] direction, as in the case of $V = 0$. We have checked that the results for other directions are qualitatively the same as the [111] direction. It can be seen from Fig. 6.4 that the transition from the normal insulator (or topological insulator) phase to the SDW phase is of the second order, and that the transition from the normal insulator (or topological insulator) phase to the CDW phase is of the first order. The phase diagram with the antiferromagnetic ordering set to be the [111] direction is shown in Fig. 6.5 as an example. The phase diagrams for the other directions and for the positive $\delta t_1$ are qualitatively the same as Fig. 6.5. The values of $\Delta$ are always nonzero and positive when $V \neq 0$. The obtained phase diagram looks similar to those of conventional correlated electron systems (i.e., the Hubbard models) [145]. Namely, strong on-site electron-electron interaction induces SDW phase and strong nearest-neighbor electron-electron interaction induces CDW phase. However, note that other phases might be found when our model is studied beyond the mean-field approximation.
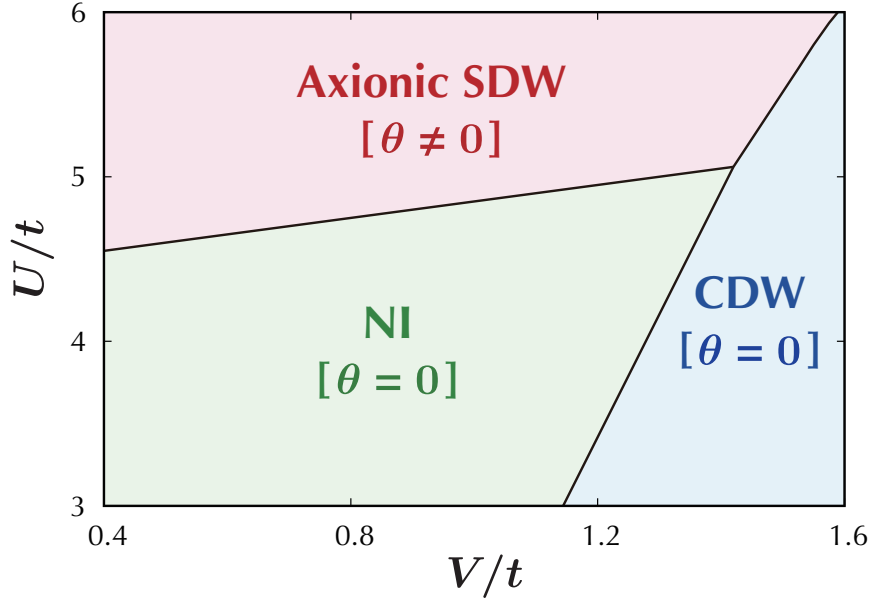
Figure 6.5: Mean-field phase diagram of the extended Fu-Kane-Mele-Hubbard model at half-filling. The strengths of the spin-orbit interaction and lattice distortion are $\lambda/t = 0.4$ and $\delta t_1/t = -0.4$, respectively. The antiferromagnetic ordering is set to be the [111] direction as an example, i.e., we have set $\langle S_{i'A} \rangle = -\langle S_{i'B} \rangle = m e_x + m e_y + m e_z$. The spin-density wave (SDW) and charge-density wave (CDW) phases are given by nonzero $m$ and $\rho$, respectively. When $m = \rho = 0$, the system is a normal insulator (NI). In all the phases, $\Delta$ take nonzero positive values. In the SDW phase, the topological magnetoelectric response described by the theta term [Eq. (6.1)] arises.

Actually, another phase has been reported between the SDW and CDW phases by studies beyond the mean-field approximation, for example, in the half-filled one-dimensional extended Hubbard model [146, 147]. As is shown later, what is different from usual systems in our model is that the topological magnetoelectric response due to the existence of the theta term can arise in the SDW phase. In this sense, we call the SDW phase in our model the "axionic SDW" (or the "axionic antiferromagnetic insulator"). For the purpose of this study, that we derive the theta term in a time-reversal symmetry broken phase, we focus on the SDW phase in the following.

## 6.4 Magnetoelectric Response of the Antiferromagnetic Insulator Phase

### 6.4.1 Low-Energy Effective Hamiltonian

Let us investigate the properties of the SDW phase, namely the antiferromagnetic insulator phase. We consider the general case characterized by the order parameter (6.19). When $U m_f \ll 2\lambda$ ($f = 1, 2, 3$), we can derive the Dirac Hamiltonian around the $\tilde{X}^r$ points which are slightly

deviated from the $X^r$ points:

$$\mathcal{H}(\tilde{X}^x + \boldsymbol{q}) = t'q_x\alpha_5 + 2\lambda q_y\alpha_2 - 2\lambda q_z\alpha_3 + \delta t'_1\alpha_4 - Um_1\alpha_1,$$
$$\mathcal{H}(\tilde{X}^y + \boldsymbol{q}) = t'q_y\alpha_5 + 2\lambda q_z\alpha_3 - 2\lambda q_x\alpha_1 + \delta t'_1\alpha_4 - Um_2\alpha_2, \tag{6.31}$$
$$\mathcal{H}(\tilde{X}^z + \boldsymbol{q}) = t'q_z\alpha_5 + 2\lambda q_x\alpha_1 - 2\lambda q_y\alpha_2 + \delta t'_1\alpha_4 - Um_3\alpha_3,$$

where $t' = t(1 + V\Delta/t)$, $\delta t'_1 = \delta t_1(1 + V\Delta/t)$, $\tilde{X}^x = \left(2\pi, \frac{Um_2}{2\lambda}, -\frac{Um_3}{2\lambda}\right)$, $\tilde{X}^y = \left(-\frac{Um_1}{2\lambda}, 2\pi, \frac{Um_3}{2\lambda}\right)$, and $\tilde{X}^z = \left(\frac{Um_1}{2\lambda}, -\frac{Um_2}{2\lambda}, 2\pi\right)$. For example, the energy spectrum around the $\tilde{X}^x$ point is readily obtained as

$$E(\tilde{X}^x + \boldsymbol{q}) = \pm\sqrt{(t'q_x)^2 + (2\lambda q_y)^2 + (2\lambda q_z)^2 + (\delta t'_1)^2 + (Um_1)^2}. \tag{6.32}$$

We see from Eq. (6.31) that the antiferromagnetic ordering opens a gap at the $\tilde{X}^r$ points, i.e., lowers the energy of the system. When $Um_f$ is not small compared to $2\lambda$, it is not apparent that the Dirac Hamiltonian can be derived. Thus in the following, we assume that $Um_f$ is small, although it is expected that the momentum points around which the Dirac Hamiltonians can be derived exist even when $Um_f$ is not small.

Let us analyze Eq. (6.31). The important point is that all the five alpha matrices which anticommute with each other are used. To be specific, let us first consider $\mathcal{H}(\tilde{X}^x + \boldsymbol{q})$. We can redefine the alpha matrices because the representation of the matrices is arbitrary. Redefining such that $\alpha_5 \to \alpha_1$, $\alpha_3 \to -\alpha_3$, and $\alpha_1 \to -\alpha_5$ ($\alpha_5 = \alpha_1\alpha_2\alpha_3\alpha_4$) for the alpha matrices, and $t'q_x \to q_x$, $2\lambda q_y \to q_y$, and $2\lambda q_z \to q_z$ for the wave vector [1], we obtain

$$\mathcal{H}(\tilde{X}^x + \boldsymbol{q}) = q_x\alpha_1 + q_y\alpha_2 + q_z\alpha_3 + \delta t'_1\alpha_4 + Um_1\alpha_5. \tag{6.33}$$

In the same manner, $\mathcal{H}(\tilde{X}^y + \boldsymbol{q})$ and $\mathcal{H}(\tilde{X}^z + \boldsymbol{q})$ can be rewritten as

$$\mathcal{H}(\tilde{X}^y + \boldsymbol{q}) = q_x\alpha_1 + q_y\alpha_2 + q_z\alpha_3 + \delta t'_1\alpha_4 + Um_2\alpha_5,$$
$$\mathcal{H}(\tilde{X}^z + \boldsymbol{q}) = q_x\alpha_1 + q_y\alpha_2 + q_z\alpha_3 + \delta t'_1\alpha_4 + Um_3\alpha_5. \tag{6.34}$$

We see that all the three effective Hamiltonians above are equivalent. Hence we can regard the Dirac quasiparticles around the $\tilde{X}^r$ points as the quasiparticles of three flavors characterized by their masses $Um_f$. Note that the mass of Dirac quasiparticles $\delta t_1$ is renormalized to be $\delta t'_1$ due to the nearest neighbor electron-electron interaction, and that the second mass $Um_f$ is induced by the on-site interaction.

## 6.4.2 The Theta Term

Here we derive the theta term in the antiferromagnetic insulator phase, in the same way as that of 3D topological insulators is derived. From the discussion above, we can write down the low-energy effective (Euclidean) action of the system, i.e., the action of the Dirac quasiparticles interacting with an external electromagnetic field $A_\mu$ as

$$S_{\text{AFI}} = \int d^4x \sum_{f=1,2,3} \bar{\psi}_f(x) \left[\gamma_\mu D_\mu - M_f e^{i\kappa_f\gamma_5}\right] \psi_f(x), \tag{6.35}$$

---

[1] When interacting with an electromagnetic field, the vector potential $\boldsymbol{A}$ is rescaled as well as the spatial coordinate $\boldsymbol{x}$. Then we see that the theta term (6.44) is invariant under rescaling. Namely, the value of $\theta$ does not depend on the values of $\lambda$ and $t$ in the low-energy limit.

where $\psi_f(x)$ is a four-component spinor, $D_\mu = \partial_\mu + ieA_\mu$, $M_f = \sqrt{(\delta t_1')^2 + (Um_f)^2}$, $\cos \kappa_f = |\delta t_1'|/M_f$, $\sin \kappa_f = Um_f/M_f$, and we have used the fact that $\alpha_4 = \gamma_0$, $\alpha_5 = -i\gamma_0\gamma_5$ and $\alpha_j = \gamma_0\gamma_j$ ($j = 1, 2, 3$). The subscript $f$ denotes the flavor. Here we have considered the case of $\delta t_1' < 0$, namely the system is a normal insulator when the interactions are weak.

We follow the Fujikawa's method [27, 28] and write down a calculation briefly in what follows. Let us consider a infinitesimal chiral transformation for each flavor:

$$\psi_f \to \psi_f' = e^{-i\kappa_f d\phi\gamma_5/2}\psi_f, \quad \bar{\psi}_f \to \bar{\psi}_f' = \bar{\psi}_f e^{-i\kappa_f d\phi\gamma_5/2}, \tag{6.36}$$

where $\phi \in [0, 1]$. The theta term is generated as a consequence of the chiral anomaly after the transformation. The partition function is transformed as

$$Z = \int \mathcal{D}[\psi, \bar{\psi}]e^{-S_{\mathrm{AFI}}[\psi, \bar{\psi}]} \to Z' = \int \mathcal{D}[\psi', \bar{\psi}']e^{-S_{\mathrm{AFI}}[\psi', \bar{\psi}']}. \tag{6.37}$$

The integrands in Eq. (6.35) is transformed as

$$\begin{aligned}\bar{\psi}_f M_f e^{i\kappa_f\gamma_5}\psi_f &\to \bar{\psi}_f M_f e^{i\kappa_f(1-d\phi)\gamma_5}\psi_f,\\\bar{\psi}_f\gamma_\mu D_\mu\psi_f &\to \bar{\psi}_f\gamma_\mu D_\mu\psi_f + (i/2)\kappa_f d\phi\partial_\mu(\bar{\psi}_f\gamma_\mu\gamma_5\psi_f).\end{aligned} \tag{6.38}$$

Then defining the Jacobian $J_f$ which is induced by the chiral transformation for each flavor $\mathcal{D}[\psi_f, \bar{\psi}_f] \to J_f\mathcal{D}[\psi_f, \bar{\psi}_f]$, the partition function becomes

$$Z' = \int \mathcal{D}[\psi, \bar{\psi}]e^{-S' + \frac{i}{2}\sum_f \kappa_f \int d^4x d\phi\partial_\mu(\bar{\psi}_f\gamma_\mu\gamma_5\psi_f) + \sum_f \ln J_f}, \tag{6.39}$$

where

$$S' = \int d^4x \sum_f \bar{\psi}_f(x)\left[\gamma_\mu D_\mu - M_f e^{i\kappa_f(1-d\phi)\gamma_5}\right]\psi_f(x), \tag{6.40}$$

and the Jacobian $J_f$ is calculated to be [27, 28]

$$J_f = \exp\left[-i\int d^4x d\phi\frac{\kappa_f e^2}{32\pi^2\hbar c}\epsilon^{\mu\nu\rho\lambda}F_{\mu\nu}F_{\rho\lambda}\right]. \tag{6.41}$$

Here $F_{\mu\nu} = \partial_\mu A_\nu - \partial_\nu A_\mu$ and we have written $\hbar$ and $c$ explicitly. We repeat this procedure infinite times, i.e., integrate the exponent of Eq. (6.39) over the variable $\phi$ from 0 to 1. Then we obtain

$$Z' = \int \mathcal{D}[\psi, \bar{\psi}]e^{-S_{\mathrm{NI}} + \frac{i}{2}\sum_f \kappa_f \int d^4x\partial_\mu(\bar{\psi}_f\gamma_\mu\gamma_5\psi_f) - S_\theta}, \tag{6.42}$$

where $S_{\mathrm{NI}}$ is the action which represents the normal insulator phase in the present case:

$$S_{\mathrm{NI}} = \int d^4x \sum_f \bar{\psi}_f(x)\left[\gamma_\mu D_\mu - M_f\right]\psi_f(x). \tag{6.43}$$

This is because the system with negative mass of the Dirac quasiparticles is identified from the $Z_2$ invariant as a normal insulator. $S_\theta$ is the theta term in the Euclidean spacetime:

$$S_\theta = i\int d^4x\frac{(\sum_f \kappa_f)e^2}{32\pi^2\hbar c}\epsilon^{\mu\nu\rho\lambda}F_{\mu\nu}F_{\rho\lambda}. \tag{6.44}$$

After dropping the irrelevant surface term [the second term of the exponent in Eq. (6.42)], we obtain the total action of the system as

$$S_{\text{AFI}} = S_{\text{NI}} + S_\theta. \tag{6.45}$$

Actually $S_\theta$ is also a surface term, since we can rewrite as $\epsilon^{\mu\nu\rho\lambda} F_{\mu\nu} F_{\rho\lambda} = 2\epsilon^{\mu\nu\rho\lambda} \partial_\mu (A_\nu F_{\rho\lambda})$. However, we are now interested in the magnetoelectric response of the system. Thus we denote the total action as above. Rewriting the theta term (6.44) in the real time ($t = -i\tau$), we obtain Eq. (6.1).

The value of $\theta$ in the antiferromagnetic insulator phase is given as $\theta = \sum_f \kappa_f = \sum_f \tan^{-1}(Um_f /|\delta t_1'|)$. It is known that $\theta = \pi$ (mod $2\pi$) in 3D topological insulators and is $\theta = 0$ in normal insulators. However, $\theta$ can be arbitrary if time-reversal symmetry of the system is broken. We can obtain the value of $\theta$ in the case of $\delta t_1 > 0$ in the same manner as above. Combining both cases, $\theta$ is written as

$$\theta = \frac{\pi}{2} \left[1 + \text{sgn}(\delta t_1)\right] - \sum_{f=1,2,3} \tan^{-1}\left[\frac{Um_f}{\delta t_1(1 + V\Delta/t)}\right], \tag{6.46}$$

where the condition that $Um_f \ll 2\lambda$ is required, and we have written $\delta t_1' = \delta t_1(1 + V\Delta/t)$ explicitly. Note that $(1 + V\Delta/t)$ is always positive, and thus the value of $\theta$ when $m_f = 0$ is determined by the sign of $\delta t_1$. The region where the value of $\theta$ becomes nonzero is shown in Fig. 6.5 as the "axionic SDW".

Here we consider the applicability of the expression (6.46) for the values of parameters. Let $\theta = \sum_f \theta_f$. When $\delta t_1 < 0$, we get $-\pi/2 < \tan^{-1}[Um_f/\delta t_1'] < 0$. Then in the limit $\delta t_1 \to 0^-$, we have $\theta_f = -\tan^{-1}[Um_f/\delta t_1'] \to \pi/2$. On the other hand, when $\delta t_1 > 0$, we get $0 < \tan^{-1}[Um_f/\delta t_1'] < \pi/2$. Then in the limit $\delta t_1 \to 0^+$, we have $\theta_f = \pi - \tan^{-1}[Um_f/\delta t_1'] \to \pi/2$. Namely, the value of $\theta_f$ is a smooth function of $\delta t_1$ in the range $0 < \theta_f < \pi$. Thus there is no constraint on the value of $\delta t_1$ in the expression (6.46). However, when $\delta t_1 = 0$, we obtain $\theta = -\sum_f (\pi/2)\text{sgn}(m_f)$, which means the value of $\theta$ is constant. As we shall see below, we are interested in the case where the dynamical axion field (i.e., the value of $\theta$ depends on space and time) is realized. Therefore, the value of $\delta t_1$ should be nonzero.

# 6.5 Discussions

It should be noted that the theta term is derived only in odd spatial dimensions. In the Kane-Mele-Hubbard model on the honeycomb lattice at half-filling, which is a two-dimensional analog of the Fu-Kane-Mele-Hubbard model, the antiferromagnetic insulator phase is also realized [76, 78, 80, 82, 85, 86]. However, the magnetoelectric response which results from the theta term does not appear in that model.

The origin that generates small deviations of the value of $\theta$ from 0 or $\pi$ in the antiferromagnetic insulator phase of the Fu-Kane-Mele-Hubbard model is the existence of the $\gamma_5$ (or $\alpha_5$ in our notation) term, which breaks time-reversal symmetry, in the low-energy effective action (6.35). What we would like to stress here is that we found the appearance of the $\gamma_5$ term in the antiferromagnetic insulator phase. This is not apparent at first sight of the mean-field Hamiltonian (6.25). Expanding the mean-field Hamiltonian around the $\tilde{X}$ points (which are slightly deviated from the original $X$ points) and relabeling the alpha matrices are essential.

In the following, we discuss two notable aspects of the antiferromagnetic insulator phase in our model.

### 6.5.1 Condensed-Matter Analog of the Aoki Phase in Lattice QCD

Here we mention the relation between the antiferromagnetic insulator phase in our model and the "Aoki phase", a phase with broken time-reversal and parity symmetries in lattice QCD. The Aoki phase is characterized as the phase induced by interactions with the $\gamma_5$ term, i.e., $\langle \bar{\psi} i \gamma_5 \psi \rangle \neq 0$ in addition to the usual mass renormalization $\langle \bar{\psi} \psi \rangle$ [128]. It can be seen from the effective Hamiltonian [Eqs. (6.33) and (6.34)] that the situation in our model is analogous. Thus it can be said that the antiferromagnetic insulator phase of the extended Fu-Kane-Mele-Hubbard model is a condensed matter analog of the Aoki phase in lattice QCD. In other words, the Aoki phase in condensed matter in three spatial dimensions can be characterized by the magnetoelectric response which results from the theta term with non-quantized value of $\theta$, i.e., by the axion electrodynamics. The existence of a similar condensed matter analog of the Aoki phase in three spatial dimensions has been pointed out in a 3D topological insulator with on-site interactions [89].

The Aoki phase has been found in lattice models for QCD such as the Wilson fermions [128, 130], the Nambu-Jona-Lasinio model on a lattice [148, 149], and the Gross-Neveu model on a lattice [128]. In the latter two models, the interactions are local. Namely, from the viewpoint of the form of interactions, it can be said that Hubbard-like models in condensed matter are similar to the Nambu-Jona-Lasinio model and the Gross-Neveu model. It is known that the existence of the Aoki phase can solve the U(1) problem in QCD. However, although the importance of the Aoki phase has been confirmed theoretically, the phase is not a realistic phase. This is because the phase is an artifact due to the nonzero lattice spacing of lattice QCD [130], and in addition, the appearance of the phase depends on the value of bare quark mass [128]. On the other hand, in condensed matter, electron systems can be naturally defined on lattices, and the value of the bare mass of Dirac fermions is tunable. In our model, as mentioned in Sec. 6.2, the value is determined by the strength of lattice distortion. Moreover, experimental searches in condensed matter are possible in principle. Further investigations of the Aoki phase in condensed matter might enable us to suggest some perception to the field of lattice QCD. This is an interesting future subject.

### 6.5.2 Dynamical Behavior of $\theta$

Let us consider briefly the dynamical behavior of $\theta$ in our model, the dynamical axion field, discussed in Ref. 67. When the spins fluctuate, i.e., when $\langle \boldsymbol{S}_A \rangle = -\langle \boldsymbol{S}_B \rangle = [m_1 + \delta m_1(\boldsymbol{r}, t)]\boldsymbol{e}_x + [m_2 + \delta m_2(\boldsymbol{r}, t)]\boldsymbol{e}_y + [m_3 + \delta m_3(\boldsymbol{r}, t)]\boldsymbol{e}_z$, we obtain the fluctuation of $\theta$ up to the linear order in $\delta m_f$ as

$$
\begin{aligned}
\delta\theta(\boldsymbol{r}, t) &\approx \sum_{f=1,2,3} \tan^{-1}\left\{ U\left[ m_f + \delta m_f(\boldsymbol{r}, t) \right] / |\delta t_1'| \right\} - \sum_{f=1,2,3} \tan^{-1}\left( U m_f / |\delta t_1'| \right) \\
&\approx U/|\delta t_1'| \sum_f \delta m_f(\boldsymbol{r}, t).
\end{aligned}
\tag{6.47}
$$

This equation suggests that the dynamical axion field can be realized by the fluctuations of the spins, i.e., the spin-wave excitations, as in the case of Ref. 67. An advantage of our analytical derivation of the expression of $\theta$ is that we can see the realization of the dynamical axion field immediately, as Eq. (6.47). In the case where we use expressions (6.2) or (6.3), it will not easy to notice the realization in our model.

Finally let us consider the consequence of the existence of the theta term in the antiferromagnetic insulator phase. Notice that the theta term (in real time) can be rewritten as

$$S_\theta = \int d^4x \frac{\theta(\boldsymbol{r},t)e^2}{8\pi^2\hbar c}\epsilon^{\mu\nu\rho\lambda}\partial_\mu A_\nu \partial_\rho A_\lambda = -\int d^4x \frac{e^2}{8\pi^2\hbar c}\epsilon^{\mu\nu\rho\lambda}[\partial_\mu\theta(\boldsymbol{r},t)]A_\nu\partial_\rho A_\lambda, \qquad (6.48)$$

where in the second equality, we have dropped the surface term and used $\epsilon^{\mu\nu\rho\lambda}\partial_\mu\partial_\rho A_\lambda = 0$. The induced current $\boldsymbol{j}$ can be obtained from the variation of the above action with respect to the vector potential $A_n$:

$$j^n = \frac{\delta S_\theta}{\delta A_n} = -\frac{e^2}{4\pi^2\hbar c}[\partial_\mu\theta(\boldsymbol{r},t)]\epsilon^{\mu n\rho\lambda}\partial_\rho A_\lambda = \frac{e^2}{2\pi\hbar c}(\boldsymbol{\nabla}\theta \times \boldsymbol{E} + \dot{\theta}\boldsymbol{B})_n, \qquad (6.49)$$

where $n = 1, 2, 3$, and $\dot{\theta} = \partial\theta/\partial t$. The electric-field induced term is the anomalous Hall effect, since it is perpendicular to the electric field. The magnetic-field induced term is the so-called chiral magnetic effect [47]. It is notable that the chiral magnetic effect can be realized. In other words, we propose a way to detect the dynamical axion field in condensed matter, which has not yet been observed experimentally. Similarly, we obtain the induced charge density $\rho$ as

$$\rho = \frac{\delta S_\theta}{\delta A_0} = -\frac{e^2}{4\pi^2\hbar c}[\partial_\mu\theta(\boldsymbol{r},t)]\epsilon^{\mu 0\rho\lambda}\partial_\rho A_\lambda = -\frac{e^2}{2\pi\hbar c}\boldsymbol{\nabla}\theta \cdot \boldsymbol{B}. \qquad (6.50)$$

# 6.6 Summary

In summary, we have studied the ground state and the topological magnetoelectric response described by the theta term, in the extended Fu-Kane-Mele-Hubbard model on a diamond lattice at half-filling, within the mean-field approximation. The mean-field phase diagram was presented. It was found that the transition from the normal insulator (or topological insulator) phase to the antiferromagnetic insulator phase is of the second-order. We obtained the Dirac-like low-energy effective Hamiltonian in the antiferromagnetic insulator phase. We found that there exists the $\gamma_5$ term in the effective Hamiltonian. This antiferromagnetic insulator phase is different from conventional one, and can be regarded as a condensed matter analog of a symmetry broken phase in lattice QCD. We derived the theta term by following the Fujikawa's method and obtained the analytical value of $\theta$. We have proposed a concrete model to describe the axion electrodynamics in the antiferromagnetic insulator phase. The dynamical axion field can be induced by the fluctuation of the order parameter. It was shown theoretically that the chiral magnetic effect can emerge as a consequence of the realization of the dynamical axion field. In other words, we proposed a way to detect the dynamical axion field in condensed matter, which has not yet been observed experimentally. In our model, the interplay of spin-orbit coupling and electron correlation results in the emergence of the topological magnetoelectric response and the realization of the dynamical axion field.

# Chapter 7

# Summary

So far we have studied the effects of electron correlations in three-dimensional (3D) spin-orbit coupled systems, based on the purpose of (1) studying the stability of 3D topological phases against strong long-range correlations, and (2) searching for novel phases and phenomena which result from the interplay of spin-orbit coupling and electron correlation. Here we would like to summarize the results obtained in this thesis.

## Stability of Three-dimensional Topological Phases

Preceding studies have mainly focused on the effects of short-range correlations in 2D topological phases. As for time-reversal invariant topological insulators, it has been shown that they are broken by time-reversal symmetry breaking orders. As for Weyl semimetals, it has been shown that they are broken by gap openings. However, the effects of long-range Coulomb interactions have not yet been revealed. One of the reasons might be on the point that it is not easy to treat strong long-range interactions properly. In order to solve this problem, we adopted the formalism based on the lattice gauge theory which has been originally used in the field of high energy
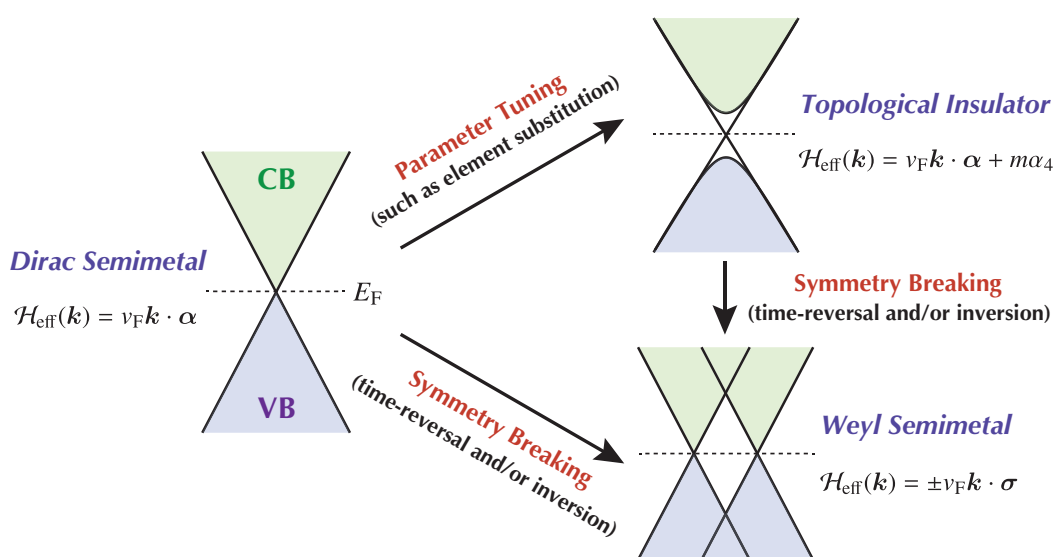


Figure 7.1: Schematic diagram of the relation of 3D topological insulators, Dirac semimetals and Weyl semimetals. $\alpha_\mu$ ($\sigma_\mu$) are $4 \times 4$ ($2 \times 2$) matrices.

physics, and recently applied to graphene. The lattice gauge theory enables us to treat strong interactions nonperturbatively. In the U(1) lattice gauge theory, the $1/r$ Coulomb interactions between bulk electrons are taken into account via a scalar field.

In this thesis, we studied the stability of a 3D topological insulator of $Bi_2Se_3$ type, a time-reversal symmetry broken Weyl semimetal with two nodes, and Dirac semimetals with four and sixteen nodes, against strong $1/r$ Coulomb interactions. 3D topological insulators such as $Bi_2Se_3$ are $p$-electron systems. This implies that on-site correlations are not strong. However, the strength of long-range correlations is determined by the dielectric constant of the system. In Weyl and Dirac semimetals, due to the vanishing density of states near the Fermi level, screening effects are expected to be weak. From these facts, long-range Coulomb interactions can be important in 3D topological phases we consider. Based on the strong coupling expansion of lattice gauge theories and the mean-field approximation, we analyzed the lattice models from the strong coupling limit. We considered all the possible order parameters in the mean-field decoupling process within the effective lattice models. It was found that all the three phases survive in the strong coupling limit. This suggests that 3D topological phases are stable against strong long-range correlations. Further, we proposed possible global phase diagrams. As shown in Fig. 7.1, 3D topological insulators, Weyl semimetals, and Dirac semimetals are related to each other. Namely, they lie next to each other in the phase diagrams. Therefore we believe the result that each phase survives in the strong coupling limit have a consistency. Our study will contribute to understanding the nature of 3D topological phases.

## Topological Magnetoelectric Response

It has been acknowledged that electron correlation and spin-orbit coupling play important roles respectively in condensed matter. Then it is natural to expect the emergence of novel phases and phenomena induced by the interplay of them. Motivated by this, we studied the electron correlation effects in a 3D spin-orbit coupled system, the Fu-Kane-Mele model on a diamond lattice. We focused on the topological magnetoelectric response in the antiferromagnetic insulator phase described by the theta term with non-quantized value of $\theta$. First we derived a low-energy effective action of the antiferromagnetic insulator phase. Then, in contrast to preceding studies, we derived an analytical expression for $\theta$ which is the most important result in this subject:

$$\theta = \frac{\pi}{2}\left[1 + \mathrm{sgn}(\delta t_1)\right] - \sum_{f=1,2,3} \tan^{-1}\left[\frac{Um_f}{\delta t_1(1 + V\Delta/t)}\right], \qquad (7.1)$$

where $m_f$ ($f = 1, 2, 3$) is the order parameter for the antiferromagnetism. When the spins (i.e., the order parameter) fluctuate around the ground-state direction, the deviation of $\theta$ is proportional to the deviation of $m_f$: $\delta\theta(\boldsymbol{r}, t) \propto \sum_f \delta m_f(\boldsymbol{r}, t)$. This means that the dynamical axion field can be realized by spin-wave excitations. As a consequence of the realization of the dynamical axion field, the following current can be induced by external electromagnetic fields:

$$\boldsymbol{j}(\boldsymbol{r}, t) = \frac{e^2}{2\pi h}\left[\boldsymbol{\nabla}\theta(\boldsymbol{r}, t) \times \boldsymbol{E} + \dot{\theta}(\boldsymbol{r}, t)\boldsymbol{B}\right], \qquad (7.2)$$

where $\dot{\theta} = \partial\theta/\partial t$. The first and second terms in the right-hand side represent the anomalous Hall effect and the chiral magnetic effect, respectively. It is notable that the chiral magnetic effect can be realized. In other words, we propose a way to detect the dynamical axion field in condensed matter, which has not yet been observed experimentally.

Further we pointed out that the antiferromagnetic insulator phase can be regarded as a condensed matter analog of the Aoki phase, a symmetry broken phase induced by interactions in lattice quantum chromodynamics (QCD). In the Aoki phase, massless pions emerge as a result of spontaneous breaking of parity and flavor symmetries. In other words, the Aoki phase in condensed matter in three spatial dimensions can be characterized by the magnetoelectric response which results from the theta term with non-quantized value of $\theta$, i.e., by the axion electrodynamics. Although the importance of the Aoki phase has been confirmed theoretically in lattice QCD, the Aoki phase is not a realistic phase. This is because the phase is an artifact due to the nonzero lattice spacing of lattice QCD, and in addition, the appearance of the phase depends on the value of bare quark mass. On the other hand, in condensed matter, electron systems can be naturally defined on lattices, and the value of the bare mass of Dirac fermions is tunable. Moreover, experimental searches in condensed matter are possible in principle. Further investigations of the Aoki phase in condensed matter might enable us to suggest some perception to the field of lattice QCD. We expect that our study enforces the connection between condensed matter physics and high energy physics.

# Acknowledgments

# Bibliography

[1] D. Thouless, M. Kohmoto, M. Nightingale, and M. den Nijs, Phys. Rev. Lett. **49**, 405 (1982).

[2] R. Kubo, J. Phys. Soc. Jpn. **12**, 570 (1957).

[3] M. Z. Hasan and C. L. Kane, Rev. Mod. Phys. **82**, 3045 (2010).

[4] X.-L. Qi and S.-C. Zhang, Rev. Mod. Phys. **83**, 1057 (2011).

[5] Y. Ando, J. Phys. Soc. Jpn. **82**, 102001 (2013).

[6] C. L. Kane and E. J. Mele, Phys. Rev. Lett. **95**, 226801 (2005).

[7] C. L. Kane and E. J. Mele, Phys. Rev. Lett. **95**, 146802 (2005).

[8] B. A. Bernevig and S.-C. Zhang, Phys. Rev. Lett. **96**, 106802 (2006).

[9] B. A. Bernevig, T. L. Hughes, and S.-C. Zhang, Science **314**, 1757 (2006).

[10] M. König, S. Wiedmann, C. Brüne, A. Roth, H. Buhmann, L. W. Molenkamp, X.-L. Qi, and S.-C. Zhang, Science **318**, 766 (2007).

[11] L. Fu and C. L. Kane, Phys. Rev. B **76**, 045302 (2007).

[12] L. Fu, C. L. Kane, and E. J. Mele, Phys. Rev. Lett. **98**, 106803 (2007).

[13] J. E. Moore and L. Balents, Phys. Rev. B **75**, 121306 (2007).

[14] D. Hsieh, D. Qian, L. Wray, Y. Xia, Y. S. Hor, R. J. Cava, and M. Z. Hasan, Nature **452**, 970 (2008).

[15] Y. Xia, D. Qian, D. Hsieh, L. Wray, A. Pal, H. Lin, A. Bansil, D. Grauer, Y. S. Hor, R. J. Cava, and M. Z. Hasan, Nat. Phys. **5**, 398 (2009).

[16] H. Zhang, C.-X. Liu, X.-L. Qi, X. Dai, Z. Fang, and S.-C. Zhang, Nat. Phys. **5**, 438 (2009).

[17] C.-X. Liu, X.-L. Qi, H. Zhang, X. Dai, Z. Fang, and S.-C. Zhang, Phys. Rev. B **82**, 045122 (2010).

[18] D. Hsieh, Y. Xia, D. Qian, L. Wray, J. H. Dil, F. Meier, J. Osterwalder, L. Patthey, J. G. Checkelsky, N. P. Ong, a V Fedorov, H. Lin, A. Bansil, D. Grauer, Y. S. Hor, R. J. Cava, and M. Z. Hasan, Nature **460**, 1101 (2009).

[19] P. Roushan, J. Seo, C. V Parker, Y. S. Hor, D. Hsieh, D. Qian, A. Richardella, M. Z. Hasan, R. J. Cava, and A. Yazdani, Nature **460**, 1106 (2009).

[20] J. H. Bardarson, J. TworzydÅĆo, P. W. Brouwer, and C. W. J. Beenakker, Phys. Rev. Lett. **99**, 106801 (2007).

[21] K. Nomura, M. Koshino, and S. Ryu, Phys. Rev. Lett. **99**, 146806 (2007).

[22] R. Yu, W. Zhang, H.-J. Zhang, S.-C. Zhang, X. Dai, and Z. Fang, Science **329**, 61 (2010).

[23] K. Nomura and N. Nagaosa, Phys. Rev. Lett. **106**, 166802 (2011).

[24] C.-Z. Chang, J. Zhang, X. Feng, J. Shen, Z. Zhang, M. Guo, K. Li, Y. Ou, P. Wei, L.-L. Wang, Z.-Q. Ji, Y. Feng, S. Ji, X. Chen, J. Jia, X. Dai, Z. Fang, S.-C. Zhang, K. He, Y. Wang, L. Lu, X.-C. Ma, and Q.-K. Xue, Science **340**, 167 (2013).

[25] J. G. Checkelsky, R. Yoshimi, A. Tsukazaki, K. S. Takahashi, Y. Kozuka, J. Falson, M. Kawasaki, and Y. Tokura, Nat. Phys. **10**, 731 (2014).

[26] X.-L. Qi, T. L. Hughes, and S.-C. Zhang, Phys. Rev. B **78**, 195424 (2008).

[27] K. Fujikawa, Phys. Rev. Lett. **42**, 1195 (1979).

[28] K. Fujikawa, Phys. Rev. D **21**, 2848 (1980).

[29] X. Wan, A. M. Turner, A. Vishwanath, and S. Y. Savrasov, Phys. Rev. B **83**, 205101 (2011).

[30] G. E. Volovik, *The Universe in a Helium Droplet* (Clarendon, Oxford, 2003).

[31] G. E. Volovik, Lect. Notes Phys. **718**, 31 (2007).

[32] S. Murakami, New J. Phys. **9**, 356 (2007).

[33] A. A. Burkov and L. Balents, Phys. Rev. Lett. **107**, 127205 (2011).

[34] A. A. Burkov, M. D. Hook, and L. Balents, Phys. Rev. B **84**, 235126 (2011).

[35] G. B. Halász and L. Balents, Phys. Rev. B **85**, 035103 (2012).

[36] A. A. Zyuzin, S. Wu, and A. A. Burkov, Phys. Rev. B **85**, 165110 (2012).

[37] W. Witczak-Krempa and Y. B. Kim, Phys. Rev. B **85**, 045124 (2012).

[38] A. Go, W. Witczak-Krempa, G. S. Jeon, K. Park, and Y. B. Kim, Phys. Rev. Lett. **109**, 066401 (2012).

[39] L. Balents, Physics **4**, 36 (2011).

[40] P. Delplace, J. Li, and D. Carpentier, Europhys. Lett. **97**, 67004 (2012).

[41] N. Nagaosa, J. Sinova, S. Onoda, A. H. MacDonald, and N. P. Ong, Rev. Mod. Phys. **82**, 1539 (2010).

[42] K.-Y. Yang, Y.-M. Lu, and Y. Ran, Phys. Rev. B **84**, 075129 (2011).

[43] A. A. Zyuzin and A. A. Burkov, Phys. Rev. B **86**, 115133 (2012).

[44] Z. Wang and S.-C. Zhang, Phys. Rev. B **87**, 161107 (2013).

[45] M. M. Vazifeh and M. Franz, Phys. Rev. Lett. **111**, 027201 (2013).

[46] P. Goswami and S. Tewari, Phys. Rev. B **88**, 245107 (2013).

[47] K. Fukushima, D. E. Kharzeev, and H. J. Warringa, Phys. Rev. D **78**, 074033 (2008).

[48] S. M. Young, S. Zaheer, J. C. Y. Teo, C. L. Kane, E. J. Mele, and A. M. Rappe, Phys. Rev. Lett. **108**, 140405 (2012).

[49] Z. Wang, Y. Sun, X.-Q. Chen, C. Franchini, G. Xu, H. Weng, X. Dai, and Z. Fang, Phys. Rev. B **85**, 195320 (2012).

[50] Z. Wang, H. Weng, Q. Wu, X. Dai, and Z. Fang, Phys. Rev. B **88**, 125427 (2013).

[51] Z. K. Liu, B. Zhou, Y. Zhang, Z. J. Wang, H. M. Weng, D. Prabhakaran, S.-K. Mo, Z. X. Shen, Z. Fang, X. Dai, Z. Hussain, and Y. L. Chen, Science **343**, 864 (2014).

[52] M. Neupane, S.-Y. Xu, R. Sankar, N. Alidoust, G. Bian, C. Liu, I. Belopolski, T.-R. Chang, H.-T. Jeng, H. Lin, A. Bansil, F. Chou, and M. Z. Hasan, Nat. Commun. **5**, 3786 (2014).

[53] S. Borisenko, Q. Gibson, D. Evtushinsky, V. Zabolotnyy, B. Büchner, and R. J. Cava, Phys. Rev. Lett. **113**, 027603 (2014).

[54] X. Cheng, R. Li, Y. Sun, X.-Q. Chen, D. Li, and Y. Li, Phys. Rev. B **89**, 245201 (2014).

[55] L. P. He, X. C. Hong, J. K. Dong, J. Pan, Z. Zhang, J. Zhang, and S. Y. Li, arXiv:1404.2557.

[56] A. H. Castro Neto, N. M. R. Peres, K. S. Novoselov, and A. K. Geim, Rev. Mod. Phys. **81**, 109 (2009).

[57] T. Sato, K. Segawa, K. Kosaka, S. Souma, K. Nakayama, K. Eto, T. Minami, Y. Ando, and T. Takahashi, Nat. Phys. **7**, 840 (2011).

[58] D. Kurebayashi and K. Nomura, J. Phys. Soc. Jpn. **83**, 063709 (2014).

[59] M. Imada, A. Fujimori, and Y. Tokura, Rev. Mod. Phys. **70**, 1039 (1998).

[60] Y. Tokura and N. Nagaosa, Science **288**, 462 (2000).

[61] E. Dagotto, Science **309**, 257 (2005).

[62] B. J. Kim, H. Jin, S. J. Moon, J.-Y. Kim, B.-G. Park, C. Leem, J. Yu, T. Noh, C. Kim, S.-J. Oh, J.-H. Park, V. Durairaj, G. Cao, and E. Rotenberg, Phys. Rev. Lett. **101**, 076402 (2008).

[63] B. J. Kim, H. Ohsumi, T. Komesu, S. Sakai, T. Morita, H. Takagi, and T. Arima, Science **323**, 1329 (2009).

[64] G. Jackeli and G. Khaliullin, Phys. Rev. Lett. **102**, 017205 (2009).

[65] A. Shitade, H. Katsura, J. Kuneš, X.-L. Qi, S.-C. Zhang, and N. Nagaosa, Phys. Rev. Lett. **102**, 256403 (2009).

[66] D. Pesin and L. Balents, Nat. Phys. **6**, 376 (2010).

[67] R. Li, J. Wang, X.-L. Qi, and S.-C. Zhang, Nat. Phys. **6**, 284 (2010).

[68] A. Rüegg and G. A. Fiete, Phys. Rev. Lett. **108**, 046401 (2012).

[69] J. Maciejko, V. Chua, and G. A. Fiete, Phys. Rev. Lett. **112**, 016404 (2014).

[70] S. Raghu, X.-L. Qi, C. Honerkamp, and S.-C. Zhang, Phys. Rev. Lett. **100**, 156401 (2008).

[71] Y. Zhang, Y. Ran, and A. Vishwanath, Phys. Rev. B **79**, 245331 (2009).

[72] M. Kurita, Y. Yamaji, and M. Imada, J. Phys. Soc. Jpn. **80**, 044708 (2011).

[73] N. A. García-Martínez, A. G. Grushin, T. Neupert, B. Valenzuela, and E. V. Castro, Phys. Rev. B **88**, 245123 (2013).

[74] M. Daghofer and M. Hohenadler, Phys. Rev. B **89**, 035103 (2014).

[75] M. W. Young, S.-S. Lee, and C. Kallin, Phys. Rev. B **78**, 125316 (2008).

[76] S. Rachel and K. Le Hur, Phys. Rev. B **82**, 075106 (2010).

[77] C. N. Varney, K. Sun, M. Rigol, and V. Galitski, Phys. Rev. B **82**, 115125 (2010).

[78] M. Hohenadler, T. C. Lang, and F. F. Assaad, Phys. Rev. Lett. **106**, 100403 (2011).

[79] S.-L. Yu, X. C. Xie, and J.-X. Li, Phys. Rev. Lett. **107**, 010401 (2011).

[80] Y. Yamaji and M. Imada, Phys. Rev. B **83**, 205122 (2011).

[81] D. Zheng, G.-M. Zhang, and C. Wu, Phys. Rev. B **84**, 205121 (2011).

[82] M. Hohenadler, Z. Y. Meng, T. C. Lang, S. Wessel, A. Muramatsu, and F. F. Assaad, Phys. Rev. B **85**, 115132 (2012).

[83] T. Yoshida, S. Fujimoto, and N. Kawakami, Phys. Rev. B **85**, 125113 (2012).

[84] Y. Tada, R. Peters, M. Oshikawa, A. Koga, N. Kawakami, and S. Fujimoto, Phys. Rev. B **85**, 165138 (2012).

[85] A. Vaezi, M. Mashkoori, and M. Hosseini, Phys. Rev. B **85**, 195126 (2012).

[86] W. Wu, S. Rachel, W.-M. Liu, and K. Le Hur, Phys. Rev. B **85**, 205102 (2012).

[87] M. Hohenadler and F. F. Assaad, J. Phys. Condens. Matter **25**, 143201 (2013).

[88] T. Liu, B. Douçot, and K. Le Hur, Phys. Rev. B **88**, 245119 (2013).

[89] A. Sekine and K. Nomura, J. Phys. Soc. Jpn. **82**, 033702 (2013).

[90] T. Yoshida, R. Peters, S. Fujimoto, and N. Kawakami, Phys. Rev. B **87**, 085134 (2013).

[91]  R. S. K. Mong, A. M. Essin, and J. E. Moore, Phys. Rev. B **81**, 245209 (2010).

[92]  H. Wei, S.-P. Chao, and V. Aji, Phys. Rev. Lett. **109**, 196403 (2012).

[93]  J. Maciejko and R. Nandkishore, Phys. Rev. B **90**, 035126 (2014).

[94]  H. Wei, S.-P. Chao, and V. Aji, Phys. Rev. B **89**, 235109 (2014).

[95]  K. G. Wilson, Phys. Rev. D **10**, 2445 (1974).

[96]  V. N. Kotov, B. Uchoa, V. M. Pereira, F. Guinea, and A. H. Castro Neto, Rev. Mod. Phys. **84**, 1067 (2012).

[97]  D. V. Khveshchenko, Phys. Rev. Lett. **87**, 246802 (2001).

[98]  D. V. Khveshchenko and H. Leal, Nucl. Phys. B **687**, 323 (2004).

[99]  D. V. Khveshchenko, J. Phys. Condens. Matter **21**, 075303 (2009).

[100]  S. Hands and C. Strouthos, Phys. Rev. B **78**, 165423 (2008).

[101]  J. E. Drut and T. A. Lähde, Phys. Rev. Lett. **102**, 026802 (2009).

[102]  J. E. Drut and T. A. Lähde, Phys. Rev. B **79**, 165425 (2009).

[103]  Y. Araki and T. Hatsuda, Phys. Rev. B **82**, 121403 (2010).

[104]  W. Armour, S. Hands, and C. Strouthos, Phys. Rev. B **84**, 075123 (2011).

[105]  J. Giedt, A. Skinner, and S. Nayak, Phys. Rev. B **83**, 045420 (2011).

[106]  P. V. Buividovich, E. V. Luschevskaya, O. V. Pavlovsky, M. I. Polikarpov, and M. V. Ulybyshev, Phys. Rev. B **86**, 045107 (2012).

[107]  Y. Araki, Phys. Rev. B **85**, 125436 (2012).

[108]  M. E. Peskin and D. V. Schroeder, *An Introduction to Quantum Field Theory* (Westview Press, 1995).

[109]  J. Kogut, E. Dagotto, and A. Kocic, Phys. Rev. Lett. **60**, 772 (1988).

[110]  E. Dagotto, J. Kogut, and A. Kocic, Phys. Rev. Lett. **62**, 1083 (1989).

[111]  M. Göckeler, R. Horsley, E. Laermann, P. Rakow, G. Schierholz, R. Sommer, and U.-J. Wiese, Nucl. Phys. B **334**, 527 (1990).

[112]  G. W. Semenoff, Phys. Rev. Lett. **53**, 2449 (1984).

[113]  D. T. Son, Phys. Rev. B **75**, 235423 (2007).

[114]  H. B. Nielsen and M. Ninomiya, Phys. Lett. B **105**, 219 (1981); Nucl. Phys. B **185**, 20 (1981); Nucl. Phys. B **193**, 173 (1981).

[115]  J. Kogut and L. Susskind, Phys. Rev. D **11**, 395 (1975).

[116] L. Susskind, Phys. Rev. D **16**, 3031 (1977).

[117] N. Kawamoto and J. Smit, Nucl. Phys. B **192**, 100 (1981).

[118] 青木慎也, 「格子上の場の理論」 (Springer Japan, 2005).

[119] C. Burden and A. N. Burkitt, Europhys. Lett. **3**, 545 (1987).

[120] *Collaboration: Authors and Editors of the Volumes III/17E-17F- 41C: Bismuth Selenide (Bi$_2$Se$_3$) Optical Properties, Dielectric Constants,* edited by O. Madelung, U. Rossler, and M. Schulz, The Landolt-Bornstein Database (Springer, Berlin, 1998).

[121] N. Kawamoto and J. Smit, Nucl. Phys. B **192**, 100 (1981).

[122] J. Hoek, N. Kawamoto, and J. Smit, Nucl. Phys. B **199**, 495 (1982).

[123] J.-M. Drouffe and J.-B. Zuber, Phys. Rep. **102**, 1 (1983).

[124] Y. Nishida, Phys. Rev. D **69**, 094501 (2004).

[125] K. Miura, T. Nakano, A. Ohnishi, and N. Kawamoto, Phys. Rev. D **80**, 074034 (2009).

[126] R. Kubo, J. Phys. Soc. Jpn. **17**, 1100 (1962).

[127] P. Menotti and A. Pelissetto, Commun. Math. Phys. **113**, 369 (1987).

[128] S. Aoki, Phys. Rev. D **30**, 2653 (1984).

[129] S. Aoki, Phys. Rev. Lett. **57**, 3136 (1986).

[130] S. Sharpe and R. Singleton, Phys. Rev. D **58**, 074501 (1998).

[131] Y. Araki and T. Kimura, Phys. Rev. B **87**, 205440 (2013).

[132] D. Baasanjav, O. A. Tretiakov, and K. Nomura, Phys. Rev. B **90**, 045149 (2014).

[133] F. D. M. Haldane, Phys. Rev. Lett. **61**, 2015 (1988).

[134] J.-N. Fuchs and P. Lederer, Phys. Rev. Lett. **98**, 016803 (2007).

[135] F. Wilczek, Phys. Rev. Lett. **58**, 1799 (1987).

[136] R. D. Peccei and H. R. Quinn, Phys. Rev. Lett. **38**, 1440 (1977); R. D. Peccei and H. R. Quinn, Phys. Rev. D **16**, 1791 (1977).

[137] S. Weinberg, Phys. Rev. Lett. **40**, 223 (1978).

[138] F. Wilczek, Phys. Rev. Lett. **40**, 279 (1978).

[139] *Axions*, ed. M. Kuster, G. Raffelt, and B. Beltrán (Springer Berlin/Heidelberg, 2008).

[140] H. Ooguri and M. Oshikawa, Phys. Rev. Lett. **108**, 161803 (2012).

[141] A. M. Essin, J. E. Moore, and D. Vanderbilt, Phys. Rev. Lett. **102**, 146805 (2009).

[142] A. M. Essin, A. M. Turner, J. E. Moore, and D. Vanderbilt, Phys. Rev. B **81**, 205104 (2010).

[143] S. Coh, D. Vanderbilt, A. Malashevich, and I. Souza, Phys. Rev. B **83**, 085108 (2011).

[144] J. Wang, R. Li, S.-C. Zhang, and X.-L. Qi, Phys. Rev. Lett. **106**, 126403 (2011).

[145] See, for example, Y. Zhang, Y. Ran, and A. Vishwanath, Phys. Rev. B **79**, 245331 (2009); M. Kurita, Y. Yamaji, and M. Imada, J. Phys. Soc. Jpn. **80**, 044708 (2011).

[146] M. Nakamura, J. Phys. Soc. Jpn. **68**, 3123 (1999); M. Nakamura, Phys. Rev. B **61**, 16377 (2000).

[147] M. Tsuchiizu and A. Furusaki, Phys. Rev. Lett. **88**, 056402 (2002).

[148] S. Aoki, S. Boettcher, and A. Gocksch, Phys. Lett. B **331**, 157 (1994).

[149] V. Azcoiti, G. Di Carlo, E. Follana, M. Giordano, and A. Vaquero, Nucl. Phys. B **875**, 45 (2013).

# List of Publications and Presentations

## Original Papers

6. *"Stability of Multinode Dirac Semimetals against Strong Long-Range Correlations"*
   Akihiko Sekine & Kentaro Nomura
   Phys. Rev. B **90**, 075137-1-7 (2014).

5. *"Axionic Antiferromagnetic Insulator Phase in a Correlated and Spin-Orbit Coupled System"*
   Akihiko Sekine & Kentaro Nomura
   J. Phys. Soc. Jpn. **83**, 104709-1-7 (2014).

4. *"Weyl Semimetal in the Strong Coulomb Interaction Limit"*
   Akihiko Sekine & Kentaro Nomura
   J. Phys. Soc. Jpn. **83**, 094710-1-8 (2014).

3. *"Strong Coupling Expansion in a Correlated Three-Dimensional Topological Insulator"*
   Akihiko Sekine, Takashi Z. Nakano, Yasufumi Araki & Kentaro Nomura
   Phys. Rev. B **87**, 165142-1-9 (2013).

2. *"Electron Correlation Induced Spontaneous Symmetry Breaking and Weyl Semimetal Phase in a Strongly Spin-Orbit Coupled System"*
   Akihiko Sekine & Kentaro Nomura
   J. Phys. Soc. Jpn. **82**, 033702-1-4 (2013).

1. *"Polar Charge Fluctuation and Superconductivity in Organic Conductors"*
   Akihiko Sekine, Joji Nasu & Sumio Ishihara
   Phys. Rev. B **87**, 085133-1-6 (2013).

## Proceedings

4. *"Weyl Semimetal with Strong Long-Range Coulomb Interactions"*
   Akihiko Sekine & Kentaro Nomura
   J. Phys.: Conf. Ser. (accepted)

3. *"Magnetoelectric Response of the Antiferromagnetic Insulator Phase in a Three-Dimensional Correlated System with Spin-Orbit Coupling"*
   Akihiko Sekine & Kentaro Nomura

J. Phys.: Conf. Ser. (accepted)

2. *"Phase Structure of Topological Insulators by Lattice Strong-Coupling Expansion"*
Yasufumi Araki, Taro Kimura, <u>Akihiko Sekine</u>, Kentaro Nomura & Takashi Z. Nakano
PoS (LATTICE 2013) 050-1-7 (2014).

1. *"Effect of Strong Coulomb Interaction in a Three-Dimensional Topological Insulator"*
<u>Akihiko Sekine</u>, Takashi Z. Nakano, Yasufumi Araki & Kentaro Nomura
JPS Conf. Proc. **3**, 016008-1-5 (2014).

# Invited Talk

<u>Akihiko Sekine</u>
*"Axionic Antiferromagnetic Insulator Phase in a Correlated and Spin-Orbit Coupled System"*
EMN Summer Meeting 2014 (Cancun, Mexico), June 9-12, 2014.

# Presentations at International Conferences and Workshops

5. <u>Akihiko Sekine</u> & Kentaro Nomura
*"Weyl Semimetal with Strong Long-Range Coulomb Interactions"* [Poster]
International Workshop on Dirac Electrons in Solids (Tokyo, Japan) P-10, January 14-15, 2015.

4. <u>Akihiko Sekine</u> & Kentaro Nomura
*"Magnetoelectric response of the antiferromagnetic insulator phase in a three-dimensional correlated system with spin-orbit coupling"* [Poster]
Strongly Correlated Electron Systems 2014 (Grenoble, France) We-256, July 7-11, 2014.

3. <u>Akihiko Sekine</u>, Takashi Z. Nakano, Yasufumi Araki & Kentaro Nomura
*"Strong Coupling Analysis of a Correlated Three-Dimensional Topological Insulator"* [Poster]
International Workshop for Young Researchers on Topological Quantum Phenomena in Condensed Matter with Broken Symmetries 2013 (Okinawa, Japan) P-39, October 22-26, 2013.

2. <u>Akihiko Sekine</u>, Takashi Z. Nakano, Yasufumi Araki & Kentaro Nomura
*"Effect of Strong Coulomb Interaction in a Three-Dimensional Topological Insulator"* [Poster]
Strongly Correlated Electron Systems 2013 (Tokyo, Japan) 8P-207, August 5-9, 2013.

1. <u>Akihiko Sekine</u> & Kentaro Nomura
*"Electron Correlation Induced Spontaneous Symmetry Breaking in a Strongly Spin-Orbit Coupled System"* [Poster]
The 5th GCOE International Symposium on "Weaving Science Web beyond Particle-Matter Hierarchy" (Sendai, Japan) P-29, March 4-6, 2013.

# Presentations at Domestic Conferences and Workshops

8. 関根聡彦，野村健太郎
   『電子相関を有するスピン軌道結合系におけるアクシオン反強磁性絶縁相』［口頭］
   日本物理学会 2014 年秋季大会（中部大学）9pAX-10, 2014 年 9 月 7-10 日.

7. 関根聡彦，野村健太郎
   『格子ゲージ理論に基づいた Weyl 半金属における電子相関効果の研究』［口頭］
   日本物理学会 第 69 回年次大会（東海大学）27pBF-4, 2014 年 3 月 27-30 日.

6. 関根聡彦，中野嵩士，荒木康史，野村健太郎
   『格子ゲージ理論に基づいた 3 次元トポロジカル絶縁体における強相関効果の研究』
   ［ポスター］
   第 7 回物性科学領域横断研究会（東京大学）P2-27, 2013 年 12 月 1-2 日.

5. 関根聡彦，中野嵩士，荒木康史，野村健太郎
   『3 次元トポロジカル絶縁体における電子相関効果の格子ゲージ理論に基づいた解析』
   ［口頭］
   日本物理学会 2013 年秋季大会（徳島大学）25aDK-5, 2013 年 9 月 25-28 日.

4. 関根聡彦，中野嵩士，荒木康史，野村健太郎
   『格子ゲージ理論に基づいた 3 次元トポロジカル絶縁体における電子相関効果の研究』
   ［口頭］
   基研研究会「固体中におけるディラック電子系物理の新展開」（京都大学）, 2013 年 6 月
   19-21 日.

3. 関根聡彦，野村健太郎
   『3 次元トポロジカル絶縁体における電子相関効果』［口頭］
   日本物理学会 第 68 回年次大会（広島大学）26aXJ-1, 2013 年 3 月 26-29 日.

2. 関根聡彦，那須譲治，石原純夫
   『ダイマー内の電荷自由度を有する相関電子系における超伝導 II』［ポスター］
   日本物理学会 2012 年秋季大会（横浜国立大学）20pPSB-65, 2012 年 9 月 18-21 日.

1. 関根聡彦，那須譲治，石原純夫
   『ダイマー内の電荷自由度を有する相関電子系における超伝導』［口頭］
   日本物理学会 第 67 回年次大会（関西学院大学）25aYF-14, 2012 年 3 月 24-27 日.